Fluctuating Surface Currents: A New Algorithm for Efficient Prediction of Casimir Interactions among Arbitrary Materials in Arbitrary Geometries
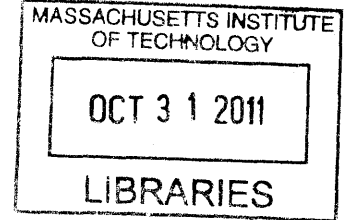
by

M. T. Homer Reid

Submitted to the Department of Physics
in partial fulfillment of the requirements for the degree of

Doctor of Philosophy

at the

MASSACHUSETTS INSTITUTE OF TECHNOLOGY

February 2011

The author hereby grants to MIT permission to reproduce and distribute publicly paper and electronic copies of this thesis document in whole or in part.

Author ....

<div align="right">Department of Physics

January 7, 2010</div>

Certified by........

<div align="right">Jacob White

Professor

Thesis Supervisor</div>

Certified by...

<div align="right">Steven G. Johnson

Professor

Thesis Supervisor</div>

Accepted by ....

<div align="right">Krishna Rajagopal

Associate Department Head for Education</div>

Fluctuating Surface Currents: A New Algorithm for Efficient Prediction of Casimir Interactions among Arbitrary Materials in Arbitrary Geometries

by

M. T. Homer Reid

Submitted to the Department of Physics
on January 6, 2011, in partial fulfillment of the
requirements for the degree of
Doctor of Philosophy

Abstract

For most of its 60 year history, the Casimir effect was an obscure theoretical back-water, but technological advances over the past decade have promoted this curious manifestation of quantum and thermal fluctuations to a position of central importance in modern experimental physics. Dramatic progress in the measurement of Casimir forces since 1997 has created a demand for theoretical tools that can predict Casimir interactions in realistic experimental geometries and in materials with realistic frequency-dependent electrical properties.

This work presents a new paradigm for efficient numerical computation of Casimir interactions. Our new technique, which we term the *fluctuating-surface-current* (FSC) approach to computational Casimir physics, borrows ideas from the boundary-element method of computational electromagnetism to express Casimir energies, forces, and torques between bodies of arbitrary shapes and materials in terms of interactions among effective electric and magnetic surface currents flowing on the surfaces of the objects. We demonstrate that the master equations of the FSC approach arise as logical consequences of either of two seemingly disparate Casimir paradigms—the *stress-tensor* approach and the *path-integral* (or *scattering*) approach—and this work thus achieves an unexpected unification of these two otherwise quite distinct theoretical frameworks.

But a theoretical technique is only as relevant as its practical implementations are useful, and for this reason we present three distinct numerical implementations of the FSC formulae, each of which poses a series of unique technical challenges. Finally, using our new theoretical paradigm and our practical implementations of it, we obtain new predictions of Casimir interactions in a number of experimentally relevant geometric and material configurations that would be difficult or impossible to treat with any other existing Casimir method.

Thesis Supervisor: Jacob White
Title: Professor

Thesis Supervisor: Steven G. Johnson
Title: Professor

This thesis is dedicated
to Don Chambers
who taught me about van der Waals forces
and also
that science is fun.

Acknowledgments 1

In January 2005 I was a broken man. Bitter and demoralized after a disastrous two-year stint as a graduate student in experimental physics, convinced I was a failure as a scientist, certain that scientific academia was the exclusive province of soulless personality-challenged automatons and that routine emotional abuse was just another component of the scientific process, I resolved to quit physics and return to industrial engineering. In a desperate last-ditch attempt to salvage some semblance of value from my years in school, I began searching for a supervisor for one final project—a master's thesis. I identified a list of eleven professors and sent cover letters and emails. Seven sent no reply. One turned out to be on sabbatical. Two wrote back politely declining.

One invited me by for a chat. "Stop by this afternoon," wrote Jacob White. "I'm sure we can come up with something."

My real graduate education began that day. Over the following years, as my master's program quickly turned back into doctoral program, I would learn how circuit simulators work and how the semiconductor industry extracts parasitics from its fabrication processes. I would get one-on-one tutelage from one of the world's leading experts on boundary-element methods and iterative solvers for engineering applications. I would learn how to use MATLAB as a fine-grained precision scalpel for surgically identifying exactly which matrix elements were responsible for the misbehavior of my numerical algorithms. Most importantly, I would learn that science could actually be *fun* again, and that there were decent, ethical people—caring people—*people-skills* people—in the sciences after all. And, for all the urgent and immediate applications of boundary-element Casimir modeling to the problems of human civilization, somehow I suspect it will be *these* lessons that resonate most deeply throughout the remainder of my life and career.

For salvaging my academic career, for sharing with me his inimitable prowess in the numerical sciences, for encouraging and supporting me throughout my graduate research, and for educating me, by his example, that scientists can be people-skills people too, I will always remain grateful to Professor Jacob White.

Acknowledgments 2

By March 2007 I was no longer a broken man, but in many ways I remained a *deluded* one. I had convinced myself that certain ill-advised, speculative, fantastical notions I had dreamed up for how to accelerate problems in computational many-body physics were going to generate enough research results to constitute a PhD thesis and present a path to graduation. My ideas were seminal! My ideas were revolutionary! Not only would my ideas lead to a PhD thesis, my ideas would change the world!

My ideas fizzled. Nothing would come of them, nor *could* anything have come of them, half-baked as they were—and yet, as clearly as I can see this today, I might nonetheless still be toiling away in myopic obscurity had not a wise mentor stepped in gently to disabuse me of my hallucinations and steer me in a vastly more productive direction.

For the wisdom to foresee that numerical techniques in computational electromagnetism could be used to predict Casimir forces, for spearheading the world's first effort in this direction, for sharing the idea with me and suggesting the use of boundary-element methods—thus putting me on a solid road toward graduation—and for his indefatigable subsequent efforts at keeping me on that road and helping me surmount bumps in it, I am deeply grateful to Professor Steven G. Johnson.

Contents

Chapter 1

Overview

During the academic year, MIT's Department of Physics convenes a weekly *physics colloquium* at which an eminent physicist regales the physics community with tales of the latest developments in various hot subfields of contemporary physics. In my first years of graduate school, too busy with coursework to attend every week's session, I developed an algorithm for determining which colloquia I would attend. Talks pertaining to my research, or to research I aspired to do in the future, I would always attend. Talks on subjects not related to my research, but still of general interest and with interesting applications to the real world, I would sometimes attend. Talks on speculative esoterica, talks on abstract technobabble, and talks that seemed to bear no fathomable relationship to any real-world phenomena I might expect to encounter in my lifetime, I would *never* attend.

Casimir physics fell squarely within this latter sector of my classification scheme. Like all physicists, I had at least *heard* of the Casimir effect, through footnotes, through lore, and from a particularly forbidding and impenetrable section in one of the Landau and Lifshitz textbooks. Some sketchy-sounding claptrap about vacuum energy and quantum fluctuations? A divergent expression for the energy that can be massaged through some sort of contrived mathematical procedure to give a finite force law? Vaguely interesting, a curious diversion, but certainly nothing you would actually want to *work* on.

My dismissive attitude might perhaps have been justifiable in any of the first 50 years after the birth of the Casimir effect, but it was already outdated when I entered graduate school in 2002, and today, in 2010, it is entirely obsolete. The advent of precision Casimir experiments in the years after 1996 promoted Casimir physics from the realm of *gedankenexperiment* to a central position in modern experimental physics, with a substantial and growing catalog of measurements of Casimir interactions in a wide range of materials and geometries. This rapid development on the experimental side has, in turn, spurred an interdisciplinary effort on the part of theoretical physicists, numerical analysts, and engineers to develop new algorithms and tools capable of predicting Casimir phenomena in realistic experimental configurations. It is this latter effort that provides the context and motivation for this thesis.

This thesis introduces a new technique for predicting Casimir forces between objects of arbitrarily complicated geometries with arbitrary material properties. Our

new technique, which we term the *fluctuating-surface-current* (FSC) approach to computational Casimir physics, combines ideas from electrical engineering, theoretical physics, and numerical analysis to yield a procedure that accurately and efficiently calculates Casimir energies, forces, and torques between objects of arbitrary two- and three-dimensional shapes with arbitrary frequency-dependent electrical characteristics. This thesis presents two separate theoretical derivations of the fundamental FSC formulae, discusses three separate practical numerical implementations of the formulae for predicting Casimir phenomena in various situations, and then uses the FSC approach to predict Casimir forces and torques in a number of new geometries that would be difficult to handle using any other Casimir method.

An Overview of this Thesis

We now offer brief synopses of the remaining chapters in this thesis.

The first three chapters beyond this introduction provide key background for what follows. **Chapter 2** reviews the physics of the Casimir effect, including three distinct theoretical interpretations of the effect and a synopsis of the current state of the art in experimental investigations. This sets the stage for an overview, in **Chapter 3**, of the two dominant paradigms that have emerged in the past decade for predicting Casimir phenomena—the *numerical stress-tensor* approach and the *path-integral* (or *scattering*) approach. The former of these two approaches relies, in practice, on a choice of numerical method for solving electromagnetic scattering problems, and the particular method we choose in this work—the *boundary-element method* (BEM)—is reviewed in **Chapter 4**.

The original contributions of this thesis begin in **Chapter 5**. In the first half of that chapter we demonstrate that BEM techniques, applied within the stress-tensor paradigm of computational Casimir physics, yield remarkably simple expressions— our *fluctuating-surface-current* formulae—for Casimir interactions (energies, forces, and torques) between objects of arbitrarily complex geometries and arbitrary material properties. Then, in the second half of the chapter, we switch gears entirely, abandon the stress-tensor paradigm, apply BEM ideas instead within the alternative context of the path-integral approach, and demonstrate nonetheless that precisely the *same* fluctuating-surface-current formulae emerge from this seemingly inequivalent approach. The fluctuating-surface-current (FSC) formulae, and our simultaneous derivation of these expressions from two entirely disparate starting points (stress tensors and path integrals), constitute the essential new theoretical contribution of this work.

But modern Casimir physics is an experimentally-driven field, and theoretical techniques in such a field are only as valuable as their real-world implementations are practical, efficient, and accurate. Thus the next three chapters of this thesis are devoted to detailed discussions of three separate numerical implementations of the FSC formulae. In **Chapter 6**, we discuss CASIMIR3D, a numerical tool that uses the FSC formulae to compute Casimir energies, forces, and torques in geometries consisting of *compact three-dimensional objects* of arbitrary shapes and of arbitrary material properties. In **Chapter 7**, we discuss CASIMIR2D, a tool similar to CASIMIR3D but

Background

New Contributions
Theory | Applications

Chapter 2
The Casimir Effect

Chapter 3
Modern Methods for Casimir Calculations

Chapter 4
The Boundary-Element Method

Chapter 5
Fluctuating Surface Currents
A New Paradigm for Efficient Casimir Computations in Arbitrary Geometries and Materials

Chapter 6
Casimir3D: Casimir Calculations for 3D Objects

Chapter 7
Casimir2D: Casimir Calculations for 2D Objects

Chapter 8
FastCasimir: Improved Scaling for Casimir Calculations

Chapter 9
Results Casimir predictions in new geometries

Figure 1-1: A schematic interrelationship of the chapters in this thesis.

designed for computing Casimir energies and forces per unit length between *quasi-2D objects*—that is, three-dimensional objects of infinite extent in one spatial dimension and constant two-dimensional cross-section in the transverse dimensions. Then, in **Chapter 8**, we discuss FASTCASIMIR, a numerical tool that uses matrix-sparsification techniques to improve the complexity scaling of CASIMIR3D for large-scale computations of Casimir interactions between perfectly electrically conducting bodies.

Our FSC formulae and its various numerical implementations are brought to fruition in **Chapter 9**. Here we present the first predictions of Casimir interactions in a number of experimentally relevant configurations that would be prohibitively expensive, if not outright impossible, to address using any other computational Casimir technique, including crossed cylindrical capsules, tetrahedral nanoparticles, disc-shaped nanoparticles of finite radius and thickness, and elongated beams of irregular polygonal cross-section.

Finally, in **Chapter 10** we present our conclusions and suggest direction for future work, and a series of technical details are relegated to the Appendices.

What's New in This Thesis

We now point out the key new results that are presented for the first time in this thesis.

The Boundary-Element Method as an Analytical Technique

The boundary-element method of computational electromagnetism, which is reviewed in Chapter 4, is a well-established technique that has been used for decades to solve electromagnetic scattering problems. However, all previous applications of this technique (of which we are aware) have used it only as a *numerical* tool. A key innovation of this thesis is our use of boundary-element ideas in an *analytical* context to prove theorems. In particular, our expressions (5.4-5.5) and (5.18-5.19) for the scattered parts of dyadic Green's functions are new, and are a critical ingredient in our stress-tensor derivation of the FSC formulae (5.1).

Analytic Evaluation of Stress-Tensor Integral

The numerical stress-tensor approach to Casimir physics, which is reviewed in Chapter 3, is a well-established technique in computational Casimir physics that expresses the Casimir force as a two-dimensional integral (with a rather complicated integrand) over a closed surface C. In all previous applications of this technique to the computation of Casimir forces in general geometries, this surface integral over C has been evaluated *numerically* using numerical cubature techniques.

In contrast, in this thesis we demonstrate that the stress-tensor expression for the Casimir force may be written in a factorized form, in which factors that depend on C are separated from those that do not, and that this separation allows the spatial integral over C to be evaluated *analytically*, in closed form, for arbitrary bounding surfaces. This obviates numerical cubature, eliminates all dependence on the arbitrary bounding surface C, and leads to a tremendously simplified version of the stress-tensor formula (our master FSC formulae (5.1)).

This story is told in Section 5.2. The key new theorem that enables it is stated and proved in Appendix C.

Evaluation of Electrodynamic Casimir Path Integrals using Surface Unknowns

The path-integral approach to Casimir computations, which is reviewed in Chapter 3, is a well-established technique in computational Casimir physics that expresses Casimir energies as functional integrals over *fields*, which are converted to finite-dimensional integrals over *sources* (or Lagrange multipliers). In early path-integral treatments of Casimir phenomena involving scalar fields, these sources were taken to be *surface unknowns* defined on the boundary surfaces of the interacting objects. However, when the path-integral technique was later extended to encompass electrodynamic Casimir interactions in general geometries, the surface unknowns were

abandoned in favor of other sets of unknowns (such as multipole moments) that do not have an immediate interpretation as surface unknowns.

In this thesis, for the first time, we use surface unknowns to evaluate electrodynamic Casimir energies. This story is told in Section 5.3, where we show that a path-integral formula for electrodynamic Casimir energies, evaluated with the help of surface unknowns, leads to the same compact and simple expressions obtained (from an entirely different starting point) in Section 5.2 (our master FSC formulae (5.1)).

Manifestly Gauge-Invariant Treatment of Electrodynamic Casimir Forces

Previous path-integral treatments of electrodynamic Casimir phenomena in general geometries have concealed the underlying gauge-invariance of the theory by working in a fixed gauge throughout the calculation. This thesis presents (in Section 5.3) a *manifestly gauge-invariant* procedure for the evaluation of electrodynamic Casimir energies.

New Techniques for Evaluation of BEM Matrix Elements

A key ingredient in BEM solvers for 3D electromagnetic scattering problems is a procedure for evaluating BEM matrix elements between localized basis functions, a task involving large numbers of multidimensional integrals with rapidly varying or even singular integrands.

This thesis presents new and comprehensive suites of techniques for evaluating these integrals in two different BEM contexts: matrix elements between RWG basis functions for scattering problems involving compact 3D objects, and matrix elements between two-dimensional rooftop functions for scattering problems involving quasi-2D objects.

A Fast Matrix-Vector Product for the Imaginary-Frequency EFIE

The precorrected-FFT technique, which was invented in the 1990s [36], improves the complexity scaling of numerical linear algebra operations involving certain matrices that arise in computational electromagnetism problems. The technique was first applied to boundary-element analysis of real-frequency scattering problems in [12].

Chapter 8 of this thesis presents the first application of the PFFT technique to the *imaginary-frequency* boundary-element method. This work also represents the first steps toward a "fast solver" (i.e. a numerical technique exhibiting reduced scaling of storage and CPU-time requirements) for computational Casimir problems.

New Predictions of Casimir Interactions in Complex Geometries and Materials

Using the new computational Casimir paradigm presented in Chapter 5, we obtain the first predictions of Casimir interactions in a number of new configurations that would be difficult, if not outright impossible, to treat using any existing method, including crossed cylindrical capsules, tetrahedral nanoparticles, disc-shaped nanoparticles of

finite radius and thickness, and elongated silicon beams of irregular polygonal cross-section.

Chapter 2

Casimir Physics: Some Theoretical and Experimental Perspectives

The late 1940s was an era of epochal advances in the understanding of the vacuum sector of quantum electrodynamics. In 1947, the Lamb shift demonstrated that QED vacuum effects modify the Coulomb force between charged particles [24, 4]. In 1948, the anomalous magnetic moment of the electron demonstrated that vacuum effects modify the coupling of a charged particle to a background magnetic field [23, 43]. And it was also in 1948 that H. B. G. Casimir published his seminal prediction that vacuum effects would give rise to attractive forces between planar metallic surfaces [7]. In contrast to the former two phenomena, however, in which the experimental discovery was contemporaneous with or even predated theoretical understanding, the latter effect had to wait almost fifty years before precision measurements [25] could conclusively establish the validity of Casimir's 1948 predictions in full detail.

This nearly half-century absence of experimental input did little to diminish the curiosity of theorists, who proceeded throughout the second half of the 20th century to refine and develop Casimir's ideas. By the time experimental data finally did begin to pour in, at the end of the 1990s, a host of alternative physical interpretations had arisen to complement Casimir's original picture of vacuum-point energies sensitive to moving material boundaries. In this chapter we will review this array of viewpoints, closing with a survey of recent progress in experimental investigations of Casimir phenomena.

2.1 The Casimir Effect as a Zero-Point Energy Phenomenon

Casimir's original treatment [7] considered the space between perfectly conducting planar surfaces as a type of electromagnetic cavity (Figure 2.1). Working in the limit in which the cross-sectional area A of the boundary surfaces is taken to infinity at fixed surface-surface separation a, Casimir solved the classical Maxwell equations for the allowable excitations of the electromagnetic field in this cavity, obtaining a countably infinite set of mode frequencies $\{\omega_n(a)\}$ depending on a. Now switching from
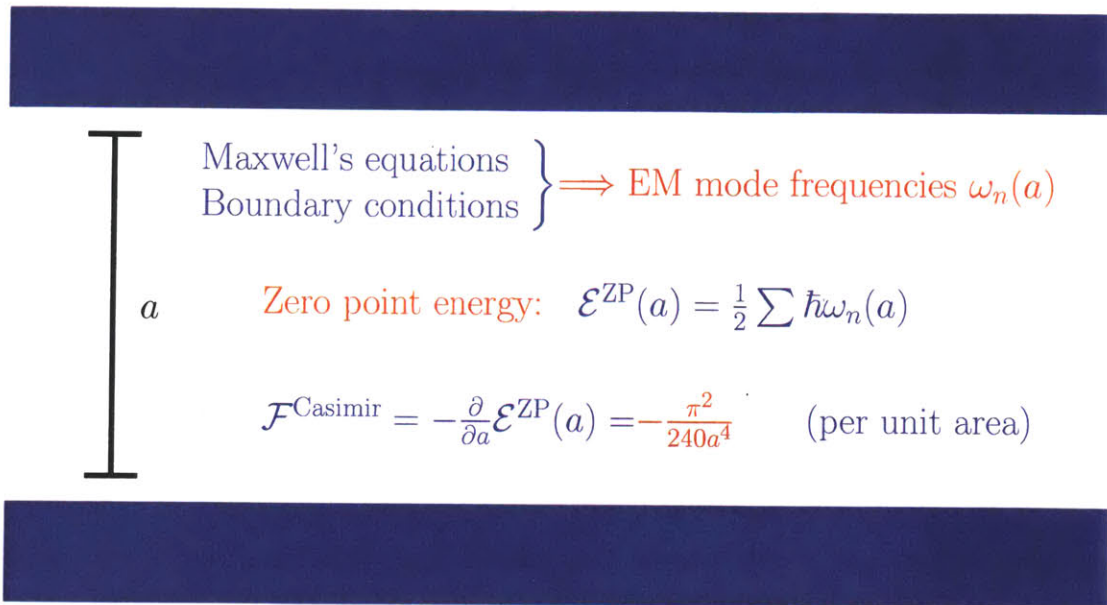
Figure 2-1: Casimir's original picture of his effect considered the space between perfectly conducting parallel plates in vacuum as a type of electromagnetic cavity. Maxwell's equations predict a countably infinite set of mode frequencies $\omega_n(a)$ that depend on the plate–plate separation a. Summing the quantum-mechanical zero-point energy of all modes yields a formally infinite energy of fluctuations, but Casimir was able to obtain a finite result for the *derivative* of this energy—the original Casimir force.

classical to quantum-mechanical thinking, Casimir ascribed to the nth cavity mode a zero-point energy $\hbar\omega_n/2$, and, summing the contributions of all modes, obtained an expression for the energy of the entire configuration in the form

$$\mathcal{E}(a) = \frac{1}{2}\sum_n \hbar\omega_n(a).$$

This expression is obviously divergent, but Casimir argued that the physically meaningful quantity is the *change* in the energy as the surface–surface separation a is varied, and, after some mathematical manipulations, arrived at his famous expression for the force-per-unit-area between the plates,

$$\mathcal{F}(a) = -\frac{1}{A}\frac{\partial\mathcal{E}}{\partial a} = -\frac{\hbar c\pi^2}{240a^4}. \tag{2.1}$$

It seems safe to assume that most physicists outside the Casimir specialty think of Casimir's force in just the way we have presented it here—as a manifestation of zero-point energy in electromagnetic cavity modes. Far less well-known is that there is an alternative viewpoint, one which emphasizes a different set of considerations and which, not incidentally for the purposes of this thesis, opens the door to new computational procedures.

2.2 The Casimir Effect as a Material-Fluctuation Phenomenon

In this alternative interpretation of the effect, which was known to Casimir himself [8] but which today is primarily associated with the work of a Russian school of physicists—Dzyaloshinkii, Lifshitz, and Pitaevskii—in the 1950s [18, 30], we think of Casimir forces between materials as an extended version of the van der Waals interaction between isolated molecular dipoles.

This point of view is sketched in Figure 2.2. Again we consider the space between planar material boundaries, but now, in contrast to the discussion of the previous section, we consider the boundary surfaces to be composed of real-world materials (i.e. solids comprised of elementary atomic or molecular constituents), not simply idealized perfect conductors (Figure 2.2(**a**)). If we were to zoom in on any microscopic volume ΔV within one of these materials, we would see, in essence, a collection of atomic- or molecular-scale electric dipoles. In the absence of an external forcing field, these dipoles will have no particular uniform orientation, and our volume ΔV will have no net dipole moment (Figure 2.2(**b**).) However, from time to time, quantum and thermal fluctuations can cause the dipoles in our little volume to fluctuate into spontaneous alignment with one another, giving the volume a net electric dipole moment, which gives rise to a net electric dipole *field* (Figure 2.2(**c**)). The influence of this field will be felt across the gap in the interior of the other material, where it will induce elemental dipoles to align in its direction (Figure 2.2(**d**).) But now we have *two* net dipole moments, one in either material, mutually aligned and thus

19
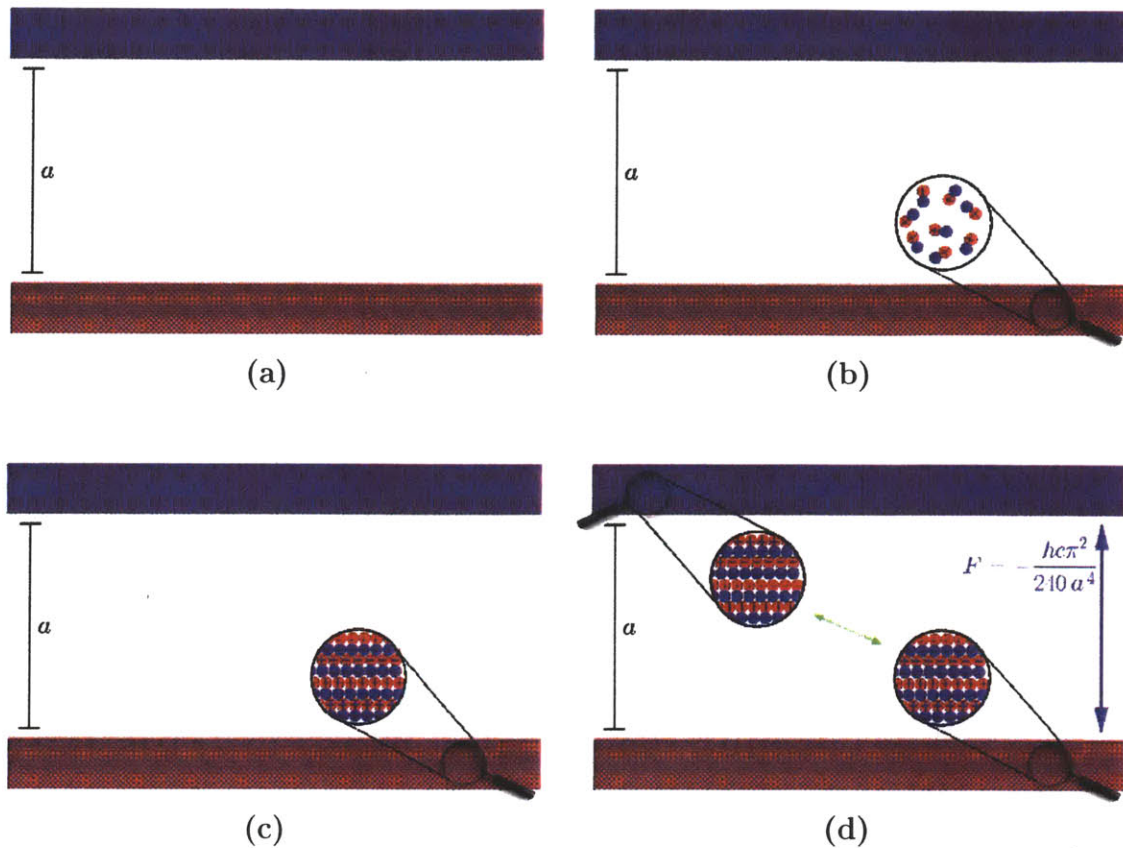
Figure 2-2: The material-fluctuation picture of the Casimir effect. **(a)** As before, we consider parallel plates separated by a distance a in vacuum, but we now allow the plates to be made of real-world materials instead of idealized perfect conductors. **(b)** If we zoom in on any microscopic volume of these materials, their atomic and molecular constituents look like microscopic electric dipoles, which (in the absence of any external forcing field) will ordinarily not be aligned in any particular direction with one another, so that there is no net dipole moment. **(c)** However, from time to time, quantum and thermal fluctuations will cause the constituent dipoles to fluctuate into a state of temporary alignment with one another, giving rise to a net dipole moment and thus a net electromagnetic field which is felt across the gap in the other material, **(d)** where it induces dipoles in *that* material to align with one another, leading to a net dipole-dipole interaction similar to the van der Waals interaction between isolated molecules. Summing these microscopic fluctuation-induced interactions over the volumes of the interacting materials (and taking into account the finite propagation speed of electromagnetic information) we recover the original Casimir force for metallic surfaces.

mutually attracting. Summing the contributions of all microscopic volumes ΔV in the material surfaces, and—a subtlety which turns out to be crucial in obtaining the correct force law—accounting for the finite speed of light, which bounds the rapidity with which information on momentary polarization fluctuations in one material can be communicated to distant points in the other material, we obtain a force between the material surfaces which turns out to be equivalent in all particulars to the force predicted by the cavity-mode arguments of the previous section.

The material-fluctuation picture of the Casimir effect has obvious intuitive appeal. If it is difficult to visualize the zero-point energies of cavity modes, and if it seems somewhat incongruous to ascribe forces between materials to phenomena occurring in the empty space surrounding those materials, it is undoubtedly much more natural to think of those forces as a spatially and temporally dispersed version of the van der Waals interaction familiar from elementary chemistry—and, moreover, such a viewpoint emphasizes the role played by the properties of the materials themselves more than what might be happening in the empty space between them.

On the other hand, when it comes to actually *computing* Casimir interactions, the material-fluctuation viewpoint affords little advantage over the zero-point-energy picture, as there is no obvious procedure for how we might go about "summing the contributions of all microscopic volumes" in the interacting materials. Fortunately, there is yet another interpretation of the Casimir effect that leads directly to well-defined computational techniques.

2.3 The Casimir Effect as a Field-Fluctuation Phenomenon

The zero-point energy picture of Section 2.1 emphasized fluctuations in the electromagnetic fields in the space between material bodies. The alternative picture of Section 2.2 shifted the focus to fluctuations in the material themselves. The two viewpoints are not, of course, really at odds with one another, as the field fluctuations can be understood as *causing* (or, just as well, *being caused by*) the polarization fluctuations; instead, the two pictures are complementary. Having clarified that, we now take up a third viewpoint, in which we shift the emphasis back to the fields in the region between the material bodies—but now, instead of thinking of individual cavity modes, we consider fluctuations in the *components* of the fields instead.

This picture is cartooned in Figure 2.3. (Whereas our previous two schematic depictions of the Casimir effect envisioned an infinite-parallel-plate geometry, we now switch over to considering the force between compact objects (in this case, a roughly cubical object and a roughly spherical object), as it is in the consideration of just these sorts of geometries—for which the zero-point energy picture would amount to an unwieldy computational procedure indeed—that the field-fluctuation viewpoint really comes into its own.)

As suggested in the figure, if we were to measure the components of the fields in the region surrounding the bodies, we would see *noise*—the instantaneous value

21

$$\left\langle E_i \right\rangle = 0$$

$$\left\langle E_i^2 \right\rangle \to \left\langle \mathcal{E} \right\rangle$$

$$\left\langle E_i E_j \right\rangle \to \left\langle T_{ij} \right\rangle$$
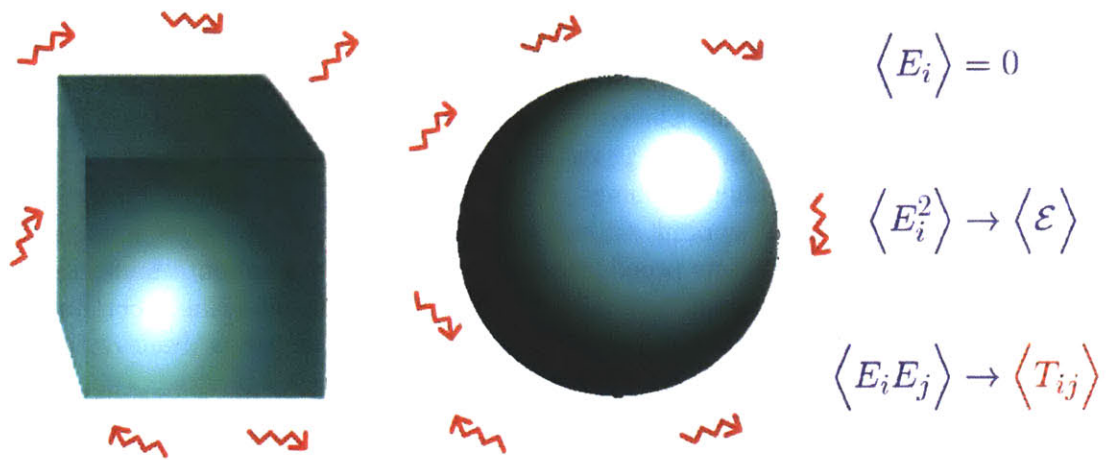
Figure 2-3: A third way to think about the Casimir effect is to emphasize the role of fluctuations in the components of the electromagnetic fields in the region surrounding the interacting objects in a Casimir geometry. In the absence of any external forcing field, the average value of any single field component vanishes, but the average value of the *squared* field components will in general be nonzero and can be used to compute an average energy density $\left\langle \mathcal{E} \right\rangle$, while the average values of *off-diagonal* products of field components can be related to a type of force density (the fluctuation-averaged Maxwell stress tensor $\left\langle T_{ij} \right\rangle$) that we can use to compute Casimir forces.

of any field component will not be strictly zero, but will instead exhibit random fluctuations. In the absence of any external forcing field, the average value of any single field component vanishes, but the average value of the *squared* field components will in general be nonzero and can be used to compute an average energy density. Indeed, if we knew the mean squared value of all field components at all points in space, we could compute the total energy of the electromagnetic fields in our material configuration—whereupon we would be right back where we started, in Section 2.1, with a divergent energy expression that we could also have obtained by considering zero-point energies in field modes.

The great virtue of the field-fluctuation viewpoint emerges when we consider the fluctuation-averaged values of *off-diagonal* products of field components. Just as the averages of squared field components yield an energy density, the averages of off-diagonal products of field components are related to a certain type of *force density* (or *pressure*)—the fluctuation-averaged Maxwell stress tensor—that we can use to compute Casimir forces.

This technique will be discussed in detail in the following chapter. In the meantime, we have gotten ahead of ourselves; we have discussed several theoretical interpretations of the Casimir effect without reminding the reader why she should *care*. Let us turn now to a survey of the experimental sector of Casimir physics.

2.4 The Casimir Effect as an Observable Phenomenon

Putting the numbers into Casimir's original formula (2.1), we find that the magnitude of the Casimir pressure felt by one of two perfectly conducting plates in the configuration of Figure 2.1 is

$$\frac{\hbar c \pi^2}{240 a^4} \approx \frac{10^{-8} \text{ atm}}{(a \text{ in } \mu\text{m})^4}.$$

Thus, at a macroscopic surface–surface separation of $a = 1$ mm, the Casimir interaction between perfectly conducting plates is an utterly negligible 20 orders of magnitude smaller than ordinary atmospheric pressure, while even at a mesoscopic separation of $a = 1$ μm the Casimir force is still a scant 10^{-8} atmospheres. (And the Casimir interaction between real materials will generally be even *smaller* than that between idealized perfect metals.)

The tiny force magnitudes expected at macroscopic and even mesoscopic distances suggest that the Casimir effect will only be observable between objects at *nanoscopic* distances from one another, and this observation helps to explain why, although there were some tentative experimental findings in the decades after Casimir's initial prediction, it was not until the advent of modern microelectronics technology that the first experiments could be performed to confirm Casimir's prediction in full detail [25].

Since the appearance of [25], the experimental Casimir field has grown by leaps and bounds, with Casimir interactions having now been observed in dozens of laboratories around the world and currently under investigation in an increasingly wide variety of

geometries and materials. Although we cannot do justice to the full breadth of the experimental situation here (a valuable survey may be found in [6]), we will single out two recent trends in experimental Casimir physics as particularly worthy of mention for the purposes of this thesis.

First, although Casimir's original predictions considered only perfectly metallic objects, and most theoretical work in the ensuing decades was restricted either to this case or to the case of dielectric objects in vacuum—for which the Casimir interactions tend to resemble at least qualitatively those for the perfect-metal case—in 2009 it was experimentally demonstrated [33] that pairs of objects comprised of certain combinations of materials, when embedded in a liquid dielectric such as ethanol, can exhibit a Casimir interaction that differs in a key qualitative way from any Casimir effect that had ever before been observed: it is *repulsive* instead of attractive. This experimental finding provoked a raft of suggestions for new experiments probing the impact of novel material configurations [41], and there is every reason to believe that experimental characterization of Casimir interactions between objects of various interesting materials will be a growth industry in the near future.

Second, although the first precision experiment [25] and many subsequent experiments used geometric configurations of relatively high symmetry—such as spheres and plates—more recently it has become fashionable to conduct Casimir experiments in highly asymmetric geometries, such as the quasi-2D silicon beams of polygonal cross-section investigated in [29]. The sharp distance dependence of the Casimir force in even the simplest Casimir situation (equation (2.1)) indicates that the Casimir effect is a sensitive probe of geometric effects, a fact which will undoubtedly remain at the forefront of experimental Casimir work in the coming years.

Thus, almost fifteen years after the dawn of the era of modern precision experimental Casimir physics, the field has entered a regime in which novel material-property effects, complex geometric configurations, and the interaction between the two can be expected to be a major theme of future work. This progress on the experimental side has, in turn, stimulated the development of theoretical tools capable of predicting Casimir interactions in arbitrary materials and geometries—a spate of recent progress to which we now turn.

Chapter 3

Modern Numerical Methods in Computational Casimir Physics

As discussed at the end of the previous chapter, the past 15 years have been an era of explosive growth in experimental Casimir physics, with Casimir phenomena currently under investigation in an increasingly broad variety of experimental configurations. This rapid experimental progress has created a demand for theoretical tools capable of predicting Casimir energies, forces, and torques among materials with arbitrary frequency-dependent material properties configured in realistic experimental geometries.

The computational methods used by Casimir, by the Russian school (Dzyaloshinkii, Lifshitz, and Pitaevskii), and indeed by all classical Casimir researchers—where the "classical" era of theoretical Casimir physics must be thought of as lasting until around 2007—were generally designed to work for one and only one specific geometry, with the entire technique reformulated for each new geometric configuration. Moreover, the geometries considered in the classical era were generally highly symmetrical idealizations of actual experimental configurations—infinite planar boundaries at constant surface-surface separation, concentric spheres, and the like. It is only in the past few years that techniques sufficiently general to be applied to arbitrary geometries, and sufficiently sophisticated to handle complex asymmetric experimental configurations, have emerged [22].

These general-purpose schemes for Casimir computations have to date adopted one of two distinct strategies: either the *numerical stress-tensor* approach, or the *path-integral* (or *scattering*) approach. (It is interesting to note that both techniques are motivated by the material-fluctuation or field-fluctuation pictures discussed in the previous chapter; Casimir's original picture of zero-point fluctuations in cavity modes has long since been essentially abandoned as a practical computational framework.) The fluctuating-surface-current (FSC) technique introduced in Chapter 5 of this thesis represents a *third* computational paradigm, which may be viewed as a logical outgrowth of either the numerical stress-tensor *or* the path-integral technique and thus amounts to a unification of these two seemingly disparate approaches. To prepare the groundwork for this eventual synthesis, in this chapter we review the numerical stress-tensor and path-integral approaches to computational Casimir ptysics.

We emphasize that none of the content of this chapter is new; instead, this chapter is a discussion of existing techniques in computational Casimir physics that are reviewed here as background for the remainder of this thesis.

3.1 The Stress-Tensor Approach to Computational Casimir Physics

In Section 2.3 we sketched an interpretation of the Casimir effect that emphasizes the role of electromagnetic-field fluctuations in the medium (or vacuum) surrounding interacting material objects. The numerical stress-tensor technique formalizes this intuitive picture into a systematic computational procedure.

3.1.1 Casimir Forces from Stress-Tensor Integration

The key cartoon depiction of the stress-tensor paradigm is Figure 2.3. If we were to measure the instantaneous values of the cartesian components of the electric and magnetic fields in the region between material bodies, we would see *noise*: the functions $E_i(\mathbf{x}, t)$ and $H_i(\mathbf{x}, t)$ are not identically vanishing, even the absence of externally imposed fields, but instead exhibit random fluctuations. For our purposes the most convenient way to characterize this noise is through the use of spectral density functions. If $f(t)$ is a time-varying quantity (such as $E_i(\mathbf{x}, t)$ for fixed i and $\mathbf{x}$), then the spectral density of fluctuations in f at frequency ω is

$$\langle f \rangle_\omega = \left\langle \int_{t_0}^{t_0+\frac{2\pi}{\omega}} e^{i\omega t} f(t) dt \right\rangle \tag{3.1}$$

where the $\langle \rangle$ notation on the right-hand side indicates an average over all possible values of the start time t_0. $\langle f \rangle_\omega$ is the noise quantity that we would measure in the laboratory with a spectrum analyzer or lock-in amplifier, and $\langle f \rangle_\omega d\omega$, speaking somewhat roughly, is the portion of all noise in f that comes from fluctuations with frequencies in the interval $[\omega, \omega + d\omega]$.

The spectral density of fluctuations in any single field component vanishes, $\langle E_i(\mathbf{x}) \rangle_\omega = \langle H_i(\mathbf{x}) \rangle_\omega = 0$, but the spectral densities of fluctuations in *squared* field components are generally nonzero and define an energy density of electromagnetic-field fluctuations,[1]

$$U(\mathbf{x}, \omega) = \frac{1}{2} \sum_i \left\{ \epsilon(\mathbf{x}) \langle E_i^2(\mathbf{x}) \rangle_\omega + \mu(\mathbf{x}) \langle H_i^2(\mathbf{x}) \rangle_\omega \right\}.$$

Taking this idea one step further, by considering the spectral densities of fluctuations in *off-diagonal* products of field components we obtain a fluctuation-induced version

---

[1] Strictly speaking, this expression for the energy density is only correct for nondispersive media; the full expression for the energy density in the presence of frequency-dependent ϵ and μ is slightly more complicated.

of the *Maxwell stress-energy tensor,*

$$T_{ij}(\mathbf{x}, \omega) = \epsilon(\mathbf{x}, \omega) \left[\left\langle E_i(\mathbf{x}) E_j(\mathbf{x}) \right\rangle_\omega - \frac{\delta_{ij}}{2} \sum_k \left\langle E_k(\mathbf{x}) E_k(\mathbf{x}) \right\rangle_\omega \right]$$
$$+ \mu(\mathbf{x}, \omega) \left[\left\langle H_i(\mathbf{x}) H_j(\mathbf{x}) \right\rangle_\omega - \frac{\delta_{ij}}{2} \sum_k \left\langle H_k(\mathbf{x}) H_k(\mathbf{x}) \right\rangle_\omega \right]. \tag{3.2}$$

We interpret T_{ij} as a flow of i-directed momentum in the j-direction, so that $\sum_j T_{ij} \hat{n}_j$ represents an i-directed *force* per unit area (a pressure) on a surface patch with normal $\hat{n}$.

The stress-tensor approach to Casimir computations now proceeds by surrounding a material body with a (fictitious, arbitrary) closed bounding surface $\mathcal{C}$ and integrating the fluctuation-induced pressure (3.2) over this surface to obtain the full i-directed Casimir force on the object as

$$\mathcal{F}_i = \int_{-\infty}^{\infty} \frac{d\omega}{2\pi} \, F_i(\omega), \tag{3.3}$$

$$F_i(\omega) = \oint_{\mathcal{C}} \left\langle T_{ij}(\mathbf{x}, \omega) \right\rangle \hat{n}_j(\mathbf{x}) \, d\mathbf{x} \tag{3.4}$$

where $\hat{n}(\mathbf{x})$ is the *inward-directed* unit normal to $\mathcal{C}$ at $\mathbf{x}$.

3.1.2 Noise Spectral Densities from Dyadic Green's Functions

Equations (3.2) and (3.4) reduce the computation of Casimir forces to the computation of spectral densities of fluctuations in products of field components. This might hardly seem much of an advance, inasmuch as there is no immediately obvious procedure for computing these spectral-density functions for a given Casimir geometry.

The development of such a procedure was the key contribution of the Russian school in the 1950s [18, 30], who used the fluctuation–dissipation theorem of statistical physics to relate fluctuations in products of field components to the scattering portions of the *dyadic Green's functions* of classical electromagnetism. At temperature $kT =$

$1/\beta$ these relations read[2]

$$\left\langle E_i(\mathbf{x})E_j(\mathbf{x}')\right\rangle_\omega = i\hbar\omega\coth\frac{\beta\hbar\omega}{2}\cdot\mathrm{Im}\;\mathcal{G}_{ij}^{\mathrm{EE,scat}}(\omega;\mathbf{x},\mathbf{x}') \tag{3.5a}$$

$$\left\langle H_i(\mathbf{x})H_j(\mathbf{x}')\right\rangle_\omega = i\hbar\omega\coth\frac{\beta\hbar\omega}{2}\cdot\mathrm{Im}\;\mathcal{G}_{ij}^{\mathrm{MM,scat}}(\omega;\mathbf{x},\mathbf{x}') \tag{3.5b}$$

where, as discussed in Appendix A, $\mathcal{G}_{ij}^{\mathrm{EE,scat}}(\omega;\mathbf{x},\mathbf{x}')$ is the i component of the scattered *electric* field at $\mathbf{x}$ due to a j-directed point *electric* current source at $\mathbf{x}'$, and $\mathcal{G}_{ij}^{\mathrm{MM,scat}}(\omega;\mathbf{x},\mathbf{x}')$ is the i component of the scattered *magnetic* field at $\mathbf{x}$ due to a j-directed point *magnetic* current source at $\mathbf{x}'$, all quantities having time dependence $\propto e^{-i\omega t}$.

The theoretical significance of (3.5) is that the $\mathcal{G}$ functions for a given Casimir geometry can be computed using techniques of *classical* electromagnetic (EM) scattering theory, and equations (3.5) thus establish a link from the deterministic world of the classical Maxwell equations to the stochastic realm of quantum-mechanical and statistical fluctuations. The *practical* significance of this for Casimir computations is that the door is now flung wide open to the vast array of techniques that have been developed over the decades for numerical solutions of Maxwell's equations. Indeed, inserting equations (3.5) into (3.2) and (3.4) results in an expression for the Casimir force involving an integral over space and frequency which may be evaluated by straightforward numerical cubature, with the value of the integrand at each cubature point obtained as the numerical solution of a classical EM scattering problem.

Choice of Scattering Methodology

With computational Casimir physics thus reduced to computational classical electromagnetism, the question now becomes *which* of the myriad numerical techniques for solving EM scattering problems is best suited for Casimir applications. To date, almost all applications of computational electromagnetism to Casimir physics have employed *finite-difference* techniques [40, 35] to solve the imaginary-frequency scattering problems. Although the finite-difference technique has the virtues of *generality* (in that it may be applied to geometries with arbitrary spatially-varying material properties with no more difficulty than to piecewise-homogeneous geometries) and *simplicity* (in that it is relatively straightforward to implement), it is not the most efficient method for solving scattering problems in the piecewise-homogeneous geometries commonly encountered in Casimir problems. Instead, more efficient methods are available, and one such method—the *boundary-element method*—will be discussed in

---

[2]The constant prefactors in our equations (3.5), as well as in our equations (3.9) below, appear to differ from those in the corresponding equations in other references, including [30] and [22]. The distinction is that the $\mathcal{G}$ quantities in our equations are precisely the fields due to point sources with no additional prefactors, whereas some authors write the relations (3.5) and (3.9) in terms of different dyadic Green's functions that equal the fields of point sources only up to a constant prefactor. For example, in Ref. [22] this constant prefactor is $i\omega$ (see footnote 4 in [22]), and hence our equations differ from the corresponding equations in that reference by a factor of $i\omega$ (or $-\xi$ in the imaginary-frequency case).

the following chapter. (Later, in Chapter 5, we will demonstrate that the boundary-element method in fact leads to a significant streamlining of the stress-tensor approach, in which the spatial integration in (3.4) may be evaluated *analytically*, leading to formulae much simpler than (3.4)—our *fluctuating-surface-current* formulae).

3.1.3   Transition to Imaginary Frequency

In the meantime, however, there is one subtlety left to discuss. To get a sense of the function $F_i(\omega)$ that we are integrating over all ω in equation (3.3), let us consider what this function looks like for a typical Casimir problem. Figure 3.1.3(**a**) plots this function for the particular case of the Casimir force (per unit area) on the upper of two perfectly-conducting metallic plates separated by a distance a in vacuum (a case in which $F_i(\omega)$ may be evaluated analytically).

It is immediately evident from this plot that the task of integrating this function numerically over all ω will be highly ill-defined, due to catastrophic cancellation errors arising from the large oscillations of the integrand. Mathematically, we can think of the bad behavior of the integrand as resulting from the existence of poles in $F(\omega)$ located in the lower-right quadrant of the complex ω plane; physically, these poles correspond to resonance frequencies of the geometry in question. In the presence of such resonance phenomena, classical EM tools can often be coaxed to work well over narrow frequency bandwidths, but are difficult to use for inherently *broadband* problems such as that defined by the infinite frequency integration in (3.3).

But this diagnosis already suggests a cure—namely, that we promote the broadband nature of Casimir problems from a curse to a blessing by availing ourselves of *Wick rotation*. Thinking of the ω integral in (3.3) as a contour integral in the complex-ω plane, we now simply *rotate* this contour 90° counter-clockwise and integrate instead along the *imaginary* ω axis, distancing ourselves from the troublesome poles in the lower half-plane. The Casimir force expression (3.3) becomes simply

$$\mathcal{F}_i = \int_0^\infty \frac{d\xi}{\pi}\, F_i(\xi). \tag{3.6}$$

As illustrated in Figure 3.1.3(**b**), the Wick rotation tames the angry oscillations in Figure 3.1.3(**a**), leaving a smooth integrand that succumbs readily to straightforward numerical cubature.

Computations at Imaginary Frequency

Figure 3.1.3 leaves no doubt that the frequency integral defining the Casimir force is best performed over the imaginary frequency axis. What are the implications of this for our computational procedure? Putting $\omega = i\xi$ in (3.4), the integrand of the ξ integral in (3.6) is

$$F_i(\xi) = \oint_C T_{ij}(\mathbf{x}, \xi)\, \hat{\mathbf{n}}_j(\mathbf{x})\, d\mathbf{x} \tag{3.7}$$

(a)

(b)
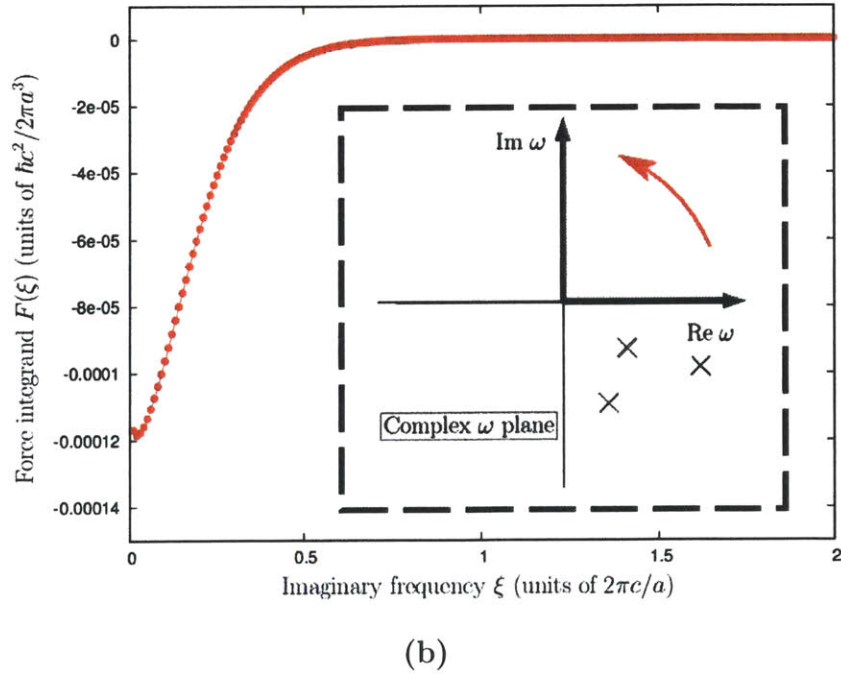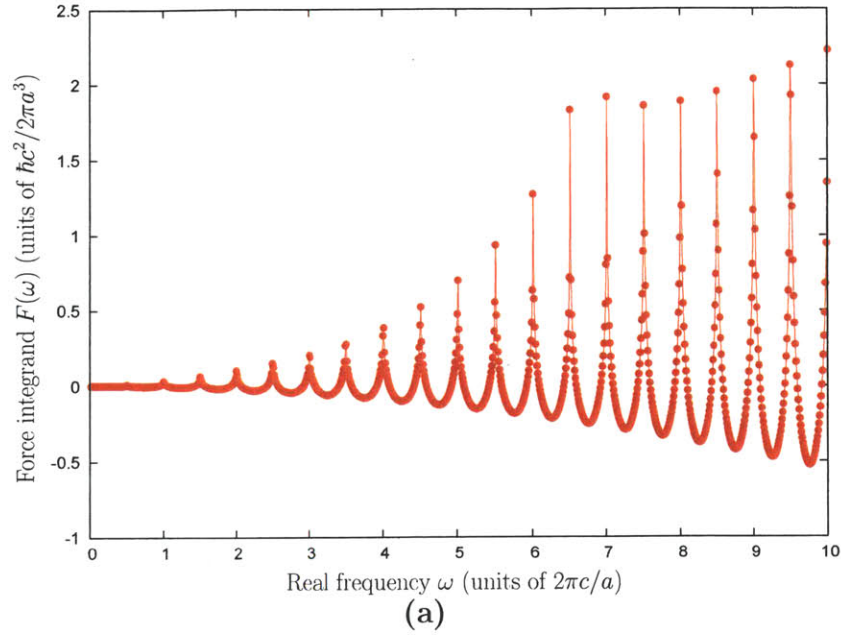
Figure 3-1: **(a)** A plot of the function $F(\omega)$, the integrand of the frequency integral (3.3), for the particular case of the Casimir force-per-unit-area between parallel metallic plates separated by a distance a in vacuum. The rapid oscillations in the integrand render the integral essentially inaccessible to numerical quadrature. Mathematically, the oscillations correspond to the existence of lower-half-plane poles in the integrand (inset of **(b)**), which suggests rotating the integration contour from the real to the imaginary axis in the complex ω plane. **(b)** The integrand of the Wick-rotated integral, $F(\xi)$, is a smooth and rapidly-decaying function of ξ that succumbs readily to numerical quadrature.

where $T_{ij}(\mathbf{x}, \xi)$ is the Wick-rotated version of the stress-energy tensor, given by the imaginary-frequency version of (3.2):

$$T_{ij}(\mathbf{x}, \xi) = \epsilon(\mathbf{x}, \xi)\left[\left\langle E_i(\mathbf{x})E_j(\mathbf{x})\right\rangle_\xi - \frac{\delta_{ij}}{2}\sum_k \left\langle E_k(\mathbf{x})E_k(\mathbf{x})\right\rangle_\xi\right]$$

$$+ \mu(\mathbf{x}, \xi)\left[\left\langle H_i(\mathbf{x})H_j(\mathbf{x})\right\rangle_\xi - \frac{\delta_{ij}}{2}\sum_k \left\langle H_k(\mathbf{x})H_k(\mathbf{x})\right\rangle_\xi\right]. \qquad (3.8)$$

Here $\epsilon(\xi)$ and $\mu(\xi)$, the permittivity and permeability functions on the imaginary axis, are defined by straightforward analytic continuation of their real-frequency counterparts; in practice, these functions may be computed from real-frequency ϵ and μ data by simple application of the Kramers-Kronig relations [19].

The notation $\langle\ \rangle_\xi$ in equation (3.8) represents a sort of Wick-rotated spectral density of fluctuations. Although it is difficult to ascribe a physical significance to equation (3.1) under the rotation $\omega \to i\xi$, the rotated versions of (3.5) are perfectly well-defined; at temperature $T = 0$ they read

$$\left\langle E_i(\mathbf{x})E_j(\mathbf{x}')\right\rangle_\xi = -\hbar\xi\mathcal{G}_{ij}^{\text{EE,scat}}(\xi; \mathbf{x}, \mathbf{x}') \qquad (3.9a)$$

$$\left\langle H_i(\mathbf{x})H_j(\mathbf{x}')\right\rangle_\xi = -\hbar\xi\mathcal{G}_{ij}^{\text{MM,scat}}(\xi; \mathbf{x}, \mathbf{x}') \qquad (3.9b)$$

where the imaginary-frequency versions of the dyadic Green's functions are defined precisely as before (for example, $\mathcal{G}^{\text{EE,scat}}$ is the scattered electric field due to a point electric current source), but now with all quantities having *exponentially growing* time dependence $\sim e^{+\xi t}$.

3.2 The Path-Integral Approach to Computational Casimir Physics

The path-integral approach to the computation of fluctuation forces was pioneered by Bordag, Robaschik, and Wieczorek [5] and by Li and Kardar [26, 27], and has since been further developed by a number of authors (see [37] for an extensive survey of recent developments.) In this section we briefly survey this technique.

3.2.1 Casimir Energy from Constrained Path Integrals

In the presence of material boundaries, the partition function for a quantum field ϕ (which may be scalar, vector, electromagnetic, or otherwise, but is here assumed bosonic) takes the form

$$Z(\beta) = \int \left[\mathcal{D}\phi(\tau, \mathbf{x})\right]_C e^{-\frac{1}{\hbar}S_\beta[\phi]} \qquad (3.10)$$

31

where the action at inverse temperature β is the spacetime integral of the Euclidean Lagrangian density for the ϕ field,

$$S_\beta[\phi] = \int_0^{\hbar\beta} d\tau \int d\mathbf{x}\, \mathcal{L}_E\Big\{\phi(\tau, \mathbf{x})\Big\}, \tag{3.11}$$

and where the notation $[\cdots]_C$ in (3.10) indicates that this is a *constrained* path integral, in which the functional integration extends only over field configurations ϕ satisfying the appropriate boundary conditions at all material boundaries.

If the boundary conditions are time independent *and* the Lagrangian density contains no terms of higher than quadratic order in ϕ and its derivatives, then it is convenient to introduce a Fourier series in the Euclidean time variable,

$$\phi(\tau, \mathbf{x}) = \sum_n \phi_n(\mathbf{x}) e^{-i\xi_n \tau}, \qquad \xi_n = \frac{2\pi n}{\hbar\beta},$$

whereupon the path integral (3.10) factorizes into a product of contributions from individual frequencies,

$$Z(\beta) = \prod_n \mathcal{Z}(\beta; \xi_n),$$

$$\mathcal{Z}(\beta; \xi_n) = \int \Big[\mathcal{D}\phi_n(\mathbf{x})\Big]_C e^{-S[\phi_n; \xi_n]}, \tag{3.12}$$

with

$$S\Big[\phi_n(\mathbf{x}); \xi_n\Big] = \beta \int d\mathbf{x}\, \mathcal{L}_E\Big\{\phi_n(\mathbf{x}) e^{-i\xi_n \tau}\Big\}$$

representing the contribution to the full action (3.11) made only by those field configurations with Euclidean-time dependence $\sim e^{-i\xi_n \tau}$. The free energy is then obtained as a sum over Matsubara frequencies,

$$F = -\frac{1}{\beta} \ln \frac{Z(\beta)}{Z_\infty(\beta)} = -\frac{1}{\beta} \sum_{n=0}^{\infty} \ln \frac{\mathcal{Z}(\beta, \xi_n)}{\mathcal{Z}_\infty(\beta, \xi_n)} \tag{3.13}$$

where $Z_\infty (\mathcal{Z}_\infty)$ is $Z(\mathcal{Z})$ evaluated with all material objects separated by infinite distances (dividing out these contributions in (3.13) is a useful convention that amounts to a choice of the zero of energy). In the zero-temperature limit, the frequency sum becomes an integral, and the zero-temperature Casimir energy is

$$\mathcal{E} = -\frac{\hbar}{2\pi} \int_0^\infty d\xi \ln \frac{\mathcal{Z}(\xi)}{\mathcal{Z}_\infty(\xi)}. \tag{3.14}$$

(Here and below we omit the β argument to $\mathcal{Z}$).

3.2.2 Enforcing Constraints via Functional δ-functions

Equations (3.13-3.14) reduce the computation of Casimir energies to the evaluation of constrained path integrals (3.12). In most branches of physics, the path integrals associated with physically interesting quantities are difficult to evaluate because the action S in the exponent contains interaction terms (terms of third or higher order in the fields and their derivatives). In Casimir physics, on the other hand, the action is not more than quadratic in ϕ, and the difficulty in evaluating expressions like (3.12) stems instead from the challenge of implementing the implicit constraint on the functional integration measure, arising from the boundary conditions and indicated by the $[\cdots]_C$ notation in (3.12).

The innovation of Bordag [5] and of Li and Kardar [26] was to represent these constraints *explicitly* through the use of functional δ functions. If the boundary conditions on ϕ may be expressed as the vanishing of a set of quantities $\{L_\alpha \phi\}$, where $\{L_\alpha\}$ will generally be some family of linear integrodifferential operators indexed by a discrete or continuous label α, then the constrained path integral may be written in the form

$$
\begin{aligned}
\mathcal{Z}(\xi_n) &= \int \left[\mathcal{D}\phi_n(\mathbf{x}) \right]_C e^{-S[\phi_n;\xi_n]} \\
&= \int \mathcal{D}\phi_n(\mathbf{x}) \prod_\alpha \delta\left(L_\alpha \phi \right) e^{-S[\phi_n;\xi_n]}
\end{aligned}
\tag{3.15}
$$

where now the functional integration over ϕ_n is *unconstrained*. A particularly convenient representation for the one-dimensional Dirac δ function is

$$
\delta(u) = \int \frac{d\lambda}{2\pi} e^{i\lambda u},
\tag{3.16}
$$

where we may think of λ as a Lagrange multiplier enforcing the constraint that u vanish. Inserting one copy of (3.16) for each δ function in the product in (3.15) yields

$$
\mathcal{Z}(\xi_n) = \int \mathcal{D}\phi_n(\mathbf{x}) \int \prod_\alpha \frac{d\lambda_\alpha}{2\pi} \, e^{-S[\phi_n;\xi_n]+i\sum_\alpha \lambda_\alpha L_\alpha \phi}.
$$

The final step is to evaluate the unconstrained integral over ϕ; since the exponent is quadratic in ϕ, this can be done *exactly* using standard techniques of Gaussian integration, yielding an expression of the form

$$
\mathcal{Z}(\xi_n) = \left\{ \# \right\} \int \prod_\alpha d\lambda_\alpha \, e^{-S^{\text{eff}}\{\lambda_\alpha\}}
\tag{3.17}
$$

(where $\{\#\}$ is a constant that cancels in the ratios in (3.13-3.14)). The constrained functional integral over the field ϕ is thus replaced by a new integral over the set of Lagrange multipliers $\{\lambda_\alpha\}$, with an effective action S^{eff} describing interactions mediated by the original fluctuating field ϕ.

33

3.2.3 Representation of Boundary Conditions

Equation (3.17) makes clear that the practical convenience of path-integral Casimir computations is entirely determined by the choice of the Lagrange multipliers $\{\lambda_\alpha\}$ and the complexity of their effective action S^{eff}; these, in turn, depend on the details of the boundary conditions imposed on the fluctuating field. For a given physical situation there may be multiple ways to express the boundary conditions, each of which will generally lead to a distinct expression for the integral in (3.17). Ultimately, of course, all choices must lead to equivalent results, but different choices may exhibit significant differences in computational complexity and in the range of geometries that can be efficiently treated. Several different representations of boundary conditions and Lagrange multipliers have appeared in the literature to date.

The original work of Bordag et al. [5] considered QED in the presence of super-conducting boundaries, with the boundary conditions taken to be the vanishing of the normal components of the dual field-strength tensor; in the notation of the previous section, $L_{\mathbf{x}}\phi = \hat{n}^\mu F_{\mu\nu}^*(\mathbf{x})$, and the set of Lagrange multipliers $\{\lambda_{\mathbf{x}}\}$ constitutes a three-component auxiliary field defined on the bounding surfaces. The method is applicable to the computation of electromagnetic Casimir energies, but the treatment was restricted to the case of parallel planar boundaries.

Li and Kardar [26, 27] considered a *scalar* field satisfying Dirichlet or Neumann boundary conditions on a prescribed boundary manifold. Here again the boundary conditions amount to the vanishing of a local operator applied to ϕ, $L_{\mathbf{x}}\phi = \phi(\mathbf{x})$ (Dirichlet) or $L_{\mathbf{x}}\phi = |\partial\phi/\partial n|_{\mathbf{x}}$ (Neumann), and we have one Lagrange multiplier $\lambda(\mathbf{x})$ for each point on the boundary manifold. In this case it is tempting to interpret $\lambda(\mathbf{x})$ as a scalar source density, confined to the boundary surfaces and with a self-interaction induced by the fluctuations of the ϕ field. This formulation was capable, in principle, of handling *arbitrarily*-shaped boundary surfaces, but was restricted to the case of scalar fields.

The technique of Refs. [26, 27] was subsequently reformulated [15, 16] in a way that allowed extension to the case of the electromagnetic field. Whereas the original formulation imposed a *local* form of the boundary conditions—and took the Lagrange multipliers $\lambda(\mathbf{x})$ to be local surface quantities—the revised formulation abandoned the surface-source picture in favor of an alternative viewpoint that emphasized incoming and outgoing electromagnetic waves. In this revised formulation, the local boundary conditions are replaced by an *integral* form of the boundary conditions, $L_\alpha\phi = \int \Psi_\alpha^*(\mathbf{x})\phi(\mathbf{x})d\mathbf{x}$ for some discrete set of functions $\{\Psi_\alpha(\mathbf{x})\}$, corresponding to the requirement that each term in a multipole expansion of ϕ separately satisfy the boundary conditions on the full boundary surface. In contrast to the continuous surface-source densities used in Refs. [26, 27], this form of the boundary conditions leads to a *discrete* set of Lagrange multipliers $\{\lambda_\alpha\}$, with one multiplier associated to each multipole; instead of representing the local value of a surface source density, we now think of λ_α as the αth multipole *moment* of a source distribution, and the effective action S^{eff} describes the interaction among multipoles. (The strategy of separately enforcing an integrated boundary condition on each term in a multipole expansion is reminiscent of classical scattering theory, and indeed the path-integral approach to

Casimir computations is sometimes known as the "scattering" approach [37].)

The great virtue of multipole expansions is that, for certain geometries, a small number of multipole coefficients may suffice to solve many problems of interest to high accuracy. This has long been understood in domains such as electrostatics and scattering theory, and in recent years has been impressively demonstrated in the Casimir context as well [15, 16, 37], where multipole expansions have been used to obtain rapidly convergent and even *analytically* tractable series for Casimir energies in certain special geometries. The trick, of course, is that the very definition of the multipoles already encodes a significant amount of information about the geometry, thus requiring relatively little additional work to pin down what more remains to be said in any particular situation.

But this blessing becomes a curse when we seek a unified formalism capable of treating all geometries on an equal footing. The very geometric specificity of the multipole description, which so streamlines the treatment of compatible or nearly-compatible geometries, has the opposite effect of *complicating* the treatment of incompatible geometries; thus, whereas a basis of spherical multipoles might allow highly efficient treatment of interacting spheres or nearly-spherical bodies, it would be a particularly *unwieldy* choice for the description of cylinders, tetrahedra, or parallelepipeds. Of course, for each new geometric configuration we could simply re-define our multipole expansion and correspondingly re-implement the full arsenal of computational machinery (a strategy pursued for an dizzying array of geometries in Ref. [37]), but such a procedure contradicts the spirit of a single, general-purpose scheme into which we simply plug an arbitrary experimental geometry and turn a crank.

Instead, the goal of designing a more general-purpose implementation of the path-integral Casimir paradigm leads us to seek a representation of the boundary conditions that, while inevitably less efficient than spherical multipoles for spheres (or cylindrical multipoles for cylinders, or ...) has the flexibility to handle all manner of surfaces within a single computational framework. This is one way of motivating the fluctuating-surface-current approach to Casimir computations, and will be pursued in detail in Chapter 5.

Chapter 4

Boundary-Element Methods for Electromagnetic Scattering

Our discussion of the numerical stress-tensor method in the previous chapter makes clear that the accuracy and efficiency of this approach to computational Casimir physics depend critically on the procedure chosen to solve the large number of electromagnetic scattering problems required to evaluate the integrals in (3.7). This chapter discusses one particular choice, the *boundary-element method*, that has proven particularly well-suited for Casimir applications.

The boundary-element method (BEM) [17, 32] is a well-established technique in computational electromagnetism that, for decades, has proven the method of choice in a wide variety of applications. The purpose of this chapter is to remind the reader of this existing set of techniques, primarily for the purposes of fixing ideas and notation for the remainder of this thesis; nothing in this chapter is new, although the explicit expressions (4.8) and (4.17) for the scattered fields have not, to our knowledge, appeared before in the form we give them.

In an EM scattering problem, we are given a scattering geometry and known *incident* fields $\mathbf{E}^{\mathrm{inc}}(\mathbf{x})$, $\mathbf{H}^{\mathrm{inc}}(\mathbf{x})$ (and/or known sources for the incident fields), and our task is to compute the *scattered* fields $\mathbf{E}^{\mathrm{scat}}(\mathbf{x})$, $\mathbf{H}^{\mathrm{scat}}(\mathbf{x})$ (with the total fields obtained by summing incident and scattered contributions). The well-known *finite-difference* (FD) [9, 34] and *finite-element* (FE) [47, 20] methods solve directly for the total fields by *locally* enforcing a differential (FD) or integral (FE) form of Maxwell's equations. A virtue of these methods is their great generality; because Maxwell's equations are only referenced locally, geometries with arbitrary spatially-varying electrical properties are handled with no less ease than piecewise homogeneous geometries. The drawback, of course, is that the methods are "too general" for many problems; indeed, many scattering geometries consist of homogeneous bodies embedded in a homogeneous medium, and the FE and FD methods fail to make use of the simplifications afforded by the known solutions of Maxwell's equations in this case.

The BEM is an alternative strategy, most directly applicable to piecewise-homogeneous scattering geometries (i.e. geometries in which the permittivity and permeability are piecewise-constant in space), that makes maximal use of the known closed-form solutions to Maxwell's equations in homogeneous media. In the BEM, instead of solving

directly for the scattered fields, we instead solve first for an intermediate quantity, namely, an *effective surface-current distribution*, confined to the surfaces of the scattering objects, that gives rise to a scattered field satisfying all boundary conditions. Once we have solved for the effective surface-current distribution, we may use it to compute the scattered fields anywhere in space.

4.1 The Boundary-Element Method for PEC Bodies

4.1.1 The Integral Equation for K

As a first illustration of the BEM, let us consider the problem of a monochromatic[1] incident field $\mathbf{E}^{\text{inc}}(\mathbf{x}, t) = \mathbf{E}^{\text{inc}}(\mathbf{x})e^{+\xi t}$ scattering off of one or more perfectly electrically conducting (PEC) bodies embedded in vacuum (factors of $e^{+\xi t}$ will henceforth be suppressed). Physically, the incident field induces a surface-current distribution $\mathbf{K}(\mathbf{x})$ on the surfaces of the scatterers, and it is this current distribution that gives rise to the scattered fields; if we knew $\mathbf{K}(\mathbf{x})$, we could use the vacuum dyadic Green's functions (Appendix A) to compute the scattered electric field anywhere in space according to

$$\mathbf{E}^{\text{scat}}(\mathbf{x}) = \oint_{\mathcal{S}} \boldsymbol{\Gamma}^{\text{EE}}(\xi; \mathbf{x}, \mathbf{x}') \cdot \mathbf{K}(\mathbf{x}')\, d\mathbf{x}' \tag{4.1}$$

where the surface integral extends over $\mathcal{S}$, the union of the surfaces of all scattering objects.[2] (Equation (4.1) applies for evaluation points $\mathbf{x}$ lying *exterior* to the scattering objects; the field vanishes at interior points because we are considering PEC bodies.)

Equation (4.1) is not immediately useful as we do not know $\mathbf{K}(\mathbf{x})$ *a priori*, but we can solve for $\mathbf{K}(\mathbf{x})$ by demanding that the field (4.1) to which it gives rise satisfies the appropriate boundary conditions. Since we are considering PEC bodies, the boundary conditions are simply that the tangential components of the total electric field vanish at the surfaces of the scatterers:

$$\left[\mathbf{E}^{\text{inc}}(\mathbf{x}) + \mathbf{E}^{\text{scat}}(\mathbf{x})\right] \times \hat{\mathbf{n}}(\mathbf{x}) = 0, \qquad \mathbf{x} \in \mathcal{S} \tag{4.2}$$

where crossing with $\hat{\mathbf{n}}(\mathbf{x})$, the normal to $\mathcal{S}$ at $\mathbf{x}$, is simply a convenient way of ex-

---

[1]The boundary-element is more typically formulated in the real-frequency context, in which case the time dependence of all quantities would be $\sim e^{-i\omega t}$ instead of $\sim e^{+\xi t}$, and it is from this context that the term "monochromatic" is borrowed. Although we are here presenting an imaginary-frequency version of the boundary element method—because this is the version that we need for the purposes of this thesis—the entire discussion of this chapter carries over immediately to the real-frequency case simply by replacing the imaginary-frequency dyadic Green's functions $\boldsymbol{\Gamma}(\xi; \mathbf{r})$ (which have exponentially-decaying spatial dependence $\boldsymbol{\Gamma} \sim e^{-\xi r/c}$) with their real-frequency counterparts $\boldsymbol{\Gamma}(\omega; \mathbf{r})$ (which have *oscillatory* spatial dependence $\boldsymbol{\Gamma} \sim e^{i\omega r/c}$).

[2]The dyadic Green's functions in Appendix A carry a superscript r indexing the homogeneous region in which they are defined; the absence of that superscript on $\boldsymbol{\Gamma}^{\text{EE}}$ in (4.1) indicates that this is a *vacuum* dyadic Green's function.

tracting the tangential components of a vector. Inserting (4.1), we obtain an integral equation for $\mathbf{K}(\mathbf{x})$:

$$\left[\oint_{\mathcal{S}} \mathbf{\Gamma}^{\mathrm{EE}}(\xi; \mathbf{x}, \mathbf{x}') \cdot \mathbf{K}(\mathbf{x}') d\mathbf{x}' \right] \times \hat{\mathbf{n}}(\mathbf{x}) = -\mathbf{E}^{\mathrm{inc}}(\mathbf{x}) \times \hat{\mathbf{n}}(\mathbf{x}). \qquad (4.3)$$

Equation (4.3) is sometimes known as the "electric-field integral equation" (EFIE).

4.1.2 Discretization

To solve (4.3) for a general geometry, we now proceed by discretizing the surfaces of the scattering objects into small surface patches and introducing a set of *localized* tangential-vector-valued basis functions $\{\mathbf{f}_\alpha\}$ compatible with our surface discretization. The $\{\mathbf{f}_\alpha\}$, which will play the dual roles of expansion functions for our surface current distribution and testing functions for the boundary condition (4.2), are the "boundary elements" from which our method derives its name. (The discussion in this chapter is independent of any particular choice of basis function; in Chapters 6 and 7 we will specialize to two specific choices of basis function that are particularly convenient in certain cases.)

Approximating the induced surface current $\mathbf{K}(\mathbf{x})$ as an expansion in the finite set $\{\mathbf{f}_\alpha\}$,

$$\mathbf{K}(\mathbf{x}) = \sum_\alpha K_\alpha \mathbf{f}_\alpha(\mathbf{x}), \qquad (4.4)$$

inserting into (4.1), and taking the inner product of (4.3) with each basis function in the set yields a linear system for the expansion coefficients $\{K_\alpha\}$:

$$\mathbf{M} \cdot \mathbf{K} = \mathbf{V} \qquad (4.5)$$

where the elements of the $\mathbf{K}$ vector are the expansion coefficients $\{K_\alpha\}$, the elements of the $\mathbf{V}$ vector are the inner products of the basis functions with the incident field,

$$\mathbf{V}_\alpha = - \int_{\sup \mathbf{f}_\alpha} \mathbf{f}_\alpha(\mathbf{x}) \cdot \mathbf{E}^{\mathrm{inc}}(\mathbf{x}) \, d\mathbf{x}$$

$$\equiv -\left\langle \mathbf{f}_\alpha \middle| \mathbf{E}^{\mathrm{inc}} \right\rangle, \qquad (4.6)$$

and the elements of the $\mathbf{M}$ matrix are the interactions of the basis functions:

$$\mathbf{M}_{\alpha\beta}(\xi) = \int_{\sup \mathbf{f}_\alpha} \int_{\sup \mathbf{f}_\beta} \mathbf{f}_\alpha(\mathbf{x}) \cdot \mathbf{\Gamma}^{\mathrm{EE}}(\xi, \mathbf{x}, \mathbf{x}') \cdot \mathbf{f}_\beta(\mathbf{x}') \, d\mathbf{x} \, d\mathbf{x}'$$

$$\equiv \left\langle \mathbf{f}_\alpha \middle| \mathbf{\Gamma}^{\mathrm{EE}} \middle| \mathbf{f}_\beta \right\rangle.$$

We will refer to the matrix defined by (4.7a) as the "EFIE matrix." Note that $M_{\alpha\beta}$ is the inner product of basis function $\mathbf{f}_\alpha$ with the electric field radiated by currents described by basis function $\mathbf{f}_\beta$.

4.1.3 Explicit Expression for Scattered Fields

After solving the linear system (4.5) for the $\{K_\alpha\}$ coefficients, we may use these coefficients to compute the scattered fields anywhere in space according to

$$\mathbf{E}^{\text{scat}}(\mathbf{x}) = \sum_\alpha K_\alpha \int_{\text{sup}\,\mathbf{f}_\alpha} \mathbf{\Gamma}^{\text{EE}}(\xi; \mathbf{x}, \mathbf{x}') \cdot \mathbf{f}_\alpha(\mathbf{x}') \, d\mathbf{x}' \tag{4.7a}$$

$$\equiv \sum_\alpha K_\alpha \left\langle \mathbf{\Gamma}^{\text{EE}}(\mathbf{x}) \middle| \mathbf{f}_\alpha \right\rangle \tag{4.7b}$$

$$\mathbf{H}^{\text{scat}}(\mathbf{x}) \equiv \sum_\alpha K_\alpha \left\langle \mathbf{\Gamma}^{\text{ME}}(\mathbf{x}) \middle| \mathbf{f}_\alpha \right\rangle. \tag{4.7c}$$

For the sequel it will be convenient to have an explicit, if formal, expression for the scattered fields in terms of the incident fields. We obtain such an expression by substituting the formal solution to (4.5), $\mathbf{K} = \mathbf{M}^{-1} \cdot \mathbf{V}$, into (4.7):

$$\mathbf{E}^{\text{scat}}(\mathbf{x}) = -\sum_{\alpha\beta} \left\langle \mathbf{\Gamma}^{\text{EE}}(\mathbf{x}) \middle| \mathbf{f}_\alpha \right\rangle \left[M^{-1}\right]_{\alpha\beta} \left\langle \mathbf{f}_\beta \middle| \mathbf{E}^{\text{inc}} \right\rangle \tag{4.8a}$$

$$\mathbf{H}^{\text{scat}}(\mathbf{x}) = -\sum_{\alpha\beta} \left\langle \mathbf{\Gamma}^{\text{ME}}(\mathbf{x}) \middle| \mathbf{f}_\alpha \right\rangle \left[M^{-1}\right]_{\alpha\beta} \left\langle \mathbf{f}_\beta \middle| \mathbf{E}^{\text{inc}} \right\rangle \tag{4.8b}$$

Equations (4.8) will play a crucial role in our application of BEM techniques to stress-tensor Casimir computations in Chapter 5.

4.2 The Boundary-Element Method for General Bodies

4.2.1 Integral Equations for K and N

In the PEC case, the mathematics of the BEM procedure neatly mirrors the physics of the actual situation. Indeed, for good conductors at moderate frequencies it really *is* true that the physical induced currents are confined near the object surfaces; the surface current distribution $\mathbf{K}(\mathbf{x})$ obtained in the BEM procedure thus has a direct physical interpretation as an induced surface current.

The situation is more complicated for general (non-PEC) objects, for here the physical induced currents are no longer confined to the surfaces, but instead extend throughout the bulk of the object. The obvious extension of the procedure outlined above would be to introduce a *volume* discretization and solve a system analogous to (4.5) for the coefficients in an expansion of a volume current density $\mathbf{J}(\mathbf{x})$. Such a procedure, while retaining the intuitive interpretation of the quantity computed as a physical current density, would suffer from poor complexity scaling, as the number of unknowns (and thus the dimension of the linear system corresponding to (4.5)) would scale like the volume, not the surface area, of the scattering objects.

To retain the advantages of a surface-only formulation, we abandon the strategy

40

of solving for the physical source density that radiates the scattered fields, and instead attempt to solve directly for the tangential components of the total fields on the boundary surfaces. The mathematical development underlying this approach is a certain vector generalization of Green's theorem known as the *Stratton-Chu* equations [44], which relate the electromagnetic fields in the interior of a closed region to the tangential components of the fields on the boundary of that region. More precisely, let Ω be a contiguous homogeneous volume in space with boundary $\partial\Omega$, and for points $\mathbf{x}$ on $\partial\Omega$ define two tangential vector fields according to

$$\mathbf{K}^{\mathrm{eff}}(\mathbf{x}) \equiv \hat{\mathbf{n}}(\mathbf{x}) \times \mathbf{H}(\mathbf{x}), \qquad \mathbf{N}^{\mathrm{eff}}(\mathbf{x}) \equiv \mathbf{E}(\mathbf{x}) \times \hat{\mathbf{n}}(\mathbf{x}) \tag{4.9}$$

where $\mathbf{E}$ and $\mathbf{H}$ are the total (incident plus scattered) fields and $\hat{\mathbf{n}}$ is the *inward-pointing* normal to $\partial\Omega$ at $\mathbf{x}$. The Stratton-Chu equations are then the following expressions for the fields at points inside Ω:

$$\mathbf{E}(\mathbf{x}) = \oint_{\partial\Omega} \left\{ \mathbf{\Gamma}^{\mathrm{EE},r}(\xi; \mathbf{x}, \mathbf{x}') \cdot \mathbf{K}^{\mathrm{eff}}(\mathbf{x}') + \mathbf{\Gamma}^{\mathrm{EM},r}(\xi; \mathbf{x}, \mathbf{x}') \cdot \mathbf{N}^{\mathrm{eff}}(\mathbf{x}') \right\} d\mathbf{x}' \tag{4.10a}$$

$$\mathbf{H}(\mathbf{x}) = \oint_{\partial\Omega} \left\{ \mathbf{\Gamma}^{\mathrm{ME},r}(\xi; \mathbf{x}, \mathbf{x}') \cdot \mathbf{K}^{\mathrm{eff}}(\mathbf{x}') + \mathbf{\Gamma}^{\mathrm{MM},r}(\xi; \mathbf{x}, \mathbf{x}') \cdot \mathbf{N}^{\mathrm{eff}}(\mathbf{x}') \right\} d\mathbf{x}' \tag{4.10b}$$

where the $\mathbf{\Gamma}$ functions are the dyadic Green's functions for the homogeneous medium Ω. (Equations (4.10) assume that there are no field sources within Ω; if there are any such sources, their contributions must be added in separately.)

Although the tangential vector fields defined by (4.10) are simply components of the $\mathbf{E}$ and $\mathbf{H}$ fields and do not correspond to actual physical source densities, nonetheless the form of equations (4.10) encourages us to think of $\mathbf{K}^{\mathrm{eff}}$ and $\mathbf{N}^{\mathrm{eff}}$ as *effective* electric and magnetic surface current densities, which, if known, would allow us to compute the fields anywhere in space, just as knowledge of $\mathbf{K}(\mathbf{x})$ suffices in the PEC case to determine uniquely the full scattered field. (To emphasize this analogy we will henceforth drop the "eff" designation from $\mathbf{K}$ and $\mathbf{N}$.)

As in the PEC case, we obtain equations determining the effective source densities by applying the boundary conditions, which are simply that the tangential components of the total $\mathbf{E}$ and $\mathbf{H}$ fields be continuous across material boundaries. Consider a scattering problem in which incident fields $\mathbf{E}^{\mathrm{inc}}, \mathbf{H}^{\mathrm{inc}}$ impinge on one or more compact objects embedded in a medium. (The objects might themselves consist of multiple distinct layers of homogeneous material, such as a dielectric sphere coated with a thin layer of conducting material; all that is important for our purposes is that space be divided up into a number of contiguous piecewise-homogeneous regions Ω_r). Consider a point $\mathbf{x}$ on the boundary between two regions Ω_r and Ω_s, and suppose the incident field sources lie in Ω_s. (For the prototypical scattering problem involving incident radiation impinging on a compact homogeneous scatterer in a medium, Ω_r would be the interior of the scatterer, while Ω_s would be the external medium.) As

41

we approach $\mathbf{x}$ from within Ω_s, the fields approach

$$\mathbf{E}^{\text{ext}}(\mathbf{x}) = \mathbf{E}^{\text{inc}}(\mathbf{x}) + \oint_{\partial\Omega_s} \left\{ \mathbf{\Gamma}^{\text{EE},s}(\mathbf{x}) \cdot \mathbf{K} + \mathbf{\Gamma}^{\text{EM},s}(\mathbf{x}) \cdot \mathbf{N} \right\} d\mathbf{x}' \qquad (4.11a)$$

$$\mathbf{H}^{\text{ext}}(\mathbf{x}) = \mathbf{H}^{\text{inc}}(\mathbf{x}) + \oint_{\partial\Omega_s} \left\{ \mathbf{\Gamma}^{\text{ME},s}(\mathbf{x}) \cdot \mathbf{K} + \mathbf{\Gamma}^{\text{MM},s}(\mathbf{x}) \cdot \mathbf{N} \right\} d\mathbf{x}' \qquad (4.11b)$$

where the s superscript identifies the dyadic Green's functions appropriate for medium Ω_s.

On the other hand, as we approach $\mathbf{x}$ from within Ω_r, the fields approach

$$\mathbf{E}^{\text{int}}(\mathbf{x}) = \oint_{\partial\Omega_r} \left\{ \mathbf{\Gamma}^{\text{EE},r}(\mathbf{x}) \cdot \mathbf{K} + \mathbf{\Gamma}^{\text{EM},r}(\mathbf{x}) \cdot \mathbf{N} \right\} d\mathbf{x}' \qquad (4.12a)$$

$$\mathbf{H}^{\text{int}}(\mathbf{x}) = \oint_{\partial\Omega_r} \left\{ \mathbf{\Gamma}^{\text{ME},r}(\mathbf{x}) \cdot \mathbf{K} + \mathbf{\Gamma}^{\text{MM},r}(\mathbf{x}) \cdot \mathbf{N} \right\} d\mathbf{x}'. \qquad (4.12b)$$

Equating tangential components of (4.11) and (4.12) yields a system of integral equations for the surface current densities:

$$\left[\oint_{\partial\Omega_r} \left\{ \mathbf{\Gamma}^{\text{EE},r} \cdot \mathbf{K} + \mathbf{\Gamma}^{\text{EM},r} \cdot \mathbf{N} \right\} d\mathbf{x}' - \oint_{\partial\Omega_s} \left\{ \mathbf{\Gamma}^{\text{EE},s} \cdot \mathbf{K} + \mathbf{\Gamma}^{\text{EM},s} \cdot \mathbf{N} \right\} d\mathbf{x}' \right]_{\|} = -\mathbf{E}^{\text{inc}}_{\|}(\mathbf{x})$$

$$\tag{4.13a}$$

$$\left[\oint_{\partial\Omega_r} \left\{ \mathbf{\Gamma}^{\text{ME},r} \cdot \mathbf{K} + \mathbf{\Gamma}^{\text{MM},r} \cdot \mathbf{N} \right\} d\mathbf{x}' - \oint_{\partial\Omega_s} \left\{ \mathbf{\Gamma}^{\text{ME},s} \cdot \mathbf{K} + \mathbf{\Gamma}^{\text{MM},s} \cdot \mathbf{N} \right\} d\mathbf{x}' \right]_{\|} = -\mathbf{H}^{\text{inc}}_{\|}(\mathbf{x})$$

$$\tag{4.13b}$$

These equations, which are the generalization of (4.3) to the case of non-PEC scatterers, are sometimes known as the Poggio-Miller-Chang-Harrington-Wu (PMCHW) equations [32].

4.2.2 Discretization

Proceeding now in precise analogy to the PEC case, we discretize the boundary surfaces $\partial\Omega_r$ and approximate the surface current distributions as expansions in a set of localized basis functions:

$$\mathbf{K}(\mathbf{x}) = \sum_\alpha K_\alpha \mathbf{f}_\alpha(\mathbf{x}), \qquad \mathbf{N}(\mathbf{x}) = -Z_0 \sum_\alpha N_\alpha \mathbf{f}_\alpha(\mathbf{x}). \qquad (4.14)$$

(Here $Z_0 \approx 377\,\Omega$ is the impedance of free space, and the constant prefactor in the definition of the N_α coefficients is a useful convention which leads to a symmetric BEM matrix.)

With the expansions (4.14), the discretized version of equations (4.13) becomes

$$\begin{pmatrix} \mathbf{M}^{\text{EE}} & \mathbf{M}^{\text{EM}} \\ \mathbf{M}^{\text{ME}} & \mathbf{M}^{\text{MM}} \end{pmatrix} \cdot \begin{pmatrix} \mathbf{K} \\ \mathbf{N} \end{pmatrix} = \begin{pmatrix} \mathbf{V}^{\text{E}} \\ \mathbf{V}^{\text{M}} \end{pmatrix} \qquad (4.15)$$

where the elements of the RHS vector are

$$\mathbf{V}_\alpha^{\mathrm{E}} = -\left\langle \mathbf{f}_\alpha | \mathbf{E}^{\mathrm{inc}} \right\rangle / Z_0, \qquad \mathbf{V}_\alpha^{\mathrm{M}} = -\left\langle \mathbf{f}_\alpha | \mathbf{H}^{\mathrm{inc}} \right\rangle,$$

and the elements of the matrix—for the simplest case of one or more homogeneous objects embedded in an external medium—are

$$\mathbf{M}_{\alpha\beta}^{\mathrm{EE}}(\xi) = \left\langle \mathbf{f}_\alpha | \boldsymbol{\Gamma}^{\mathrm{EE},e}(\xi) + \boldsymbol{\Gamma}^{\mathrm{EE},r}(\xi) | \mathbf{f}_\beta \right\rangle / Z_0$$

$$\mathbf{M}_{\alpha\beta}^{\mathrm{EM}}(\xi) = -\left\langle \mathbf{f}_\alpha | \boldsymbol{\Gamma}^{\mathrm{EM},e}(\xi) + \boldsymbol{\Gamma}^{\mathrm{EM},r}(\xi) | \mathbf{f}_\beta \right\rangle$$

$$\mathbf{M}_{\alpha\beta}^{\mathrm{ME}}(\xi) = \left\langle \mathbf{f}_\alpha | \boldsymbol{\Gamma}^{\mathrm{ME},e}(\xi) + \boldsymbol{\Gamma}^{\mathrm{ME},r}(\xi) | \mathbf{f}_\beta \right\rangle$$

$$\mathbf{M}_{\alpha\beta}^{\mathrm{MM}}(\xi) = -Z_0 \left\langle \mathbf{f}_\alpha | \boldsymbol{\Gamma}^{\mathrm{MM},e}(\xi) + \boldsymbol{\Gamma}^{\mathrm{MM},r}(\xi) | \mathbf{f}_\beta \right\rangle.$$

if basis functions $\mathbf{f}_\alpha$ and $\mathbf{f}_\beta$ both exist on the surface of the rth object, or

$$\mathbf{M}_{\alpha\beta}^{\mathrm{EE}}(\xi) = \left\langle \mathbf{f}_\alpha | \boldsymbol{\Gamma}^{\mathrm{EE},e}(\xi) | \mathbf{f}_\beta \right\rangle / Z_0,$$

$$\mathbf{M}_{\alpha\beta}^{\mathrm{EM}}(\xi) = -\left\langle \mathbf{f}_\alpha | \boldsymbol{\Gamma}^{\mathrm{EM},e}(\xi) | \mathbf{f}_\beta \right\rangle,$$

$$\mathbf{M}_{\alpha\beta}^{\mathrm{ME}}(\xi) = \left\langle \mathbf{f}_\alpha | \boldsymbol{\Gamma}^{\mathrm{ME},e}(\xi) | \mathbf{f}_\beta \right\rangle,$$

$$\mathbf{M}_{\alpha\beta}^{\mathrm{MM}}(\xi) = -Z_0 \left\langle \mathbf{f}_\alpha | \boldsymbol{\Gamma}^{\mathrm{MM},e}(\xi) | \mathbf{f}_\beta \right\rangle.$$

if basis functions $\mathbf{f}_\alpha$ and $\mathbf{f}_\beta$ exist on the surfaces of different objects (and where the e superscript identifies the dyadic Green's functions appropriate for the external medium). (Physically, two surface current elements on the surface of the same object interact with one another both through the medium interior to that object and through the exterior medium, while currents on different objects interact only through the exterior medium).

We will refer to the matrix $\mathbf{M}(\xi)$ defined by the above equations as the "PMCHW matrix."

4.2.3   Explicit Expression for Scattered Fields

After solving (4.15) for the surface-current expansion coefficients, we may use them to compute the scattered fields anywhere in space according to

$$\mathbf{E}^{\mathrm{scat}}(\mathbf{x}) = \sum_\alpha \left\{ K_\alpha \left\langle \boldsymbol{\Gamma}^{\mathrm{EE},e}(\mathbf{x}) | \mathbf{f}_\alpha \right\rangle - Z_0 N_\alpha \left\langle \boldsymbol{\Gamma}^{\mathrm{EM},e}(\mathbf{x}) | \mathbf{f}_\alpha \right\rangle \right\} \qquad (4.16a)$$

$$\mathbf{H}^{\mathrm{scat}}(\mathbf{x}) = \sum_\alpha \left\{ K_\alpha \left\langle \boldsymbol{\Gamma}^{\mathrm{ME},e}(\mathbf{x}) | \mathbf{f}_\alpha \right\rangle - Z_0 N_\alpha \left\langle \boldsymbol{\Gamma}^{\mathrm{MM},e}(\mathbf{x}) | \mathbf{f}_\alpha \right\rangle \right\}. \qquad (4.16b)$$

(These are for the case of evaluation points $\mathbf{x}$ in the exterior region; the corresponding expressions for $\mathbf{x}$ interior to object r, which we will not need, contain minus signs relative to (4.16) and only reference the subset of the expansion coefficients

corresponding to basis functions defined on the surface of object r).

As in the PEC case, we can write explicit formal expressions for the scattered fields in terms of the incident fields. To facilitate this process we define some notation for the blocks of the inverse of the PMCHW matrix in (4.15):

$$
\begin{pmatrix} \mathbf{M}^{\mathrm{EE}} & \mathbf{M}^{\mathrm{EM}} \\ \mathbf{M}^{\mathrm{ME}} & \mathbf{M}^{\mathrm{MM}} \end{pmatrix}^{-1} \equiv \begin{pmatrix} \mathbf{A} & \mathbf{B} \\ \mathbf{C} & \mathbf{D} \end{pmatrix}.
$$

The formal solution of (4.15) is then

$$
\mathbf{K} = \mathbf{A} \cdot \mathbf{V}^{\mathrm{E}} + \mathbf{B} \cdot \mathbf{V}^{\mathrm{M}}
$$
$$
\mathbf{N} = \mathbf{C} \cdot \mathbf{V}^{\mathrm{E}} + \mathbf{D} \cdot \mathbf{V}^{\mathrm{M}}
$$

and the non-PEC analogue of equation (4.8) is

$$
\begin{aligned}
\mathbf{E}^{\mathrm{scat}}(\mathbf{x}) \\
= -\sum_{\alpha\beta} \Bigg\{ & \left\langle \boldsymbol{\Gamma}^{\mathrm{EE}}(\mathbf{x}) \middle| \mathbf{f}_\alpha \right\rangle \left[A_{\alpha\beta} \right] \left\langle \mathbf{f}_\beta \middle| \mathbf{E}^{\mathrm{inc}} \right\rangle \\
& + \left\langle \boldsymbol{\Gamma}^{\mathrm{EE}}(\mathbf{x}) \middle| \mathbf{f}_\alpha \right\rangle \left[B_{\alpha\beta} \right] \left\langle \mathbf{f}_\beta \middle| \mathbf{H}^{\mathrm{inc}} \right\rangle \\
& + \left\langle \boldsymbol{\Gamma}^{\mathrm{EM}}(\mathbf{x}) \middle| \mathbf{f}_\alpha \right\rangle \left[C_{\alpha\beta} \right] \left\langle \mathbf{f}_\beta \middle| \mathbf{E}^{\mathrm{inc}} \right\rangle \\
& + \left\langle \boldsymbol{\Gamma}^{\mathrm{EM}}(\mathbf{x}) \middle| \mathbf{f}_\alpha \right\rangle \left[D_{\alpha\beta} \right] \left\langle \mathbf{f}_\beta \middle| \mathbf{H}^{\mathrm{inc}} \right\rangle \Bigg\}
\end{aligned} \tag{4.17a}
$$

$$
\begin{aligned}
\mathbf{H}^{\mathrm{scat}}(\mathbf{x}) \\
= -\sum_{\alpha\beta} \Bigg\{ & \left\langle \boldsymbol{\Gamma}^{\mathrm{ME}}(\mathbf{x}) \middle| \mathbf{f}_\alpha \right\rangle \left[A_{\alpha\beta} \right] \left\langle \mathbf{f}_\beta \middle| \mathbf{E}^{\mathrm{inc}} \right\rangle \\
& + \left\langle \boldsymbol{\Gamma}^{\mathrm{ME}}(\mathbf{x}) \middle| \mathbf{f}_\alpha \right\rangle \left[B_{\alpha\beta} \right] \left\langle \mathbf{f}_\beta \middle| \mathbf{H}^{\mathrm{inc}} \right\rangle \\
& + \left\langle \boldsymbol{\Gamma}^{\mathrm{MM}}(\mathbf{x}) \middle| \mathbf{f}_\alpha \right\rangle \left[C_{\alpha\beta} \right] \left\langle \mathbf{f}_\beta \middle| \mathbf{E}^{\mathrm{inc}} \right\rangle \\
& + \left\langle \boldsymbol{\Gamma}^{\mathrm{MM}}(\mathbf{x}) \middle| \mathbf{f}_\alpha \right\rangle \left[D_{\alpha\beta} \right] \left\langle \mathbf{f}_\beta \middle| \mathbf{M}^{\mathrm{inc}} \right\rangle \Bigg\}.
\end{aligned} \tag{4.17b}
$$

4.2.4 Summary

This completes our brief overview of the boundary-element method. The most important results for what follows are the explicit expressions (4.8) and (4.17) for the scattered fields in terms of the incident fields. The critical advantage of these expres-

sions is that they furnish a certain separation of the scattering geometry (the details of which are encapsulated in the basis functions $\{\mathbf{f}_\alpha\}$ and in the inverse BEM matrices) from the incident fields $\{\mathbf{E}, \mathbf{H}\}^{\text{inc}}$ and the scattered-field evaluation point $\mathbf{x}$. As we will see in the next chapter, it precisely this explicit factorization that allows analytical progress to be made within the stress-tensor formulation of computational Casimir physics.

Chapter 5

Fluctuating Surface Currents: A Novel Paradigm for Efficient Numerical Computation of Casimir Interactions among Objects of Arbitrary Materials and Geometries

We now have all the pieces needed to motivate the derivation of the fluctuating-surface-current formulae that constitute the central theoretical contribution of this thesis. After stating the formulae in Section 5.1, we will present two separate derivations, one within the framework of the stress-tensor approach to Casimir computations (Section 5.2), and the other within the path-integral framework (Section 5.3).

5.1 The Fluctuating-Surface Current Formulae

The fluctuating-surface-current technique expresses the zero-temperature Casimir energy of a configuration of objects, and the zero-temperature Casimir force and torque on one of those objects, in the forms

$$\mathcal{E} = \frac{\hbar}{2\pi} \int_0^\infty d\xi \, \log \frac{\det \mathbf{M}(\xi)}{\det \mathbf{M}_\infty(\xi)} \tag{5.1a}$$

$$\mathcal{F}_i = -\frac{\hbar}{2\pi} \int_0^\infty d\xi \, \mathrm{Tr} \left\{ \mathbf{M}^{-1}(\xi) \cdot \frac{\partial \mathbf{M}(\xi)}{\partial \mathbf{r}_i} \right\} \tag{5.1b}$$

$$\mathcal{T} = -\frac{\hbar}{2\pi} \int_0^\infty d\xi \, \mathrm{Tr} \left\{ \mathbf{M}^{-1}(\xi) \cdot \frac{\partial \mathbf{M}(\xi)}{\partial \theta} \right\}. \tag{5.1c}$$

In these equations,

- $\mathbf{M}(\xi)$ is a matrix describing the interactions, at imaginary frequency ξ, of tangential electric and magnetic currents flowing on the surfaces of the interacting objects in our Casimir geometry, as approximated by expansions in some finite set of localized tangential-vector-valued expansion functions. (In fact, $\mathbf{M}$ is nothing but the the BEM matrix described in Chapter 4—either the EFIE matrix for a Casimir problem involving perfectly conducting objects, or the PMCHW matrix for more general objects.)

- The matrix $\partial \mathbf{M}/\partial \mathbf{r}_i$ in (5.1b) is the derivative of $\mathbf{M}(\xi)$ with respect to an infinitesimal displacement of one of the interacting objects in our Casimir geometry—namely, the object on which we are computing the force.

- The matrix $\partial \mathbf{M}/\partial \theta$ in (5.1c) is the derivative of $\mathbf{M}(\xi)$ with respect to an infinitesimal *rotation* of one of the interacting objects in our Casimir geometry about some axis, and $\mathcal{T}$ on the LHS of that equation is then the torque about that axis.

Readers familiar with the path-integral approach to computational Casimir physics will recognize the FSC energy formula (5.1a) as bearing a striking resemblance to the corresponding formula for the Casimir energy that arises in the path-integral formalism [37]. In both cases, the energy is computed as an integral over all imaginary frequencies, with the integrand proportional to the logarithm of a ratio of matrix determinants. The distinction lies in the *nature* of the matrix in question: in the usual path-integral formalism, $\mathbf{M}$ is a classical scattering matrix describing relationships among incoming and outgoing waves of the electromagnetic field, whereas in the FSC approach $\mathbf{M}$ is the BEM matrix (Chapter 4) describing the interactions of fluctuating surface currents on the surfaces of the objects in our Casimir geometry.

Finite-Temperature Expressions

Equations (5.1) are for temperature $T = 0$. At nonzero temperatures, the imaginary-frequency integrals go over to Matsubara sums in the usual way [22, 30]:

$$\frac{\hbar}{2\pi} \int_0^\infty d\xi\, I(\xi) \quad \to \quad k_{\mathrm{B}}T \sum_{n=0}^{\infty}{}' I(\xi_n)$$

where the nth Matsubara frequency is $\xi_n = 2n\pi k_{\mathrm{B}}T/\hbar$ and where the primed summation indicates that the $n = 0$ term enters with weight $1/2$.

5.2 Stress-Tensor Derivation of the FSC Formulae

Our first derivation of the FSC formulae proceeds by applying BEM ideas to the numerical stress-tensor method reviewed in Chapter 3. As discussed in that chapter, to compute the Casimir force on an object using the numerical stress-tensor method we surround the object by a closed bounding surface $\mathcal{C}$ and write the i-directed

Casimir force on the object as a combined integral over imaginary frequency and over $\mathcal{C}$:

$$\mathcal{F}_i = \int_0^\infty \frac{d\xi}{\pi} F_i(\xi) \tag{5.2}$$

$$F_i(\xi) = -\hbar\xi \oint_C \left\{ \epsilon(\mathbf{x};\xi) \left[\mathcal{G}_{ij}^{\mathrm{EE,scat}}(\xi,\mathbf{x},\mathbf{x}) - \frac{\delta_{ij}}{2}\mathcal{G}_{kk}^{\mathrm{EE,scat}}(\xi,\mathbf{x},\mathbf{x}) \right] \right. \tag{5.3}$$

$$\left. + \ \mu(\mathbf{x};\xi) \left[\mathcal{G}_{ij}^{\mathrm{MM,scat}}(\xi,\mathbf{x},\mathbf{x}) - \frac{\delta_{ij}}{2}\mathcal{G}_{kk}^{\mathrm{MM,scat}}(\xi,\mathbf{x},\mathbf{x}) \right] \right\} \hat{\mathbf{n}}_j(\mathbf{x}) \, d\mathbf{x}$$

where the dyadic Green's functions $\mathcal{G}(\xi)$ are the solutions of classical scattering problems at imaginary frequency ξ.

The naïve way to apply BEM ideas to stress-tensor Casimir computations would be simply to evaluate the spatial integral in (5.3) numerically, with the value of the integrand at each point computed by using a numerical BEM technique to solve the scattering problems implicit in the definition of the $\mathcal{G}$ dyadics. Although this procedure leads to a perfectly workable computational scheme,[1] and one which is already significantly more efficient than using finite-difference methods to evaluate the integrand in (5.3) [40], in fact it is possible to do much better.[2]

The key observation is that the BEM technique allows us to write down compact closed-form expressions for the dyadic Green's functions $\mathcal{G}^{\mathrm{EE,scat}}$ and $\mathcal{G}^{\mathrm{MM,scat}}$ in (5.3) in which the dependence of these quantities on the bounding contour is separated from the dependence on the Casimir geometry. Upon plugging these expressions into (5.3), it then emerges that *the surface integral can be evaluated analytically* once and for all, obviating numerical cubature for the spatial integral, eliminating the dependence on the arbitrary bounding contour $\mathcal{C}$, and leaving behind compact expressions that refer only to our particular Casimir geometry—the FSC formulae.

The derivation of these ideas is straightforward, but unavoidably involves some lengthy mathematical expressions. To present the ideas in the simplest context first, we begin by considering the case of PEC objects in vacuum, then generalize to arbitrary materials.

5.2.1 The PEC Case

If we take the incident field in (4.8) to be the field of a j-directed point electric current source at $\mathbf{x}'$, $E_i^{\mathrm{inc}}(\mathbf{x}) = \Gamma_{ij}^{\mathrm{EE}}(\mathbf{x},\mathbf{x}')$, then the scattered electric field computed

---

[1]Stress-tensor integration with the $\mathcal{G}$ dyadics computed using numerical BEM techniques is implemented in the `Casimir3D` package described in the following chapter, and may be selected in place of the FSC formulae through command-line options.

[2]After the first application of FSC techniques to the computation of Casimir interactions in general geometries [39], the same results were re-obtained using a numerical BEM solver [49].

from (4.17a) is just the scattered part of the electric-electric dyadic Green's function:

$$\mathcal{G}_{ij}^{\mathrm{EE,scat}}(\mathbf{x}, \mathbf{x}') = -\sum_{\alpha\beta} \left\langle \boldsymbol{\Gamma}_i^{\mathrm{EE}}(\mathbf{x}) \middle| \mathbf{f}_\alpha \right\rangle \left[M^{-1} \right]_{\alpha\beta} \left\langle \mathbf{f}_\beta \middle| \boldsymbol{\Gamma}_j^{\mathrm{EE}}(\mathbf{x}') \right\rangle. \tag{5.4}$$

(Throughout this section we work at a fixed imaginary frequency ξ and omit the ξ arguments to $\mathcal{G}$ and $\boldsymbol{\Gamma}$).

Similarly, to compute the scattering part of the magnetic-magnetic dyadic Green's function we take the incident field to be that of a point *magnetic* current source, $E_i^{\mathrm{inc}}(\mathbf{x}) = \Gamma_{ij}^{\mathrm{EM}}(\mathbf{x}, \mathbf{x}')$, and use (4.17b) to compute the scattered *magnetic* field:

$$\mathcal{G}_{ij}^{\mathrm{MM,scat}}(\mathbf{x}, \mathbf{x}') = -\sum_{\alpha\beta} \left\langle \boldsymbol{\Gamma}_i^{\mathrm{ME}}(\mathbf{x}) \middle| \mathbf{f}_\alpha \right\rangle \left[M^{-1} \right]_{\alpha\beta} \left\langle \mathbf{f}_\beta \middle| \boldsymbol{\Gamma}_j^{\mathrm{EM}}(\mathbf{x}') \right\rangle. \tag{5.5}$$

Writing out the inner products in full detail and rewriting the $\boldsymbol{\Gamma}$ tensors in terms of the $\mathbf{G}$ and $\mathbf{C}$ tensors (Appendix A), we may write these expressions in the form

$$\mathcal{G}_{ij}^{\mathrm{EE,scat}}(\mathbf{x}, \mathbf{x}') = -Z_0^2 \kappa^2 \sum_{\alpha\beta} \left[M^{-1} \right]_{\alpha\beta} \left[\int_{\sup \mathbf{f}_\alpha} G_{ik}(\mathbf{x}, \mathbf{r}) f_{\alpha k}(\mathbf{r})\, d\mathbf{r} \right] \left[\int_{\sup \mathbf{f}_\beta} f_{\beta l}(\mathbf{r}') G_{lj}(\mathbf{r}', \mathbf{x}')\, d\mathbf{r}' \right]$$

$$\tag{5.6a}$$

$$\mathcal{G}_{ij}^{\mathrm{MM,scat}}(\mathbf{x}, \mathbf{x}') = +\kappa^2 \sum_{\alpha\beta} \left[M^{-1} \right]_{\alpha\beta} \left[\int_{\sup \mathbf{f}_\alpha} C_{ik}(\mathbf{x}, \mathbf{r}) f_{\alpha k}(\mathbf{r})\, d\mathbf{r} \right] \left[\int_{\sup \mathbf{f}_\beta} f_{\beta l}(\mathbf{r}') C_{lj}(\mathbf{r}', \mathbf{x}')\, d\mathbf{r}' \right]$$

$$\tag{5.6b}$$

(with summation over repeated indices implied; here $\kappa = \xi/c$ and the κ arguments to G and C are suppressed). Inserting into (5.3) and interchanging the order of the $\mathbf{x}$ and $\mathbf{r}, \mathbf{r}'$ integrations then immediately yields

$$F_i(\xi) = \hbar Z_0 \kappa \sum_{\alpha\beta} \left[M^{-1} \right]_{\alpha\beta} \int_{\sup \mathbf{f}_\alpha} d\mathbf{r} \int_{\sup \mathbf{f}_\beta} d\mathbf{r}'\, f_{\alpha k}(\mathbf{r}) \cdot \mathcal{I}_{ikl}(\mathbf{r}, \mathbf{r}') \cdot f_{\beta l}(\mathbf{r}') \tag{5.7}$$

where we have defined

$$\mathcal{I}_{ikl}(\mathbf{r}, \mathbf{r}') = \kappa^2 \oint_C \Bigg\{ G_{ik}(\mathbf{x}, \mathbf{r}) G_{lj}(\mathbf{r}', \mathbf{x}) - \frac{\delta_{ij}}{2} G_{mk}(\mathbf{x}, \mathbf{r}) G_{lm}(\mathbf{r}', \mathbf{x})$$

$$- C_{ik}(\mathbf{x}, \mathbf{r}) C_{lj}(\mathbf{r}', \mathbf{x}) + \frac{\delta_{ij}}{2} C_{mk}(\mathbf{x}, \mathbf{r}) C_{lm}(\mathbf{r}', \mathbf{x}) \Bigg\} \hat{n}_j(\mathbf{x})\, d\mathbf{x}. \tag{5.8}$$

The symmetry of the M matrix in (5.7) allows us to rewrite that equation in the form

$$F_i(\xi) = \frac{\hbar}{2} \cdot Z_0 \kappa \sum_{\alpha\beta} \left[M^{-1} \right]_{\alpha\beta} \int_{\sup \mathbf{f}_\alpha} d\mathbf{r} \int_{\sup \mathbf{f}_\beta} d\mathbf{r}'\, f_{\alpha k}(\mathbf{r}) \cdot \overline{\mathcal{I}}_{ikl}(\mathbf{r}, \mathbf{r}') \cdot f_{\beta l}(\mathbf{r}') \tag{5.9}$$

where we have defined a symmetrized version of the $\mathcal{I}$ kernel,

$$\overline{\mathcal{I}}_{ikl}(\mathbf{r}, \mathbf{r}') \equiv \mathcal{I}_{ikl}(\mathbf{r}, \mathbf{r}') + \mathcal{I}_{ilk}(\mathbf{r}', \mathbf{r}). \tag{5.10}$$

The point of this symmetrization is that, as demonstrated in Appendix C, it allows the surface integrals in the definition of $\overline{\mathcal{I}}$ to be evaluated in closed form for *any* topological two-sphere $\mathcal{C}$, with the result

$$\overline{\mathcal{I}}_{ikl}(\mathbf{r}, \mathbf{r}') = \begin{cases} 0, & \text{if both } \mathbf{r}, \mathbf{r}' \text{ lie inside } \mathcal{C} \\[2mm] \dfrac{\partial}{\partial \mathbf{r}_i} G_{kl}(\mathbf{r} - \mathbf{r}') & \text{if } \mathbf{r} \text{ lies inside and } \mathbf{r}' \text{ lies outside } \mathcal{C} \\[2mm] -\dfrac{\partial}{\partial \mathbf{r}_i} G_{kl}(\mathbf{r} - \mathbf{r}') & \text{if } \mathbf{r} \text{ lies outside and } \mathbf{r}' \text{ lies inside } \mathcal{C} \\[2mm] 0, & \text{if both } \mathbf{r}, \mathbf{r}' \text{ lie outside } \mathcal{C}. \end{cases} \tag{5.11}$$

Note that we may write (5.11) in the slightly simpler form

$$\overline{\mathcal{I}}_{ikl}(\mathbf{r}, \mathbf{r}') = \begin{cases} 0, & \text{if } \mathbf{r}, \mathbf{r}' \text{ lie on the same side of } \mathcal{C} \\[2mm] \dfrac{\partial}{\partial \mathbf{r}_i^{\mathrm{I}}} G_{kl}(\mathbf{r}^{\mathrm{I}} - \mathbf{r}^{\mathrm{E}}) & \text{if } \mathbf{r}, \mathbf{r}' \text{ lie on opposite sides of } \mathcal{C} \end{cases} \tag{5.12}$$

where, in the second case, $\mathbf{r}^{\mathrm{I}}$ ($\mathbf{r}^{\mathrm{E}}$) is whichever of of $\mathbf{r}, \mathbf{r}'$ lies in the interior (exterior) of $\mathcal{C}$.

Armed with equation (5.12), we can now analyze the integral over the supports of basis functions $\mathbf{f}_\alpha, \mathbf{f}_\beta$ in equation (5.9). Let us label the objects in our Casimir geometry $\mathcal{O}_1, \mathcal{O}_2, \cdots$, where $\mathcal{O}_1$ is the object on which we are computing the force; thus object $\mathcal{O}_1$ lies in the interior of the bounding surface $\mathcal{C}$, while all other objects lie in the exterior of $\mathcal{C}$. The first case of equation (5.12) then tells us that the integral over $\mathbf{f}_\alpha, \mathbf{f}_\beta$ vanishes unless precisely one of the two basis functions lies on object $\mathcal{O}_1$. Suppose $\mathbf{f}_\alpha$ lies on $\mathcal{O}_1$, while $\mathbf{f}_\beta$ lies on $\mathcal{O}_n$ with $n \geq 2$. Using the second case of (5.12), the integral in (5.9) then reads

$$Z_0 \kappa \int_{\sup \mathbf{f}_\alpha} d\mathbf{r} \int_{\sup \mathbf{f}_\beta} d\mathbf{r}' \, f_{\alpha k}(\mathbf{r}) \cdot \overline{\mathcal{I}}_{ikl}(\mathbf{r}, \mathbf{r}') \cdot f_{\beta l}(\mathbf{r}')$$

$$= Z_0 \kappa \int_{\sup \mathbf{f}_\alpha} d\mathbf{r} \int_{\sup \mathbf{f}_\beta} d\mathbf{r}' \, f_{\alpha k}(\mathbf{r}) \cdot \frac{\partial}{\partial \mathbf{r}_i} G_{kl}(\mathbf{r} - \mathbf{r}') \cdot f_{\beta l}(\mathbf{r}')$$

$$= - \int_{\sup \mathbf{f}_\alpha} d\mathbf{r} \int_{\sup \mathbf{f}_\beta} d\mathbf{r}' \, \mathbf{f}_\alpha(\mathbf{r}) \cdot \frac{\partial}{\partial \mathbf{r}_i} \mathbf{\Gamma}^{\mathrm{EE}} \cdot \mathbf{f}_\beta(\mathbf{r}'). \tag{5.13}$$

But this is nothing but minus the derivative of the α, β element of the BEM matrix $\mathbf{M}$ with respect to an infinitesimal rigid displacement of object $\mathcal{O}_1$ in the i direction,

$$= -\frac{\partial}{\partial \mathbf{r}_i} M_{\alpha\beta}. \tag{5.14}$$

An analogous analysis holds for the case in which $\mathbf{f}_\beta$ lies on $\mathcal{O}_1$ and $\mathbf{f}_\alpha$ lies on $\mathcal{O}_n$, $n \geq 2$.

In view of these observations, we can now rewrite equation (5.9) to read

$$F_i(\xi) = -\frac{\hbar}{2} \sum_{\alpha\beta} \left[M^{-1} \right]_{\alpha\beta} \cdot \frac{\partial M_{\alpha\beta}}{\partial \mathbf{r}_i}$$

$$= -\frac{\hbar}{2} \mathrm{Tr} \left\{ \mathbf{M}^{-1} \cdot \frac{\partial \mathbf{M}}{\partial \mathbf{r}_i} \right\} \tag{5.15}$$

(where we have invoked the symmetry of $\mathbf{M}$) and the full Casimir force (5.2) is

$$\mathcal{F}_i = -\frac{\hbar}{2\pi} \int_0^\infty d\xi \, \mathrm{Tr} \left\{ \mathbf{M}^{-1} \cdot \frac{\partial \mathbf{M}}{\partial \mathbf{r}_i} \right\}. \tag{5.16}$$

Next, using the general relation for the derivative of the determinant of a matrix with respect to a parameter,

$$\frac{\partial \log \det \mathbf{A}(\lambda)}{\partial \lambda} = \mathrm{Tr} \left\{ \mathbf{A}^{-1} \cdot \frac{\partial \mathbf{A}}{\partial \lambda} \right\},$$

we can identify (5.16) as minus the $\mathbf{r}_i$ derivative of an energy expression,

$$\mathcal{F}_i = -\frac{\partial \mathcal{E}}{\partial \mathbf{r}_i}$$

where

$$\mathcal{E} = \frac{\hbar}{2\pi} \int_0^\infty d\xi \log \frac{\det \mathbf{M}}{\det \mathbf{M}_\infty} \tag{5.17}$$

where $\mathbf{M}_\infty$ is $\mathbf{M}$ computed with all objects removed to infinite separations, and subtracting $\log \det \mathbf{M}_\infty$ is a convenient normalization that amounts to a choice of the zero of energy.

Equations (5.16) and (5.17) are our fluctuating surface current formulae. Although derived here for the particular case of PEC objects in vacuum (for which $\mathbf{M}$ is the EFIE matrix discussed in Chapter 4), these formulae remain valid, in precisely the forms we have quoted them here, for arbitrary material configurations, but with $\mathbf{M}$ replaced by the PMCHW matrix. We next turn to a demonstration of this fact.

5.2.2 The General Case

Generalizing to the case of arbitrary materials embedded is now just a straightforward, if notationally cumbersome, procedure.

52

The first step is to obtain the analogues of (5.4) and (5.5) for the non-PEC case. If we take the incident fields in equation (4.17) to be the fields of a j-directed point electric current source at $\mathbf{x}'$, i.e.

$$E_i^{\text{inc}}(\mathbf{x}) = \Gamma_{ij}^{\text{EE}}(\mathbf{x}, \mathbf{x}'), \qquad H_i^{\text{inc}}(\mathbf{x}) = \Gamma_{ij}^{\text{ME}}(\mathbf{x}, \mathbf{x}'),$$

then the scattered $\mathbf{E}$ field computed from (4.17a) is just the scattered portion of the electric-electric dyadic Green's function:

$$
\begin{aligned}
\mathcal{G}_{ij}^{\text{EE,scat}}(\mathbf{x}, \mathbf{x}') = -\sum_{\alpha\beta} \Bigg\{ & \left\langle \Gamma_i^{\text{EE}}(\mathbf{x}) \middle| \mathbf{f}_\alpha \right\rangle \left[A \right]_{\alpha\beta} \left\langle \mathbf{f}_\beta \middle| \Gamma_j^{\text{EE}}(\mathbf{x}') \right\rangle \\
& + \left\langle \Gamma_i^{\text{EE}}(\mathbf{x}) \middle| \mathbf{f}_\alpha \right\rangle \left[B \right]_{\alpha\beta} \left\langle \mathbf{f}_\beta \middle| \Gamma_j^{\text{ME}}(\mathbf{x}') \right\rangle \\
& \left\langle \Gamma_i^{\text{EM}}(\mathbf{x}) \middle| \mathbf{f}_\alpha \right\rangle \left[C \right]_{\alpha\beta} \left\langle \mathbf{f}_\beta \middle| \Gamma_j^{\text{EE}}(\mathbf{x}') \right\rangle \\
& + \left\langle \Gamma_i^{\text{EM}}(\mathbf{x}) \middle| \mathbf{f}_\alpha \right\rangle \left[D \right]_{\alpha\beta} \left\langle \mathbf{f}_\beta \middle| \Gamma_j^{\text{ME}}(\mathbf{x}') \right\rangle \Bigg\}.
\end{aligned}
\tag{5.18}
$$

Similarly, taking the incident fields to be the fields of a point *magnetic* source, and using (4.17b) to compute the scattered *magnetic* field, yields the scattered portion of the magnetic-magnetic dyadic Green's function:

$$
\begin{aligned}
\mathcal{G}_{ij}^{\text{MM,scat}}(\mathbf{x}, \mathbf{x}') = -\sum_{\alpha\beta} \Bigg\{ & \left\langle \Gamma_i^{\text{ME}}(\mathbf{x}) \middle| \mathbf{f}_\alpha \right\rangle \left[A \right]_{\alpha\beta} \left\langle \mathbf{f}_\beta \middle| \Gamma_j^{\text{EM}}(\mathbf{x}') \right\rangle \\
& + \left\langle \Gamma_i^{\text{ME}}(\mathbf{x}) \middle| \mathbf{f}_\alpha \right\rangle \left[B \right]_{\alpha\beta} \left\langle \mathbf{f}_\beta \middle| \Gamma_j^{\text{MM}}(\mathbf{x}') \right\rangle \\
& \left\langle \Gamma_i^{\text{MM}}(\mathbf{x}) \middle| \mathbf{f}_\alpha \right\rangle \left[C \right]_{\alpha\beta} \left\langle \mathbf{f}_\beta \middle| \Gamma_j^{\text{EM}}(\mathbf{x}') \right\rangle \\
& + \left\langle \Gamma_i^{\text{MM}}(\mathbf{x}) \middle| \mathbf{f}_\alpha \right\rangle \left[D \right]_{\alpha\beta} \left\langle \mathbf{f}_\beta \middle| \Gamma_j^{\text{MM}}(\mathbf{x}') \right\rangle \Bigg\}.
\end{aligned}
\tag{5.19}
$$

As before, we write out the full inner products in these equations with the $\boldsymbol{\Gamma}$ dyadics

rewritten in terms of the **G** and **C** dyadics:

$$
\mathcal{G}_{ij}^{\text{EE,scat}}(\mathbf{x}, \mathbf{x}')
$$

$$
= -\sum_{\alpha\beta} \Bigg\{ Z_0^2 Z^{e2} \kappa^{e2} \Big[A \Big]_{\alpha\beta} \left[\int_{\text{sup}\, \mathbf{f}_\alpha} G_{ik}(\mathbf{x}, \mathbf{r}) f_{\alpha k}(\mathbf{r})\, d\mathbf{r} \right] \left[\int_{\text{sup}\, \mathbf{f}_\beta} f_{\beta l}(\mathbf{r}') G_{lj}(\mathbf{r}', \mathbf{x}')\, d\mathbf{r}' \right]
$$

$$
- Z_0 Z^e \kappa^{e2} \Big[B \Big]_{\alpha\beta} \left[\int_{\text{sup}\, \mathbf{f}_\alpha} G_{ik}(\mathbf{x}, \mathbf{r}) f_{\alpha k}(\mathbf{r})\, d\mathbf{r} \right] \left[\int_{\text{sup}\, \mathbf{f}_\beta} f_{\beta l}(\mathbf{r}') C_{lj}(\mathbf{r}', \mathbf{x}')\, d\mathbf{r}' \right]
$$

$$
+ Z_0 Z^e \kappa^{e2} \Big[C \Big]_{\alpha\beta} \left[\int_{\text{sup}\, \mathbf{f}_\alpha} C_{ik}(\mathbf{x}, \mathbf{r}) f_{\alpha k}(\mathbf{r})\, d\mathbf{r} \right] \left[\int_{\text{sup}\, \mathbf{f}_\beta} f_{\beta l}(\mathbf{r}') G_{lj}(\mathbf{r}', \mathbf{x}')\, d\mathbf{r}' \right]
$$

$$
- \kappa^{e2} \Big[D \Big]_{\alpha\beta} \left[\int_{\text{sup}\, \mathbf{f}_\alpha} C_{ik}(\mathbf{x}, \mathbf{r}) f_{\alpha k}(\mathbf{r})\, d\mathbf{r} \right] \left[\int_{\text{sup}\, \mathbf{f}_\beta} f_{\beta l}(\mathbf{r}') C_{lj}(\mathbf{r}', \mathbf{x}')\, d\mathbf{r}' \right] \Bigg\}
$$

$$
\mathcal{G}_{ij}^{\text{MM,scat}}(\mathbf{x}, \mathbf{x}')
$$

$$
= -\sum_{\alpha\beta} \Bigg\{ - \kappa^{e2} \Big[A \Big]_{\alpha\beta} \left[\int_{\text{sup}\, \mathbf{f}_\alpha} C_{ik}(\mathbf{x}, \mathbf{r}) f_{\alpha k}(\mathbf{r})\, d\mathbf{r} \right] \left[\int_{\text{sup}\, \mathbf{f}_\beta} f_{\beta l}(\mathbf{r}') C_{lj}(\mathbf{r}', \mathbf{x}')\, d\mathbf{r}' \right]
$$

$$
- \frac{\kappa^{e2}}{Z_0 Z^e} \Big[B \Big]_{\alpha\beta} \left[\int_{\text{sup}\, \mathbf{f}_\alpha} C_{ik}(\mathbf{x}, \mathbf{r}) f_{\alpha k}(\mathbf{r})\, d\mathbf{r} \right] \left[\int_{\text{sup}\, \mathbf{f}_\beta} f_{\beta l}(\mathbf{r}') G_{lj}(\mathbf{r}', \mathbf{x}')\, d\mathbf{r}' \right]
$$

$$
+ \frac{\kappa^{e2}}{Z_0 Z^e} \Big[C \Big]_{\alpha\beta} \left[\int_{\text{sup}\, \mathbf{f}_\alpha} G_{ik}(\mathbf{x}, \mathbf{r}) f_{\alpha k}(\mathbf{r})\, d\mathbf{r} \right] \left[\int_{\text{sup}\, \mathbf{f}_\beta} f_{\beta l}(\mathbf{r}') C_{lj}(\mathbf{r}', \mathbf{x}')\, d\mathbf{r}' \right]
$$

$$
+ \frac{\kappa^{e2}}{Z_0^2 Z^{e2}} \Big[D \Big]_{\alpha\beta} \left[\int_{\text{sup}\, \mathbf{f}_\alpha} G_{ik}(\mathbf{x}, \mathbf{r}) f_{\alpha k}(\mathbf{r})\, d\mathbf{r} \right] \left[\int_{\text{sup}\, \mathbf{f}_\beta} f_{\beta l}(\mathbf{r}') G_{lj}(\mathbf{r}', \mathbf{x}')\, d\mathbf{r}' \right] \Bigg\}.
$$

(Note that the wavenumber and relative wave impedance that enter here are those of the *external* medium in our Casimir geometry, κ^e and Z^e, because the surface $\mathcal{C}$ on which we evaluate the stress tensor lies entirely within this medium.)

Substituting these expressions into (5.7) and rearranging the order of integration

54

now yields the analogue of equation (5.9):

$$\mathcal{F}_i(\xi) = \frac{\hbar}{2} \sum_{\alpha\beta} \left\{ \Big[A \Big]_{\alpha\beta} \cdot Z_0 Z^e \kappa^e \int_{\sup f_\alpha} d\mathbf{r} \int_{\sup f_\beta} d\mathbf{r}' \, f_{\alpha k}(\mathbf{r}) \cdot \overline{\mathcal{I}}_{ikl}(\mathbf{r},\mathbf{r}') \cdot f_{\beta l}(\mathbf{r}') \right.$$

$$- \Big[B \Big]_{\alpha\beta} \cdot \kappa^e \int_{\sup f_\alpha} d\mathbf{r} \int_{\sup f_\beta} d\mathbf{r}' \, f_{\alpha k}(\mathbf{r}) \cdot \overline{\mathcal{J}}_{ikl}(\mathbf{r},\mathbf{r}') \cdot f_{\beta l}(\mathbf{r}')$$

$$+ \Big[C \Big]_{\alpha\beta} \cdot \kappa^e \int_{\sup f_\alpha} d\mathbf{r} \int_{\sup f_\beta} d\mathbf{r}' \, f_{\alpha k}(\mathbf{r}) \cdot \overline{\mathcal{J}}_{ikl}(\mathbf{r},\mathbf{r}') \cdot f_{\beta l}(\mathbf{r}')$$

$$\left. + \Big[D \Big]_{\alpha\beta} \cdot \frac{\kappa^e}{Z_0 Z^e} \int_{\sup f_\alpha} d\mathbf{r} \int_{\sup f_\beta} d\mathbf{r}' \, f_{\alpha k}(\mathbf{r}) \cdot \overline{\mathcal{I}}_{ikl}(\mathbf{r},\mathbf{r}') \cdot f_{\beta l}(\mathbf{r}') \right\}$$

$$(5.20)$$

where the $\overline{\mathcal{J}}$ kernel is defined and evaluated in Appendix C, with a result directly analogous to (5.12):

$$\overline{\mathcal{J}}_{ikl}(\mathbf{r},\mathbf{r}') = \begin{cases} 0, & \text{if } \mathbf{r}, \mathbf{r}' \text{ lie on the same side of } \mathcal{C} \\ \dfrac{\partial}{\partial \mathbf{r}_i^{\mathrm{I}}} C_{kl}(\mathbf{r}^{\mathrm{I}} - \mathbf{r}^{\mathrm{E}}) & \text{if } \mathbf{r}, \mathbf{r}' \text{ lie on opposite sides of } \mathcal{C}. \end{cases} \qquad (5.21)$$

Proceeding in direct analogy to the discussion surrounding equation (5.14), it is now a short step to identify the integrals in equation (5.20) as just the derivatives of the elements of the PMCHW matrix, whence we can identify that equation as nothing but the PMCHW analogue of equation (5.15),

$$F_i(\xi) = -\frac{\hbar}{2}\mathrm{Tr}\left\{ \mathbf{M}^{-1} \cdot \frac{\partial \mathbf{M}}{\partial \mathbf{r}_i} \right\} \qquad (5.22)$$

which has precisely the same appearance as (5.15), but with $\mathbf{M}$ now standing for the PMCHW matrix instead of the EFIE matrix as in (5.15).

5.3 Path-Integral Derivation of the FSC Formulae

It is remarkable that the FSC formulae (5.1), which we derived above in the context of the stress-tensor approach to Casimir computations, can be derived on the basis of entirely separate considerations within the path-integral framework. In this section we present this alternate derivation.

The novel path-integral formulation that we present here differs in at two key respects from typical path-integral computations of electrodynamic Casimir phenomena. First, whereas most authors make a specific choice of gauge, thus concealing the underlying gauge invariance of the theory, here we write the Euclidean Lagrangian for the electromagnetic field in a way that preserves manifest gauge invariance throughout the calculation (Section 5.3.1). Second, whereas other electrodynamic path-integral

formulations convert the functional integral over fields into a functional integral over *volumetric* unknowns—such as the multipole moments of a source distribution—our treatment uses *surface* unknowns (namely, electric and magnetic surface currents). Surface unknowns have been used elsewhere in path-integral analysis of *scalar*-field fluctuations [26, 27], and special surface unknowns were used in [5] and [14] to compute electrodynamic Casimir phenomena for the special case of the infinite-parallel-plate geometry. However, this work represents the first use of surface unknowns to compute *electrodynamic* Casimir forces in *general* geometries.

5.3.1   Euclidean Lagrangian for the Electromagnetic Field

The first step in applying the path-integral formalism to the computation of electromagnetic Casimir energies is to write down a Euclidean action for the electromagnetic field. To this end, we begin by recalling that the usual (real-frequency) Lagrangian for the electromagnetic field is

$$S = \int \frac{d\omega}{2\pi} \int d\mathbf{x}\, \mathcal{L}(\omega, \mathbf{x})$$

$$\mathcal{L}(\omega, \mathbf{x}) = \frac{1}{2}\Big(\epsilon(\omega, \mathbf{x})|\mathbf{E}(\omega, \mathbf{x})|^2 - \mu(\omega, \mathbf{x})|\mathbf{H}(\omega, \mathbf{x})|^2\Big).$$

To rewrite this in terms of the four-vector potential $A^\mu(\omega, \mathbf{x})$ (with $A^0 = \Phi$, the usual scalar potential) we write[3]

$$E_i = i\omega A^i - \partial_i A^0 \qquad H_i = \frac{1}{\mu}\varepsilon_{ijk}\partial_j A^k$$

to obtain (with the ω and $\mathbf{x}$ dependence of A^μ suppressed)

$$\mathcal{L}(\omega, \mathbf{x}) = \frac{\epsilon(\omega, \mathbf{x})}{2}\Big(-i\omega A^{i*} - \partial_i A^{0*}\Big)\Big(i\omega A^i - \partial_i A^0\Big) - \frac{1}{2\mu(\omega, \mathbf{x})}\Big(\varepsilon_{ijk}\varepsilon_{ilm}\partial_j A^{k*}\partial_l A^m\Big)$$

$$= \frac{\epsilon(\omega, \mathbf{x})}{2}\Big(\omega^2 A^{i*}A^i - i\omega\partial_i A^{0*}A^i + i\omega A^{i*}\partial_i A^0 + \partial_i A^{0*}\partial_i A^{0*}\Big)$$

$$- \frac{1}{2\mu(\omega, \mathbf{x})}\Big(\partial_i A^{j*}\partial_i A^j - \partial_i A^{j*}\partial_j A^i\Big).$$

Integrate by parts to shift all derivatives over onto non-conjugated quantities:

$$= \frac{\epsilon(\omega, \mathbf{x})}{2}\Big(\omega^2 A^{i*}A^i + i\omega A^{0*}\partial_i A^i + i\omega A^{i*}\partial_i A^0 - A^{0*}\partial_i\partial_i A^0\Big)$$

$$+ \frac{1}{2\mu(\omega, \mathbf{x})}\Big(A^{i*}\partial_j\partial_j A^i - A^{i*}\partial_i\partial_j A^j\Big).$$

---

[3]Here and throughout this thesis we use the symbol ε to denote the Levi-Civita symbol, while the symbol ϵ is reserved for dielectric permittivities.

The transition to imaginary frequency is effected by the replacements[4]

$$\omega \to i\xi, \qquad A^0 \to iA^0, \qquad A^{0*} \to iA^{0*}$$

under which the Euclidean Lagrangian density reads

$$\mathcal{L}_{\mathrm{E}}(\xi, \mathbf{x}) = \frac{\epsilon(i\xi, \mathbf{x})}{2}\left(-\xi^2 A^{i*}A^i - i\xi A^{0*}\partial_i A^i - i\xi A^{i*}\partial_i A^0 + A^{0*}\partial_i\partial_i A^0\right)$$
$$+ \frac{1}{2\mu(i\xi, \mathbf{x})}\left(A^{i*}\partial_j\partial_j A^i - A^{i*}\partial_i\partial_j A^j\right) \tag{5.23}$$

or, introducing a convenient matrix-vector notation,

$$= \frac{1}{2}\begin{pmatrix} A^0 \\ A^1 \\ A^2 \\ A^3 \end{pmatrix}^\dagger \left[\mathfrak{D}'_{\epsilon\mu}(\xi)\right]\begin{pmatrix} A^0 \\ A^1 \\ A^2 \\ A^3 \end{pmatrix} \tag{5.24}$$

with

$$\mathfrak{D}'_{\epsilon\mu}(\xi) = \begin{pmatrix} \epsilon(\partial_x^2 + \partial_y^2 + \partial_z^2) & -i\epsilon\xi\partial_x & -i\epsilon\xi\partial_y & -i\epsilon\xi\partial_z \\ -i\epsilon\xi\partial_x & -\epsilon\xi^2 + \frac{1}{\mu}(\partial_y^2 + \partial_z^2) & -\frac{1}{\mu}\partial_x\partial_y & -\frac{1}{\mu}\partial_x\partial_z \\ -i\epsilon\xi\partial_y & -\frac{1}{\mu}\partial_y\partial_x & -\epsilon\xi^2 + \frac{1}{\mu}(\partial_x^2 + \partial_z^2) & -\frac{1}{\mu}\partial_y\partial_z \\ -i\epsilon\xi\partial_z & -\frac{1}{\mu}\partial_z\partial_x & -\frac{1}{\mu}\partial_z\partial_y & -\epsilon\xi^2 + \frac{1}{\mu}(\partial_x^2 + \partial_y^2) \end{pmatrix}.$$

To proceed it will actually be useful to rewrite this in the form

$$\mathcal{L}_{\mathrm{E}}(\xi, \mathbf{x}) = \frac{1}{2}\begin{pmatrix} \sqrt{\epsilon\mu} \cdot A^0 \\ A^1 \\ A^2 \\ A^3 \end{pmatrix}^\dagger \left[\mathfrak{D}_{\epsilon\mu}(\xi)\right]\begin{pmatrix} \sqrt{\epsilon\mu} \cdot A^0 \\ A^1 \\ A^2 \\ A^3 \end{pmatrix} \tag{5.25}$$

with now

$$\mathfrak{D}_{\epsilon\mu}(\xi) = \begin{pmatrix} \frac{1}{\mu}(\partial_x^2 + \partial_y^2 + \partial_z^2) & -i\sqrt{\frac{\epsilon}{\mu}}\xi\partial_x & -i\sqrt{\frac{\epsilon}{\mu}}\xi\partial_y & -i\sqrt{\frac{\epsilon}{\mu}}\xi\partial_z \\ -i\sqrt{\frac{\epsilon}{\mu}}\xi\partial_x & -\epsilon\xi^2 + \frac{1}{\mu}(\partial_y^2 + \partial_z^2) & -\frac{1}{\mu}\partial_x\partial_y & -\frac{1}{\mu}\partial_x\partial_z \\ -i\sqrt{\frac{\epsilon}{\mu}}\xi\partial_y & -\frac{1}{\mu}\partial_y\partial_x & -\epsilon\xi^2 + \frac{1}{\mu}(\partial_x^2 + \partial_z^2) & -\frac{1}{\mu}\partial_y\partial_z \\ -i\sqrt{\frac{\epsilon}{\mu}}\xi\partial_z & -\frac{1}{\mu}\partial_z\partial_x & -\frac{1}{\mu}\partial_z\partial_y & -\epsilon\xi^2 + \frac{1}{\mu}(\partial_x^2 + \partial_y^2) \end{pmatrix}.$$

---

[4]The seeming incongruity between the latter two prescriptions here is not a typo!

We will use the notation $\mathcal{A}^\mu$ to denote the four-vector in (5.25), i.e.

$$\begin{pmatrix} \mathcal{A}^0 \\ \mathcal{A}^1 \\ \mathcal{A}^2 \\ \mathcal{A}^3 \end{pmatrix} = \begin{pmatrix} \sqrt{\epsilon\mu} \cdot A^0 \\ A^1 \\ A^2 \\ A^3 \end{pmatrix}.$$

$\mathcal{A}$ will be the four-vector field over which we path-integrate, and equation (5.25) is almost, but not quite, the quantity that enters into the exponent of the constrained path-integral expression (3.10) for the Casimir energy. To complete the story, we must add a Fadeev-Popov gauge-fixing term. To identify an appropriate form for such a term, we take a page from the usual QED path-integration procedure by writing $\mathfrak{D}_{\epsilon\mu}$ as the sum of a diagonal term and a rank-one update, then taking the gauge-fixing term proportional to the rank-one update. More specifically, we write

$$\mathfrak{D}_{\epsilon\mu} = \mathbf{U}_1 - \mathbf{U}_2$$

$$\mathbf{U}_1 = \begin{pmatrix} -\epsilon\xi^2 + \frac{1}{\mu}\nabla^2 & 0 & 0 & 0 \\ 0 & -\epsilon\xi^2 + \frac{1}{\mu}\nabla^2 & 0 & 0 \\ 0 & 0 & -\epsilon\xi^2 + \frac{1}{\mu}\nabla^2 & 0 \\ 0 & 0 & 0 & -\epsilon\xi^2 + \frac{1}{\mu}\nabla^2 \end{pmatrix}$$

$$\mathbf{U}_2 = \begin{pmatrix} -\epsilon\xi^2 & i\sqrt{\frac{\epsilon}{\mu}}\xi\partial_x & i\sqrt{\frac{\epsilon}{\mu}}\xi\partial_y & i\sqrt{\frac{\epsilon}{\mu}}\xi\partial_z \\ i\sqrt{\frac{\epsilon}{\mu}}\xi\partial_x & \frac{1}{\mu}\partial_x^2 & \frac{1}{\mu}\partial_x\partial_y & \frac{1}{\mu}\partial_x\partial_z \\ i\sqrt{\frac{\epsilon}{\mu}}\xi\partial_y & \frac{1}{\mu}\partial_y\partial_x & \frac{1}{\mu}\partial_y^2 & \frac{1}{\mu}\partial_y\partial_z \\ i\sqrt{\frac{\epsilon}{\mu}}\xi\partial_z & \frac{1}{\mu}\partial_z\partial_x & \frac{1}{\mu}\partial_z\partial_y & \frac{1}{\mu}\partial_z^2 \end{pmatrix}$$

and we now take the Fadeev-Popov gauge-fixing term to be simply

$$\mathfrak{D}_{\mathrm{FP}} = \frac{1}{\alpha_{\mathrm{FP}}}\mathbf{U}_2$$

where the Fadeev-Popov gauge-choice parameter α_{FP} may be chosen arbitrarily and is absent from all physical predictions, as will be explicitly verified below.

The final expression for the Euclidean electromagnetic Lagrangian density is

$$\mathcal{L}_E\left\{\mathcal{A}^\mu(\mathbf{x})e^{-i\xi\tau}\right\} = \frac{1}{2}\begin{pmatrix} \mathcal{A}^0 \\ \mathcal{A}^1 \\ \mathcal{A}^2 \\ \mathcal{A}^3 \end{pmatrix}^\dagger \left[\mathfrak{D}_{\epsilon\mu}(\xi) + \mathfrak{D}_{\mathrm{FP}}(\xi)\right]\begin{pmatrix} \mathcal{A}^0 \\ \mathcal{A}^1 \\ \mathcal{A}^2 \\ \mathcal{A}^3 \end{pmatrix} \quad (5.26)$$

and, following the general procedure discussed in Chapter 3, we write the electromagnetic Casimir (free) energy of a collection of objects at inverse temperature β in the

form

$$\mathcal{E} = -\frac{1}{\beta} \ln \frac{Z(\beta)}{Z_\infty(\beta)} = -\frac{1}{\beta} \sum_{n=0}^{\infty} \ln \frac{\mathcal{Z}(\beta, \xi_n)}{\mathcal{Z}_\infty(\beta, \xi_n)} \qquad \left(\xi_n \equiv \frac{2\pi n}{\hbar \beta} \right) \qquad (5.27)$$

$$\mathcal{Z}(\beta, \xi) = \int \left[\mathcal{D}\mathcal{A}^\mu \right]_{\mathrm{C}} e^{-\frac{\beta}{2} \int \mathcal{A} \cdot \mathfrak{D}(\xi) \cdot \mathcal{A} \, dx} \qquad (5.28)$$

with the notation $[\cdots]_{\mathrm{C}}$ indicating that the functional integration ranges only over field configurations that satisfy the boundary conditions in the presence of our interacting material objects.

5.3.2 Boundary Conditions on the Electromagnetic Field

In a scattering geometry consisting of one or more homogeneous material bodies embedded in a homogeneous medium, the boundary conditions on the electromagnetic field are simply that the tangential **E** and **H** fields be continuous across all material boundaries: if **x** is a point on the surface of an object, then we require

$$\mathbf{t}^a \cdot \left[\mathbf{E}^{\mathrm{in}}(\mathbf{x}) - \mathbf{E}^{\mathrm{out}}(\mathbf{x}) \right] = 0$$

$$\mathbf{t}^a \cdot \left[\mathbf{H}^{\mathrm{in}}(\mathbf{x}) - \mathbf{H}^{\mathrm{out}}(\mathbf{x}) \right] = 0$$

where $\{\mathbf{E}, \mathbf{H}\}^{\mathrm{in,out}}$ are the fields evaluated just inside and just outside the object surface at **x**, and where $\mathbf{t}^a$ ($a \in \{1,2\}$) are vectors tangent to the surface at **x**. In terms of the modified four-vector potential $\mathcal{A}^\mu$, these conditions may be written in the form

$$t_i^a \left\{ L_{i\mu}^{\mathrm{E,in}}(\mathbf{x}) - L_{i\mu}^{\mathrm{E,out}}(\mathbf{x}) \right\} \mathcal{A}^\mu(\mathbf{x}) = 0 \qquad (5.30a)$$

$$t_i^a \left\{ L_{i\mu}^{\mathrm{M,in}}(\mathbf{x}) - L_{i\mu}^{\mathrm{M,out}}(\mathbf{x}) \right\} \mathcal{A}^\mu(\mathbf{x}) = 0 \qquad (5.30b)$$

where $\mathbf{L}^{\mathrm{E},r}$ and $\mathbf{L}^{\mathrm{M},r}$ are differential operators that operate on $\mathcal{A}^\mu$ to yield the components of the **E** and **H** fields in region r. In a homogeneous region with spatially constant $\epsilon(\xi, \mathbf{x}) = \epsilon^r(\xi), \mu(\xi, \mathbf{x}) = \mu^r(\xi)$, these take the form

$$\mathbf{L}^{\mathrm{E},r} = \begin{pmatrix} -\frac{1}{\sqrt{\epsilon^r \mu^r}} \cdot \partial_x & i\xi & 0 & 0 \\ -\frac{1}{\sqrt{\epsilon^r \mu^r}} \cdot \partial_y & 0 & i\xi & 0 \\ -\frac{1}{\sqrt{\epsilon^r \mu^r}} \cdot \partial_z & 0 & 0 & i\xi \end{pmatrix}, \qquad \mathbf{L}^{\mathrm{M},r} = \frac{1}{\mu^r} \begin{pmatrix} 0 & 0 & -\partial_z & \partial_y \\ 0 & \partial_z & 0 & -\partial_x \\ 0 & -\partial_y & \partial_x & 0 \end{pmatrix}.$$

$$(5.31)$$

Equations (5.30) are a set of four boundary conditions for each point **x** on the surfaces of the material bodies in our geometry; in the language of the Section 3.2, these are our constraints $L_\alpha \phi$, and to each constraint we now associate a Lagrange multiplier. We use the symbols $K^a(\mathbf{x})$ and $N^a(\mathbf{x})$ ($a = 1, 2$), respectively, to denote the Lagrange

multipliers associated with constraints (5.30a) and (5.30b) at the single point $\mathbf{x}$. Then the δ functions that enforce the boundary conditions (5.30) at $\mathbf{x}$ are

$$\delta\left(\mathbf{E}_{\parallel}^{\text{in}}(\mathbf{x}) - \mathbf{E}_{\parallel}^{\text{out}}(\mathbf{x})\right) = \int \frac{d\mathbf{K_x}}{(2\pi)^2} e^{i\mathbf{K_x} \cdot [\mathbf{L}_{\mu}^{\text{E,in}} - \mathbf{L}_{\mu}^{\text{E,out}}]\mathcal{A}^{\mu}(\mathbf{x})}$$

$$\delta\left(\mathbf{H}_{\parallel}^{\text{in}}(\mathbf{x}) - \mathbf{H}_{\parallel}^{\text{out}}(\mathbf{x})\right) = \int \frac{d\mathbf{N_x}}{(2\pi)^2} e^{i\mathbf{N_x} \cdot [\mathbf{L}_{\mu}^{\text{M,in}} - \mathbf{L}_{\mu}^{\text{M,out}}]\mathcal{A}^{\mu}(\mathbf{x})}$$

where we may think of $\{\mathbf{K_x}, \mathbf{N_x}\} = \sum_{a=1}^{2}\{K^a, N^a\}\mathbf{t}^a$ as vectors in the tangent space to the boundary surface at $\mathbf{x}$. Aggregating the corresponding δ functions for all points on the surface of a single object, we obtain *functional* δ-functions,

$$\int \mathcal{D}\mathbf{K}(\mathbf{x}) e^{i \int_{\mathcal{S}} \mathbf{K}(\mathbf{x}) \cdot [\mathbf{L}_{\mu}^{\text{E,in}} - \mathbf{L}_{\mu}^{\text{E,out}}]\mathcal{A}^{\mu}(\mathbf{x}) d\mathbf{x}} \tag{5.32a}$$

$$\int \mathcal{D}\mathbf{N}(\mathbf{x}) e^{i \int_{\mathcal{S}} \mathbf{N}(\mathbf{x}) \cdot [\mathbf{L}_{\mu}^{\text{M,in}} - \mathbf{L}_{\mu}^{\text{M,out}}]\mathcal{A}^{\mu}(\mathbf{x}) d\mathbf{x}} \tag{5.32b}$$

where the integral in the exponent is over the surface $\mathcal{S}$ of an object in our geometry, and where the functional integrations $\int \mathcal{D}\mathbf{K}$, $\int \mathcal{D}\mathbf{N}$ extend over all possible tangential vector fields on $\mathcal{S}$.

Since $\mathbf{K}$ and $\mathbf{N}$ are tangential vector fields on $\mathcal{S}$ that enforce the continuity of the tangential electric and magnetic fields, respectively, it is tempting to interpret these quantities as electric and magnetic surface current densities, and with their introduction our path-integral formalism begins to exhibit the first glimmers of resemblance to the boundary-element method (in the PMCHW formulation) discussed in Chapter 4.

5.3.3 Evaluation of the Constrained Path Integral

In general we will have one copy of the functional δ-functions (5.32) for the surface of each object in our geometry. For the particular case of two objects, the constrained path integral takes the form

$$\mathcal{Z}(\beta, \xi) = \int \left[\mathcal{D}\mathcal{A}^{\mu}\right]_C e^{-\frac{\beta}{2} \int \mathcal{A} \cdot \mathfrak{D} \cdot \mathcal{A} \, d\mathbf{x}}$$

$$= \int \mathcal{D}\mathbf{K}_1 \int \mathcal{D}\mathbf{K}_2 \int \mathcal{D}\mathbf{N}_1 \int \mathcal{D}\mathbf{N}_2 \int \mathcal{D}\mathcal{A}^{\mu} \bigg\{$$

$$e^{-\frac{\beta}{2} \int \mathcal{A} \cdot \mathfrak{D} \cdot \mathcal{A} \, d\mathbf{x}}$$

$$\times e^{+i \int_{\mathcal{S}_1} \left\{ \mathbf{K}_1 \cdot (\mathbf{L}^{\text{E},1} - \mathbf{L}^{\text{E},0}) + \mathbf{N}_1 \cdot (\mathbf{L}^{\text{M},1} - \mathbf{L}^{\text{M},0}) \right\} \cdot \mathcal{A} \, d\mathbf{x}}$$

$$\times e^{+i \int_{\mathcal{S}_2} \left\{ \mathbf{K}_2 \cdot (\mathbf{L}^{\text{E},2} - \mathbf{L}^{\text{E},0}) + \mathbf{N}_2 \cdot (\mathbf{L}^{\text{M},2} - \mathbf{L}^{\text{M},0}) \right\} \cdot \mathcal{A} \, d\mathbf{x}} \bigg\}$$

with $\int_{\mathcal{S}_{1,2}}$ denoting integration over the surfaces of objects 1 and 2.

To proceed, it is now convenient to think of breaking up the functional integration over $\mathcal{A}^\mu$ into three components, $\int \mathcal{D}\mathcal{A}^\mu = \int \mathcal{D}\mathcal{A}^\mu_e \int \mathcal{D}\mathcal{A}^\mu_1 \int \mathcal{D}\mathcal{A}^\mu_2$, where $\mathcal{A}^\mu_r$ is the field in the interior of region r ($r = 1, 2$ for the interiors of objects 1 and 2, and $r = e$ for the external medium). The matrix $\mathfrak{D}(\mathbf{x})$, which depends on $\mathbf{x}$ through ϵ and μ, is constant in each region due to the piecewise homogeneity of the geometry, while the operators $L^{EM,r}$ only operate on the fields in region r. The functional integral becomes

$$\mathcal{Z}(\beta, \xi) = \int \mathcal{D}\mathbf{K}_1 \, \mathcal{D}\mathbf{K}_2 \, \mathcal{D}\mathbf{N}_1 \, \mathcal{D}\mathbf{N}_2 \, \mathcal{D}\mathcal{A}^\mu_e \, \mathcal{D}\mathcal{A}^\mu_1 \, \mathcal{D}\mathcal{A}^\mu_2 \Big\{$$

$$e^{-\frac{\beta}{2} \int_{V_e} \mathcal{A}_e \cdot \mathfrak{D}_e \cdot \mathcal{A}_e \, -\frac{\beta}{2} \int_{V_1} \mathcal{A}_1 \cdot \mathfrak{D}_1 \cdot \mathcal{A}_1 \, -\frac{\beta}{2} \int_{V_2} \mathcal{A}_2 \cdot \mathfrak{D}_2 \cdot \mathcal{A}_2}$$

$$\times e^{+i \int_{\mathcal{S}_1} \left\{ [\mathbf{K}_1 \cdot \mathbf{L}^{E,1} + \mathbf{N}_1 \cdot \mathbf{L}^{M,1}] \cdot \mathcal{A}_1 - [\mathbf{K}_1 \cdot \mathbf{L}^{E,e} + \mathbf{N}_1 \cdot \mathbf{L}^{M,e}] \cdot \mathcal{A}_e \right\} dx}$$

$$\times e^{+i \int_{\mathcal{S}_2} \left\{ [\mathbf{K}_2 \cdot \mathbf{L}^{E,2} + \mathbf{N}_2 \cdot \mathbf{L}^{M,2}] \cdot \mathcal{A}_2 - [\mathbf{K}_2 \cdot \mathbf{L}^{E,e} + \mathbf{N}_2 \cdot \mathbf{L}^{M,e}] \cdot \mathcal{A}_e \right\} dx} \Big\} \tag{5.33}$$

with $\int_{V_r}$ denoting volume integration over the interior of region r. Now performing the functional integrals over the fields $\mathcal{A}^\mu_r$ immediately yields an expression of the form (3.17):

$$\mathcal{Z}(\beta, \xi) = \big\{ \# \big\} \int \mathcal{D}\mathbf{K}_1 \mathcal{D}\mathbf{K}_2 \mathcal{D}\mathbf{N}_1 \mathcal{D}\mathbf{N}_2 \, e^{-\frac{1}{\beta} S^{\mathrm{eff}}[\mathbf{K}_1, \mathbf{K}_2, \mathbf{N}_1, \mathbf{N}_2]} \tag{5.34}$$

where $\big\{ \# \big\}$ is an unimportant constant that cancels upon taking the ratio in (5.27) (and which will not be written out in the equations below), and where the effective action for the surface currents contains several terms, which we will now investigate individually.

First consider terms arising from integrating the $\mathcal{A}^\mu_1$ field out of (5.33). Schematically, we have

$$\int \mathcal{D}\mathcal{A}^\mu_1 \, e^{-\frac{\beta}{2} \int \mathcal{A}_1 \cdot \mathfrak{D}_1 \cdot \mathcal{A}_1 + i \int_{\mathcal{S}_1} [\mathbf{K}_1 \cdot \mathbf{L}^{E,1} + \mathbf{N}_1 \cdot \mathbf{L}^{M,1}] \cdot \mathcal{A}_1}$$

$$= e^{-\frac{1}{2\beta} \int\int_{\mathcal{S}_1} [\mathbf{K}_1 \cdot \mathbf{L}^{E,1} + \mathbf{N}_1 \cdot \mathbf{L}^{M,1}] \cdot \mathfrak{D}_1^{-1} \cdot [\mathbf{K}_1 \cdot \mathbf{L}^{E,1} + \mathbf{N}_1 \cdot \mathbf{L}^{M,1}]}$$

$$\equiv e^{-\frac{1}{\beta} S_1[\mathbf{K}_1, \mathbf{N}_1]}$$

where S_1 describes interactions of the electric and magnetic currents on $\mathcal{S}_1$ mediated

61

by virtual photons traveling through the interior of object 1:

$$S_1\left[\mathbf{K}_1, \mathbf{N}_1\right] = \frac{1}{2}\int_{\mathcal{S}_1} d\mathbf{x} \int_{\mathcal{S}_1} d\mathbf{x}' \bigg\{ \mathbf{K}_1(\mathbf{x}) \cdot \boldsymbol{\gamma}^{\mathrm{EE},1}(\mathbf{x},\mathbf{x}') \cdot \mathbf{K}_1(\mathbf{x}')$$

$$+\mathbf{K}_1(\mathbf{x}) \cdot \boldsymbol{\gamma}^{\mathrm{EM},1}(\mathbf{x},\mathbf{x}') \cdot \mathbf{N}_1(\mathbf{x}')$$

$$+\mathbf{N}_1(\mathbf{x}) \cdot \boldsymbol{\gamma}^{\mathrm{ME},1}(\mathbf{x},\mathbf{x}') \cdot \mathbf{K}_1(\mathbf{x}')$$

$$+\mathbf{N}_1(\mathbf{x}) \cdot \boldsymbol{\gamma}^{\mathrm{MM},1}(\mathbf{x},\mathbf{x}') \cdot \mathbf{N}_1(\mathbf{x}') \bigg\} \tag{5.35}$$

with the components of the tensor kernels given by (P,Q $\in$ {E,H})

$$\gamma_{ij}^{\mathrm{PQ},1} = L_{i\mu}^{\mathrm{P1}}\mathfrak{D}_{1\mu\nu}^{-1}L_{j\nu}^{\mathrm{Q1}}. \tag{5.36}$$

The matrix multiplications in equation (5.36) are most easily evaluated in momentum space, where we have

$$\mathbf{L}^{\mathrm{E},1} = \begin{pmatrix} -i\frac{1}{\sqrt{\epsilon^1\mu^1}}k_x & i\xi & 0 & 0 \\ -i\frac{1}{\sqrt{\epsilon^1\mu^1}}k_y & 0 & i\xi & 0 \\ -i\frac{1}{\sqrt{\epsilon^1\mu^1}}k_z & 0 & 0 & i\xi \end{pmatrix} \qquad \mathbf{L}^{\mathrm{M},1} = \frac{1}{\mu^1}\begin{pmatrix} 0 & 0 & -ik_z & ik_y \\ 0 & ik_z & 0 & -ik_x \\ 0 & -ik_y & ik_x & 0 \end{pmatrix}$$

and

$$\mathfrak{D}_1^{-1} = \left[\mathfrak{D}_{\epsilon\mu} + \mathfrak{D}_{\mathrm{FP}}\right]^{-1}$$

$$= -\left[\frac{1}{\mu^1}\left(\kappa^2 + \mathbf{k}^2\right)\mathbf{1} + \left(1 - \frac{1}{\alpha_{\mathrm{FP}}}\right)\mathbf{U}_2\right]^{-1}$$

$$= -\frac{\mu^1}{\kappa^2 + \mathbf{k}^2}\left[\mathbf{1} + \mu^1\left(\frac{1 - \alpha_{\mathrm{FP}}}{\kappa^2 + \mathbf{k}^2}\right)\mathbf{U}_2\right] \tag{5.37}$$

where $\mathbf{1}$ is the 4×4 unit matrix, $\{\epsilon^1, \mu^1\}$ are the (spatially constant) permittivity and permeability of region 1 at imaginary frequency ξ,

$$\kappa = \sqrt{\epsilon^1\mu^1} \cdot \xi,$$

and the momentum-space form of the $\mathbf{U}_2$ matrix is

$$\mathbf{U}_2 = -\frac{1}{\mu^1}\begin{pmatrix} \kappa^2 & \kappa k_x & \kappa k_y & \kappa k_z \\ \kappa k_x & k_x^2 & k_x k_y & k_x k_z \\ \kappa k_y & k_y k_x & k_y^2 & k_y k_z \\ \kappa k_z & k_z k_x & k_z k_y & k_z^2 \end{pmatrix}.$$

We first observe that the second term in square brackets in (5.37) makes no contri-

bution to the γ kernels in (5.36). Indeed, we have $(c = 1/\sqrt{\epsilon^1\mu^1})$

$$\mathbf{L}^{E,1} \cdot \mathbf{U}_2 \cdot (\mathbf{L}^{E,1})^T$$

$$= \frac{1}{\mu^1}\begin{pmatrix} -ick_x & i\xi & 0 & 0 \\ -ick_y & 0 & i\xi & 0 \\ -ick_z & 0 & 0 & i\xi \end{pmatrix} \cdot \begin{pmatrix} \kappa^2 & \kappa k_x & \kappa k_y & \kappa k_z \\ \kappa k_x & k_x^2 & k_x k_y & k_x k_z \\ \kappa k_y & k_y k_x & k_y^2 & k_y k_z \\ \kappa k_z & k_z k_x & k_z k_y & k_z^2 \end{pmatrix} \cdot \begin{pmatrix} -ick_x & -ick_y & -ick_z \\ i\xi & 0 & 0 \\ 0 & i\xi & 0 \\ 0 & 0 & i\xi \end{pmatrix}$$

$$= \begin{pmatrix} 0 & 0 & 0 \\ 0 & 0 & 0 \\ 0 & 0 & 0 \end{pmatrix}$$

and the other three possible $\mathbf{LUL}$ sandwiches also vanish identically:

$$\mathbf{L}^{E,1} \cdot \mathbf{U}_2 \cdot (\mathbf{L}^{M,1})^T \quad = \quad \mathbf{L}^{M,1} \cdot \mathbf{U}_2 \cdot (\mathbf{L}^{E,1})^T \quad = \quad \mathbf{L}^{M,1} \cdot \mathbf{U}_2 \cdot (\mathbf{L}^{M,1})^T \quad = \quad 0.$$

This furnishes the promised demonstration that the gauge-choice parameter α_{FP} in (5.37) makes no appearance in the effective action (5.35), thus explicitly confirming the gauge invariance of our procedure.

Having verified that only the first term in (5.36) contributes to the γ kernels in (5.36), these kernels are now easy to evaluate. First,

$$\gamma^{EE,1} = -\frac{\mu^1}{\kappa^2 + \mathbf{k}^2}\left[\mathbf{L}^{E,1} \cdot \mathbf{1} \cdot (\mathbf{L}^{E,1})^T\right]$$

$$= -\frac{\mu^1}{\kappa^2 + \mathbf{k}^2}\begin{pmatrix} -ick_x & i\xi & 0 & 0 \\ -ick_y & 0 & i\xi & 0 \\ -ick_z & 0 & 0 & i\xi \end{pmatrix} \cdot \begin{pmatrix} -ick_x & -ick_y & -ick_z \\ i\xi & 0 & 0 \\ 0 & i\xi & 0 \\ 0 & 0 & i\xi \end{pmatrix}$$

$$= \xi \cdot \frac{Z_0 Z^1}{\kappa(\kappa^2 + \mathbf{k}^2)}\left[\begin{pmatrix} \kappa^2 & 0 & 0 \\ 0 & \kappa^2 & 0 \\ 0 & 0 & \kappa^2 \end{pmatrix} + \begin{pmatrix} k_x^2 & k_x k_y & k_x k_z \\ k_y k_x & k_y^2 & k_y k_z \\ k_z k_x & k_z k_y & k_z^2 \end{pmatrix}\right]$$

But a quick comparison with the momentum-space forms of the dyadic Green's functions in Appendix A reveals this to be nothing but ξ times the electric-electric dyadic Green's function, i.e.

$$\gamma^{EE,1}(\xi; \mathbf{k}) = \xi \cdot \mathbf{\Gamma}^{EE,1}(\xi; \mathbf{k})$$

or, transforming back to real space,

$$\gamma^{EE,1}(\xi; \mathbf{x}, \mathbf{x}') = \xi \cdot \mathbf{\Gamma}^{EE,1}(\xi; \mathbf{x}, \mathbf{x}')$$

and the striking similarity of our formalism to the boundary-element method begins to come into even sharper relief.

Next,

$$\gamma^{\mathrm{EM},1} = -\frac{\mu^1}{\kappa^2 + \mathbf{k}^2}\left[\mathbf{L}^{\mathrm{E},1} \cdot \mathbf{1} \cdot (\mathbf{L}^{\mathrm{M},1})^{\mathrm{T}}\right]$$

$$= -\frac{1}{\kappa^2 + \mathbf{k}^2}\begin{pmatrix} -ick_x & i\xi & 0 & 0 \\ -ick_y & 0 & i\xi & 0 \\ -ick_z & 0 & 0 & i\xi \end{pmatrix} \cdot \begin{pmatrix} 0 & 0 & 0 \\ 0 & ik_z & -ik_y \\ -ik_z & 0 & ik_x \\ ik_y & -ik_x & 0 \end{pmatrix}$$

$$= -\frac{\xi}{\kappa^2 + \mathbf{k}^2}\begin{pmatrix} 0 & -k_z & k_y \\ k_z & 0 & -k_x \\ -k_y & k_x & 0 \end{pmatrix}$$

and again comparing with Appendix A reveals that we have simply

$$\gamma^{\mathrm{EM},1} = \xi \cdot \mathbf{\Gamma}^{\mathrm{EM},1}.$$

Having established the obvious pattern, it is now a short step to confirm that the remaining two cases of the γ kernel in (5.36) are simply

$$\gamma^{\mathrm{ME},1} = \xi \cdot \mathbf{\Gamma}^{\mathrm{ME},1}$$
$$\gamma^{\mathrm{MM},1} = \xi \cdot \mathbf{\Gamma}^{\mathrm{MM},1}$$

and equation (5.35), the portion of the effective action for surface currents that arises from integrating the photon field in the interior of object 1 out of (5.33), reads simply

$$S_1\Big[\mathbf{K}_1, \mathbf{N}_1\Big] = \frac{\xi}{2}\int_{\mathcal{S}_1} d\mathbf{x} \int_{\mathcal{S}_1} d\mathbf{x}'\Big\{ \ \mathbf{K}_1(\mathbf{x}) \cdot \mathbf{\Gamma}^{\mathrm{EE},1}(\xi, \mathbf{x}, \mathbf{x}') \cdot \mathbf{K}_1(\mathbf{x}) \tag{5.38}$$

$$+\mathbf{K}_1(\mathbf{x}) \cdot \mathbf{\Gamma}^{\mathrm{EM},1}(\xi, \mathbf{x}, \mathbf{x}') \cdot \mathbf{N}_1(\mathbf{x}) \tag{5.39}$$

$$+\mathbf{N}_1(\mathbf{x}) \cdot \mathbf{\Gamma}^{\mathrm{ME},1}(\xi, \mathbf{x}, \mathbf{x}') \cdot \mathbf{K}_1(\mathbf{x}) \tag{5.40}$$

$$+\mathbf{N}_1(\mathbf{x}) \cdot \mathbf{\Gamma}^{\mathrm{ME},1}(\xi, \mathbf{x}, \mathbf{x}') \cdot \mathbf{N}_1(\mathbf{x})\Big\}. \tag{5.41}$$

In precisely analogous fashion, we find that the contribution to the effective action arising from integrating out the photon field in the interior of region 2 reads

$$S_2\Big[\mathbf{K}_2, \mathbf{N}_2\Big] = \frac{\xi}{2}\int_{\mathcal{S}_2} d\mathbf{x} \int_{\mathcal{S}_2} d\mathbf{x}'\Big\{ \ \mathbf{K}_2(\mathbf{x}) \cdot \mathbf{\Gamma}^{\mathrm{EE},2}(\xi, \mathbf{x}, \mathbf{x}') \cdot \mathbf{K}_2(\mathbf{x}) \tag{5.42}$$

$$+\mathbf{K}_2(\mathbf{x}) \cdot \mathbf{\Gamma}^{\mathrm{EM},2}(\xi, \mathbf{x}, \mathbf{x}') \cdot \mathbf{N}_2(\mathbf{x}) \tag{5.43}$$

$$+\mathbf{N}_2(\mathbf{x}) \cdot \mathbf{\Gamma}^{\mathrm{ME},2}(\xi, \mathbf{x}, \mathbf{x}') \cdot \mathbf{K}_2(\mathbf{x}) \tag{5.44}$$

$$+\mathbf{N}_2(\mathbf{x}) \cdot \mathbf{\Gamma}^{\mathrm{ME},2}(\xi, \mathbf{x}, \mathbf{x}') \cdot \mathbf{N}_2(\mathbf{x})\Big\}. \tag{5.45}$$

Finally, we consider integrating the photon field in the exterior region ($\mathcal{A}_e$) out of

64

equation (5.33). Although the computations proceed exactly as before, the resulting contribution to the effective action is more complicated. In addition to terms analogous to (5.41) and (5.45) describing the self-interactions of currents on $\mathcal{S}_1$ and $\mathcal{S}_2$, we now have terms describing interactions between currents on *different* object surfaces, with all interactions now mediated by photons propagating in the external medium:

$$
\begin{aligned}
S_e&\left[\mathbf{K}_1, \mathbf{N}_1, \mathbf{K}_2, \mathbf{N}_2\right]\\
&= \frac{\xi}{2} \int_{\mathcal{S}_1} d\mathbf{x} \int_{\mathcal{S}_1} d\mathbf{x}' \begin{pmatrix} \mathbf{K}_1(\mathbf{x}) \\ \mathbf{N}_1(\mathbf{x}) \end{pmatrix} \cdot \begin{pmatrix} \Gamma^{\mathrm{EE},e} & \Gamma^{\mathrm{EM},e} \\ \Gamma^{\mathrm{ME},e} & \Gamma^{\mathrm{MM},e} \end{pmatrix} \cdot \begin{pmatrix} \mathbf{K}_1(\mathbf{x}') \\ \mathbf{N}_1(\mathbf{x}') \end{pmatrix} \\
&+ \frac{\xi}{2} \int_{\mathcal{S}_2} d\mathbf{x} \int_{\mathcal{S}_2} d\mathbf{x}' \begin{pmatrix} \mathbf{K}_2(\mathbf{x}) \\ \mathbf{N}_2(\mathbf{x}) \end{pmatrix} \cdot \begin{pmatrix} \Gamma^{\mathrm{EE},e} & \Gamma^{\mathrm{EM},e} \\ \Gamma^{\mathrm{ME},e} & \Gamma^{\mathrm{MM},e} \end{pmatrix} \cdot \begin{pmatrix} \mathbf{K}_2(\mathbf{x}') \\ \mathbf{N}_2(\mathbf{x}') \end{pmatrix} \\
&+ \frac{\xi}{2} \int_{\mathcal{S}_1} d\mathbf{x} \int_{\mathcal{S}_2} d\mathbf{x}' \begin{pmatrix} \mathbf{K}_1(\mathbf{x}) \\ \mathbf{N}_1(\mathbf{x}) \end{pmatrix} \cdot \begin{pmatrix} \Gamma^{\mathrm{EE},e} & \Gamma^{\mathrm{EM},e} \\ \Gamma^{\mathrm{ME},e} & \Gamma^{\mathrm{MM},e} \end{pmatrix} \cdot \begin{pmatrix} \mathbf{K}_2(\mathbf{x}') \\ \mathbf{N}_2(\mathbf{x}') \end{pmatrix} \\
&+ \frac{\xi}{2} \int_{\mathcal{S}_2} d\mathbf{x} \int_{\mathcal{S}_1} d\mathbf{x}' \begin{pmatrix} \mathbf{K}_2(\mathbf{x}) \\ \mathbf{N}_2(\mathbf{x}) \end{pmatrix} \cdot \begin{pmatrix} \Gamma^{\mathrm{EE},e} & \Gamma^{\mathrm{EM},e} \\ \Gamma^{\mathrm{ME},e} & \Gamma^{\mathrm{MM},e} \end{pmatrix} \cdot \begin{pmatrix} \mathbf{K}_1(\mathbf{x}') \\ \mathbf{N}_1(\mathbf{x}') \end{pmatrix}.
\end{aligned} \tag{5.46}
$$

Combining (5.41), (5.45), and (5.46), the path integral (5.34) now reads

$$
\mathcal{Z}(\beta, \xi) = \int \mathcal{D}\mathbf{K}_i \mathcal{D}\mathbf{N}_i \exp \left\{ -\frac{\xi}{2\beta} \int \begin{pmatrix} \mathbf{K}_1 \\ \mathbf{N}_1 \\ \mathbf{K}_2 \\ \mathbf{N}_2 \end{pmatrix}^{\mathrm{T}} \cdot \begin{pmatrix} & & \\ & \boldsymbol{\Gamma} & \\ & & \end{pmatrix} \cdot \begin{pmatrix} \mathbf{K}_1 \\ \mathbf{N}_1 \\ \mathbf{K}_2 \\ \mathbf{N}_2 \end{pmatrix} \right\}
$$
$$\tag{5.47}$$

with

$$
\begin{pmatrix} & \\ & \boldsymbol{\Gamma} & \\ & \end{pmatrix} = \begin{pmatrix} \Gamma^{\mathrm{EE},1} + \Gamma^{\mathrm{EE},e} & \Gamma^{\mathrm{EM},1} + \Gamma^{\mathrm{EM},e} & \Gamma^{\mathrm{EE},e} & \Gamma^{\mathrm{EM},e} \\ \Gamma^{\mathrm{ME},1} + \Gamma^{\mathrm{ME},e} & \Gamma^{\mathrm{ME},1} + \Gamma^{\mathrm{MM},e} & \Gamma^{\mathrm{ME},e} & \Gamma^{\mathrm{MM},e} \\ \Gamma^{\mathrm{EE},e} & \Gamma^{\mathrm{EM},e} & \Gamma^{\mathrm{EE},2} + \Gamma^{\mathrm{EE},e} & \Gamma^{\mathrm{EM},2} + \Gamma^{\mathrm{EM},e} \\ \Gamma^{\mathrm{ME},e} & \Gamma^{\mathrm{MM},e} & \Gamma^{\mathrm{ME},2} + \Gamma^{\mathrm{ME},e} & \Gamma^{\mathrm{ME},2} + \Gamma^{\mathrm{MM},e} \end{pmatrix}.
$$

The quantity $\boldsymbol{\Gamma} \cdot \begin{pmatrix} \mathbf{K} \\ \mathbf{N} \end{pmatrix}$ in (5.47) is nothing but the left-hand side of equation (4.13).

Having elucidated the structure of the effective action for surface currents, the remainder of our derivation is now straightforward. To evaluate the functional integral over sources in (5.47), we approximate $\mathbf{K}$ and $\mathbf{N}$ as expansions in a finite set of tangential basis functions representing surface currents flowing on the surface of the interacting Casimir objects, just as we did in equation (4.14):

$$
\mathbf{K}(\mathbf{x}) = \sum K_\alpha \mathbf{f}_\alpha(\mathbf{x}), \qquad \mathbf{N}(\mathbf{x}) = -Z_0 \sum N_\alpha \mathbf{f}_\alpha(\mathbf{x}).
$$

We now insert these expansions into (5.47) and approximate the function-dimensional integrals over $\mathbf{K}$ and $\mathbf{N}$ as *finite-dimensional* integrals over the K_α and N_α coefficients:

$$
\int \mathcal{D}\mathbf{K}_i \mathcal{D}\mathbf{N}_i \quad \Longrightarrow \quad \mathcal{J} \int \prod_\alpha dK_\alpha \prod_\alpha dN_\alpha
$$

65

where $\mathcal{J}$, the Jacobian of the variable transformation, is an unimportant constant that cancels upon taking the ratio in (5.27) (and which will not be written out in the equations below). Equation (5.47) now becomes simply

$$\mathcal{Z}(\beta, \xi) = \int \prod_\alpha dK_\alpha \prod_\alpha dN_\alpha e^{-\frac{\xi}{2\beta}\left(\begin{smallmatrix}\mathbf{K}\\\mathbf{N}\end{smallmatrix}\right)^{\mathbf{T}} \cdot \mathbf{M}(\xi) \cdot \left(\begin{smallmatrix}\mathbf{K}\\\mathbf{N}\end{smallmatrix}\right)},$$

a finite-dimensional Gaussian integral which we evaluate immediately to obtain

$$= \left\{ \# \right\} \cdot \left[\det \mathbf{M}(\xi) \right]^{-1/2} \tag{5.48}$$

where $\mathbf{M}(\xi)$ is nothing but the PMCHW matrix discussed in Chapter 4 (and, once again, $\left\{ \# \right\}$ is just an irrelevant constant into which the $\xi/2\beta$ prefactor in the exponent disappears). Now finally inserting (5.48) into (5.28) and (5.27) leads immediately back to our FSC formulae (5.1), and our derivation is complete.

5.4   Equality of the Partial Traces

An important practical simplification of the FSC formulae follows from the structure of the BEM matrices. Recall from (5.1) that the quantity that enters into the FSC expression for the Casimir force is

$$\mathrm{Tr}\ \mathbf{M}^{-1} \cdot \frac{\partial \mathbf{M}}{\partial \mathbf{r}_i} = \sum_{\alpha\beta} M_{\alpha\beta}^{-1} \left[\frac{\partial M_{\alpha\beta}}{\partial \mathbf{r}_i} \right] \tag{5.49}$$

(with a similar expression for the torque). As before, let the objects in our Casimir geometry be labeled $\mathcal{O}_n$, $n = 1, 2, \cdots$, with $\mathcal{O}_1$ the object on which we are computing the Casimir force, and let D_n be the dimension of the subblock of the $\mathbf{M}$ matrix corresponding to object $\mathcal{O}_n$ (that is, D_n is the number of localized basis functions defined on the surface of $\mathcal{O}_n$.) The dimension of the full matrix is $D = \sum D_n$. We know that the only nonzero entries of the derivative matrix $\partial \mathbf{M}/\partial r_i$ are those corresponding to pairs of basis functions of which precisely one is located on the surface of object $\mathcal{O}_1$. We can thus split the sum in (5.49) into two pieces:

$$\sum_{\alpha\beta} M_{\alpha\beta}^{-1} \left[\frac{\partial M_{\alpha\beta}}{\partial \mathbf{r}_i} \right] = \sum_{\alpha=1}^{D_1} \sum_{\beta=D_1+1}^{D} M_{\alpha\beta}^{-1} \left[\frac{\partial M_{\alpha\beta}}{\partial \mathbf{r}_i} \right] + \sum_{\alpha=D_1+1}^{D} \sum_{\beta=1}^{D_1} M_{\alpha\beta}^{-1} \left[\frac{\partial M_{\alpha\beta}}{\partial \mathbf{r}_i} \right]. \tag{5.50}$$

The first piece on the RHS here is the sum of the first D_1 diagonal elements of the matrix $\mathbf{M}^{-1} \cdot \frac{\partial \mathbf{M}}{\partial r_i}$, while the second piece is the sum of the remaining $D - D_1$ elements. But from the symmetry of $\mathbf{M}$ it now follows that the two pieces here are *equal*, and thus to compute the full trace we need only sum the first D_1 diagonal elements of

$\mathbf{M}^{-1} \cdot \frac{d\mathbf{M}}{d\mathbf{r}_i}$ (or the latter $D - D_1$ elements, if they are fewer) and double the result, i.e.

$$\text{Tr } \mathbf{M}^{-1} \cdot \frac{\partial \mathbf{M}}{\partial \mathbf{r}_i} = 2 \sum_{\alpha=1}^{D_1} \sum_{\beta=D_1+1}^{D} M_{\alpha\beta}^{-1} \left[\frac{\partial M_{\alpha\beta}}{\partial \mathbf{r}_i} \right].$$

In practice, a convenient way to evaluate this quantity is to LU-factorize the matrix $\mathbf{M}$, solve the linear systems $\mathbf{M} \cdot \mathbf{X}_m = \mathbf{B}_m$ where the vectors $\mathbf{X}_m$ are the first D_1 columns of $\frac{\partial \mathbf{M}}{\partial \mathbf{r}_i}$, then extract and sum the mth elements of the vectors $\mathbf{B}_m$ and double the result. The equality of the partial traces then ensures that this operation requires just D_1 linear solves, in contrast to the full D solves that would be required in the absence of the simplification.

Chapter 6

CASIMIR3D: A Numerical Implementation of the FSC Formulae for Compact 3D Objects

Chapter 5 presented the theoretical underpinnings of our master FSC formulae (5.1), but said little about how these formulae might be implemented in practice. In this and the following two chapters we remedy this deficiency, presenting three separate numerical implementations of the FSC formulae.

The implementation presented in this chapter, CASIMIR3D, predicts Casimir forces, energies, and torques between compact three-dimensional objects. We begin in Section 6.1 by describing a particular choice of basis functions—the "RWG" functions, introduced in 1982 and today used extensively in computational electromagnetism— that CASIMIR3D uses to represent tangential current distributions on the surfaces of compact 3D objects. In Section 6.2 we discuss the implications of this choice of basis functions for the computation of the elements of the BEM matrices that enter into the FSC formulae. After the relatively involved nature of Section 6.2, all remaining details of the numerical implementation of CASIMIR3D are comparatively straightforward, and are briefly summarized in Section 6.3. (Details on the usage of the CASIMIR3D software package, including command-line syntax, are relegated to Appendix G.)

6.1 RWG Basis Functions for 3D BEM Problems

The first and most important decision we make in crafting a practical implementation of the fluctuating-surface-current formulae is a choice of localized basis functions to represent our fluctuating surface currents. For CASIMIR3D we choose the "RWG" basis functions, introduced by Rao, Wilton, and Glisson in 1982 [38], which have proven a particularly useful choice for representing tangential current flow on the surfaces of compact three-dimensional objects. To fix ideas and notation for the remainder of this chapter, in this section we review the definition of the RWG basis functions.
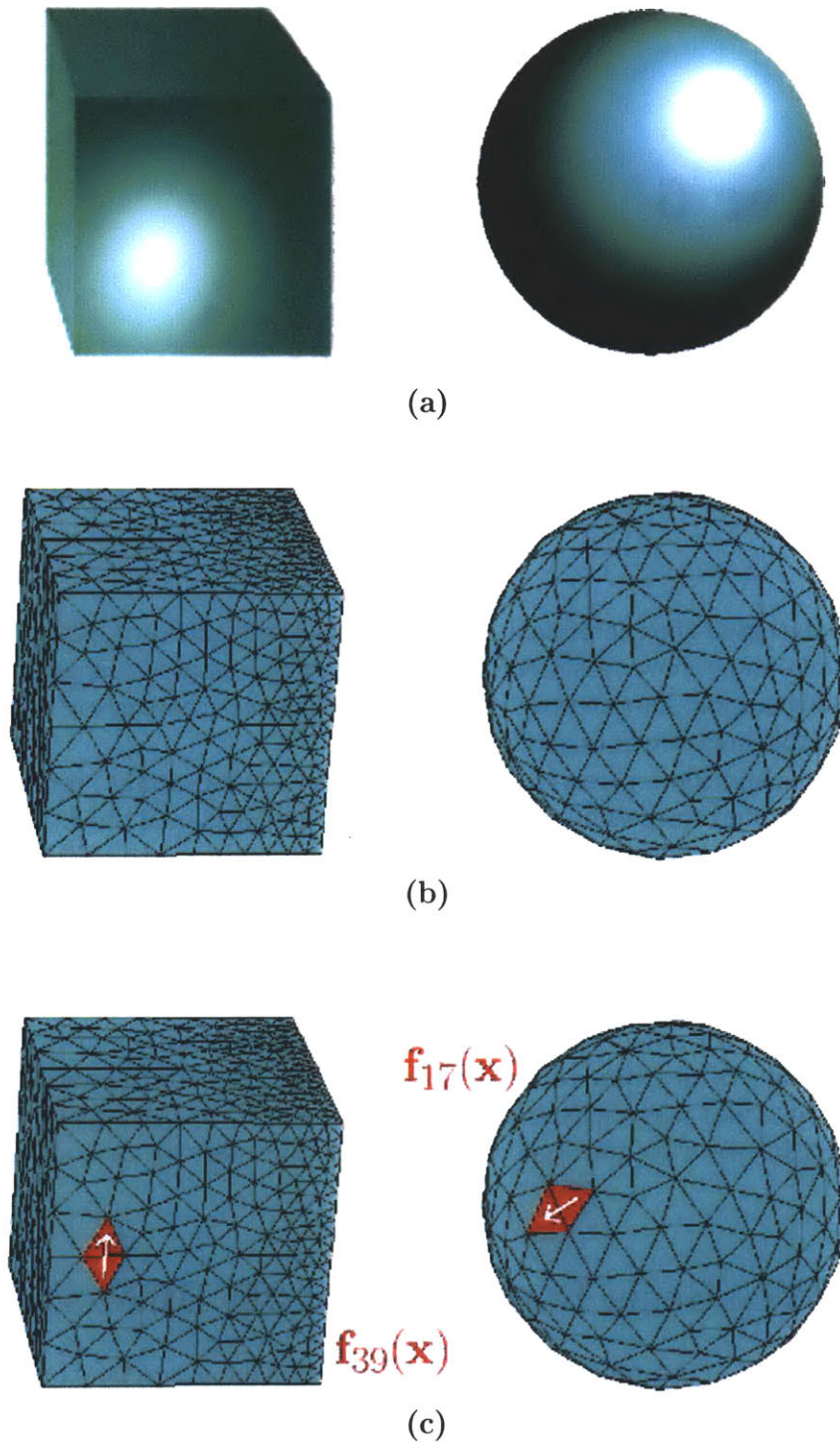
Figure 6-1: To represent tangential currents on the surfaces of compact 3D objects such as a cube and sphere (**a**), we approximate the surfaces of the objects as unions of planar triangles (**b**), then assign a single vector-valued basis function (the "RWG" basis function, (**c**)) to each adjacent pair of triangles.
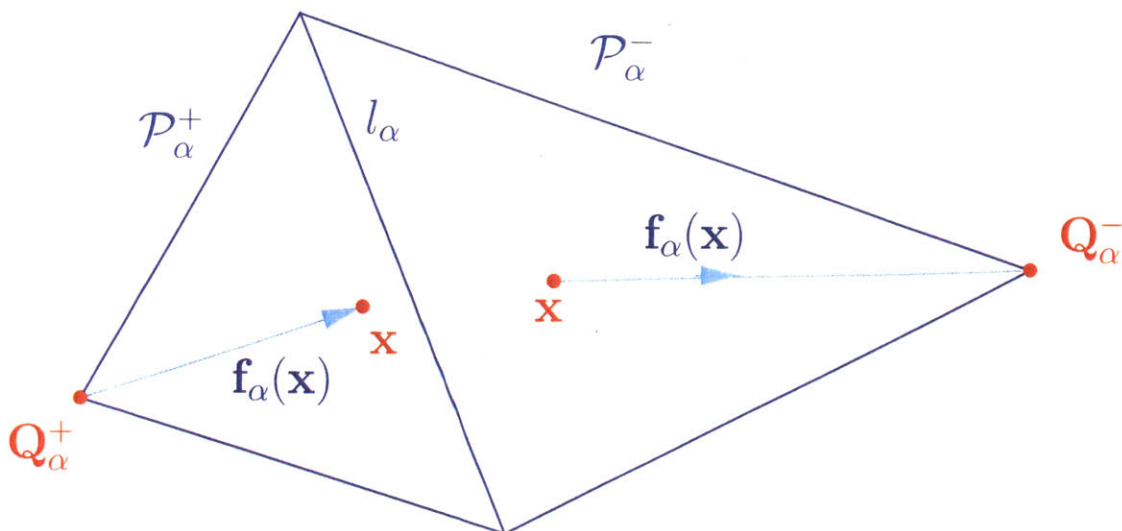
Figure 6-2: To the αth internal edge in our discretized surface mesh, l_α, we associate a single RWG basis function $\mathbf{f}_\alpha(\mathbf{x})$. This basis function describes a surface current distribution that emanates from one of the two vertices opposite l_α (we call this vertex $\mathbf{Q}_\alpha^+$), increases in magnitude as it flows toward l_α, then crosses over the edge and decreases in magnitude as it flows toward the opposing vertex (which we call $\mathbf{Q}_\alpha^-$). We use the labels $\mathcal{P}_\alpha^+$ and $\mathcal{P}_\alpha^-$ to denote the triangular panels on which the current is increasing and decreasing. As illustrated in the figure, the value of the basis function at a point $\mathbf{x}$ is proportional to $\mathbf{x} - \mathbf{Q}_\alpha^+$ (for $\mathbf{x} \in \mathcal{P}_\alpha^+$) or to $\mathbf{Q}_\alpha^- - \mathbf{x}$. (for $\mathbf{x} \in \mathcal{P}_\alpha^-$).

To describe surface currents with RWG basis functions, we begin by approximating the surfaces of compact 3D objects as unions of planar triangles, a discretization process illustrated in Figure 6.1 for the approximately cubical and approximately spherical objects whose Casimir interaction we considered in Chapter 3. (For objects with curved surfaces, such as a sphere, the planar triangles can of course furnish only an approximate representation of the true geometry, but the approximation can be improved to any desired degree of accuracy simply by using smaller and smaller triangles.)

We now associate one vector-valued RWG basis function to each internal edge in the triangulation. As pictured in Figure 6.1, the basis function $\mathbf{f}_\alpha$ associated with the αth internal edge is nonvanishing only within the two triangular panels that share that edge; we arbitrarily designate one of these panels the "positive" panel associated with $\mathbf{f}_\alpha$ (and denote it $\mathcal{P}_\alpha^+$), while the other panel is the "negative" panel (denoted $\mathcal{P}_\alpha^-$). We use the labels $\mathbf{V}_{1\alpha}, \mathbf{V}_{2\alpha}$ for the endpoints of the shared edge and $\mathbf{Q}_\alpha^+, \mathbf{Q}_\alpha^-$ for the vertices opposing that edge within the positive and negative panels.

The RWG basis function $\mathbf{f}_\alpha$ then describes a current distribution that originates from vertex $\mathbf{Q}_\alpha^+$, flows across panel $\mathcal{P}_\alpha^+$ toward the common edge of the two panels with increasing magnitude until it reaches that edge, then crosses over into $\mathcal{P}_\alpha^-$ and

flows toward $\mathbf{Q}_\alpha^-$ with decreasing magnitude until it is sunk into that vertex. More explicitly, we have

$$\mathbf{f}_\alpha(\mathbf{x}) = \begin{cases} +\dfrac{l_\alpha}{2A_\alpha^+}(\mathbf{x} - \mathbf{Q}_\alpha^+) & \mathbf{x} \in \mathcal{P}_\alpha^+ \\ -\dfrac{l_\alpha}{2A_\alpha^-}(\mathbf{x} - \mathbf{Q}_\alpha^-) & \mathbf{x} \in \mathcal{P}_\alpha^- \end{cases} \tag{6.1}$$

where $l_\alpha, A_\alpha^+, A_\alpha^-$ are the length of the shared edge and the areas of the two panels.

An important feature of the RWG basis function is that the charge density associated with the current distribution it describes is *constant* on each of the two panels and of strength designed to ensure that the total charge density vanishes:

$$\nabla \cdot \mathbf{f}_\alpha(\mathbf{x}) = \begin{cases} +\dfrac{l_\alpha}{A_\alpha^+} & \mathbf{x} \in \mathcal{P}_\alpha^+ \\ -\dfrac{l_\alpha}{A_\alpha^-} & \mathbf{x} \in \mathcal{P}_\alpha^- \end{cases}$$

6.2 Evaluation of BEM Matrix Elements Between RWG Basis Functions

Appendix B reduces the computation of BEM matrix elements between localized basis functions to the evaluation of three types of integrals (the "L-functions") over the supports of the basis functions. In this section we consider the evaluation of the L-functions for the specific choice of RWG basis functions.

6.2.1 RWG Matrix Elements from Panel-Panel Integrals

Because each RWG basis function is supported on precisely on two triangular panels, each L-function decomposes into a sum of four panel-panel integrals:

$$\begin{aligned} L_\bullet(\kappa; \mathbf{f}_\alpha, \mathbf{f}_\beta) \quad = \quad & L_\bullet(\kappa; \mathcal{P}_\alpha^+, Q_\alpha^+; \mathcal{P}_\beta^+, Q_\beta^+) \\ & -L_\bullet(\kappa; \mathcal{P}_\alpha^+, Q_\alpha^+; \mathcal{P}_\beta^-, Q_\beta^-) \\ & -L_\bullet(\kappa; \mathcal{P}_\alpha^-, Q_\alpha^-; \mathcal{P}_\beta^+, Q_\beta^+) \\ & +L_\bullet(\kappa; \mathcal{P}_\alpha^-, Q_\alpha^-; \mathcal{P}_\beta^-, Q_\beta^-). \end{aligned} \tag{6.2}$$

(and similarly for L_∇ and $L_\times$; note that the panel-panel L-functions depend not only on the two panels but also on which of the panel vertices are the current source/sink

vertices.) Inserting the definition (6.1), the three panel-panel L functions are

$$L_{\bullet}(\kappa; \mathcal{P}, Q; \mathcal{P}', Q')$$
$$= \frac{ll'}{4AA'} \int_{\mathcal{P}} d\mathbf{x} \int_{\mathcal{P}'} d\mathbf{x}' \, (\mathbf{x} - \mathbf{Q}) \cdot (\mathbf{x}' - \mathbf{Q}') \phi\Big(\kappa; |\mathbf{x} - \mathbf{x}'|\Big) \qquad (6.3a)$$

$$L_{\nabla}(\kappa; \mathcal{P}, Q; \mathcal{P}', Q')$$
$$= \frac{ll'}{4AA'} \int_{\mathcal{P}} d\mathbf{x} \int_{\mathcal{P}'} d\mathbf{x}' \, 4 \cdot \phi\Big(\kappa; |\mathbf{x} - \mathbf{x}'|\Big) \qquad (6.3b)$$

$$L_{\times}(\kappa; \mathcal{P}, Q; \mathcal{P}', Q')$$
$$= \frac{ll'}{4AA'} \int_{\mathcal{P}} d\mathbf{x} \int_{\mathcal{P}'} d\mathbf{x}' \, \Big[\big[(\mathbf{x} - \mathbf{Q}) \times (\mathbf{x}' - \mathbf{Q}')\big] \cdot (\mathbf{x} - \mathbf{x}')\Big] \psi\Big(\kappa; |\mathbf{x} - \mathbf{x}'|\Big) \qquad (6.3c)$$

where the scalar ϕ and ψ functions were defined in Appendix B.

To evaluate integrals over a triangular panel with vertices $(\mathbf{V}_1, \mathbf{V}_2, \mathbf{V}_3)$ we parameterize points in the triangle according to

$$\mathbf{x} = \mathbf{V}_1 + u(\mathbf{V}_2 - \mathbf{V}_1) + v(\mathbf{V}_3 - \mathbf{V}_2) \qquad 0 \le u \le 1, \qquad 0 \le v \le u \qquad (6.4)$$
$$\equiv \mathbf{V}_1 + u\mathbf{A} + v\mathbf{B}, \qquad \Big(\mathbf{A} \equiv \mathbf{V}_2 - \mathbf{V}_1, \quad \mathbf{B} \equiv \mathbf{V}_3 - \mathbf{V}_2\Big)$$

and write

$$\int_{\mathcal{P}} d\mathbf{x} \, f(\mathbf{x}) = 2A \int_0^1 du \int_0^u dv f\big(\mathbf{x}(u, v)\big)$$

where the function $\mathbf{x}(u, v)$ is given by (6.4) and the factor of $2A$ (twice the area of the triangular panel) is the Jacobian of the variable transformation. Applying this procedure to both the $\mathbf{x}$ and $\mathbf{x}'$ integrals in (6.3), the panel-panel L-functions reduce to integrals over a four-dimensional region consisting of the product of two standard triangles:

$$L_{\bullet}(\kappa; \mathcal{P}, Q; \mathcal{P}', Q') = ll' \int du \, dv \, du' \, dv' \, h_{\bullet}(u, v, u', v') \phi\Big(\kappa; R(u, v, u', v')\Big) \qquad (6.5a)$$

$$L_{\nabla}(\kappa; \mathcal{P}, Q; \mathcal{P}', Q') = ll' \int du \, dv \, du' \, dv' \, h_{\nabla}(u, v, u', v') \phi\Big(\kappa; R(u, v, u', v')\Big) \qquad (6.5b)$$

$$L_{\times}(\kappa; \mathcal{P}, Q; \mathcal{P}', Q') = ll' \int du \, dv \, du' \, dv' \, h_{\times}(u, v, u', v') \psi\Big(\kappa; R(u, v, u', v')\Big) \qquad (6.5c)$$

where

$$\int du \, dv \, du' \, dv' \equiv \int_0^1 du \int_0^u dv \int_0^1 du' \int_0^{u'} dv',$$

73

the R function is the distance between parameterized points in the two triangles,

$$R(u, v, u', v') = \left| (\mathbf{V}_1 + u\mathbf{A} + v\mathbf{B}) - (\mathbf{V}_1' + u'\mathbf{A}' + v'\mathbf{B}') \right|,$$

and the h functions are polynomials in u, v, u', v' whose coefficients express geometric information about the triangles:

$$h_\bullet(u, v, u', v') = \left(\mathbf{x}(u, v) - \mathbf{Q} \right) \cdot \left(\mathbf{x}'(u, v) - \mathbf{Q}' \right) \tag{6.6a}$$

$$h_\triangledown(u, v, u', v') = 4 \tag{6.6b}$$

$$h_\times(u, v, u', v') = \left[\left(\mathbf{x}(u, v) - \mathbf{Q} \right) \times \left(\mathbf{x}'(u', v') - \mathbf{Q}' \right) \right] \cdot \left[\mathbf{x}(u, v) - \mathbf{x}'(u', v') \right] \tag{6.6c}$$

with the notation

$$\mathbf{x}(u, v) = (\mathbf{V}_1 + u\mathbf{A} + v\mathbf{B}), \qquad \mathbf{x}'(u', v') = (\mathbf{V}_1' + u'\mathbf{A}' + v'\mathbf{B}')$$

$$\mathcal{P} = (\mathbf{V}_1, \mathbf{V}_2, \mathbf{V}_3), \qquad \mathbf{A} = \mathbf{V}_2 - \mathbf{V}_1, \qquad \mathbf{B} = \mathbf{V}_3 - \mathbf{V}_2$$

$$\mathcal{P}' = (\mathbf{V}_1', \mathbf{V}_2', \mathbf{V}_3'), \qquad \mathbf{A}' = \mathbf{V}_2' - \mathbf{V}_1', \qquad \mathbf{B}' = \mathbf{V}_3' - \mathbf{V}_2'.$$

6.2.2 Panel-Panel Integrals between Distant Panels

When panels $\mathcal{P}, \mathcal{P}'$ in (6.3) are relatively far away from one another, the integrands vary relatively slowly over the domain of integration, and the integrals may be evaluated by straightforward numerical cubature.

To quantity the notion of "relatively far away," we introduce a relative distance function between panels according to

$$\mathrm{RD}(\mathcal{P}, \mathcal{P}') = \frac{|\mathbf{x}_0 - \mathbf{x}_0'|}{\mathrm{MAX}\left(\mathrm{rad}(\mathcal{P}), \mathrm{rad}(\mathcal{P}') \right)} \tag{6.7}$$

where $\mathbf{x}_0, \mathbf{x}_0'$ are the panel centroids and $\mathrm{rad}(\mathcal{P})$ is the radius of the minimal circle centered at the centroid of $\mathcal{P}$ that fully encompasses $\mathcal{P}$. This relative distance between panels then determines the order of the numerical cubature scheme needed to evaluate the integrals in (6.5).

I have found it adequate to use a nested cubature scheme, in which a single cubature rule for the standard triangle is used twice, once for the (u, v) integral and once for the (u', v') integral. More specifically, let $\{u_i, v_i\}$ be the points and $\{w_i\}$ the weights of an N^C-point cubature rule for the standard triangle, so that

$$\int_0^1 du \int_0^u dv \, f(u, v) \approx \sum_{m=1}^{N^C} w_m f(u_m, v_m).$$

74

Then I evaluate the integrals in (6.5) via the prescription

$$\int du\, dv\, du'\, dv'\, \mathcal{I}(u,v,u',v') \approx \sum_{m=1}^{N^C} \sum_{n=1}^{N^C} w_m w_n \mathcal{I}(u_m, v_m, u_n, v_n).$$

When $\mathrm{RD}(\mathcal{P}, \mathcal{P}') > 8$, I have found that a fourth-order cubature rule with $N^C = 6$ yields sufficient accuracy (relative errors of 10^{-6} or less), while in the range $4 < \mathrm{RD}(\mathcal{P}, \mathcal{P}') < 8$, a seventh-order rule with $N^C = 15$ is adequate. (These two rules and many more are contained in the invaluable trove of cubature rules presented in Reference [10]).

6.2.3 Panel-Panel Integrals between Nearby Panels: Desingularization

When the relative distance between panels $\mathcal{P}, \mathcal{P}'$ is less than 4, the integrands vary rapidly over the domain of integration and low-order cubature schemes are inaccurate. As long as $\mathcal{P}, \mathcal{P}'$ contain no common points, this difficulty could in principle be addressed in brute-force fashion simply by using higher-order cubature schemes. But this would be computationally costly, particularly inasmuch as a typical Casimir problem will require us to recompute the elements of the BEM matrix elements at dozens or hundreds of frequencies to evaluate the integral over ξ in (5.1). Moreover, even the highest-order numerical cubature scheme will be powerless to adjudicate the singularities in the integrands of (6.3) that arise whenever $\mathcal{P}, \mathcal{P}'$ have one or more points in common. Although these are of course *integrable* singularities, their existence thwarts straightforward numerical cubature and requires a more sophisticated approach.

The computation of singular or nearly-singular panel-panel integrals for numerical BEM schemes is a well-studied topic in the computational electromagnetism community (a useful recent review is Ref. [46]). Although no universal consensus has emerged to define a single optimal computational approach, two techniques in particular have come into common usage: *desingularization* [48], in which the most singular term in the Taylor[1] expansions of the singular kernels in (6.3) are subtracted off and integrated analytically or quasi-analytically, and *Taylor's method* [45], in which the four-dimensional integrals in (6.3) are rearranged in ways that allow the use of *Duffy transformations* [11] to eliminate the singularities altogether.

As useful as both of these techniques are, neither method in isolation suffices for the purposes of CASIMIR3D. The desingularization technique, as typically implemented, subtracts only the most singular term from the singular kernel (for, in general, it is only this term that may be analytically integrated), leaving behind an integrand that, while nonsingular, still exhibits sufficiently rapid variation to require large numbers of integrand samples to evaluate the full four-dimensional integral by numerical cubature. On the other hand, Taylor's method succeeds in reducing the

---

[1]The two Taylors in this discussion—one known for his series, the other for his method of evaluating singular triangle-triangle integrals—are not to be confused with one another!

four-dimensional integral to a three-, two-, or one-dimensional integral, but with an integrand that—while again explicitly nonsingular—is expensive to evaluate.

Thus both methods, while removing integrand singularities, nonetheless leave behind multidimensional integrals that are expensive to evaluate by numerical cubature. While this expense may be acceptable for typical BEM solvers—which operate at a single frequency—for Casimir applications, as noted above, we must recompute matrix elements at dozens or hundreds of frequencies, and this requirement motivates us to concoct a more efficient scheme.

In CASIMIR3D we construct such a scheme by *combining* and *extending* the desingularization and Taylor-method techniques. First, we extend the desingularization technique by subtracting *multiple* (up to 4) terms from the Taylor expansions of the singular kernels. This leaves behind smooth, slowly-varying integrands that are integrated already to high accuracy by low-level cubature rules. Second, we evaluate the contributions of the singular terms using a modified version of the Taylor method, in which we extend Taylor's original procedure to the case of general kernel functions and polynomial factors. Although our extended Taylor method for evaluating singular integrals is not without computational expense, all the integrals that we will need turn out to be *frequency independent*; thus we need only compute these quantities *once* per Casimir calculation, after which we may store and reuse them for rapid recomputation of BEM matrix elements.

The panel-integral scheme implemented by CASIMIR3D differs from standard techniques discussed in the literature in at least four ways. First, we *combine* the ideas of desingularization and the Taylor method, two methods that have heretofore remained separate. Second, we *extend* both of these procedures, by subtracting several more terms than usual from the singular kernels, and by expanding the Taylor method to allow treatment of arbitrary kernel functions and integrand polynomials. Third, our method is specifically optimized for use in *broadband* problems, in which BEM matrix elements must be recomputed at a large number of separate frequencies. Finally, our method works at *imaginary frequencies*, as required for Casimir problems. (Notwithstanding this last point, the central ideas are equally applicable to real-frequency problems, and the panel-integration module of our CASIMIR3D code indeed contains implementations of our technique for both real- and imaginary-frequency panel integrals.)

More specifically, we define desingularized versions of ϕ and ψ according to

$$\phi^{\mathrm{DS}}(\kappa, r) = \frac{1}{4\pi r}\left(e^{-\kappa r} - 1 + \kappa r - \frac{1}{2}(\kappa r)^2 + \frac{1}{6}(\kappa r)^3\right)$$
$$\equiv \frac{1}{4\pi r} \cdot \texttt{ExpRel}(4, \kappa r)$$

and similarly

$$\psi^{\mathrm{DS}}(\kappa, r) = (-\kappa r - 1)\frac{1}{4\pi r^3} \cdot \texttt{ExpRel}(4, \kappa r)$$

where the `ExpRel` function is defined in Appendix D.

76

The integrals in (6.5) are now evaluated as

$$\int \left\{ h_\bullet(u,v,u',v')\phi(\kappa,R) \right\} du\, dv\, du'\, dv'$$

$$= \int \left\{ h_\bullet(u,v,u',v')\phi^{\mathrm{DS}}(\kappa,R) \right\} du\, dv\, du'\, dv'$$

$$+ \sum_{n=0}^{3} \frac{(-\kappa)^n}{4\pi n!} \int \left\{ h_\bullet(u,v,u',v')R^{n-1} \right\} du\, dv\, du'\, dv' \qquad (6.8a)$$

$$\int \left\{ h_\nabla(u,v,u',v')\phi(\kappa,R) \right\} du\, dv\, du'\, dv'$$

$$= \int \left\{ h_\nabla(u,v,u',v')\phi^{\mathrm{DS}}(\kappa,R) \right\} du\, dv\, du'\, dv'$$

$$+ \sum_{n=0}^{3} \frac{(-\kappa)^n}{4\pi n!} \int \left\{ h_\nabla(u,v,u',v')R^{n-1} \right\} du\, dv\, du'\, dv' \qquad (6.8b)$$

$$\int \left\{ h_\times(u,v,u',v')\psi(\kappa,R) \right\} du\, dv\, du'\, dv'$$

$$= \int \left\{ h_\times(u,v,u',v')\psi^{\mathrm{DS}}(\kappa,R) \right\} du\, dv\, du'\, dv'$$

$$+ \sum_{n=0}^{4} C_n \frac{\kappa^n}{4\pi} \int \left\{ h_\times(u,v,u',v')R^{n-3} \right\} du\, dv\, du'\, dv' \qquad (6.8c)$$

where R is short for $R(u,v,u',v')$, and where, in the last line, the coefficients are $\{C_0, C_1, C_2, C_3, C_4\} = \{-1, 0, \frac{1}{2}, -\frac{1}{3}, \frac{1}{3}\}$.

As noted above, a key feature of the decomposition here is that the singular portions of the integrals are *frequency-independent*, as witness the fact that κ appears only as a multiplicative prefactor outside the integrals in the summation terms in (6.8). Thus, for a given Casimir geometry, we can evaluate these integrals once and for all at the beginning of our calculation, then reuse the results as many times as necessary to assemble the full frequency-dependent integrals.

Evaluation of desingularization integrals

The desingularization integrals that enter into the summation terms in (6.8) all have the form

$$\int \left\{ h(u,v,u',v')R^p \right\} du\, dv\, du'\, dv', \qquad -3 \le p \le 2 \qquad (6.9)$$

where, as noted above, h is a polynomial in u,v,u',v'.

If the original panels $\mathcal{P}, \mathcal{P}'$ have no points in common, then R does not vanish within the region of integration and the integral is nonsingular. In this case I have found it entirely sufficient to use an *adaptive* numerical cubature scheme [2, 3] to evaluate (6.9). Although adaptive cubature schemes can require large numbers of

numerical integrand samples to converge, the fact that the integrals need only be computed once per evaluation of the full frequency integral (5.1) loosens the constraints on the efficiency with which we evaluate (6.9).[2]

If the original panels $\mathcal{P}, \mathcal{P}'$ have points in common, then R vanishes within the domain of integration and the integral is singular (for $p < 0$.) In this case we avail ourselves of the generalized Taylor method for the evaluation of singular panel-panel integrals described in Appendix D.

6.2.4 Special Cases for Panel-Panel Integrals

The methods presented in the previous two subsections suffice to compute the panel-panel L-functions (6.5) in most cases of interest, but there are two particular cases in which we proceed slightly differently.

First, for the *common-panel* case (i.e. the evaluation of (6.3) in the case $\mathcal{P} = \mathcal{P}'$), although the desingularization technique described in the previous section works perfectly well, in practice it is actually faster simply to use the full Taylor method of Appendix D with the g function taken as the full ϕ kernel. (The $L_\times$ integral vanishes in the common-panel case, so we do not need the case $g = \psi$.) Of course, we could also use the full Taylor method for the common-edge and common-vertex cases, but they are slightly more time-consuming in that case (requiring a two-dimensional and three-dimensional numerical cubature, respectively, as compared to the one-dimensional quadrature required in the common-panel case) and thus in practice we use the desingularization scheme for these cases.

However (and this is our second special case), when the κ parameter in the L-functions (6.3) is greater than or on the order of the inverse panel size (as measured, for example, by the panel radius $\mathrm{rad}(\mathcal{P})$), then the desingularization technique does not work well. (Large values of κ arise in two cases: (1) at high imaginary frequencies ξ, and (2) in the interior of imperfect conductors such as gold).

For panels with one or more common vertices in the high-κ case, we simply revert to the full Taylor method of Appendix D with the g functions taken to be the full ϕ or ψ kernels. As described in the Appendix, the Taylor method for these g functions is well-defined and accurate in the limit $\kappa \to \infty$.

For panels with no common vertices in the high-κ case, neither the desingularization nor Taylor methods are available. However, we are assisted here by the fact that the L-functions between panels with no common points decay *exponentially* with κ in the large κ regime, whereas the L-functions between panels with one or more common points decay only *algebraically* with κ, as summarized in Table 6.1. Thus the former are significantly smaller than the latter (generally by several orders of magnitude) and are calculated already to sufficient accuracy by simple (non-desingularized) numerical cubature, as discussed in Section 6.2.2.

---

[2]If necessary for future applications, the evaluation of of (6.9) could be accelerated, at the cost of some tedious work, by evaluating the v or v' integrals analytically, leaving behind a three-dimensional integral (with an extremely complicated integrand) that will succumb to adaptive numerical cubature more rapidly than the four-dimensional integral (6.9).

# vertices shared by $\mathcal{P}, \mathcal{P}'$	Asymptotic behavior of $L(\kappa, \mathcal{P}, \mathcal{P}')$ as $\kappa \to \infty$
0	$\sim e^{-\kappa R_{min}}$
1 (common vertex)	$\sim \kappa^{-3}$
2 (common edge)	$\sim \kappa^{-2}$
3 (common panel)	$\sim \kappa^{-1}$

Table 6.1: Decay rates of panel-panel L-functions in the large-κ regime. (R_{min} is the minimum distance between $\mathcal{P}, \mathcal{P}'$.)

6.3 Miscellaneous Implementation Notes on CASIMIR3D

The evaluation of BEM matrix elements for RWG basis functions, discussed at length in the previous section, is by far the most challenging component in the implementation of CASIMIR3D. Once this step is complete, the evaluation of the master FSC formulae (5.1) now proceeds entirely straightforwardly using a bevy of standard numerical techniques, which we now briefly summarize.

Calculation of Determinant. The Casimir energy integrand is given by (5.1a) in terms of the determinants of the $\mathbf{M}$ and $\mathbf{M}_\infty$ matrices. For a Casimir geometry consisting of N interacting objects, these matrices exhibit a block structure of the form

$$\mathbf{M} = \begin{pmatrix} \mathbf{T}_1 & \mathbf{U}_{12} & \mathbf{U}_{13} & \cdots & \mathbf{U}_{1N} \\ \mathbf{U}_{21} & \mathbf{T}_2 & \mathbf{U}_{23} & \cdots & \mathbf{U}_{2N} \\ \mathbf{U}_{31} & \mathbf{U}_{32} & \mathbf{T}_3 & \cdots & \mathbf{U}_{3N} \\ \vdots & \vdots & \vdots & \ddots & \vdots \\ \mathbf{U}_{N1} & \mathbf{U}_{N2} & \mathbf{U}_{N3} & \cdots & \mathbf{T}_N \end{pmatrix}, \quad \mathbf{M}_\infty = \begin{pmatrix} \mathbf{T}_1 & 0 & 0 & \cdots & 0 \\ 0 & \mathbf{T}_2 & 0 & \cdots & 0 \\ 0 & 0 & \mathbf{T}_3 & \cdots & 0 \\ \vdots & \vdots & \vdots & \ddots & \vdots \\ 0 & 0 & 0 & \cdots & \mathbf{T}_N \end{pmatrix}$$

(6.10)

where block $\mathbf{T}_m$ describes the mutual interactions of basis functions on object m, while block $\mathbf{U}_{mn}$ describes the interactions of basis functions on object m with functions on object n.

To evaluate $\log \frac{\det \mathbf{M}}{\det \mathbf{M}_\infty}$, we resort to the standard numerical technique of LU-factorization. Let this factorization for the $\mathbf{M}$ matrix be $\mathbf{M} = \mathbf{L} \cdot \mathbf{U}$,[3] so that $\mathbf{U}$ is upper-triangular and $\mathbf{L}$ is lower-triangular with ones on its diagonal (and thus unit determinant). Similarly, let $\mathbf{T}_n = \mathbf{l}_n \cdot \mathbf{u}_n$ be the LU-factorization of the $\mathbf{T}_n$ block matrix (where the lower case letters indicate matrices of lesser dimension than $\mathbf{L}, \mathbf{U}$.)

---

[3]The $\mathbf{U}$ matrix here is not to be confused with the $\mathbf{U}_{mn}$ block matrices in (6.10). The collision of terminology is unfortunate, but the usage of the symbol $\mathbf{U}$ on both sides is so entrenched that there is little we can do about it now.

Then we have

$$\log \frac{\det \mathbf{M}}{\det \mathbf{M}_\infty} = \log \frac{\det \mathbf{U}}{\prod_n \det \mathbf{u}_n}$$

$$= \log \frac{\prod_i (\mathbf{U})_{ii}}{\prod_n \prod_i (\mathbf{u}_n)_{ii}}$$

$$= \sum \log \frac{(\mathbf{U})_{ii}}{(\mathbf{u}_n)_{ii}}$$

where our schematic notation in the third line indicates that quantity in the numerator runs over all diagonal elements of $\mathbf{U}$, while the quantity in the numerator runs over the diagonal elements of $\mathbf{u}_1$, then over the diagonal elements of $\mathbf{u}_2$, etc.

The first equality here follows because $\det \mathbf{M} = \det \mathbf{L} \cdot \det \mathbf{U} = \det \mathbf{U}$, while $\det \mathbf{M}_\infty$, which is the product of the determinants of the diagonal blocks of $\mathbf{M}$, is obtained similarly. The second equality follows because the determinant of a triangular matrix is the product of its diagonal entries. Since there are as many factors in the numerator as in the denominator of the second line, we can sum the logarithms of their pairwise ratios, as in the third line, a better-conditioned numerical procedure than taking the logarithm of the ratios of the overall products as in the second line. (Indeed, from the expression on the third line above we can simply *omit* the portion corresponding to the first diagonal block $\mathbf{T}_1$, because the upper-right block of $\mathbf{U}$ actually coincides with $\mathbf{u}_1$.)

Calculation of Trace. The derivative of the $\mathbf{M}$ matrix with respect to displacement or rotation of the first object in our Casimir geometry has the form

$$\Delta \mathbf{M} = \begin{pmatrix} 0 & \Delta \mathbf{U}_{12} & \Delta \mathbf{U}_{13} & \cdots & \Delta \mathbf{U}_{1N} \\ \Delta \mathbf{U}_{21} & 0 & 0 & \cdots & 0 \\ \Delta \mathbf{U}_{31} & 0 & 0 & \cdots & 0 \\ \vdots & \vdots & \vdots & \ddots & \vdots \\ \Delta \mathbf{U}_{N1} & 0 & 0 & \cdots & 0 \end{pmatrix}, \qquad (6.11)$$

where Δ is short for $\partial/\partial r_i$ (for displacements) or $\partial/\partial \theta$ (for rotations). Let $\mathbf{V}_i$, $i = 1, \cdots, D_1$ be the first D_1 columns of the matrix $\Delta \mathbf{M}$ (where D_1, the dimension of the matrix subblock corresponding to object 1, is proportional to the number of basis functions defined on the surface of object 1). Then, following the observations of Section (5.4), the quantity that enters into the integrand of equations (5.1b) and (5.1c) is

$$\mathrm{Tr}\left\{ \mathbf{M}^{-1} \cdot \Delta \mathbf{M} \right\} = 2 \sum_{i=1}^{D_1} \left(\mathbf{M}^{-1} \cdot \mathbf{V}_i \right)_i.$$

In other words, for each of the D_1 vectors $\mathbf{V}_i$, we compute the vector $\mathbf{M}^{-1} \cdot \mathbf{V}_i$ and add the ith component of this vector to a running sum, which we double at the end of the calculation to obtain the integrand of (5.1b) or (5.1c). (To compute $\mathbf{M}^{-1} \cdot \mathbf{V}_i$

we solve the linear system $\mathbf{M} \cdot \mathbf{X} = \mathbf{V}_i$ using the LU-factorization of $\mathbf{M}$.)

Dense-Direct Linear Algebra. In CASIMIR3D, which is designed to work with matrices of total dimension less than or on the order of 10^4, the full BEM matrices are explicitly computed and stored in memory, and the LU-factorizations needed to compute the Casimir energy, force, and torque integrands in (5.1) are computed using the LAPACK suite of dense-direct numerical linear algebra codes. (A technique for reducing the scaling of memory and CPU time requirements is discussed in Chapter 8 of this thesis.)

Frequency Integration. We evaluate the ξ integral in (5.1) using a straightforward one-dimensional adaptive numerical cubature with the infinite interval $\xi \in [0, \infty]$ compactified to $[0, 1]$:

$$
\int_0^\infty d\xi \, f(\xi) = \int_0^1 dt \, f\Big(\xi(t)\Big) J(t)
$$

$$
\approx \sum w_n f\Big(\xi(t_n)\Big) J(t_n). \tag{6.12}
$$

In the first line here we have put $\xi(t) = t/(1-t)$ (with $J(t) = 1/(1-t)^2$ the Jacobian of the transformation), while the second line represents an evaluation of the t integral via adaptive numerical quadrature, with the weights w_n and points t_n chosen adaptively by the adaptive quadrature algorithm. (In CASIMIR3D we use a modified version of the QUADPACK algorithm[4] as reimplemented in the GSL.[5])

Evaluation of Multiple Displacements at Once. In a typical Casimir calculation we seek not merely the Casimir energy and force of a single geometric configuration, but rather a full *curve* predicting the energy and/or force as we vary the relative distance and/or orientation of the interacting objects (we will refer to such variations as "geometrical transformations"). For example, for the sphere-cube example of Figure 6.1, we may seek to evaluate the Casimir quantities at several different values of the surface–surface separation. To this end it is important to observe that rigid displacements and rotations of the objects in a geometry affect only the $\mathbf{U}_{mn}$ block matrices in (6.10), leaving the $\mathbf{T}_m$ blocks unchanged; once we have computed the $\mathbf{T}_m$ matrices at a given imaginary frequency ξ we can reuse them to compute the Casimir quantities under multiple geometric transformations. On the other hand, when we change the frequency ξ we must recompute all matrix blocks.

This suggests that, when computing a full force curve, we should *not* evaluate the ξ integral in (5.1) separately for each geometrical transformation, but should instead think of integrating a vector of integrands all at once, with each component of the vector corresponding to a Casimir quantity at a separate geometric transformation. Thus, the function $f(\xi)$ in (6.12) becomes a vector $f_i(\xi)$; at each frequency point

---

[4]http://www.netlib.org/quadpack
[5]http://www.gnu.org/software/gsl

ξ_n chosen by the adaptive quadrature scheme we assemble the $\mathbf{T}_n$ matrices in (6.10) only once, then *reuse* these matrices to compute the Casimir quantities under multiple geometric transformations. (For energy calculations, the diagonal entries of the $\mathbf{u}_n$ factors in the LU factorization of $\mathbf{T}_n$ matrices can of course be reused as well.)

Chapter 7

CASIMIR2D: A Numerical Implementation of the FSC Formulae for Quasi-2D Objects

Many experimental Casimir geometries [29] consist of two or more objects elongated in one spatial direction (call it the z direction) with essentially constant two-dimensional cross-section in the transverse plane, and with the length of the objects in the z-direction being much larger than the characteristic feature size or surface–surface separation in the xy-plane. For such *quasi-2D* geometries, it is convenient to idealize the objects as being of *infinite* extent in the z-direction and to compute Casimir energies, forces, and torques *per unit length* (in the z-direction). This is the task for which CASIMIR2D is designed.

The structure of this chapter mirrors that of the previous chapter. In Section 7.1 we describe the localized basis functions used by CASIMIR2D to represent tangential current distributions on the surfaces of quasi-2D objects. Section 7.2 discusses the implications of this choice of basis functions for the computation of the elements of the BEM matrices that enter into the FSC formulae. Other aspects of the numerical implementation of CASIMIR2D are summarized in Section 7.3, and details on the usage of the CASIMIR2D software package are relegated to Appendix H.

7.1 TDRT Basis Functions for 2D BEM Problems

7.1.1 Definition of TDRT Basis Functions

Two-dimensional rooftop (TDRT) basis functions are a convenient set of expansion functions for surface currents on quasi-2D objects. (Two-dimensional BEM schemes using linearly varying surface unknowns have appeared before [31], but the particular functions we define below are used here for the first time in the context of imaginary-frequency BEM solvers for Casimir computations). As depicted in Figure 7-1(a), we begin by approximating the cross-sectional boundaries of quasi-2D objects as collections of straight-line segments; we refer to the endpoints of these segments as

(a)

(b)

(c)

(d)
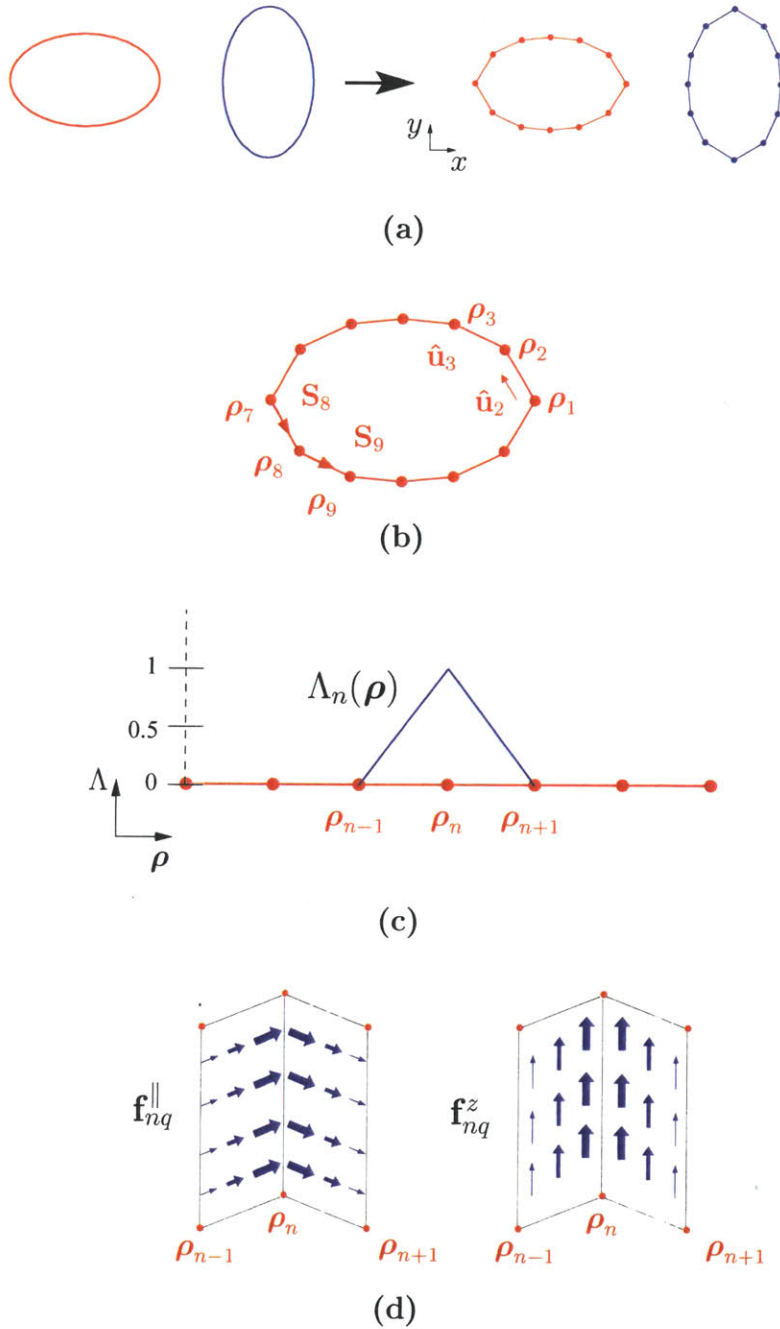
Figure 7-1: Two-dimensional rooftop (TDRT) basis functions. **(a)** The cross-sectional boundaries of quasi-2D objects are discretized into finite line segments. **(b)** Notation: $\mathbf{S}_n$ is the directed line segment connecting control point $\boldsymbol{\rho}_{n-1}$ to $\boldsymbol{\rho}_n$. $\hat{\mathbf{u}}_n$ is a unit vector in the direction of $\mathbf{S}_n$. **(c)** To each control point $\boldsymbol{\rho}_n$ we associate a "rooftop" function $\Lambda_n(\boldsymbol{\rho})$, which takes the value $\Lambda = 1$ at the central control point, falls linearly to zero at the adjacent control points, and vanishes everywhere else. **(d)** To each control point we associate one $\|$-type and one z-type basis function; the former describes currents flowing around the perimeter of an object, while the latter describes currents flowing down the infinite length of the object.

84

control points. We use the symbol $\boldsymbol{\rho} = (x, y)$ to label points in the cross-sectional plane, and we denote the nth control point in our geometry by $\boldsymbol{\rho}_n = (x_n, y_n)$; the directed line segment from $\boldsymbol{\rho}_{n-1}$ to $\boldsymbol{\rho}_n$ is $\mathbf{S}_n$, its length is $l_n = |\boldsymbol{\rho}_n - \boldsymbol{\rho}_{n-1}|$, and $\hat{\mathbf{u}}_n = \mathbf{S}_n/l_n$ is a unit vector in its direction (Figure 7-1(**b**)).

To each control point $\boldsymbol{\rho}_n$ we now associate a rooftop function $\Lambda_n(\boldsymbol{\rho})$. This function is only nonvanishing for points $\boldsymbol{\rho}$ contained within the two line segments that meet at $\boldsymbol{\rho}_n$; as illustrated in Figure 1(**b**), it attains a maximum value of unity at the central control point ($\boldsymbol{\rho} = \boldsymbol{\rho}_n$), falls linearly to zero at each of the two neighboring control points ($\boldsymbol{\rho} = \boldsymbol{\rho}_{n\pm1}$), and vanishes everywhere else.

We next define two vector-valued basis functions associated with each control point; each function is localized within two adjacent line segments in the $\boldsymbol{\rho}$ plane and varies sinusoidally in the z direction. A first function describes surface currents running around the perimeter of the object:

$$\mathbf{f}_{nq}^{\|}(\boldsymbol{\rho}, z) = \begin{cases} i\Lambda_n(\boldsymbol{\rho})e^{iqz}\hat{\mathbf{u}}_n, & \boldsymbol{\rho} \in \mathbf{S}_n \\ i\Lambda_n(\boldsymbol{\rho})e^{iqz}\hat{\mathbf{u}}_{n+1} & \boldsymbol{\rho} \in \mathbf{S}_{n+1} \end{cases} \tag{7.1}$$

A second function describes surface currents flowing down the length of the object:

$$\mathbf{f}_{nq}^z(\boldsymbol{\rho}, z) = \Lambda_n(\boldsymbol{\rho})e^{iqz}\hat{\mathbf{z}}. \tag{7.2}$$

The functions (7.1) and (7.2) are our TDRT basis functions. (The factor of i in the definition of the $\mathbf{f}^{\|}$ function is a useful convention that amounts to choosing the $z-$oscillation in the currents described by the $\mathbf{f}^{\|}$ and $\mathbf{f}^z$ functions to be 90° out of phase with one another.)

Using the TDRT basis functions, we may approximate a general surface current distribution as an expansion of the form

$$\mathbf{K}(\mathbf{x}) = \sum_{n=1}^{N} \int \frac{dq}{2\pi} \left\{ K_{nq}^{\|}\mathbf{f}_{nq}^{\|}(\mathbf{x}) + K_{nq}^z\mathbf{f}_{nq}^z(\mathbf{x}) \right\} \tag{7.3}$$

where N is the total number of control points in our discretized geometry.

7.1.2 Integrals over TDRT Basis Functions

In what follows we will frequently need to evaluate integrals over TDRT basis functions of the general form

$$L(mq, nq') \equiv \left\langle \mathbf{f}_{mq}(\mathbf{x}) \middle| \Gamma(\kappa; \mathbf{x} - \mathbf{x}') \middle| \mathbf{f}_{nq'}(\mathbf{x}') \right\rangle \tag{7.4}$$

where $\mathbf{f}_{mq}$ and $\mathbf{f}_{nq'}$ are TDRT functions and the kernel $\boldsymbol{\Gamma}$ depends only on the 3D difference vector $(\mathbf{x} - \mathbf{x}') = (\boldsymbol{\rho} - \boldsymbol{\rho}', z - z')$. All such integrals take the general form

$$L(mq, nq')$$
$$= \int d\boldsymbol{\rho} \int d\boldsymbol{\rho}' \Big\{ z, z' - \text{independent factor} \Big\} \int_{-\infty}^{\infty} dz \int_{-\infty}^{\infty} dz' e^{i(q'z'-qz)} G\big(\kappa; \mathbf{x} - \mathbf{x}'\big)$$

where the $d\boldsymbol{\rho}, d\boldsymbol{\rho}'$ line integrals extend over line segments in the cross-sectional plane and G is a scalar kernel function.

To evaluate the z', z integral here, we change variables to $t = z' + z$, $u = z' - z$:

$$\int_{-\infty}^{\infty} dz \int_{-\infty}^{\infty} dz' e^{i(q'z'-qz)} G\big(\kappa; \mathbf{x} - \mathbf{x}'\big)$$
$$= \frac{1}{2} \int_{-\infty}^{\infty} dt\, e^{\frac{i}{2}(q'-q)t} \int_{-\infty}^{\infty} du\, e^{\frac{i}{2}(q'+q)u} G(\kappa; \boldsymbol{\rho} - \boldsymbol{\rho}', u)$$
$$= \delta(q' - q) \cdot \mathcal{I}(\kappa; q; \boldsymbol{\rho} - \boldsymbol{\rho}')$$

where we have defined a two-dimensional kernel function,

$$\mathcal{I}(\kappa; q; \boldsymbol{\rho} - \boldsymbol{\rho}') \equiv 2\pi \int_{-\infty}^{\infty} du\, e^{iqu} G(\kappa; \boldsymbol{\rho} - \boldsymbol{\rho}', u).$$

Thus TDRT functions with different values of q have vanishing inner products (7.4).

We will need to evaluate $\mathcal{I}$ for three specific choices of the scalar kernel G, as tabulated in the following table:

$G(\kappa; \mathbf{x} - \mathbf{x}')$	$\mathcal{I}(\kappa; q; \boldsymbol{\rho} - \boldsymbol{\rho}')$
$\dfrac{e^{-\kappa|\mathbf{x}-\mathbf{x}'|}}{4\pi|\mathbf{x} - \mathbf{x}'|}$	$K_0\big(\alpha_{\kappa q}|\boldsymbol{\rho} - \boldsymbol{\rho}'|\big)$
$\big(1 + \kappa|\mathbf{x} - \mathbf{x}'|\big) \cdot \dfrac{e^{-\kappa|\mathbf{x}-\mathbf{x}'|}}{4\pi|\mathbf{x} - \mathbf{x}'|^3}$	$\dfrac{\alpha_{\kappa q}}{|\boldsymbol{\rho} - \boldsymbol{\rho}'|} K_1\big(\alpha_{\kappa q}|\boldsymbol{\rho} - \boldsymbol{\rho}'|\big)$
$(z' - z) \cdot \big(1 + \kappa|\mathbf{x} - \mathbf{x}'|\big) \cdot \dfrac{e^{-\kappa|\mathbf{x}-\mathbf{x}'|}}{4\pi|\mathbf{x} - \mathbf{x}'|^3}$	$iqK_0\big(\alpha_{\kappa q}|\boldsymbol{\rho} - \boldsymbol{\rho}'|\big)$

Here K_0 and K_1 are modified Bessel functions of the second kind, and

$$\alpha_{\kappa q} \equiv \sqrt{\kappa^2 + q^2}.$$

7.2 Evaluation of BEM Matrix Elements Between TDRT Basis Functions

7.2.1 Block Structure of the BEM Matrix

To elucidate the block structure of the BEM matrix in the case of TDRT basis functions, we recall the original provenance of this matrix as the set of coefficients in a linear system of equations, obtained by discretizing an integral equation, of the form

$$\mathbf{M} \cdot \mathbf{K} = \mathbf{V}, \tag{7.5}$$

where the unknown vector $\mathbf{K}$ contains the coefficients in an expansion of a surface-current distribution in some set of tangential vector-valued basis functions. For the particular case of TDRT basis functions, this expansion takes the form (7.3), and the discretized integral equation (7.5) is thus nominally an *infinite-dimensional* system because of the continuous nature of the q index:

$$\sum_{n'} \int \frac{dq'}{2\pi} M_{nq,n'q'} K_{n'q'} = V_{nq}. \tag{7.6}$$

However, as discussed in the previous section, all elements of the $\mathbf{M}$ matrix contain a factor of $\delta(q - q')$, and the infinite linear system (7.6) thus block-factorizes into an infinite set of *finite-dimensional* systems, one for each q:

$$\mathbf{M}_q \cdot \mathbf{K}_q = \mathbf{V}_q. \tag{7.7}$$

In view of this block-factorization, the log-determinant that enters into the FSC energy expression (5.1a) is

$$\log \det \mathbf{M} = \int_{-\infty}^{\infty} \frac{dq}{2\pi} \log \det \mathbf{M}_q$$

$$= \int_{0}^{\infty} \frac{dq}{\pi} \log \left| \det \mathbf{M}_q \right|.$$

Inserting this into the master FSC formulae, we obtain expressions for the Casimir energy and force *per unit length* of our quasi-2D structure:

$$\mathcal{E} = \frac{\hbar}{2\pi^2} \int_0^\infty d\xi \int_0^\infty dq \, \frac{\log \det \mathbf{M}(\xi, q)}{\log \det \mathbf{M}_\infty(\xi, q)} \tag{7.8a}$$

$$\mathcal{F}_i = -\frac{\hbar}{2\pi^2} \int_0^\infty d\xi \int_0^\infty dq \, \mathrm{Tr}\left\{ \mathbf{M}^{-1}(\xi, q) \cdot \frac{\partial \mathbf{M}(\xi, q)}{\partial \mathbf{x}_i} \right\}. \tag{7.8b}$$

Equations (7.8) are the versions of the master FSC formulae (5.1) appropriate for quasi-2D geometries.

7.2.2 Matrix Elements between TDRT Basis Functions

The structure of the BEM matrix in the EFIE and PMCHW formulations was discussed in Chapter 4 and is reviewed in Appendix B. Each pair of basis functions $(\mathbf{f}_\alpha, \mathbf{f}_\beta)$ contributes one entry (EFIE) or a 2×2 block of entries (PMCHW) to the BEM matrix; these entries, in turn, are obtained as linear combinations of three types of integrals over the supports of the two basis functions (the "L-functions" of B).

For TDRT basis functions, the α subscript is a compound index, $\alpha = (tmq)$, where $t \in \{\|, z\}$ labels the type of basis function, m labels the control point to which the basis function is associated, and q is the z-wavevector. To elucidate the general structure of the L-functions for TDRT basis functions, we consider the particular case of the $L_\bullet$ function between two z-type basis functions:

$$L_\bullet(\kappa; \mathbf{f}_{mq}^z, \mathbf{f}_{nq'}^z) \equiv \int_{\sup \mathbf{f}_{mq}^z} d\mathbf{x} \int_{\sup \mathbf{f}_{nq'}^z} d\mathbf{x}' \left[\mathbf{f}_{mq}^{z*}(\mathbf{x}) \cdot \mathbf{f}_{nq'}^z(\mathbf{x}') \right] G_0(\kappa; \mathbf{x} - \mathbf{x}')$$

$$= \int d\boldsymbol{\rho} \int d\boldsymbol{\rho}' \Lambda_m(\boldsymbol{\rho}) \Lambda_n(\boldsymbol{\rho}') \int_{-\infty}^{\infty} dz \int_{-\infty}^{\infty} dz' e^{i(q'z' - qz)} G_0(\kappa; \mathbf{x} - \mathbf{x}').$$

This integral is of the general type considered in Section 7.1.2, and we find

$$L_\bullet(\kappa; \mathbf{f}_{mq}^z, \mathbf{f}_{nq'}^z) = \delta(q - q') L_\bullet(\kappa; q; \mathbf{f}_{mq}^z, \mathbf{f}_{nq}^z)$$

where

$$L_\bullet(\kappa; q; \mathbf{f}_{mq}^z, \mathbf{f}_{nq}^z) = \int d\boldsymbol{\rho} \int d\boldsymbol{\rho}' \Lambda_m(\boldsymbol{\rho}) \Lambda_n(\boldsymbol{\rho}') K_0 \left(\alpha_{\kappa q} |\boldsymbol{\rho} - \boldsymbol{\rho}'| \right) \tag{7.9}$$

defines a modified version of the $L_\bullet$ function appropriate for the particular case of TDRT basis functions.

Computation of the elements of the $\mathbf{M}(\xi, q)$ matrices in equations (7.8) now reduces to the evaluation of these modified L-functions for various combinations of TDRT functions $(s, t \in \{\|, z\})$:

$$\left\langle \mathbf{f}_{mq}^s \middle| \mathbf{M}(\xi, q) \middle| \mathbf{f}_{nq}^t \right\rangle = -\kappa^e Z^e \left[L_\bullet^{st}(\kappa^e, q, m, n) + \frac{1}{(\kappa^e)^2} L_\nabla^{st}(\kappa^e, q, m, n) \right]$$

in the PEC case, or

$$\left\langle \mathbf{f}_{mq}^s \middle| \mathbf{M}(\xi, q) \middle| \mathbf{f}_{nq}^t \right\rangle$$

$$= \begin{pmatrix} -\kappa^e Z^e \left[L_\bullet^{st}(\kappa^e, q, m, n) + \frac{1}{(\kappa^e)^2} L_\nabla^{st}(\kappa^e, q, m, n) \right] & -L_\times^{st}(\kappa^e, q, m, n) \\ -L_\times^{st}(\kappa^e, q, m, n) & +\frac{\kappa^e}{Z^e} \left[L_\bullet^{st}(\kappa^e, q, m, n) + \frac{1}{(\kappa^e)^2} L_\nabla^{st}(\kappa^e, q, m, n) \right] \end{pmatrix} \tag{7.10}$$

88

in the PMCHW case; here

$$\kappa^e = \sqrt{\epsilon^e(i\xi)\mu^e(i\xi)} \cdot \frac{\xi}{c}, \qquad Z^e = \sqrt{\frac{\mu^e(i\xi)}{\epsilon^e(i\xi)}}$$

are the imaginary wavevector and the relative wave impedance of the external medium in our scattering geometry at imaginary frequency ξ. (Equation (7.10) is for the case in which $\mathbf{f}_{mq}^s$, $\mathbf{f}_{nq}^t$ lie on the surfaces of different objects, so that only κ^e, Z^e are relevant. If, instead, the two basis functions both lie on the surface of the object n, then the matrix elements are augmented by similar contributions with $\{\kappa^e, Z^e\} \rightarrow \{\kappa^n, Z^n\}$, as discussed in Appendix B).

7.2.3 Modified L-functions as Segment-Segment Integrals

Integrals such as that in (7.9) extend over the supports of two TDRT basis functions within the cross-sectional plane. Since each basis function is supported on two line segments, each L-function is a sum of four segment-segment integrals,

$$\begin{aligned}
L_\bullet^{st}(\kappa, q, \mathbf{f}_{mq}^s, \mathbf{f}_{nq}^t) = {} & L_\bullet^{st}\big(\kappa, q; \boldsymbol{\rho}_{m-1}, \boldsymbol{\rho}_m, +; \boldsymbol{\rho}_{n-1}, \boldsymbol{\rho}_n, +\big) \\
& + L_\bullet^{st}\big(\kappa, q; \boldsymbol{\rho}_{m-1}, \boldsymbol{\rho}_m, +; \boldsymbol{\rho}_n, \boldsymbol{\rho}_{n+1}, -\big) \\
& + L_\bullet^{st}\big(\kappa, q; \boldsymbol{\rho}_m, \boldsymbol{\rho}_{m+1}, -; \boldsymbol{\rho}_{n-1}, \boldsymbol{\rho}_n, +\big) \\
& + L_\bullet^{st}\big(\kappa, q; \boldsymbol{\rho}_m, \boldsymbol{\rho}_{m+1}, -; \boldsymbol{\rho}_n, \boldsymbol{\rho}_{n+1}, -\big) \qquad (7.11)
\end{aligned}$$

(and similarly for L_∇ and $L_\times$). The $\boldsymbol{\rho}$ arguments to the segment-segment L functions indicate the segment over which we integrate, while the $\pm$ arguments indicate whether the rooftop function is rising or falling on the corresponding line segment. (More precisely, the argument is $+$ when the rooftop function is rising as we traverse the line segment in the direction of current flow described by the $\|$-type basis function, and $-$ otherwise).

In all there are twelve segment-segment L-functions for each pair of line segments. Writing out the integrands of these twelve functions reveals that they may be obtained

as linear combinations of a smaller set of 6 segment-segment integrals:

$$L_\bullet^{\|\|}\big(\kappa, q; \mathbf{A}, \mathbf{B}, \sigma; \mathbf{C}, \mathbf{D}, \tau\big) = \cos\theta\, \mathcal{I}_4 \tag{7.12a}$$

$$L_\nabla^{\|\|}\big(\kappa, q; \mathbf{A}, \mathbf{B}, \sigma; \mathbf{C}, \mathbf{D}, \tau\big) = \frac{\sigma\tau}{ll'}\mathcal{I}_1 \tag{7.12b}$$

$$L_\times^{\|\|}\big(\kappa, q; \mathbf{A}, \mathbf{B}, \sigma; \mathbf{C}, \mathbf{D}, \tau\big) = iq\sin\theta\, \mathcal{I}_4 \tag{7.12c}$$

$$\cdot\; L_\bullet^{\|z}\big(\kappa, q; \mathbf{A}, \mathbf{B}, \sigma; \mathbf{C}, \mathbf{D}, \tau\big) = 0 \tag{7.12d}$$

$$L_\nabla^{\|z}\big(\kappa, q; \mathbf{A}, \mathbf{B}, \sigma; \mathbf{C}, \mathbf{D}, \tau\big) = \sigma\frac{q}{l}\mathcal{I}_3 \tag{7.12e}$$

$$L_\times^{\|z}\big(\kappa, q; \mathbf{A}, \mathbf{B}, \sigma; \mathbf{C}, \mathbf{D}, \tau\big) = i\Big(\hat{u}_y\mathcal{I}_5 + \hat{u}_x\mathcal{I}_6\Big) \tag{7.12f}$$

$$L_\bullet^{z\|}\big(\kappa, q; \mathbf{A}, \mathbf{B}, \sigma; \mathbf{C}, \mathbf{D}, \tau\big) = 0 \tag{7.12g}$$

$$L_\nabla^{z\|}\big(\kappa, q; \mathbf{A}, \mathbf{B}, \sigma; \mathbf{C}, \mathbf{D}, \tau\big) = \tau\frac{q}{l'}\mathcal{I}_2 \tag{7.12h}$$

$$L_\times^{z\|}\big(\kappa, q; \mathbf{A}, \mathbf{B}, \sigma; \mathbf{C}, \mathbf{D}, \tau\big) = i\Big(\hat{u}'_y\mathcal{I}_5 - \hat{u}'_x\mathcal{I}_6\Big) \tag{7.12i}$$

$$L_\bullet^{zz}\big(\kappa, q; \mathbf{A}, \mathbf{B}, \sigma; \mathbf{C}, \mathbf{D}, \tau\big) = \mathcal{I}_4 \tag{7.12j}$$

$$L_\nabla^{zz}\big(\kappa, q; \mathbf{A}, \mathbf{B}, \sigma; \mathbf{C}, \mathbf{D}, \tau\big) = q^2\mathcal{I}_4 \tag{7.12k}$$

$$L_\times^{zz}\big(\kappa, q; \mathbf{A}, \mathbf{B}, \sigma; \mathbf{C}, \mathbf{D}, \tau\big) = 0 \tag{7.12l}$$

where

$$\mathbf{u} = \mathbf{B} - \mathbf{A}, \qquad l = |\mathbf{u}|, \qquad \hat{\mathbf{u}} = \frac{\mathbf{u}}{l}$$

$$\mathbf{u}' = \mathbf{D} - \mathbf{C}, \qquad l' = |\mathbf{u}'|, \qquad \hat{\mathbf{u}}' = \frac{\mathbf{u}'}{l'}$$

$$\sin\theta = \big(\hat{\mathbf{u}} \times \hat{\mathbf{u}}'\big) \cdot \hat{\mathbf{z}}$$

and the $\mathcal{I}$ quantities are two-dimensional integrals defined over a pair of line segments

$(\mathbf{X}_{\mathrm{S}} \rightarrow \mathbf{X}_{\mathrm{E}})$, $(\mathbf{X}'_{\mathrm{S}} \rightarrow \mathbf{X}'_{\mathrm{E}})$:

$$\begin{Bmatrix} \mathcal{I}_1 \\ \mathcal{I}_2 \\ \mathcal{I}_3 \\ \mathcal{I}_4 \end{Bmatrix} (\alpha_{\kappa q}; \mathbf{X}_{\mathrm{S}}, \mathbf{X}_{\mathrm{E}}; \mathbf{X}'_{\mathrm{S}}, \mathbf{X}'_{\mathrm{E}})$$

$$\equiv ll' \int_0^1 du \int_0^1 du' \begin{Bmatrix} 1 \\ u \\ u' \\ uu' \end{Bmatrix} K_0\Big(\alpha_{\kappa q} R(u, u')\Big) \tag{7.13a}$$

$$\begin{Bmatrix} \mathcal{I}_5 \\ \mathcal{I}_6 \end{Bmatrix} (\alpha_{\kappa q}; \mathbf{X}_{\mathrm{S}}, \mathbf{X}_{\mathrm{E}}; \mathbf{X}'_{\mathrm{S}}, \mathbf{X}'_{\mathrm{E}})$$

$$\equiv ll' \alpha_{\kappa q} \int_0^1 du \int_0^1 du' \begin{Bmatrix} uu' R_x(u, u') \\ uu' R_y(u, u') \end{Bmatrix} \frac{K_1\Big(\alpha_{\kappa q} R(u, u')\Big)}{R(u, u')} \tag{7.13b}$$

with (Figure 7-2)

$$R(u, u') = \big|\mathbf{R}(u, u')\big|$$
$$\mathbf{R}(u, u') = \mathbf{X}_{\mathrm{S}} + u(\mathbf{X}_{\mathrm{E}} - \mathbf{X}_{\mathrm{S}}) - \mathbf{X}'_{\mathrm{S}} - u'(\mathbf{X}'_{\mathrm{E}} - \mathbf{X}'_{\mathrm{S}})$$
$$= \mathbf{R}_0 + u\mathbf{L} - u'\mathbf{L}' \tag{7.14}$$

$$\mathbf{R}_0 = \mathbf{X}_{\mathrm{S}} - \mathbf{X}'_{\mathrm{S}}, \qquad \mathbf{L} = \mathbf{X}_{\mathrm{E}} - \mathbf{X}_{\mathrm{S}} \qquad \mathbf{L}' = \mathbf{X}'_{\mathrm{E}} - \mathbf{X}'_{\mathrm{S}}.$$

The endpoints of the line segments in the $\mathcal{I}$ integrals are determined from the $(\mathbf{A}, \mathbf{B}, \sigma, \mathbf{C}, \mathbf{D}, \tau)$ arguments to the segment-segment L functions in (7.12) according to

$$\{\mathbf{X}_{\mathrm{S}}, \mathbf{X}_{\mathrm{E}}\} = \begin{cases} \{\mathbf{A}, \mathbf{B}\} & \sigma = + \\ \{\mathbf{B}, \mathbf{A}\} & \sigma = - \end{cases}, \qquad \{\mathbf{X}'_{\mathrm{S}}, \mathbf{X}'_{\mathrm{E}}\} = \begin{cases} \{\mathbf{C}, \mathbf{D}\} & \tau = + \\ \{\mathbf{D}, \mathbf{C}\} & \tau = - \end{cases}$$

We pause briefly to comment on our choice of notation. The segment-segment L functions on the right-hand side of (7.11) depend both on the line segments over which we are integrating *and* on the $\pm$ arguments indicating the growth or decay of the rooftop functions on those line segments. This dependence is reflected in the appearance of explicit factors of σ and τ in equations (7.12). In contrast, the $\mathcal{I}$ integrals in (7.13) depend only on the endpoints of the line segments and take no $\pm$ arguments. This simplifies the subsequent discussion, particularly for the evaluation of nearby segment-segment integrals in Section 7.2.6.

7.2.4 Derivatives of L-functions

For analytic force calculations we need derivatives of L-functions with respect to rigid relative displacements of the underlying basis functions. For the case of TDRT basis functions the L-function derivatives are given by the same expressions as (7.12), but

91
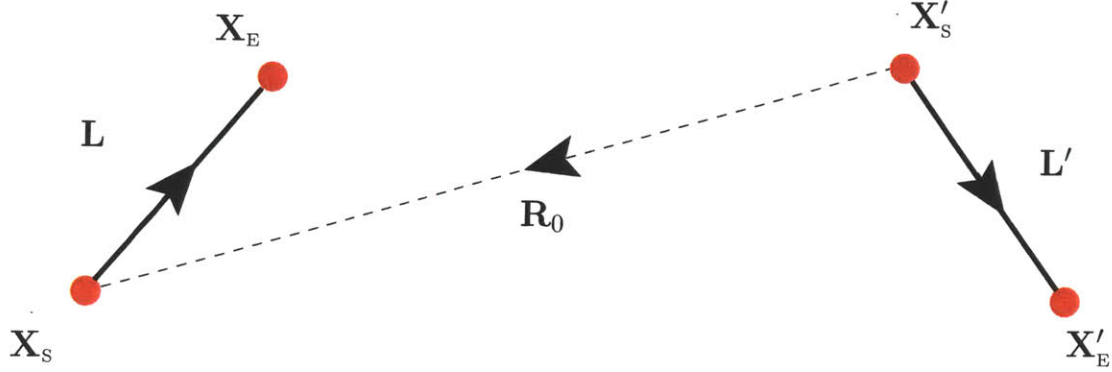
Figure 7-2: Geometry and notation for computation of segment-segment integrals.

with the $\mathcal{I}_{1-6}$ integrals replaced by their derivatives with respect to the components of the $\mathbf{R}_0$ vector in (7.14).

Before proceeding, it is convenient to introduce a slight refinement of our notation that will allows us to present the remainder of this discussion in a more coherent and unified fashion. For a given pair of line segments we define a three-index integral quantity according to

$$\mathcal{I}_r^{pq}(\alpha, \mathbf{X}_{\mathrm{S}}, \mathbf{X}_{\mathrm{E}}; \mathbf{X}_{\mathrm{S}}', \mathbf{X}_{\mathrm{E}}') \equiv ll' \int_0^1 du \int_0^1 du'\, u^p\, u'^q\, \mathcal{K}_r\big(R(u, u')\big) \tag{7.15}$$

where $\mathcal{K}_r$ is one of three possible kernel functions:

$$\mathcal{K}_0(R) = K_0(\alpha R), \qquad \mathcal{K}_1(R) = \alpha \frac{K_1(\alpha R)}{R}, \qquad \mathcal{K}_2(R) = \alpha^2 \frac{K_2(\alpha R)}{R^2}.$$

In terms of this notation, the six integrals that enter into the RHS of (7.12) are

$$
\begin{aligned}
I_1 &= \mathcal{I}_0^{00} & I_2 &= \mathcal{I}_0^{10} \\
I_3 &= \mathcal{I}_0^{01} & I_4 &= \mathcal{I}_0^{11} \\
I_5 &= R_{0x}\mathcal{I}_1^{11} + L_x\mathcal{I}_1^{21} - L_x'\mathcal{I}_1^{12} & I_6 &= R_{0y}\mathcal{I}_1^{11} + L_y\mathcal{I}_1^{21} - L_y'\mathcal{I}_1^{12}.
\end{aligned}
\tag{7.16}
$$

Equation (7.15) depends on $\mathbf{R}_0$ only through the quantity $R(u, u')$ in the kernel. The derivative of this quantity with respect to (say) the x component of $\mathbf{R}_0$ is

$$\frac{\partial}{\partial R_{0x}} R(u, u') = \frac{R_{0x} + uL_x - u'L_x'}{R(u, u')}$$

and applying this formula to (7.15) yields an expression for the derivatives of the segment-segment integrals:

$$\frac{\partial}{\partial R_{0x}} \mathcal{I}_r^{pq} = -R_{0x}\mathcal{I}_{r+1}^{pq} - L_x\mathcal{I}_{r+1}^{p+1,q} + L_x'\mathcal{I}_{r+1}^{p,q+1} \qquad \text{(for } r = 0, 1).$$

92

With these results we can write expressions for the derivatives of the six integrals that appear on the right-hand side of (7.12); for example, the x derivatives $\mathcal{I}_{1-4}$ read

$$\frac{\partial}{\partial R_{0x}} \left\{ \begin{array}{c} \mathcal{I}_1 \\ \mathcal{I}_2 \\ \mathcal{I}_3 \\ \mathcal{I}_4 \end{array} \right\} = -R_{0x} \left\{ \begin{array}{c} \mathcal{I}_1^{00} \\ \mathcal{I}_1^{01} \\ \mathcal{I}_1^{10} \\ \mathcal{I}_1^{11} \end{array} \right\} - L_x \left\{ \begin{array}{c} \mathcal{I}_1^{10} \\ \mathcal{I}_1^{11} \\ \mathcal{I}_1^{20} \\ \mathcal{I}_1^{21} \end{array} \right\} + L_x' \left\{ \begin{array}{c} \mathcal{I}_1^{01} \\ \mathcal{I}_1^{02} \\ \mathcal{I}_1^{11} \\ \mathcal{I}_1^{12} \end{array} \right\} \tag{7.17}$$

and the y derivatives of $\mathcal{I}_{1-4}$ are similar. The corresponding expressions for the derivatives of $\mathcal{I}_{5-6}$ are also similar, but **(1)** involve the $\mathcal{I}_2$ integrals instead of the $\mathcal{I}_1$ integrals, and **(2)** are lengthier, as each of the three terms in the expressions for $\mathcal{I}_5$ and $\mathcal{I}_6$ in (7.16) expands into three terms upon differentiating. In addition, the expressions for $\partial \mathcal{I}_5/\partial R_{0x}$ and $\partial \mathcal{I}_6/\partial R_{0y}$ each contain one additional term arising from chain-rule differentiation of the first terms in (7.16).

The upshot of this treatment is that the derivatives of the L-functions may be accommodated simply by enlarging the set of segment-segment integrals (7.15) we compute for each pair of line segments. We now turn to a consideration of the evaluation of these integrals.

7.2.5 Segment-Segment Integrals between Distant Segments

The treatment of segment-segment integrals breaks down along lines similar to those discussed in the case of panel-panel integrals in the previous chapter. The behavior of the integrand in (7.15) is governed by the kernels $\mathcal{K}_r(R)$; when the two line segments are relatively far apart, the integrand is a slowly varying function of u, u', and the integral may be evaluated by straightforward numerical cubature over the square $[0, 1] \times [0, 1]$. When the line segments are closer together, simple numerical cubature is inaccurate and we must resort to more sophisticated methods.

To quantify the notion of "relatively far apart," we define a relative distance function between line segments (in analogy to Equation (6.7) for triangular panels) to be the distance between the centers of the segments normalized by the length of the larger segment:

$$\text{RD}(\mathbf{S}_m, \mathbf{S}_n) = \frac{|\boldsymbol{\rho}_0 - \boldsymbol{\rho}_0'|}{\max(|\mathbf{S}_m|, |\mathbf{S}_n|)}. \tag{7.18}$$

For line segments of relative distance $RD > 10$, CASIMIR2D evaluates (7.15) using a seventh-order cubature rule (with 12 cubature points) over the square $\{u, u'\} = [0, 1] \times [0, 1]$. For less-distant pairs of line segments we must wheel out more heavily artillery, as discussed in the next section.

7.2.6 Segment-Segment Integrals between Nearby Segments: Desingularization

We evaluate segment-segment integrals between nearby segments using a desingularization technique similar to that introduced for panel-panel integrals in the previous

chapter. Availing ourselves of the known asymptotic behavior of the modified Bessel functions near the origin,[1] we define desingularized versions of the K_{0-2} functions in (7.15) according to

$$\mathcal{K}_0^{\text{DS}}(\alpha R) = K_0(\alpha R) + \log R + \left(\log \frac{\alpha}{2} + \gamma \right)$$

$$\mathcal{K}_1^{\text{DS}}(\alpha R) = \frac{1}{R} K_1(\alpha R) - \frac{1}{\alpha R^2} - \frac{\alpha}{2} \log R - \frac{\alpha}{2} \left(\log \frac{\alpha}{2} + \gamma - \frac{1}{2} \right)$$

$$\mathcal{K}_2^{\text{DS}}(\alpha R) = \frac{1}{R^2} K_2(\alpha R) - \frac{2}{\alpha^2 R^2} + \frac{1}{2R^2} + \frac{\alpha^2}{8} \log R + \frac{\alpha^2}{8} \left(\log \frac{\alpha}{2} + \gamma - \frac{3}{4} \right)$$

with Euler's constant $\gamma = 0.577216 \cdots$.

We now separate the integral (7.15) into non-singular and singular portions:

$$\mathcal{I}_r^{pq} = \mathcal{I}_r^{\text{DS},pq} + \mathcal{I}_r^{\text{S},pq}$$

where $\mathcal{I}_r^{\text{DS},pq}$ is just (7.15) with each kernel function replaced by its desingularized version, and where the singular contributions are given by

$$\mathcal{I}_0^{\text{S},pq} \equiv -ll' \left[\mathcal{J}_2^{pq} + \Gamma_1 \mathcal{J}_1^{pq} \right] \tag{7.19a}$$

$$\mathcal{I}_1^{\text{S},pq} \equiv ll'\alpha \left[\frac{1}{\alpha} \mathcal{J}_3^{pq} + \frac{\alpha}{2} \mathcal{J}_2^{pq} + \Gamma_2 \mathcal{J}_1^{pq} \right] \tag{7.19b}$$

$$\mathcal{I}_2^{\text{S},pq} \equiv ll'\alpha^2 \left[\frac{2}{\alpha^2} \mathcal{J}_4^{pq} - \frac{1}{2} \mathcal{J}_3^{pq} - \frac{\alpha^2}{8} \mathcal{J}_2^{pq} - \Gamma_3 \mathcal{J}_1^{pq} \right] \tag{7.19c}$$

with

$$\Gamma_1 = \log \frac{\alpha}{2} + \gamma, \qquad \Gamma_2 = \frac{\alpha}{2} \left(\Gamma_1 - \frac{1}{2} \right), \qquad \Gamma_3 = \frac{\alpha^2}{8} \left(\Gamma_1 - \frac{3}{4} \right),$$

and

$$\mathcal{J}_r^{pq} = \int_0^1 du \int_0^1 du' \, u^p u'^q S_r \left(R(u, u') \right), \tag{7.20}$$

$$\left\{ \begin{array}{c} S_1 \\ S_2 \\ S_3 \\ S_4 \end{array} \right\} (R) = \left(\begin{array}{c} 1 \\ \log R \\ 1/R^2 \\ 1/R^4 \end{array} \right).$$

We note that (7.19) depends on the frequency parameters ξ and q only through α, which enters (7.19) only as a multiplicative prefactor, while the $\mathcal{J}_r^{pq}$ quantities are *frequency-independent*. Thus these quantities need only be evaluated *once* for a given geometry, whereupon they may be reused as often as necessary to recompute BEM matrix elements at various values of ξ, q during the evaluation of the ξ, q integrals in (7.8).

A detailed discussion of techniques for evaluating the $\mathcal{J}_r^{pq}$ is presented in Appendix

---

[1] http://functions.wolfram.com/Bessel-TypeFunctions/BesselK/06/01/04/01/02/

F.

7.3 Miscellaneous Implementation Notes on CASIMIR2D

Almost all of the technical implementation notes discussed in Section 6.3 for CASIMIR3D carry over *mutatis mutandis* to CASIMIR2D. These include the computational advantages of simultaneously evaluating the Casimir quantities for multiple geometric transformations at each imaginary frequency point, as well as the use of LU-factorization (as computed by dense-direct linear algebra software) to evaluate determinants and solve linear systems. (In CASIMIR2D the matrices are *complex-valued*, not real-valued as in CASIMIR3D, but in practice this introduces no new complications beyond replacing calls to real-valued LAPACK routines with calls to their complex-valued counterparts.)

The only additional practical complication that arises in the case of CASIMIR2D is the need to evaluate integrals over the full upper-right quadrant of the (ξ, q) plane in equations (7.8), as compared to the single-dimensional quadrature over ξ required for CASIMIR3D. In CASIMIR2D we evaluate this integral using a simple two-dimensional generalization of equation (6.12): we put $\xi(t) = t/(1-t)$, $q(s) = s/(1-s)$, map the (ξ, q) integral into an integral over the square $\{s, t\} = [0,1] \times [0,1]$, and evaluate this integral using two-dimensional adaptive numerical cubature:

$$\int_0^\infty d\xi \int_0^\infty dq \, f(\xi, q) = \int_0^1 dt \int_0^1 ds \, f\Big(\xi(t), q(s)\Big) J(t, s)$$

$$\approx \sum w_n f\Big(\xi(t_n, s_n)\Big) J(t_n, s_n) \tag{7.21}$$

where $J(t, s) = 1/[(1-t)(1-s)]^2$ is the Jacobian of the transformation, and where the weights w_n and cubature points t_n, s_n are chosen *adaptively* by the adaptive cubature algorithm.

Chapter 8

FASTCASIMIR: An Accelerated Matrix-Vector Product for Casimir Operations

The FSC formulae (5.1) for Casimir energies, forces, and torques require the computation of linear-algebraic quantities (matrix determinants, matrix traces, and solutions of linear systems) involving matrices whose dimensions are proportional to the number of localized basis functions used to represent tangential currents on the surfaces of the interacting objects in a Casimir geometry.

For moderate-sized problems (involving matrices of dimensions $D \lesssim 10^4$), the FSC formulae may be evaluated using dense-direct methods of linear algebra, with memory scaling like $O(D^2)$ and CPU time scaling like $O(D^3)$. However, for larger problems this complexity scaling is unacceptable, and we must instead pursue *fast solvers*—techniques that exploit the known structure of the problem to reduce the complexity scaling to more tractable levels.

This chapter takes a first step toward the development of a fast Casimir solver by presenting a key ingredient in the development of such a solver: an *accelerated matrix-vector-product routine* for the EFIE matrix $\mathbf{M}(\xi)$ that enters into the FSC formulae (5.1) for Casimir energies, forces, and torques between perfectly conducting bodies.

Our approach is based on the *precorrected-fast-Fourier-transform* (PFFT) approach to matrix sparsification [36, 12]. This technique was invented in the 1990s to reduce the complexity scaling of linear-algebraic operations in computational electromagnetism problems; the idea is to exploit certain aspects of the known structure of the problem to improve the scaling of both the storage and the CPU time needed for a matrix-vector product from $O(N^2)$ to $O(N \log N)$. The PFFT technique has previously been applied to *real-frequency* scattering problems discretized with RWG basis functions, first in Ref. [12] and subsequently by a number of authors (see Ref. [28] for a review).

In this chapter we apply the PFFT method to the solution of *imaginary-frequency* scattering problems. We describe a PFFT-accelerated numerical procedure for approximating the matrix-vector product $\mathbf{M}(\xi) \cdot \mathbf{X}$, where $\mathbf{X}$ is an arbitrary numerical

vector and $\mathbf{M}(\xi)$ is the imaginary-frequency BEM matrix. (For simplicity, we consider here only the case of perfectly electrically conducting (PEC) bodies, so that $\mathbf{M}(\xi)$ is the EFIE matrix that enters into equation (4.5).) This represents a first step toward the development of a full "fast solver" (i.e. a solver with quasilinear scaling of storage and CPU time) for Casimir applications.

The remainder of this chapter is organized as follows. In Section 8.1 we discuss the basic ideas behind the PFFT technique for accelerating matrix-vector products with the EFIE matrix. In Section 8.2 we discuss an important subtlety that must be addressed in order for the PFFT-accelerated matrix-vector product to operate effectively. Finally, in Section 8.3 we discuss how our fast matrix-vector product routine might be used to accelerate practical Casimir computations.

What's New in this Chapter

As noted above, although the PFFT technique is not new, it is presented here for the first time in the context of the *imaginary-frequency* version of the boundary-element method. This changes the kernel that enters into the convolution and correction steps (discussed below) from an *oscillatory* kernel into a *decaying* kernel. (On the other hand, the projection and interpolation steps are not affected by the transition to imaginary frequency; our implementation of these steps is not essentially distinct from that of Ref. [12], and is discussed below only for the sake of completeness.)

The implementational subtlety discussed in Section 8.2 is not unique to the imaginary-frequency context, and would be relevant to a real-frequency PFFT implementation using RWG basis functions. However, to our knowledge this subtlety has not been previously addressed in print, and thus the discussion of Section 8.2 is, to the best of our knowledge, new.

8.1   A Precorrected-FFT-Based Procedure for Accelerating the Matrix-Vector Product

8.1.1   Overview

For a discretized geometry containing a total of N RWG basis functions, the computational cost of a *direct* calculation of the matrix-vector product $\mathbf{M} \cdot \mathbf{X}$ scales like N^2. We may think of this as the cost of separately computing N numbers (the inner products of the scattered field with N basis functions), each of which depends linearly on N numbers (the coefficients in the expansion (4.4)). To improve on this $O(N^2)$ scaling, we clearly need some method of computing our N numbers all at once.

Such a method is provided by the PFFT algorithm [36]. The basic steps in a PFFT evaluation of the product $\mathbf{M} \cdot \mathbf{X} = \mathbf{B}$ are sketched in Figure 1 and may be summarized as follows.

1. We begin by surrounding our scattering geometry by a regularly-spaced 3D grid (Figure 1a), containing a total of N_{G} grid points.
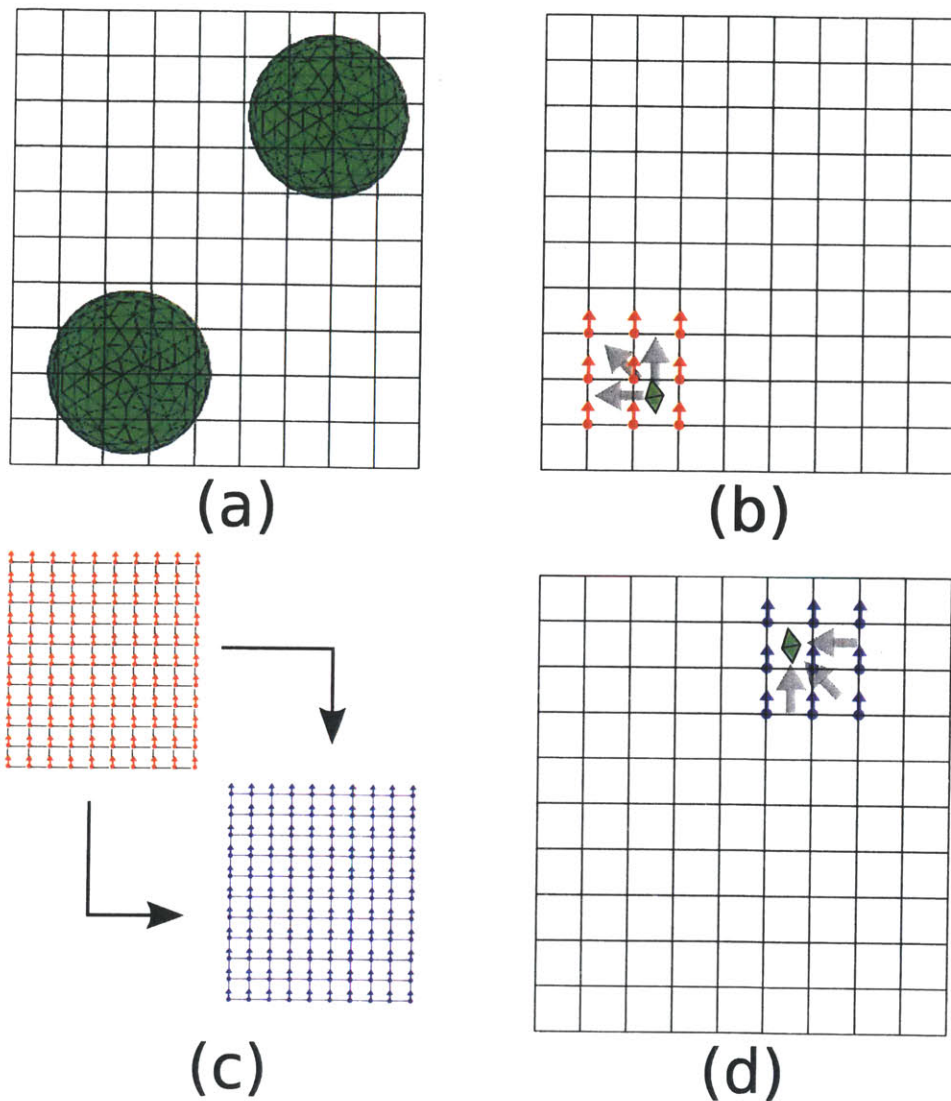
Figure 8-1: Figure 1: Schematic depiction of PFFT procedure for computing the matrix-vector product $\mathbf{M} \cdot \mathbf{X} = \mathbf{B}$. **(a)** The discretized scattering geometry is surrounded by a uniform 3D grid (for clarity, only a 2D cross section is shown in the figure). **(b)** *Projection*: For each RWG basis function $\mathbf{f}_\alpha$ in the discretized geometry, we identify a set of *equivalent point dipole sources* located on grid points near $\mathbf{f}_\alpha$ and chosen to reproduce the electric field of $\mathbf{f}_\alpha$ at distant points. Repeating this procedure for all basis functions, and weighting the resulting dipole sources by the entries of the $\mathbf{X}$ vector, yields a full grid of dipole sources. **(c)** *FFT convolution*: We perform an FFT-accelerated convolution operation to transform the full grid of dipole sources (shown here as red arrows) into a full grid of *electric field values* (shown as blue arrows). **(d)** *Interpolation*: We interpolate among the electric field values tabulated on the grid to construct an approximant to the electric field in the interstitial regions, and we evaluate the inner product of each basis function $\mathbf{f}_\beta$ with this interpolated field. This approximates the βth entry in the product vector $\mathbf{B}$. A subsequent correction step (not shown) improves the accuracy with which nearby panel-panel interactions are treated.

2. *Projection:* For each localized basis function $\mathbf{f}_\alpha$ in our discretized scattering geometry, we construct a set of *equivalent point current sources*, located on grid points near the support of $\mathbf{f}_\alpha$ and chosen to reproduce the electric field of $\mathbf{f}_\alpha$ at distant points (Figure 1b). Then, given the vector $\mathbf{X}$ of basis function weights, we superimpose the equivalent point current sources for all basis functions, weighted by the entries of $\mathbf{X}$, onto the grid, thus obtaining a full grid of point current sources.

3. *FFT Convolution:* We use fast-Fourier-transform (FFT) convolution techniques to transform the full grid of *point current sources* into a full grid of *electric field values* (Figure 1c) with computational complexity scaling like $O(N_\mathrm{G} \log N_\mathrm{G})$. After this operation, we have the value of the scattered field, due to the full grid of point sources, at each grid point.

4. *Interpolation:* In the interstitial regions between grid points, we construct an approximant $\mathbf{E}^{\mathrm{scat}}_{\mathrm{approx}}(\mathbf{x})$ to the scattered field by interpolating among the exact known values on the grid points. Using this approximate representation of the scattered field, we estimate the inner product of the scattered field with each basis function, $< \mathbf{f}_\alpha, \mathbf{E}^{\mathrm{scat}}_{\mathrm{approx}} >$; this approximately calculates the entry B_α in the output vector $\mathbf{B}$.

5. *Correction:* The procedure described so far accurately approximates the contributions to B_α from basis functions located far from $\mathbf{f}_\alpha$, but inaccurately represents the contributions of nearby basis functions (including the contribution of $\mathbf{f}_\alpha$ itself). For this reason we must *correct* the $\mathbf{B}$ vector to replace the (inaccurate) grid-approximate treatment of the interactions of nearby basis functions with a more accurate treatment.

Each of these steps will be discussed further in the following sections.

8.1.2 Projection

The projection step is illustrated in Figure 1(b). We seek to "project" a single RWG basis function $\mathbf{f}_\alpha$ onto a set of grid points $\{\mathbf{x}_\mathbf{n}\}$, where by "project" we mean "identify a set of point current sources at the points $\{\mathbf{x}_\mathbf{n}\}$ whose aggregate $\mathbf{E}$–field at distant points reproduces the $\mathbf{E}$-field due to $\mathbf{f}_\alpha$." (Here $\mathbf{n} = (n_x, n_y, n_z)$ is a compound subscript indexing points in the grid).

In our case we choose the $\mathbf{x}_\mathbf{n}$ to be a $3{\times}3{\times}3$ cube of points centered at the grid point closest to the centroid of $\mathbf{f}_\alpha$ (we refer to this cube of points as the "projection stencil" for $\mathbf{f}_\alpha$, and the number of points it contains is $N_\mathrm{PI} = 27$ in our case). For each cartesian direction $i \in \{x, y, z\}$ we fix the magnitudes of the i-directed point sources on the projection stencil by requiring that the lowest-order multipole moments of the source distribution represented by these point sources match the multipole moments of the source distribution represented by the i-component of basis function $\mathbf{f}_\alpha$.

More specifically, let $P_{\alpha i \mathbf{n}}$ be the strength of the i-directed point source at grid point $\mathbf{x}_\mathbf{n}$ in the projection of the i-component of basis function $\mathbf{f}_\alpha$. Then, for each

element in a set $\{\phi_m(\mathbf{x})\}$ of multipole functions, we require

$$\sum_{\mathbf{n}} P_{\alpha i \mathbf{n}} \phi_m(\mathbf{x_n} - \mathbf{x}_0) = \int_{\sup \mathbf{f}_\alpha} f_{\alpha i}(\mathbf{x}) \phi_m(\mathbf{x} - \mathbf{x}_0) \, d\mathbf{x} \qquad \left(\forall m\right) \qquad (8.1)$$

where the sum on the left-hand side ranges over all N_{PI} points in the projection stencil, $\mathbf{x}_0$ is the center about which we match multipole moments, and the multipole functions are

$$\{\phi_m(\mathbf{x})\} = \{1, x, y, z, x^2, xy, xz, y^2 \cdots\}.$$

If the number $N_{\mathrm{multipole}}$ of multipole functions is equal to N_{PI}, we thus obtain an $N_{\mathrm{PI}} \times N_{\mathrm{PI}}$ linear system for the $P_{\alpha i \mathbf{n}}$ coefficients, while if $N_{\mathrm{multipole}} \neq N_{\mathrm{PI}}$ we have a non-square system which we solve in a least-squares sense using singular-value decomposition (SVD) techniques.

The computation of the $P_{\alpha i \mathbf{n}}$ coefficients need only be performed once for a given scattering geometry and grid. Then, given the weights $\{K_\alpha\}$ of an expansion of some current distribution $\mathbf{K}(\mathbf{x})$ in RWG basis functions, $\mathbf{K}(\mathbf{x}) = \sum K_\alpha \mathbf{f}_\alpha(\mathbf{x})$, we obtain a full grid of equivalent point sources by accumulating the contributions of each basis function at each grid point—that is, we set the magnitude of the i-directed source at grid point $\mathbf{x}_n$ equal to

$$S_{i\mathbf{n}} = \sum_{\alpha} P_{\alpha i \mathbf{n}} \mathbf{K}_\alpha \qquad (8.2)$$

If we think of the quantities $S_{i\mathbf{n}}$, the magnitudes of the $i-$directed equivalent point sources at all grid points, as the components of an N_{G}-component vector $\mathbf{S}_i$, then equation (8.2) takes the form of a matrix-vector product for each cartesian component i,

$$\mathbf{S}_i = \mathbf{P}_i \cdot \mathbf{K} \qquad (8.3)$$

where, for each i, $\mathbf{P}_i$ is an $N_{\mathrm{G}} \times N$ matrix. Crucial to the performance of our algorithm is the fact that this matrix is *sparse*—indeed, each coefficient K_α in the $\mathbf{K}$ vector contributes to precisely N_{PI} elements of the $\mathbf{S}_i$ vector, so the storage required for $\mathbf{P}_i$, and the CPU time required to perform the matrix-vector product (8.3), are proportional to $N_{\mathrm{PI}}N$, i.e. $\mathcal{O}(N)$.

8.1.3 FFT Convolution

At this point we have point dipole sources at each of the points in our grid, and we would like to compute the electric field due to these point sources. The standard expression for the $\mathbf{E}$-field due to an electric current distribution is

$$\mathbf{E}(\mathbf{x}) = \int \mathbf{\Gamma}^{\mathrm{EE}}(\xi; \mathbf{x}, \mathbf{x}') \cdot \mathbf{J}(\mathbf{x}') d\mathbf{x}'$$

where the dyadic Green's function, defined in Appendix A, may be thought of as a sum of two terms:

$$\mathbf{\Gamma}(\xi; \mathbf{x}, \mathbf{x}') = \mathbf{\Gamma}^{(1)}(\xi; \mathbf{x} - \mathbf{x}') + \mathbf{\Gamma}^{(2)}(\xi; \mathbf{x} - \mathbf{x}') \tag{8.4}$$

$$\Gamma_{ij}^{(1)}(\xi; \mathbf{x} - \mathbf{x}') = -\kappa Z_0 \frac{e^{-\kappa|\mathbf{x}-\mathbf{x}'|}}{4\pi|\mathbf{x} - \mathbf{x}'|} \delta_{ij} \tag{8.5}$$

$$\Gamma_{ij}^{(2)}(\xi; \mathbf{x} - \mathbf{x}') = \frac{Z_0}{\kappa} \partial_i \partial_j \frac{e^{-\kappa|\mathbf{x}-\mathbf{x}'|}}{4\pi|\mathbf{x} - \mathbf{x}'|}. \tag{8.6}$$

(Here $\kappa \equiv \xi/c$; because $\mathbf{\Gamma}^{\mathrm{EE}}$ is the only dyadic Green's function that will appear in this chapter, we abbreviate it to $\mathbf{\Gamma}$ for convenience).

In our case, we seek to evaluate the $\mathbf{E}$ field due to the grid of point sources,

$$J_i(\mathbf{x}) = \sum_{\mathbf{n}} S_{i\mathbf{n}} \delta(\mathbf{x} - \mathbf{x_n}).$$

We will use the symbol $F_{i\mathbf{n}}$ to denote the ith cartesian components of this field at $\mathbf{x_n}$. We then find

$$F_{i\mathbf{n}} \equiv E_i(\mathbf{x_n}) = \sum_{\mathbf{n'}} \Gamma_{ij}(\mathbf{x_n} - \mathbf{x_{n'}}) S_{j\mathbf{n'}}. \tag{8.7}$$

A naïve evaluation of this sum for each of the N_{G} elements requires $O(N_{\mathrm{G}}^2)$ operations. To do better, we introduce the discrete Fourier transforms (DFTs) of the Γ and S quantities:

$$\Gamma_{ij\mathbf{k}}(\mathbf{x}) \equiv \sum_{\mathbf{n}} \Gamma_{ij}(\mathbf{x}) e^{-i\mathbf{k}\cdot\mathbf{x_n}}, \qquad S_{j\mathbf{k}} \equiv \sum_{\mathbf{n}} S_j(\mathbf{x}) e^{-i\mathbf{k}\cdot\mathbf{x_n}}$$

where the sum runs over all points in the grid. Then equation (8.7) reads

$$F_{i\mathbf{n}} = \sum_{\mathbf{n'}} \left\{ \sum_{\mathbf{k}} \Gamma_{ij\mathbf{k}} e^{i\mathbf{k}\cdot(\mathbf{x_n}-\mathbf{x_{n'}})} \right\} \left\{ \sum_{\mathbf{k'}} S_{j\mathbf{k'}} e^{i\mathbf{k'}\cdot\mathbf{x_{n'}}} \right\}$$

Rearrange:

$$= \sum_{\mathbf{k}} \sum_{\mathbf{k'}} \Gamma_{ij\mathbf{k}} S_{j\mathbf{k'}} e^{i\mathbf{k_n}} \times \underbrace{\sum_{\mathbf{n'}} e^{i(\mathbf{k'}-\mathbf{k})\cdot\mathbf{x_{n'}}}}_{=N_{\mathrm{G}}\delta_{\mathbf{k},\mathbf{k'}}}$$

$$= N_{\mathrm{G}} \sum_{\mathbf{k}} \left\{ \Gamma_{ij\mathbf{k}} S_{j\mathbf{k}} \right\} e^{i\mathbf{k_n}}.$$

Thus $F_{i\mathbf{n}}$ is just the *inverse* DFT of a quantity whose Fourier component at $\mathbf{k}$ is the product of the Fourier components of Γ_{ij} and S_j at $\mathbf{k}$.

This then suggests the following algorithm for computing the numbers $F_{i\mathbf{n}}$.

(0) Compute and store the forward DFTs of the Γ_{ij} kernels. (This step depends only

on the grid and the frequency, and hence the kernel DFTs may be computed once and stored, then reused multiple times to compute multiple matrix-vector products.)

(1) Compute the forward DFTs of the $S_{i\mathbf{n}}$ vectors.

(2) Compute the momentum-space products $\mathbf{\Gamma}_{ij\mathbf{k}} \cdot \mathbf{S}_{j\mathbf{k}}$ for each index pair ij and each momentum vector $\mathbf{k}$.

(3) Compute the *inverse* DFTs of the momentum-space products.

This procedure yields the full set of quantities $\{F_{i\mathbf{n}}\}$ with asymptotic CPU time scaling like $O(N_G \log N_G)$ (the time required to evaluate forward and backward DFTs using fast Fourier transform techniques). Formally, we write

$$\mathbf{F}_i = \tilde{\mathbf{\Gamma}}_{ij} \cdot \mathbf{S}_j \qquad (8.8)$$

where $\tilde{\mathbf{\Gamma}}_{ij}$ is an implicitly defined $N_G \times N_G$ matrix whose operation on a vector of length N_G requires CPU time scaling like $O(N_G \log N_G)$.

8.1.4 Interpolation

The interpolation step is illustrated in Figure 1(c). In the interstitial regions between grid points, we interpolate among the values of the electric field at the grid points to construct an approximant $\mathbf{E}^{\text{scat}}_{\text{approx}}$ to the scattered field; the inner product of $\mathbf{E}^{\text{scat}}_{\text{approx}}$ with basis function $\mathbf{f}_\alpha$ approximates B_α, the αth entry in the output vector $\mathbf{B}$.

More specifically, let us write the ith cartesian component of $\mathbf{E}^{\text{scat}}_{\text{approx}}$ as an expansion in the same multipole functions ϕ_m used in the projection step, centered at the origin $\mathbf{x}_0$ about which we computed multipole moments for basis function $\mathbf{f}_\alpha$:

$$E^{\text{scat}}_{\text{approx},i}(\mathbf{x}) = \sum_m D_{im}\phi_m(\mathbf{x} - \mathbf{x}_0). \qquad (8.9)$$

We fix the values of the D coefficients by requiring that $\mathbf{E}^{\text{scat}}_{\text{approx},i}$ match the known values of the electric field on all grid points in the projection stencil for $\mathbf{f}_\alpha$:

$$\sum_m D_{im}\phi_m(\mathbf{x_n} - \mathbf{x}_0) = F_{i\mathbf{n}} \qquad \left(\forall \mathbf{n} \in \text{projection stencil for } \mathbf{f}_\alpha\right) \qquad (8.10)$$

The inner product of $\mathbf{f}_\alpha$ with $\mathbf{E}^{\text{scat}}_{\text{approx}}$ is now

$$B^{\text{approx}}_\alpha = \left\langle \mathbf{f}_\alpha, \mathbf{E}^{\text{scat}}_{\text{approx}} \right\rangle = \sum_i \int_{\text{sup}\,\mathbf{f}_\alpha} f_{\alpha i}(\mathbf{x}) E^{\text{scat}}_{\text{approx},i}(\mathbf{x})\, d\mathbf{x}$$

Insert (8.9):

$$= \sum_i \sum_m D_{im} \int_{\mathrm{sup}\,\mathbf{f}_\alpha} f_{\alpha i}(\mathbf{x}) \phi_m(\mathbf{x} - \mathbf{x}_0)\, d\mathbf{x}.$$

Insert (8.1):

$$= \sum_i \sum_m D_{im} \sum_\mathbf{n} C_{i\alpha\mathbf{n}} \phi_m(\mathbf{x}_m - \mathbf{x}_0)$$

Finally, insert (8.10):

$$= \sum_i \sum_\mathbf{n} C_{i\alpha\mathbf{n}} F_{i\mathbf{n}}.$$

Thus the interpolation step uses the same coefficients as the projection step; the projection and interpolation operations are mutually adjoint. Using the matrix-vector product notation of equation (8.3), we can write the preceding equation in the form

$$\mathbf{B}^{\mathrm{approx}} = \sum_i \mathbf{P}_i^{\mathrm{T}} \cdot \mathbf{F}_i. \qquad (8.11)$$

As in the projection step, the sparsity of the matrix $\mathbf{P}_i$ ensures that the storage and CPU time required for this operation are $\mathcal{O}(N)$.

8.1.5 Correction

Summarizing the content of the previous three sections, we may aggregate equations (8.3), (8.8), and (8.11) to obtain a formal expression for the grid approximation to the matrix-vector product:

$$\mathbf{B}^{\mathrm{approx}} = \left[\mathbf{P}^{\mathrm{T}} \cdot \tilde{\mathbf{\Gamma}} \cdot \mathbf{P} \right] \cdot \mathbf{K} \qquad (8.12)$$

(where for simplicity we are employing a shorthand in which some notational details are omitted).

Consider the quantity $B_\alpha^{\mathrm{approx}}$, the αth component of the approximate product vector $\mathbf{B}^{\mathrm{approx}}$. This number is a sum of contributions from all basis functions in our geometry. The computational procedure summarized by equation (8.12) does a decent job of approximating the contributions of basis functions $\mathbf{f}_\beta$ that are relatively far away from $\mathbf{f}_\alpha$ (because the grid approximation to the field of $\mathbf{f}_\beta$ is more accurate as we get further away from $\mathbf{f}_\beta$), but a poor job of representing the contributions from basis functions *nearby* $\mathbf{f}_\alpha$ (including, of course, the contribution of $\mathbf{f}_\alpha$ itself).

To improve the accuracy with which we account for the contribution of $\mathbf{f}_\beta$ to B_α, we will *correct* equation (8.12) by subtracting the grid-approximate contribution of

$\mathbf{f}_\beta$ and instead adding in the exact contribution:

$$\mathbf{B}_\alpha^{\text{approx,corrected}} = \mathbf{B}_\alpha^{\text{approx}} - \sum_\beta \left\{ \left[\mathbf{P}^{\text{T}} \cdot \tilde{\mathbf{\Gamma}} \cdot \mathbf{P}\right]_{\alpha\beta} - \mathbf{M}_{\alpha\beta} \right\} K_\beta$$

$$= \mathbf{B}_\alpha^{\text{approx}} - \sum_\beta C_{\alpha\beta} K_\beta \tag{8.13}$$

where the sum is over all basis functions $\mathbf{f}_\beta$ that are nearby $\mathbf{f}_\alpha$, and where the elements of the *correction matrix* are

$$C_{\alpha\beta} = \begin{cases} \left[\mathbf{P}^{\text{T}} \cdot \tilde{\mathbf{\Gamma}} \cdot \mathbf{P}\right]_{\alpha\beta} - \mathbf{M}_{\alpha\beta} & \text{if } \mathbf{f}_\alpha \text{ is nearby } \mathbf{f}_\beta \\ \\ 0, & \text{otherwise.} \end{cases}$$

This matrix is *sparse*, with the number of nonzero entries per row bounded above by a constant N^{nearby} (the maximum number of basis functions that lie nearby any other basis function), and hence may be stored and applied to a vector with memory and CPU time proportional to $N^{\text{nearby}} \cdot N$, i.e. $\mathcal{O}(N)$. (The threshold separation distance beneath which two basis functions may be considered "nearby" one another is an implementation parameter that may be adjusted upward for greater accuracy at the cost of greater memory and CPU time requirements.)

The computation of the exact matrix elements $\mathbf{M}_{\alpha\beta}$ is straightforward and may be done efficiently using the techniques described in Chapter 6. On the other hand, the computation of the $\alpha\beta$ matrix element of the $\mathbf{P}^{\text{T}}\mathbf{\Gamma}\mathbf{P}$ matrix involves summations over the elements in the projection stencils of $\mathbf{f}_\alpha$ and $\mathbf{f}_\beta$ together with a real-space convolution operation of the form 8.7 (but carried out over a reduced portion of the grid). Although this calculation is expensive, it need only be done once for a given geometry and frequency, after which the correction matrix may be stored and reused to compute any desired number of approximate matrix-vector products.

8.1.6   Summary

Summarizing the above sections, our final formal expression for the PFFT-accelerated approximation to the matrix-vector product $\mathbf{B} = \mathbf{M} \cdot \mathbf{K}$ is

$$\mathbf{B}^{\text{approx,corrected}} = \left\{ \mathbf{P}^{\text{T}} \cdot \tilde{\mathbf{\Gamma}} \cdot \mathbf{P} - \mathbf{C} \right\} \cdot \mathbf{K}. \tag{8.14}$$

As discussed above, the storage and CPU time required by the $\mathbf{P}$ and $\mathbf{C}$ matrices are $\mathcal{O}(N)$, while those for $\tilde{\mathbf{\Gamma}}$ are $\mathcal{O}(N_{\text{G}} \log N_{\text{G}})$.
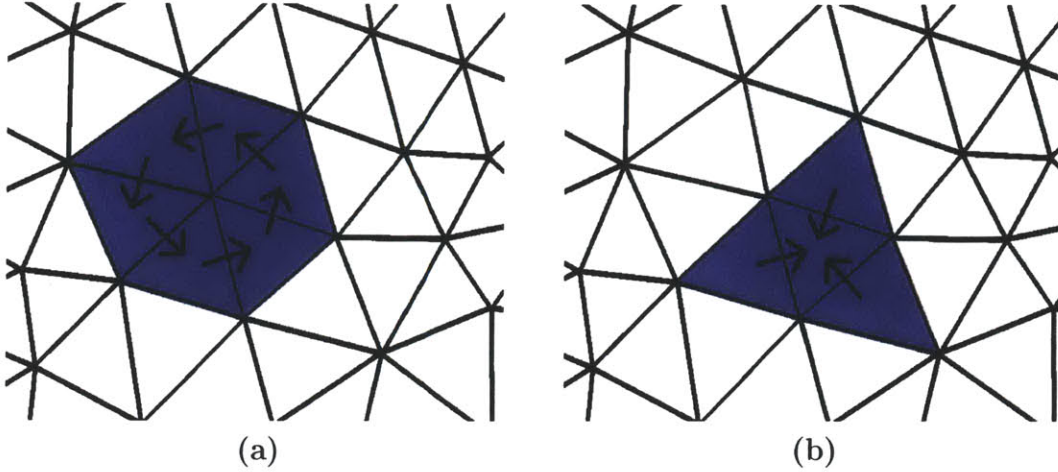
Figure 8-2: Reorganization of RWG basis functions into loop and star basis functions. **(a)** To each internal vertex in our mesh discretization, we assign a "loop" function, obtained as a linear combination of the RWG functions on the panels touching the vertex. **(b)** To each panel in our mesh discretization we assign a "star" function, obtained as a linear combination of the four RWG functions that are nonvanishing on that panel.

8.2 An Important Subtlety

A naïve implementation of the matrix-vector product scheme described above will lead to systematic errors that impede the convergence of iterative solvers. In this section we illustrate the nature of the difficulty and discuss a technique for avoiding it.

8.2.1 Loop-Star Decomposition of the RWG Basis Function Expansion

The easiest way to understand the nature of the difficulty is to recall that our expansion of the surface current in terms of RWG basis functions,

$$\mathbf{K}(\mathbf{x}) = \sum K_\alpha \mathbf{f}_\alpha(\mathbf{x}), \qquad (8.15)$$

can alternatively be written as an expansion in the so-called "loop" and "star" basis functions,

$$\mathbf{K}(\mathbf{x}) = \sum_{m=1}^{N_\mathrm{L}} K_m^\mathrm{L} \mathbf{L}_m(\mathbf{x}) + \sum_{m=1}^{N_\mathrm{S}} K_m^\mathrm{S} \mathbf{S}_m(\mathbf{x}) \qquad (8.16)$$

where the loop and star functions $\mathbf{L}_m(\mathbf{x})$ and $\mathbf{S}_m(\mathbf{x})$ are linear combinations of the $\mathbf{f}_\alpha$, as illustrated in Figure 8-2.

As is well known, any well-behaved vector field $\mathbf{K}(\mathbf{x})$ may be decomposed as a

sum of divergence-free and curl-free terms, a procedure known as a *Helmholtz decomposition*. The loop-star expansion (8.16) represents what we might term a *partial* Helmholtz decomposition, because the first term (the "loop" contribution) is divergence-free, although the second term (the "star" contribution) has both non-vanishing divergence and curl. Indeed, as indicated in Figure 2(a), each panel in the support of the loop function is the "positive" panel (in the sense of Chapter 6) associated with one of the RWG functions in the loop, and the "negative" panel of another function in the loop, whereupon the total scalar charge density described by the loop function thus vanishes *identically* on that panel, i.e. $\nabla \cdot \mathbf{L}_m \doteq 0$ for all loop functions $\mathbf{L}_m$.

8.2.2 Erroneous Propagation of Divergenceless Sources

Using the loop-star expansion, we can now understand the origin of the small errors in the PFFT matrix-vector product.

We first observe that the second term in (8.4) (the "electrostatic" term in the dyadic Green's function), when convolved with a divergenceless current source, yields an identically vanishing field:

$$E_i^{(2)}(\mathbf{x}) = \int \Gamma_{ij}^{(2)}(\xi; \mathbf{x} - \mathbf{x}') J_j(\mathbf{x}') d\mathbf{x}'$$

$$= \int \left[\partial_i \partial_j \Phi(|\mathbf{x} - \mathbf{x}'|) \right] \left[J_j(\mathbf{x}') \right] d\mathbf{x}'$$

(where $\Phi(r) \sim e^{-\kappa r}/r$). Now integrate by parts:

$$= \int \left[\partial_i \Phi(|\mathbf{x} - \mathbf{x}'|) \right] \left[\underbrace{\partial_j J_j(\mathbf{x}')}_{=0} \right] d\mathbf{x}'$$

$$= 0$$

for divergenceless $\mathbf{J}$.

From this observation, and from the discussion of the previous subsection, it now follows that the portion of the scattered electric field obtained by convolving $\mathbf{\Gamma}^{(2)}$ with the first term in the expansion (8.16) should give rise to an identically vanishing $\mathbf{E}$ field, since, as noted above, the first term in (8.16) term is explicitly divergence-free. The difficulty is that *this property is not preserved by the grid-projection operation*, nor, indeed, could it possibly be: the only set of spatially dispersed *pointlike* current sources with everywhere vanishing divergence is a set in which all sources have exactly zero strength. Instead, the grid-projected approximate representation of our current distribution (8.15) will contain small inaccuracies, which in turn will translate into small inaccuracies in the grid representation of the propagated electric fields; these inaccuracies will contaminate the interactions of both nearby and distant basis functions, and thus are not mitigated by the correction step. Although the resulting error in any one evaluation of the approximate matrix-vector product (MVP)

107

will be small, a typical application of the procedure described here will involve the calculation of many hundreds or thousands of approximate MVPs, usually inside a loop in an iterative numerical procedure such as GMRES or the Arnoldi iteration, and the accumulation of small errors of the sort discussed here is enough to thwart the convergence of such iterative schemes.

8.2.3 Modified PFFT Technique

However, this diagnosis of the disease suggests an immediate cure. Since we know that the loop portion of our original surface current expansion is explicitly divergenceless, and thus that the $\Gamma^{(2)}$ term in the Green's function must propagate no field corresponding to these sources, we can simply *turn off* the contribution of $\Gamma^{(2)}$ to the implicit matrix Γ that enters into (8.14) (of course we must also zero out the contributions of $\Gamma^{(2)}$ to the corresponding portions of the correction matrix $\mathbf{C}$). Instead, when evaluating the contribution to the approximate product vector $\mathbf{B}^{\text{approx,corrected}}$ arising from the *loop* portion of the input vector $\mathbf{K}$, we carry out a modified version of the PFFT procedure in which only the first term in the Green's function (8.4) is retained. (When evaluating the contribution of the *star* portion, we must of course retain both terms in (8.4).) This simple fix eliminates the small but convergence-confounding errors and helps to ensure rapid convergence of iterative schemes based on the fast MVP.

8.3 Fast Casimir Computations with the Accelerated Matrix-Vector Product

In this chapter we have taken a first step toward a fast solver for Casimir problems by implementing a matrix-vector product (MVP) for the imaginary-frequency BEM matrix for PEC bodies. The question of how to *use* this fast MVP in an actual fast solver is reserved for future work; in this final section we briefly anticipate three possible approaches.

1. A first idea is to use the fast MVP in the context of a Lanczos or Arnoldi method to estimate the extremal eigenvalues of the BEM matrix, then use these estimate to approximate the determinants in the master FSC formula (5.1a).

   Such an approach would depend sensitively on the nature of the eigenvalue distributions of $\mathbf{M}$ and $\mathbf{M}_\infty$ in (5.1). *If* the logarithm of the ratio of determinants in (5.1a) is dominated by contributions from the extremal eigenvalues, then an iterative procedure for calculating the spectral extremes could lead to an efficient computational procedure.

   On the other hand, if the extremal eigenvalues of $\mathbf{M}$ and $\mathbf{M}_\infty$ are similar in magnitude, then these eigenvalues will make little contribution to the log-det ratio in (5.1a); in this case, our iterative eigenvalue calculator may need to burrow well in to the innards of the eigenvalue spectra, rendering an iterative procedure of dubious value.

2. A second approach would be to apply the fast MVP to the trace formulae in (5.1b-c), with the linear-system solves implicit in the definition of the inverse matrix $\mathbf{M}^{-1}$ carried out using an iterative solver such as GMRES. As discussed in Section 5.4, the equality of the partial traces ensures that we would never need to do more than D_1 solves (where D_1 is the dimension of the matrix subblock corresponding to the object on which we are computing the force or torque), and in practice the trace may turn out to be dominated by a subset of the diagonal matrix entries (which, offhand, we might anticipate would be those entries corresponding to basis functions lying closest to the other interacting objects in our Casimir geometry).

On the other hand, before we could solve the linear systems that enter into the trace formulae, we would need to assemble the RHS vectors, which in this case would be the first D_1 columns of the derivative matrices $\partial\mathbf{M}/\partial\mathbf{r}_i$ or $\partial\mathbf{M}/\partial\theta$. If we need only a small constant number of linear solves, the RHS vectors could be assembled directly with cost scaling like $\mathcal{O}(N)$ each; alternatively, a modification of the fast-solver technique discussed in this chapter could be used to obtain grid-ready representations of these vectors.

3. Finally, perhaps the most naïve application of the fast MVP would be to bypass the FSC formulae and instead evaluate the stress-tensor integral in (5.3) *numerically* (i.e. by numerical cubature)—with the integrand at each cubature point obtained by solving a numerical BEM problem, and with the linear BEM system solved approximately via GMRES (or similar) with the fast MVP. Coming from a dense-direct linear-algebra perspective (as is natural for the CASIMIR3D and CASIMIR2D implementations presented in Chapters 6 and 7), it is difficult to see how the large number of MVPs required for such a procedure could possibly render it competitive with the other two possible applications of the fast MVP proposed above, but in the absence of detailed comparisons for large problems we must keep an open mind.

Chapter 9

Results: New Predictions of Casimir Interactions in Experimentally Relevant Geometries and Materials

Chapter 5 discussed the theoretical underpinnings of the fluctuating-surface-current approach to computational Casimir physics, while Chapters 6, 7, and 8 discussed its practical numerical implementation. In this chapter we at last get down to the *fruits* of the FSC approach—new predictions of Casimir interactions in experimentally relevant geometries and materials that would be difficult, it not outright impossible, to treat with any other existing method.

Casimir energy of identical spheres, parallel capsules, and crossed capsules

Figure 9-1 shows plots of Casimir energy versus separation distance for three pairs of perfectly conducting objects: identical spheres of radius R, identical capsules with parallel axes, and identical capsules with perpendicular axes ("crossed capsules.") (A "capsule" is a cylinder of radius R with hemispherical endcaps, of total length $L = 6R$ in this case.) The energy curve for the crossed capsules interpolates between the curve for the spheres at short distances and the curve for the parallel capsules at large distances. We may understand this result as follows: At short distances, the interaction is dominated by contributions from the portions of the surfaces that lie in closest proximity to each other. For the crossed capsules, this region of nearest proximity is restricted to a length $\sim R$ around the centers of the capsules and hence exhibits the same scaling as the region of nearest proximity for the two spheres in the short-distance limit. In contrast, for parallel capsules, the strongly-interacting region extends down the entire length of the capsule and hence scales with an additional factor of L at short distances. At large distances, the interaction becomes pointlike and the energy of interaction between identical capsules becomes independent of the
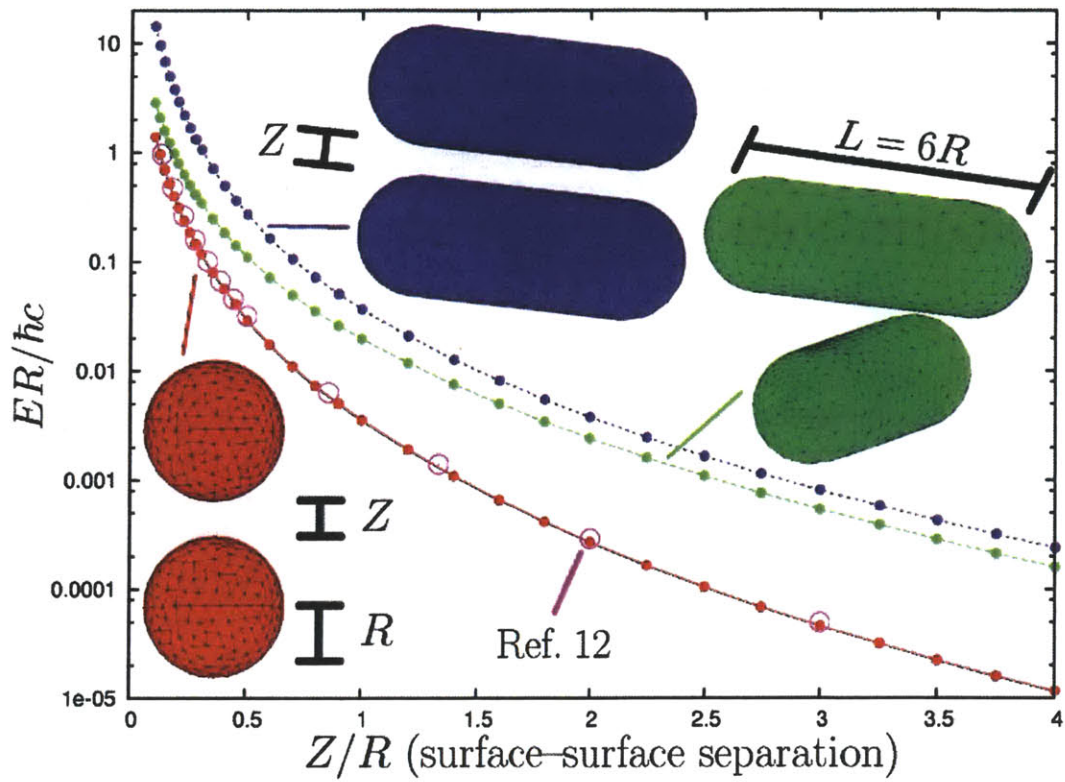
Figure 9-1: Casimir energy vs. separation distance for three pairs of perfectly conducting objects: identical spheres (red curve), identical capsules with parallel axes (blue curve), and identical capsules with perpendicular axes (green curve). The hollow circles represent the sphere-sphere data of Ref. [15].
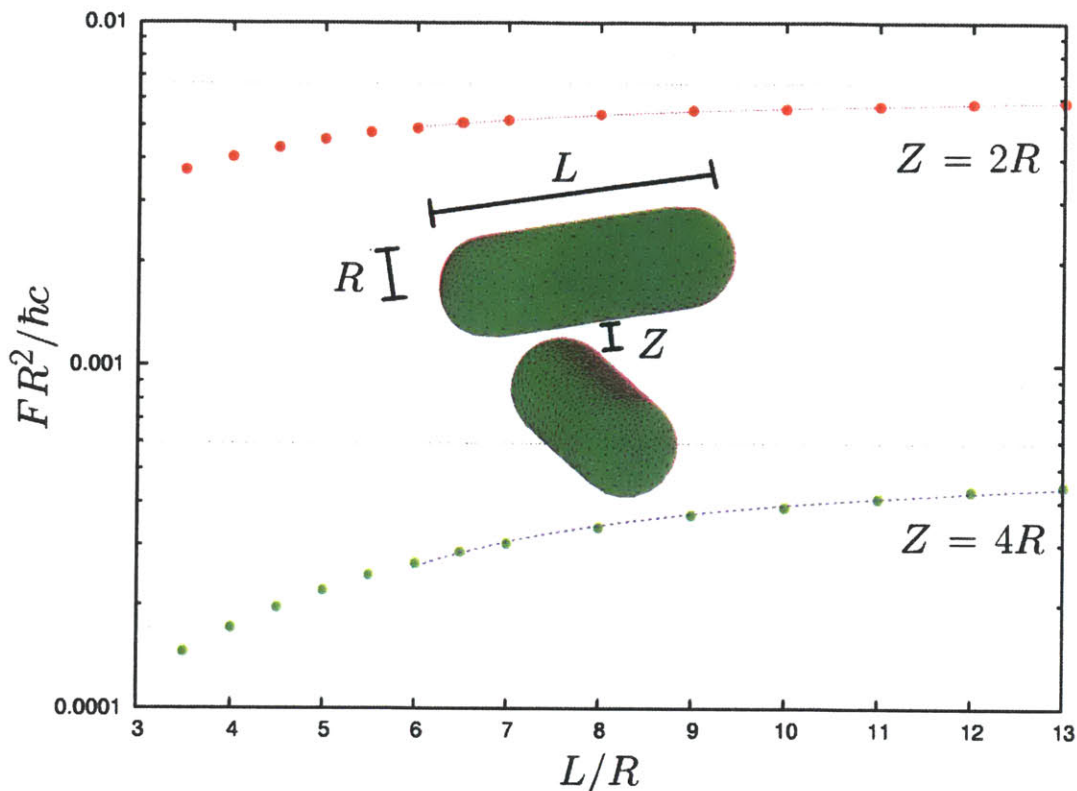
Figure 9-2: Magnitude of attractive Casimir force between crossed capsules of radius R as a function of capsule length, for surface–surface separations $Z = 2R$ and $Z = 4R$. The dashed lines denote the asymptotic ($L \to \infty$) limits of the force, as roughly extrapolated from our finite-L data. The solid lines are fits of the large-L data to the form $a + b/L$, although our data are insufficient to establish the precise asymptotic L-dependence of the force.

orientation.

Casimir Force vs. Length For Crossed Capsules.

The Casimir force between crossed cylinders, in the limit in which the length L of the cylinders is much longer than their surface–surface separation Z, is experimentally accessible [13] and interesting in its own right as a finite interaction between effectively infinite objects. Figure 3 plots the magnitude of the attractive Casimir force between crossed metallic capsules of radius R, at fixed surface–surface separations of $Z = 2R$ and $Z = 4R$, as a function of the capsule length L. In the limit $L \to \infty$ our capsules become infinite cylinders and the force approaches a Z-dependent constant (denoted by the dashed lines in the figure.)
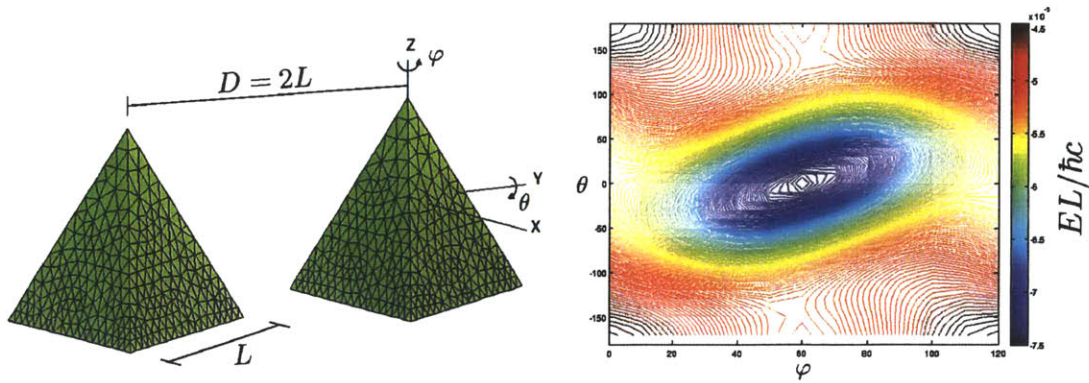
113

Figure 9-3: Contour plot of Casimir energy vs. orientation angles for tetrahedral nanoparticles separated by a distance $D = 2L$.

Tetrahedral nanoparticles

Several groups have succeeded in producing tetrahedral nanoparticles of dimensions ~ 10–50 nm [1, 21], and Casimir forces may dominate the interactions between electrostatically neutral particles of this type. Our method allows the first predictions of Casimir interactions between perfectly conducting tetrahedral particles. Figure 9-3 depicts a contour plot of Casimir energy vs. orientation angles for two perfectly conducting tetrahedra originally separated by a distance $D = 2L$ in the y direction, where L is the tetrahedron edge length. To one of the tetrahedra we apply a rotation through an angle φ about the z axis followed by a rotation through an angle θ about the y axis; the fixed origin of these rotations, depicted as the origin of the coordinate axes in Figure 9-3, is the point lying a distance $H/2$ below the apex of the tetrahedron, where $H = \sqrt{3}L/2$ is the height of the tetrahedron. The contour plot reveals a clear minimum at $(\theta, \phi)=(0,60°)$, corresponding to the closest approach of a vertex of the base of the rotated tetrahedron to the unrotated tetrahedron, as might be expected for an attractive interaction.

Attractive and repulsive Casimir forces between silicon and teflon spheres and cubes immersed in ethanol

Ref. [41], using the methods of Ref. [15], predicted Casimir forces between spheres and slabs composed of various materials and suspended in ethanol. Figure 9 uses the FSC technique to reproduce the results of Ref. [41] for the Casimir force between teflon and (undoped) silicon spheres, then extends these results by plotting Casimir forces between spheres and cubes of the same material properties (with the cubes sized to have the same volume as the corresponding spheres). For each geometry, we plot the ratio of the computed Casimir force to the force predicted by the perfect-metal proximity force approximation (PFA) for that geometry; since the PFA always predicts an attractive force, a positive (negative) ratio implies an attractive (repulsive) Casimir force. It is interesting that all four geometries exhibit a repulsive–attractive

114
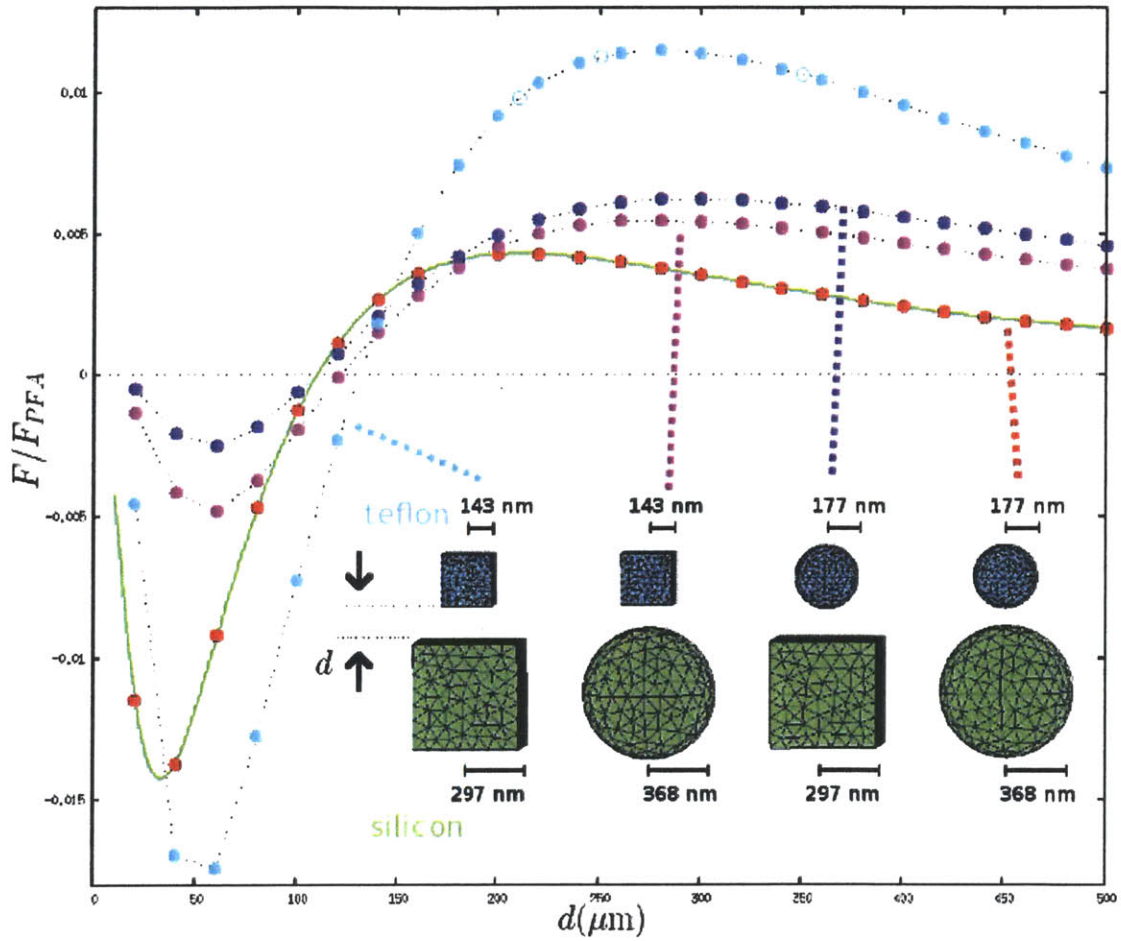
Figure 9-4: Casimir force between silicon and teflon spheres and cubes immersed in ethanol, normalized by the PFA predictions (see text). For the sphere-sphere case, the solid circles represent data computed using the methods described in this paper, while the thick solid line reproduces data from Ref. [41]. For the other three cases, the solid and hollow circles represent data computed using the methods described in this thesis, and the dotted lines are a guide to the eye.

force crossover at approximately the same surface–surface separation distance.

Finite-size effects in nanoparticle diclusters

Ref. [41] predicted Casimir forces between dielectric slabs, of infinite cross-sectional-area, embedded in ethanol. It is interesting to ask how these predictions are modified for *finite* slabs (discs). Figure 9 plots the PFA-normalized Casimir force between pairs of puck-shaped nanoparticles, one composed of polystyrene and the other of doped silicon, immersed in ethanol. For comparison, the dotted curves indicate the (PFA-normalized) force between pairs of infinite slabs of the same materials. For small values of the surface–surface separation d, the normalized puck-puck force tends to the slab-slab limit, but finite-size effects cause the curves to deviate beyond separations of $d \sim R/2$ (with R the puck radius).

Rotational stability of dielectric nanoparticles

For the nanoparticle pair corresponding to the intermediate curve in Figure 9 (dopant density of $1.4 \cdot 10^{19}$ cm $^{-3}$ for the silicon nanoparticle), we now fix the centroids of the nanoparticles and plot the Casimir energy (Figure 9-6) as a function of rotation angles (see the inset of Figure 9-6) for two centroid–centroid separation distances S of 700 and 500 nm. The slight shift in the value of S changes the stable equilibrium (right).

Casimir Forces between Quasi-2D Silicon Beams

Modern lithographic and etching techniques allow the fabrication of high-aspect-ratio structures, such as the coupled silicon waveguides suspended over a substrate reported in Ref. [29], in which elongated beams of constant cross-section are kept within transverse separations of a few hundred nanometers over a length of several microns or longer. The cross-sectional profile of the waveguides in such an experiment may exhibit irregular non-rectangular shapes, for which purpose a general-purpose geometric tool such as CASIMIR2D is ideal for predicting Casimir interactions. As just one example, Figure 9-7 plots the Casimir force per unit length, as predicted by CASIMIR2D, for a discretized version of a hypothetical structure consisting of two silicon waveguides suspended over a silicon substrate.

116
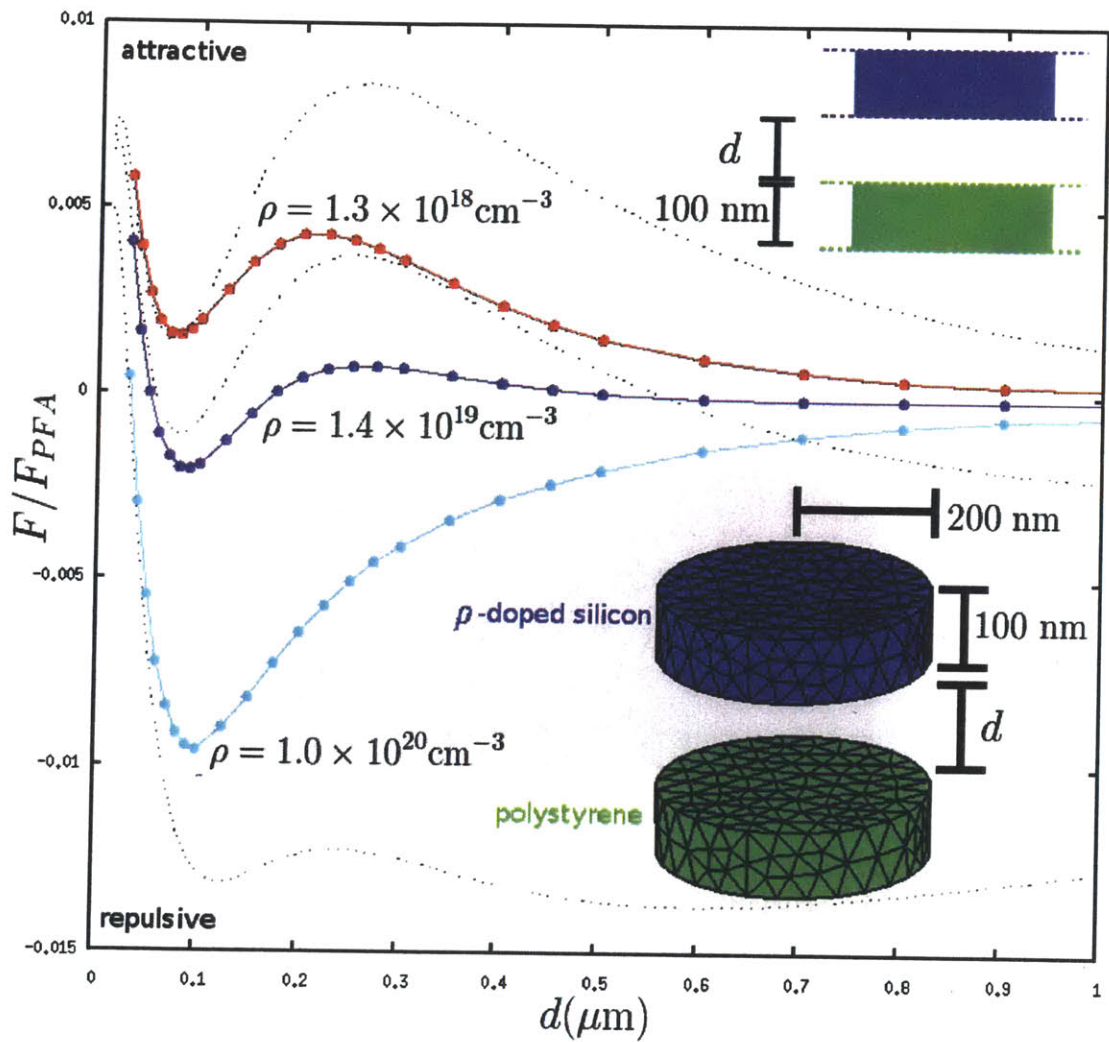
Figure 9-5: Casimir force between puck-shaped polystyrene and doped-silicon nanoparticles immersed in ethanol. The dotted curves indicate the force on *slabs* of the same materials and thickness but infinite cross-sectional area [41].
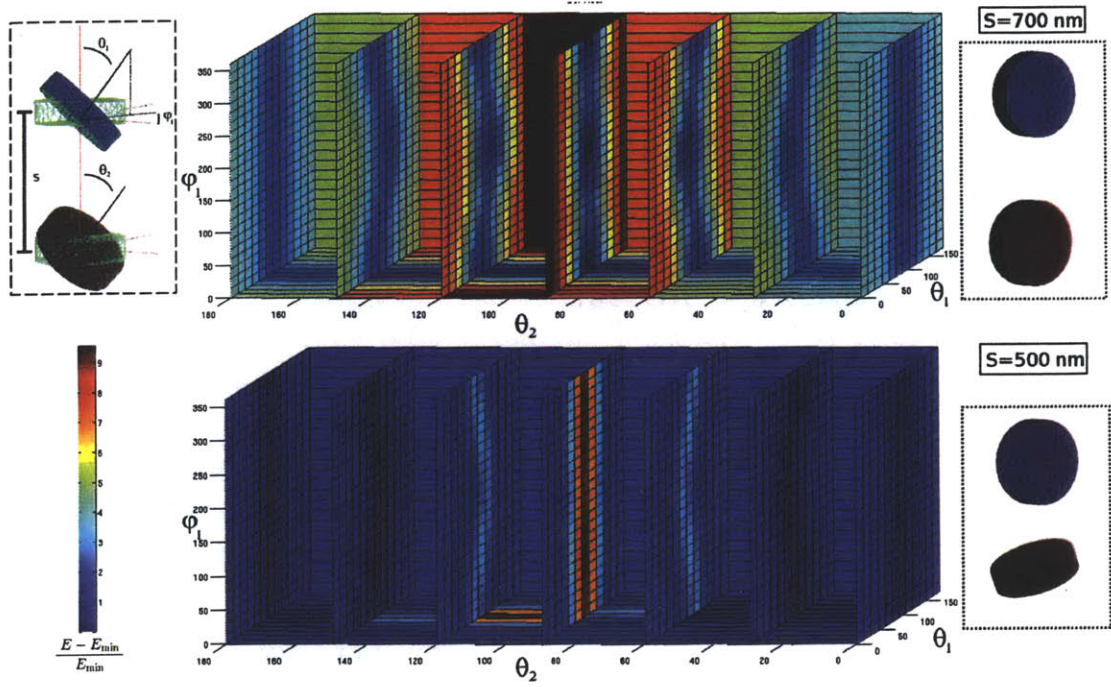
Figure 9-6: Rotational stability of hockey-puck shaped nanoparticles suspended in ethanol. One nanoparticle is composed of polystyrene, and the other of silicon with a dopant concentration of $1.4 \cdot 10^{19}$ cm^{-3} (corresponding to the middle curve in the previous plot). We fix the centers of the particles at center–center separations of $S = \{500, 700\}$ nm allow them to rotate about their centers. The minimum-energy configurations are depicted in the insets at right. (All angles are measured in degrees.)
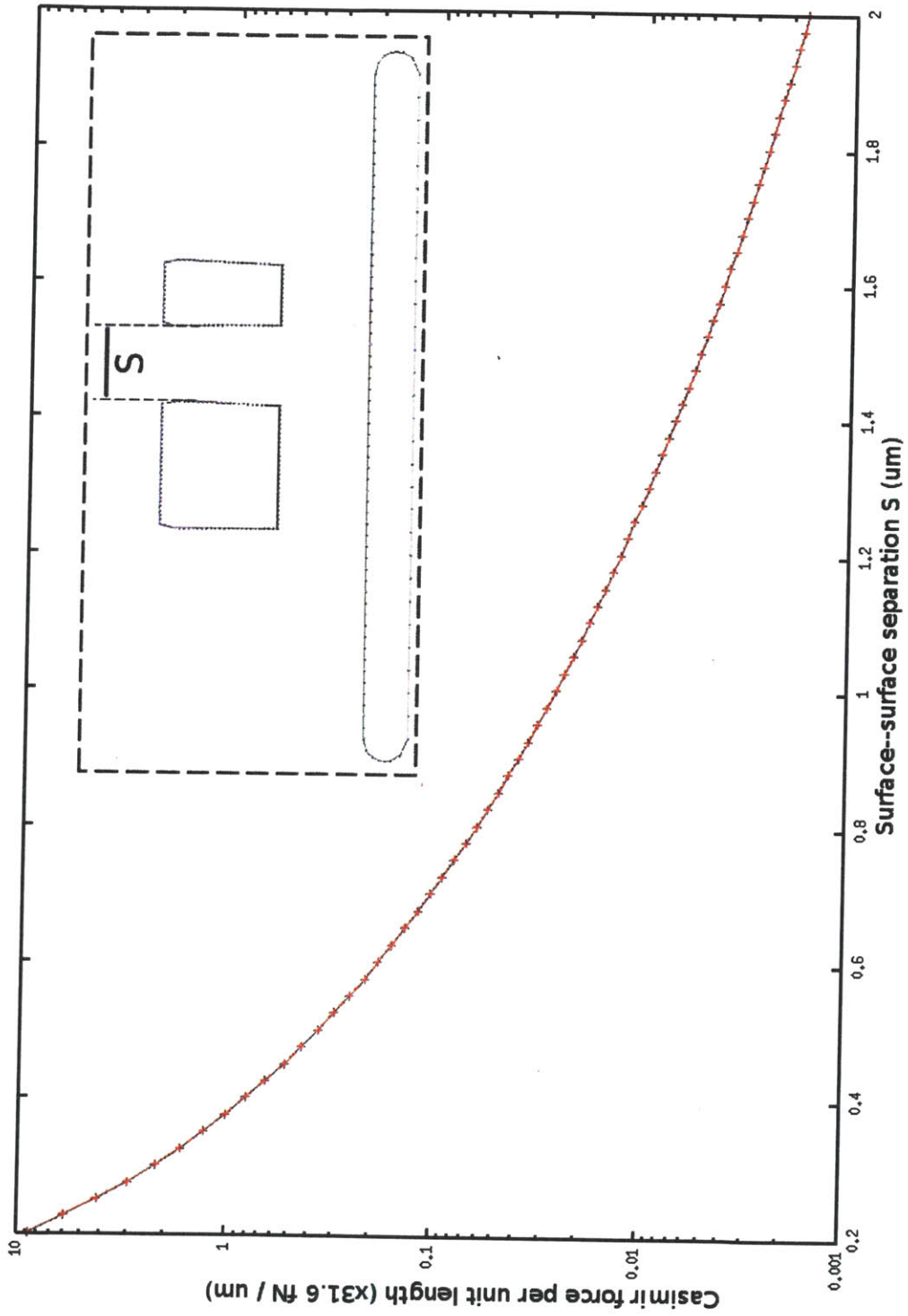
Figure 9-7: Casimir force per unit length, as a function of surface–surface separation, as predicted by CASIMIR2D, for a hypothetical geometry consisting of elongated silicon beams of irregular cross-section suspended over a silicon substrate (inset).

119

Chapter 10

Conclusions and Future Work

This thesis has presented a new paradigm for computational Casimir physics. Our *fluctuating-surface-current* (FSC) method expresses Casimir energies, forces, and torques—among objects of arbitrary shapes and materials—in terms of the interactions of effective electric and magnetic *surface currents* flowing on the surfaces of the interacting objects. Upon discretizing object geometries and approximating the surface currents as expansions in a finite set of localized basis functions, the FSC technique leads to expressions for all Casimir quantities that are not only simple and compact but also fully *general*, in the sense that they may be applied, *mutatis mutandis*, to any number of distinct Casimir geometries with no need to reformulate the underlying computational procedure in each case.

The FSC formulae were first stated in Chapter 5 of this thesis, where they were demonstrated to emerge as simple logical consequences of either of two seemingly disparate theoretical frameworks—the *stress-tensor* and the *path-integral* (or *scattering*) approach to computational Casimir physics. In addition to furnishing a useful new technique for practical Casimir computations, this thesis thus achieves an unexpected unification of these two otherwise quite distinct paradigms.

But theoretical Casimir methods are only as useful as their real-world implementations are practical, efficient, and accurate, and for this reason in Chapters 6, 7, and 8 we presented three separate numerical implementations of the FSC formulae. Practical implementations of the FSC formulae turn out to pose a number of numerical challenges—the most significant of which involves the efficient and accurate numerical evaluation of huge numbers of singular or nearly-singular multidimensional integrals—and this thesis developed a number of responses to these challenges, which were discussed in Chapters 6 through 8 and codified in technical detail in a series of Appendices.

After considering abstract theoretical underpinnings in Chapter 5 and practical numerical implementations in Chapters 6 through 8, the fruits of the FSC technique were finally harvested in Chapter 9. There we demonstrated that the FSC approach is capable of efficiently predicting Casimir interactions in a variety of geometries that would be difficult or simply impossible to treat using any existing Casimir method. Thus, beyond the intrinsic interest of the theoretical perspective it furnishes or the practical relevance of the numerical techniques that go into its implementation, the

FSC technique will be, quite simply, the hands-down computational method of choice for many experimentally relevant Casimir configurations today and in the future.

Future Work

The FSC formulae, equations (5.1), obtain Casimir energies, forces, and torques in terms of the determinant and trace of certain matrices describing the interactions of discretized surface currents. The dimensions of these matrices are proportional to the number of localized basis functions needed for an accurate description of surface currents in a given Casimir geometry; for the examples presented in Chapter 9, this number was in the range $N \sim 10^3 - 10^4$, and thus the dimensions of the matrices in (5.1) are small enough that determinants and traces may be evaluated using dense-direct linear algebra, with $\mathcal{O}(N^2)$ memory and $\mathcal{O}(N^3)$ CPU-time scaling.

For future applications, it may be necessary to consider more complicated geometries, in which the number of basis functions grows in excess of a few tens of thousands. For such large problems, $O(N^3)$ methods are computationally infeasible, and we must pursue alternative approaches.

This general state of affairs is ubiquitous in the history of computational science: a new computational method, which relies in practice on numerical linear algebra, will often be developed and demonstrated first in a dense–direct $(\mathcal{O}(N^3))$ context; later, after this initial proof-of-concept, second-generation implementations will emerge to improve the complexity scaling to $\mathcal{O}(N \log N)$ or similar. This thesis may be thought of as an initial statement and proof-of-concept of the FSC technique (as demonstrated in Chapter 9, our first-generation implementations already achieve some decidedly nontrivial advances in computational Casimir physics) together with some first steps (Chapter 8) in the direction of a second-generation implementation with improved complexity scaling. An obvious direction for future work will be to continue down the road begun in Chapter 8 towards a comprehensive fast solver for Casimir applications.

Appendix A

Dyadic Green's Functions

The dyadic Green's functions of classical electromagnetism appear in many contexts throughout this thesis, and for this reason we collect here a compendium of definitions and relations involving these quantities. This material is of course not new, but is reproduced here to fix ideas and notation for the purposes of this thesis.

In the presence of known volume densities of electric and magnetic current $\mathbf{J}(\mathbf{x}), \mathbf{M}(\mathbf{x})$ at a fixed imaginary frequency ξ, the components of the electric and magnetic fields are given by linear integral relations of the form

$$E_i(\mathbf{x}) = \int \left\{ \Gamma_{ij}^{\mathrm{EE}}(\xi; \mathbf{x}, \mathbf{x}') J_j(\mathbf{x}') + \Gamma_{ij}^{\mathrm{EM}}(\xi; \mathbf{x}, \mathbf{x}') M_j(\mathbf{x}') \right\} d\mathbf{x}'$$

$$H_i(\mathbf{x}) = \int \left\{ \Gamma_{ij}^{\mathrm{ME}}(\xi; \mathbf{x}, \mathbf{x}') J_j(\mathbf{x}') + \Gamma_{ij}^{\mathrm{MM}}(\xi; \mathbf{x}, \mathbf{x}') M_j(\mathbf{x}') \right\} d\mathbf{x}'.$$

These relations define the four dyadic Green's functions Γ.

In an infinite homogeneous medium with spatially constant relative permeability and permittivity $\epsilon(\xi; \mathbf{x}) = \epsilon^r(\xi)$, $\mu(\xi; \mathbf{x}) = \mu^r(\xi)$, the four Γ functions may be expressed in terms of just two tensors:

$$\mathbf{\Gamma}^{\mathrm{EE,r}}(\xi, \mathbf{r}, \mathbf{r}') = -Z_0 Z^r \kappa^r \, \mathbf{G}(\kappa^r, \mathbf{r}, \mathbf{r}'), \qquad \mathbf{\Gamma}^{\mathrm{ME,r}}(\xi, \mathbf{r}, \mathbf{r}') = \kappa^r \mathbf{C}(\kappa^r, \mathbf{r}, \mathbf{r}'),$$

$$\mathbf{\Gamma}^{\mathrm{EM,r}}(\xi, \mathbf{r}, \mathbf{r}') = -\kappa^r \, \mathbf{C}(\kappa^r, \mathbf{r}, \mathbf{r}') \qquad \mathbf{\Gamma}^{\mathrm{MM,r}}(\xi, \mathbf{r}, \mathbf{r}') = -\frac{\kappa^r}{Z_0 Z^r} \mathbf{G}(\kappa^r, \mathbf{r}, \mathbf{r}')$$

(A.1)

$$\left(Z_0 = \sqrt{\frac{\mu_0}{\epsilon_0}}, \qquad Z^r = \sqrt{\frac{\mu^r}{\epsilon^r}}, \qquad \kappa^r = \sqrt{\mu_0 \mu^r \epsilon_0 \epsilon^r} \cdot \xi \right)$$

where $\mathbf{G}$, sometimes referred to as the "photon Green's function," is the solution to the equation

$$\left[\nabla \times \nabla \times + (\kappa^r)^2 \right] \mathbf{G}(\kappa^r; \mathbf{r} - \mathbf{r}') = \delta(\mathbf{r} - \mathbf{r}') \mathbf{1};$$

(A.2)

and $\mathbf{C}$ is defined by

$$\mathbf{C} = \frac{1}{\kappa^r} \nabla \times \mathbf{G}.$$

(A.3)

Explicit expressions for the components of $\mathbf{G}$ and $\mathbf{C}$ are

$$G_{ij} = \left[\delta_{ij} - \frac{1}{\kappa^2}\partial_i\partial_j\right]G_0, \qquad C_{ij} = -\frac{1}{\kappa}\varepsilon_{ijk}\partial_k G_0 \qquad (A.4)$$

where G_0 is the scalar Green's function for the Helmholtz equation,

$$G_0(\kappa; \mathbf{r} - \mathbf{r}') = \frac{e^{-\kappa|\mathbf{r}-\mathbf{r}'|}}{4\pi|\mathbf{r} - \mathbf{r}'|} \qquad (A.5)$$

which satisfies

$$\left[\nabla^2 - \kappa^2\right]G_0(\kappa; \mathbf{r} - \mathbf{r}') = \delta(\mathbf{r} - \mathbf{r}').$$

With these expressions, we can verify that equation (A.3) is actually just the first half of a pair of reciprocal curl identities relating $\mathbf{G}$ and $\mathbf{C}$:

$$\frac{1}{\kappa^r}\nabla \times \mathbf{G} = \mathbf{C}, \qquad \frac{1}{\kappa^r}\nabla \times \mathbf{C} = -\mathbf{G}. \qquad (A.6)$$

(As usual with tensors and dyadics, the vector notation here is suggestive but vague; the precise meaning of (A.3) is

$$\frac{1}{\kappa}\varepsilon_{iAB}\partial_A G_{Bj} = C_{ij}, \qquad \frac{1}{\kappa}\varepsilon_{iAB}\partial_A C_{Bj} = -G_{ij}.) \qquad (A.7)$$

In a general inhomogeneous region, the dyadic Green's functions may be expressed as the sum of two terms,

$$\mathbf{\Gamma}^{\mathrm{EE}}(\xi; \mathbf{x}, \mathbf{x}') = \mathbf{\Gamma}^{\mathrm{EE},\times}(\xi; \mathbf{x} - \mathbf{x}') + \mathcal{G}^{\mathrm{EE,scat}}(\xi; \mathbf{x}, \mathbf{x}') \qquad (A.8)$$

(and similarly for the other three $\mathbf{\Gamma}$ functions); here $\mathbf{\Gamma}^{\mathrm{EE},\times}$ is the *homogeneous* DGF for an infinite medium with constant ϵ^r, μ^r set equal to their values at $\mathbf{x}$, and $\mathcal{G}^{\mathrm{EE,scat}}$, the *scattering part* of the DGF, describes the fields scattered from the inhomogeneities in the geometry. The first term in (A.8) is singular as $\mathbf{x} \to \mathbf{x}'$, but the second term is perfectly well-defined in that limit and is the quantity that enters into the fluctuation–dissipation expressions for the spectral density of fluctuations in products of field components, as discussed in Chapter 3.

Before proceeding we pause briefly to comment on our choice of notation. The four dyadic Green's functions $\mathbf{\Gamma}^{\mathrm{PQ}}$ (P,Q $\in$ {E,M}) depend both on the imaginary frequency and on the homogeneous region in which they are defined, through the material-property functions $\{\epsilon^r(i\xi), \mu^r(i\xi)\}$ for that region. Thus these functions are properly thought of as functions of imaginary frequency, and they carry a superscript (r) indexing the homogeneous region in which they are defined, i.e.

$$\mathbf{\Gamma}^{\mathrm{PQ}} = \mathbf{\Gamma}^{\mathrm{PQ},r}(\xi, \mathbf{r}, \mathbf{r}').$$

In contrast, the $\mathbf{G}$ and $\mathbf{C}$ dyadics are universal functions, defined mathematically by (A.4) and (A.5), that depend on ϵ, μ, and ξ only through the single parameter κ, and

124

hence these functions are

$$\mathbf{G} = \mathbf{G}(\kappa; \mathbf{r}, \mathbf{r}')$$
$$\mathbf{C} = \mathbf{C}(\kappa; \mathbf{r}, \mathbf{r}').$$

Momentum-Space Representations of Dyadic Green's Functions

The momentum-space representation of the scalar Green's function is (A.5)

$$G_0(\kappa; \mathbf{r}) = \int \frac{d\mathbf{k}}{(2\pi)^3} \tilde{G}_0(\kappa; \mathbf{k}) e^{i\mathbf{k}\cdot\mathbf{r}}$$

with

$$\tilde{G}_0(\kappa; \mathbf{k}) = \frac{1}{\kappa^2 + \mathbf{k}^2}.$$

The momentum-space version of (A.4) reads

$$G_{ij} = \left[\delta_{ij} + \frac{k_i k_j}{\kappa^2}\right] G_0, \qquad C_{ij} = -\frac{i}{\kappa}\varepsilon_{ijk}k_k G_0 \tag{A.9}$$

or, in matrix format,

$$\mathbf{G}(\mathbf{k}) = \frac{1}{\kappa^2(\kappa^2 + \mathbf{k}^2)}\left[\begin{pmatrix} \kappa^2 & 0 & 0 \\ 0 & \kappa^2 & 0 \\ 0 & 0 & \kappa^2 \end{pmatrix} + \begin{pmatrix} k_x^2 & k_x k_y & k_x k_z \\ k_y k_x & k_y^2 & k_y k_z \\ k_z k_x & k_z k_y & k_z^2 \end{pmatrix}\right] \tag{A.10a}$$

$$\mathbf{C}(\mathbf{k}) = \frac{i}{\kappa(\kappa^2 + \mathbf{k}^2)}\begin{pmatrix} 0 & -k_z & k_y \\ k_z & 0 & -k_x \\ -k_y & k_x & 0 \end{pmatrix}. \tag{A.10b}$$

Appendix B

BEM Matrix Elements between Localized Basis Functions

In Chapter 4 we reviewed the boundary-element method (BEM) of computational electromagnetism, and in Chapter 5 we showed that the matrices that enter into BEM calculations also enter in to a certain set of formulae—our master FSC formulae (5.1)—for Casimir phenomena. For reference, in this Appendix we write out the precise forms of these matrices, using a notation that clarifies the discussion of the matrix-element calculations presented in Chapters 6 and 7. This material is of course not new, but is instead merely a distillation of the content of Chapter 4 (which itself was of course not new, but was instead merely a review of a well-established technique in computational electromagnetism).

The elements of the BEM matrices in the EFIE and PMCHW formulations involve inner products of basis functions with the dyadic Green's functions of Appendix A. More specifically,

1. *EFIE Matrix Elements*: For the electric-field integral equation, appropriate to the case of PEC scatterers, each pair of localized basis functions $(\mathbf{f}_\alpha, \mathbf{f}_\beta)$ contributes a single matrix element to the BEM matrix,

$$
\begin{aligned}
M_{\alpha\beta}(\xi) &= \left\langle \mathbf{f}_\alpha \middle| \mathbf{\Gamma}^{\mathrm{EE},e}(\xi) \middle| \mathbf{f}_\beta \right\rangle \\
&= -Z_0 Z^e \kappa^e \left\langle \mathbf{f}_\alpha \middle| \mathbf{G}(\kappa^e) \middle| \mathbf{f}_\beta \right\rangle
\end{aligned}
$$

    where κ^e, Z^e are the imaginary wavenumber and the relative wave impedance of the external medium (in which the PEC bodies are embedded) at imaginary frequency ξ.

2. *PMCHW Matrix Elements*: In the PMCHW formulation appropriate for the case of general material bodies, each pair of localized basis functions $(\mathbf{f}_\alpha, \mathbf{f}_\beta)$ contributes a 2 × 2 block of matrix elements to the BEM matrix.

    If $\mathbf{f}_\alpha, \mathbf{f}_\beta$ *lie on the surfaces of two different objects*, this block of elements takes

127

the form

$$\left\langle \mathbf{f}_\alpha \middle| \mathbf{M}(\xi) \middle| \mathbf{f}_\beta \right\rangle = \begin{pmatrix} \dfrac{1}{Z_0}\left\langle \mathbf{f}_\alpha \middle| \boldsymbol{\Gamma}^{\mathrm{EE},e}(\xi) \middle| \mathbf{f}_\beta \right\rangle & -\left\langle \mathbf{f}_\alpha \middle| \boldsymbol{\Gamma}^{\mathrm{EM},e}(\xi) \middle| \mathbf{f}_\beta \right\rangle \\[2mm] \left\langle \mathbf{f}_\alpha \middle| \boldsymbol{\Gamma}^{\mathrm{ME},e}(\xi) \middle| \mathbf{f}_\beta \right\rangle & -Z_0\left\langle \mathbf{f}_\alpha \middle| \boldsymbol{\Gamma}^{\mathrm{MM},e}(\xi) \middle| \mathbf{f}_\beta \right\rangle \end{pmatrix} \tag{B.1}$$

$$= \begin{pmatrix} -\kappa^e Z^e\left\langle \mathbf{f}_\alpha \middle| \mathbf{G}(\kappa^e) \middle| \mathbf{f}_\beta \right\rangle & -\kappa^e\left\langle \mathbf{f}_\alpha \middle| \mathbf{C}(\kappa^e) \middle| \mathbf{f}_\beta \right\rangle \\[2mm] -\kappa^e\left\langle \mathbf{f}_\alpha \middle| \mathbf{C}(\kappa^e) \middle| \mathbf{f}_\beta \right\rangle & +\dfrac{\kappa^e}{Z^e}\left\langle \mathbf{f}_\alpha \middle| \mathbf{G}(\kappa^e) \middle| \mathbf{f}_\beta \right\rangle \end{pmatrix} \tag{B.2}$$

where κ^e, Z^e are the imaginary wavevector and relative wave impedance of the external medium at imaginary frequency ξ.

If $\mathbf{f}_\alpha, \mathbf{f}_\beta$ lie on the surfaces of the same object (call it object r), then equations (B.1) and (B.2) are augmented by contributions from the medium interior to object r:

$$\left\langle \mathbf{f}_\alpha \middle| \mathbf{M}(\xi) \middle| \mathbf{f}_\beta \right\rangle = \begin{pmatrix} \dfrac{1}{Z_0}\left\langle \mathbf{f}_\alpha \middle| \boldsymbol{\Gamma}^{\mathrm{EE},e} + \boldsymbol{\Gamma}^{\mathrm{EE},r} \middle| \mathbf{f}_\beta \right\rangle & -\left\langle \mathbf{f}_\alpha \middle| \boldsymbol{\Gamma}^{\mathrm{EM},e} + \boldsymbol{\Gamma}^{\mathrm{EM},r} \middle| \mathbf{f}_\beta \right\rangle \\[2mm] \left\langle \mathbf{f}_\alpha \middle| \boldsymbol{\Gamma}^{\mathrm{ME},e} + \boldsymbol{\Gamma}^{\mathrm{ME},r} \middle| \mathbf{f}_\beta \right\rangle & -Z_0\left\langle \mathbf{f}_\alpha \middle| \boldsymbol{\Gamma}^{\mathrm{MM},e} + \boldsymbol{\Gamma}^{\mathrm{MM},r} \middle| \mathbf{f}_\beta \right\rangle \end{pmatrix}$$

$$= \begin{pmatrix} -\kappa^e Z^e\left\langle \mathbf{f}_\alpha \middle| \mathbf{G}(\kappa^e) \middle| \mathbf{f}_\beta \right\rangle - \kappa^r Z^r\left\langle \mathbf{f}_\alpha \middle| \mathbf{G}(\kappa^r) \middle| \mathbf{f}_\beta \right\rangle & -\kappa^e\left\langle \mathbf{f}_\alpha \middle| \mathbf{C}(\kappa^e) \middle| \mathbf{f}_\beta \right\rangle - \kappa^r\left\langle \mathbf{f}_\alpha \middle| \mathbf{C}(\kappa^r) \middle| \mathbf{f}_\beta \right\rangle \\[2mm] -\kappa^e\left\langle \mathbf{f}_\alpha \middle| \mathbf{C}(\kappa^e) \middle| \mathbf{f}_\beta \right\rangle - \kappa^r\left\langle \mathbf{f}_\alpha \middle| \mathbf{C}(\kappa^r) \middle| \mathbf{f}_\beta \right\rangle & +\dfrac{\kappa^e}{Z^e}\left\langle \mathbf{f}_\alpha \middle| \mathbf{G}(\kappa^e) \middle| \mathbf{f}_\beta \right\rangle + \dfrac{\kappa^r}{Z^r}\left\langle \mathbf{f}_\alpha \middle| \mathbf{G}(\kappa^r) \middle| \mathbf{f}_\beta \right\rangle \end{pmatrix}$$

where κ^r, Z^r are the imaginary wavevector and relative wave impedance, at imaginary frequency ξ, of the medium interior to object r.

The inner products with the $\mathbf{G}$ and $\mathbf{C}$ dyadics can, in turn, be represented in terms of three separate types of integrals:

$$\left\langle \mathbf{f}_\alpha \middle| \mathbf{G}(\kappa) \middle| \mathbf{f}_\beta \right\rangle = -\kappa L_\bullet(\kappa, \mathbf{f}_\alpha, \mathbf{f}_\beta) - \dfrac{1}{\kappa} L_\nabla(\kappa, \mathbf{f}_\alpha, \mathbf{f}_\beta)$$

$$\left\langle \mathbf{f}_\alpha \middle| \mathbf{C}(\kappa) \middle| \mathbf{f}_\beta \right\rangle = -L_\times(\kappa, \mathbf{f}_\alpha, \mathbf{f}_\beta)$$

128

where the L-functions are

$$L_\bullet\left(\kappa, \mathbf{f}_\alpha, \mathbf{f}_\beta\right) = \int_{\sup \mathbf{f}_\alpha} d\mathbf{x} \int_{\sup \mathbf{f}_\beta} d\mathbf{x}' \left[\mathbf{f}_\alpha(\mathbf{x}) \cdot \mathbf{f}_\beta(\mathbf{x}')\right] G_0(\kappa; |\mathbf{x} - \mathbf{x}'|) \tag{B.3a}$$

$$L_\nabla\left(\kappa, \mathbf{f}_\alpha, \mathbf{f}_\beta\right) = \int_{\sup \mathbf{f}_\alpha} d\mathbf{x} \int_{\sup \mathbf{f}_\beta} d\mathbf{x}' \left[\left(\nabla \cdot \mathbf{f}_\alpha(\mathbf{x})\right)\left(\nabla \cdot \mathbf{f}_\beta(\mathbf{x}')\right)\right] G_0(\kappa; |\mathbf{x} - \mathbf{x}'|) \tag{B.3b}$$

$$L_\times\left(\kappa, \mathbf{f}_\alpha, \mathbf{f}_\beta\right) = \int_{\sup \mathbf{f}_\alpha} d\mathbf{x} \int_{\sup \mathbf{f}_\beta} d\mathbf{x}' \left[\mathbf{f}_\alpha(\mathbf{x}) \times \mathbf{f}_\beta(\mathbf{x}')\right] \cdot \nabla G_0(\kappa, |\mathbf{x} - \mathbf{x}'|) \tag{B.3c}$$

where

$$G_0(\kappa; r) \equiv \frac{e^{-\kappa r}}{4\pi r}$$

is the scalar Green's function for the imaginary-frequency Helmholtz equation.

For some purposes it is convenient to use the symbols ϕ and ψ for G_0 and for the scalar part of its gradient, i.e.

$$\phi(\kappa; r) \equiv \frac{e^{-\kappa r}}{4\pi r}$$

$$\psi(\kappa; r) \equiv -(1 + \kappa r)\frac{e^{-\kappa r}}{4\pi r^3}$$

so that $\nabla \phi(\mathbf{r}) = \mathbf{r}\psi(\mathbf{r})$.

Appendix C

Proof of Integral Identities

In this Appendix we state and prove a new integral identity that underlies the stress-tensor derivation of the FSC formulae presented in Chapter 5. We emphasize that this integral identity is new and is stated, proved, and used for the first time in this thesis, although an identity bearing at least a superficial resemblance appears in equation A.6 of Ref. [42].

In Chapter 5, we introduced a three-index integral kernel $\mathcal{I}$ defined by

$$\mathcal{I}_{ikl}(\mathbf{r}, \mathbf{r}') = \kappa^2 \oint_C V_A(\mathbf{r}, \mathbf{r}', \mathbf{x}) \, n_A(\mathbf{x}) \, d\mathbf{x} \tag{C.1}$$

where the integration is over a closed surface in space (a topological two-sphere) C and the integrand contains products of factors of dyadic Green's functions:

$$V_A(\mathbf{r}, \mathbf{r}', \mathbf{x}) = G^1_{ik} G^2_{lA} - \frac{\delta_{iA}}{2} G^1_{Bk} G^2_{lB} - C^1_{ik} C^2_{lA} + \frac{\delta_{iA}}{2} C^1_{Bk} C^2_{lB}. \tag{C.2}$$

Here the $\mathbf{G}$ and $\mathbf{C}$ dyadics are those defined by equations (A.2) and (A.3); we use capital Roman letters $(A, B, \cdots)$ to denote contracted indices, and we are using a shorthand notation in which κ arguments are suppressed and spatial arguments replaced by superscripts,

$$G^1_{ij} \equiv G_{ij}(\kappa, \mathbf{x} - \mathbf{r}), \qquad G^2_{ij} \equiv G_{ij}(\kappa, \mathbf{r}' - \mathbf{x}).$$

We also defined a symmetrized version of $\mathcal{I}$:

$$\overline{\mathcal{I}}_{ikl}(\mathbf{r}, \mathbf{r}') = \mathcal{I}_{ikl}(\mathbf{r}, \mathbf{r}') + \mathcal{I}_{ilk}(\mathbf{r}', \mathbf{r})$$

$$\equiv \kappa^2 \oint_C \overline{V}_A(\mathbf{x}) \, n_A(\mathbf{x}) \, d\mathbf{x} \tag{C.3}$$

with

$$\overline{V}_A(\mathbf{x}) = G^1_{ik} G^2_{lA} + G^1_{kA} G^2_{il} - \delta_{iA} G^1_{Bk} G^2_{lB} - C^1_{ik} C^2_{lA} - C^1_{kA} C^2_{il} + \delta_{iA} C^1_{Bk} C^2_{lB}. \tag{C.4}$$

The goal of this Appendix is to demonstrate that, by appealing to the defining prop-

erties of the **G** and **C** dyadics, *the surface integral in (C.3) can be evaluated in closed form*, with the result

$$
\overline{\mathcal{I}}_{ikl}(\mathbf{r}, \mathbf{r}') = \begin{cases}
0, & \text{if both } \mathbf{r}, \mathbf{r}' \text{ lie inside } \mathcal{C} \\[2mm]
\dfrac{\partial}{\partial \mathbf{r}_i} G_{kl}(\mathbf{r} - \mathbf{r}') & \text{if } \mathbf{r} \text{ lies inside and } \mathbf{r}' \text{ lies outside } \mathcal{C} \\[2mm]
-\dfrac{\partial}{\partial \mathbf{r}_i} G_{kl}(\mathbf{r} - \mathbf{r}') & \text{if } \mathbf{r} \text{ lies outside and } \mathbf{r}' \text{ lies inside } \mathcal{C} \\[2mm]
0, & \text{if both } \mathbf{r}, \mathbf{r}' \text{ lie outside } \mathcal{C}.
\end{cases}
\tag{C.5}
$$

For the purposes of this Appendix it will be convenient to work in length units such that $\kappa \equiv 1$. With this convention, the **G** and **C** dyadics are related to the scalar Green's function for the Helmholtz equation according to

$$
G_{ij} = \left[\delta_{ij} - \partial_i \partial_j \right] G_0, \qquad C_{ij} = -\varepsilon_{ijk} \partial_k G_0,
\tag{C.6}
$$

and G_0 satisfies

$$
\left[\partial_A \partial_A - 1 \right] G_0(\mathbf{r}) = \delta(\mathbf{r}).
\tag{C.7}
$$

The evaluation of the surface integral (C.3) now proceeds in several stages.

C.1 Apply Divergence Theorem

The first step is to recast the surface integral in (C.3) as a volume integral over the volume bounded by $\mathcal{C}$,

$$
\oint_{\mathcal{C}} \overline{V}_A n_A \, dA = \int_{\mathcal{V}} \partial_A \overline{V}_A \, dV \qquad \left(\mathcal{C} = \partial \mathcal{V} \right)
$$

$$
= \int_{\mathcal{V}} W \, dV
$$

where we put $W \equiv \partial_A \overline{V}_A$.

Each of the six terms in $\overline{V}_A$ contains two factors and hence contributes two terms to W (by the chain rule for differentiation). Terms of the form $\partial_A C_{iA}$ vanish; to each of the remaining (nonvanishing) terms we assign a label, as tabulated in Table C.1. Note that derivatives of G_{ij}^2 enter with a minus sign, because we are differentiating with respect to $\mathbf{x}$, which enters the argument of G_{ij}^2 with a minus sign.

132

Table C.1: Terms in $W \equiv \partial_A \overline{V}_A$.

Label	Term	Label	Term
W^1	$\left[\partial_A G^1_{ik}\right]\left[G^2_{lA}\right]$	W^6	$\left[G^1_{kA}\right]\left[\partial_i G^2_{lA}\right]$
W^2	$-\left[G^1_{ik}\right]\left[\partial_A G^2_{lA}\right]$	W^7	$-\left[\partial_A C^1_{ik}\right]\left[C^1_{lA}\right]$
W^3	$\left[\partial_A G^1_{kA}\right]\left[G^2_{il}\right]$	W^8	$\left[C^1_{kA}\right]\left[\partial_A C^2_{il}\right]$
W^4	$-\left[G^1_{kA}\right]\left[\partial_A G^2_{il}\right]$	W^9	$\left[\partial_i C^1_{Ak}\right]\left[C^2_{lA}\right]$
W^5	$-\left[\partial_i G^1_{kA}\right]\left[G^2_{lA}\right]$	W^{10}	$-\left[C^1_{Ak}\right]\left[\partial_i C^2_{lA}\right]$

C.2 Treatment of W^2 and W^3

We first consider the terms labeled W^2 and W^3 in Table C.1. Starting with the first of these, we have

$$W^2 = -\left[G^1_{ik}\right]\left[\partial_A G^2_{lA}\right]$$

Expand the second factor using (C.6):

$$= -\left[G^1_{ik}\right]\left[\partial_l(1 - \partial_A \partial_A)G^2_0\right]$$

Apply (C.7):

$$= +\left[G^1_{ik}\right]\left[\partial_l \delta(\mathbf{2})\right]$$

Integrate by parts:

$$\sim +\left[\partial_l G^1_{ik}\right]\left[\delta(\mathbf{2})\right] \tag{C.8}$$

where $\sim$ means "equivalent as long as we are underneath the volume-integration sign." (Note that the minus sign coming from the integration by parts is cancelled

133

by the minus sign coming from the fact that $\mathbf{x}$ enters $\mathbf{2}$ with a minus sign, as noted above).

By analogous operations, we find

$$W^3 \sim -\Big[\delta(\mathbf{1})\Big]\Big[\partial_k G_{il}^2\Big]. \tag{C.9}$$

We now set aside results (C.8) and (C.9) for future use.

C.3   Treatment of Remaining Terms

C.3.1   Rewrite in terms of G_0

Turning next to the remaining 8 terms in Table 1, we begin by using (C.6) to rewrite everything in terms of the scalar Green's function:

$$
\begin{aligned}
W^1 &+ W^4 + W^5 + W^6 \\
&= \Big[\partial_A G_{ik}^1 - \partial_i G_{kA}^1\Big]\Big[G_{lA}^2\Big] + \Big[G_{kA}^1\Big]\Big[\partial_i G_{lA}^2 - \partial_A G_{il}^2\Big] \\
&= \Big[\delta_{ik}\partial_A G_0^1 - \delta_{kA}\partial_i G_0^1\Big]\Big[\delta_{lA}G_0^2 - \partial_l\partial_A G_0^2\Big] \\
&\quad + \Big[\delta_{kA}G_0^1 - \partial_k\partial_A G_0^1\Big]\Big[\delta_{lA}\partial_i G_0^2 - \delta_{il}\partial_A G_0^2\Big]
\end{aligned} \tag{C.10}
$$

$$
\begin{aligned}
W^7 &+ W^8 + W^9 + W^{10} \\
&= -\varepsilon_{ikB}\varepsilon_{lAC}\Big[\partial_A\partial_B G_0^1\Big]\Big[\partial_C G_0^2\Big] + \varepsilon_{kAB}\varepsilon_{ilC}\Big[\partial_B G_0^1\Big]\Big[\partial_A\partial_C G_0^2\Big] \\
&\quad + \varepsilon_{AkB}\varepsilon_{lAC}\Big[\partial_i\partial_B G_0^1\Big]\Big[\partial_C G_0^2\Big] - \varepsilon_{AkB}\varepsilon_{lAC}\Big[\partial_B G_0^1\Big]\Big[\partial_i\partial_C G_0^2\Big].
\end{aligned}
$$

We can trade Levi-Civita symbols for Kronecker deltas using the identity

$$
\begin{aligned}
\varepsilon_{ABC}\varepsilon_{DEF} &= \delta_{AD}\Big[\delta_{BE}\delta_{CF} - \delta_{BF}\delta_{CE}\Big] + \delta_{AE}\Big[\delta_{BF}\delta_{CD} - \delta_{BD}\delta_{CF}\Big] + \delta_{AF}\Big[\delta_{BD}\delta_{CE} - \delta_{BE}\delta_{CD}\Big].
\end{aligned}
$$

We then find

$$
\begin{aligned}
W^7 &+ W^8 + W^9 + W^{10} \\
&= \Big[\partial_A\partial_A G_0^1\Big]\Big[\delta_{il}\partial_k G_0^2 - \delta_{kl}\partial_i G_0^2\Big] - \Big[\delta_{ik}\partial_l G_0^1 - \delta_{kl}\partial_i G_0^1\Big]\Big[\partial_A\partial_A G_0^2\Big] \\
&\quad - \delta_{il}\Big[\partial_k\partial_A G_0^1\Big]\Big[\partial_A G_0^2\Big] + \delta_{ik}\Big[\partial_A G_0^1\Big]\Big[\partial_l\partial_A G_0^2\Big] \\
&\quad - \Big[\partial_i G_0^1\Big]\Big[\partial_k\partial_l G_0^2\Big] + \Big[\partial_k\partial_l G_0^1\Big]\Big[\partial_i G_0^2\Big].
\end{aligned} \tag{C.11}
$$

C.3.2 Label Individual Terms

To proceed, we now assign a new label to each separate term in (C.10) and (C.11):

$$W^1 + W^4 + W^5 + W^6 + W^7 + W^8 + W^9 + W^{10} = \sum_{n=1}^{16} X^n$$

Table C.2: Terms in X.

Label	Term	Label	Term
X^1	$-\delta_{kl}\left[\partial_i G_0^1\right]\left[G_0^2\right]$	X^9	$-\delta_{kl}\left[\partial_A\partial_A G_0^1\right]\left[\partial_i G_0^2\right]$
X^2	$\left[\partial_i G_0^1\right]\left[\partial_k\partial_l G_0^2\right]$	X^{10}	$+\partial_{il}\left[\partial_A\partial_A G_0^1\right]\left[\partial_k G_0^2\right]$
X^3	$\delta_{ik}\left[\partial_l G_0^1\right]\left[G_0^2\right]$	X^{11}	$+\delta_{kl}\left[\partial_i G_0^1\right]\left[\partial_A\partial_A G_0^2\right]$
X^4	$-\delta_{ik}\left[\partial_A G_0^1\right]\left[\partial_A\partial_l G_0^2\right]$	X^{12}	$-\delta_{ik}\left[\partial_l G_0^1\right]\left[\partial_A\partial_A G_0^2\right]$
X^5	$-\delta_{il}\left[G_0^1\right]\left[\partial_k G_0^2\right]$	X^{13}	$-\delta_{il}\left[\partial_A\partial_k G_0^1\right]\left[\partial_A G_0^2\right]$
X^6	$\delta_{kl}\left[G_0^1\right]\left[\partial_i G_0^2\right]$	X^{14}	$+\delta_{ik}\left[\partial_A G_0^1\right]\left[\partial_l\partial_A G_0^2\right]$
X^7	$\delta_{il}\left[\partial_A\partial_k G_0^1\right]\left[\partial_A G_0^2\right]$	X^{15}	$-\left[\partial_i G_0^1\right]\left[\partial_k\partial_l G_0^2\right]$
X^8	$-\left[\partial_k\partial_l G_0^1\right]\left[\partial_i G_0^2\right]$	X^{16}	$\left[\partial_k\partial_l G_0^1\right]\left[\partial_i G_0^2\right]$

C.3.3 Recombine Terms

We first note the obvious cancellations:

$$\begin{aligned}
X^2 + X^{15} &= 0 & X^4 + X^{14} &= 0 \\
X^7 + X^{13} &= 0 & X^8 + X^{16} &= 0
\end{aligned}$$

135

Summing and appropriately recombining the remaining terms, we find

$$X^1 + X^3 + X^{11} + X^{12} = \left[\delta_{kl}\partial_i G_0^1 - \delta_{ik}\partial_l G_0^1\right]\left[\partial_A\partial_A G_0^2 - G_0^2\right]$$

and

$$X^5 + X^6 + X^9 + X^{10} = \left[\partial_A\partial_A G_0^1 - G_0^1\right]\left[\delta_{il}\partial_k G_0^1 - \delta_{kl}\partial_i G_0^1\right].$$

From (C.6) it follows that

$$\left[\delta_{kl}\partial_i G_0 - \delta_{ik}\partial_l G_0\right] = \left[\partial_i G_{kl} - \partial_l G_{ik}\right].$$

Using this and (C.7), we can rewrite the previous two equations in the form

$$X^1 + X^3 + X^{11} + X^{12} = \left[\partial_i G_{kl}^1 - \partial_l G_{ik}^1\right]\left[\delta(2)\right] \tag{C.12}$$

and

$$X^5 + X^6 + X^9 + X^{10} = \left[\delta(1)\right]\left[\partial_k G_{il}^2 - \partial_i G_{kl}^2\right]. \tag{C.13}$$

C.4 Final Steps

Finally, we combine equations (C.8), (C.9), (C.12) and (C.13) to obtain

$$\overline{\mathcal{I}}_{ikl} = \int_\mathcal{V}\left\{W^2 + W^3 + X^1 + X^3 + X^{11} + X^{12} + X^5 + X^6 + X^9 + X^{10}\right\}d\mathbf{x}$$

$$= \int_\mathcal{V}\left\{\left[\partial_i G_{kl}^1\right]\delta(2) - \delta(1)\left[\partial_i G_{kl}^2\right]\right\}d\mathbf{x}$$

Writing out the function arguments, this reads

$$\overline{\mathcal{I}}_{ikl}(\mathbf{r}, \mathbf{r}') = \int_\mathcal{V}\left\{\left[\partial_i G_{kl}(\mathbf{x} - \mathbf{r})\right]\delta(\mathbf{r}' - \mathbf{x}) - \delta(\mathbf{x} - \mathbf{r})\left[\partial_i G_{kl}(\mathbf{r}' - \mathbf{x})\right]\right\}d\mathbf{x}. \tag{C.14}$$

We now proceed on a case-by-case basis depending on the positions of $\mathbf{r}, \mathbf{r}'$.

- First, if $\mathbf{r}$ and $\mathbf{r}'$ both lie outside the bounding surface $\mathcal{C}$, then neither δ function contributes and we have $\overline{\mathcal{I}} = 0$.

- If $\mathbf{r}$ lies inside $\mathcal{C}$ while $\mathbf{r}'$ lies outside $\mathcal{C}$, then only the second δ function contributes, and we find

$$\mathcal{I}_{ikl}(\mathbf{r}, \mathbf{r}') = -\partial_i G_{kl}(\mathbf{r}' - \mathbf{r})$$
$$= +\partial_i G_{kl}(\mathbf{r} - \mathbf{r}')$$

- If $\mathbf{r}$ lies outside $\mathcal{C}$ while $\mathbf{r}'$ lies inside $\mathcal{C}$, then only the first δ function contributes, and we find

$$\mathcal{I}_{ikl}(\mathbf{r}, \mathbf{r}') = \partial_i G_{kl}(\mathbf{r}' - \mathbf{r})$$
$$= -\partial_i G_{kl}(\mathbf{r} - \mathbf{r}').$$

- Finally, if both $\mathbf{r}$ and $\mathbf{r}'$ lie inside $\mathcal{C}$ then both δ functions contribute, their contributions cancel, and we find $\overline{\mathcal{I}} = 0$.

The result (C.5) is thus established, and our proof is complete.

The $\overline{\mathcal{J}}$ Kernel

The development of Chapter 5 also makes reference to a version of the $\mathcal{I}$ kernel defined in analogy to equations (C.1) and (C.2), but with the "$GG - CC$" structure of (C.2) replaced by a "$CG + GC$" structure:

$$\mathcal{J}_{ikl}(\mathbf{r}, \mathbf{r}') = \kappa^2 \oint_{\mathcal{C}} Y_A(\mathbf{r}, \mathbf{r}', \mathbf{x})\, n_A(\mathbf{x})\, d\mathbf{x} \tag{C.15}$$

$$Y_A(\mathbf{r}, \mathbf{r}', \mathbf{x}) = C^1_{ik}G^2_{lA} - \frac{\delta_{iA}}{2}C^1_{Bk}G^2_{lB} + G^1_{ik}C^2_{lA} - \frac{\delta_{iA}}{2}G^1_{Bk}C^2_{lB}. \tag{C.16}$$

We also define a symmetrized version defined in analogy to (C.3):

$$\overline{\mathcal{J}}_{ikl}(\mathbf{r}, \mathbf{r}') = \mathcal{J}_{ikl}(\mathbf{r}, \mathbf{r}') + \mathcal{J}_{ilk}(\mathbf{r}', \mathbf{r}).$$

In Appendix A (Equation A.6) we noted that the curl operation takes $\mathbf{G}$ into $\mathbf{C}$ and $\mathbf{C}$ into $-\mathbf{G}$. With this observation we see that (C.16) is obtained from (C.2) simply by taking the curl with respect to the k index, and thus that the $\overline{\mathcal{J}}$ kernel is the result of the same operation applied to the $\overline{\mathcal{I}}$ kernel:

$$\overline{\mathcal{J}}_{ikl}(\mathbf{r}, \mathbf{r}') = \frac{1}{\kappa}\varepsilon_{kAB}\partial_A \overline{\mathcal{I}}_{iBl}(\mathbf{r}, \mathbf{r}')$$

$$= \begin{cases} 0, & \text{if both } \mathbf{r}, \mathbf{r}' \text{ lie inside } \mathcal{C} \\[2mm] \dfrac{\partial}{\partial r_i}C_{kl}(\mathbf{r} - \mathbf{r}') & \text{if } \mathbf{r} \text{ lies inside and } \mathbf{r}' \text{ lies outside } \mathcal{C} \\[2mm] -\dfrac{\partial}{\partial r_i}C_{kl}(\mathbf{r} - \mathbf{r}') & \text{if } \mathbf{r} \text{ lies outside and } \mathbf{r}' \text{ lies inside } \mathcal{C} \\[2mm] 0, & \text{if both } \mathbf{r}, \mathbf{r}' \text{ lie outside } \mathcal{C}. \end{cases}$$

137

Appendix D

Evaluation of Singular Panel-Panel Integrals

In this Appendix we discuss a technique for evaluating singular panel-panel integrals of the type that enter into the computation of BEM matrix elements in Chapter 6. The technique that we present here is an expanded and generalized version of a technique published earlier by Taylor [45].

A problem that arises frequently in the numerical implementation of the FSC formulae using RWG basis functions (Chapter 6) is the evaluation of integrals of the form

$$\mathcal{I} = \frac{1}{4AA'} \int_{\mathcal{P}} d\mathbf{x} \int_{\mathcal{P}'} d\mathbf{x}' \, h(\mathbf{x}, \mathbf{x}') \, g(|\mathbf{x} - \mathbf{x}'|) \tag{D.1}$$

where $\mathcal{P}, \mathcal{P}'$ are triangular panels sharing one or more vertices (A, A' are the areas of the panels), h is a polynomial in the components of $\mathbf{x}, \mathbf{x}'$, and the kernel $g(r)$ depends only on the distance $r = |\mathbf{x} - \mathbf{x}'|$.

In many cases of interest, $g(r)$ will be singular at $r = 0$, precluding the evaluation of (D.1) by straightforward numerical cubature. In principle, we could proceed by writing the four-dimensional integral as four nested one-dimensional integrals (in which the limits of the inner integrals will depend on the outer integration variables) and evaluate the integral using four nested one-dimensional numerical quadratures, with the innermost quadratures evaluated using a singularity-aware quadrature rule. Alternatively, we could introduce a regularization parameter η to mitigate the singularities in g (for example, if g were $1/r^2$, we could put $g_\eta = 1/(r^2 + \eta^2)$), then evaluate (D.1) at multiple finite values of η and attempt to extrapolate to the $\eta \to 0$ limit. But neither of these methods would offer anything like the kind of efficiency needed to evaluate, in a reasonable amount of time, the millions of singular panel-panel integrals that arise in a typical Casimir computation.

The way out of this morass was shown by Taylor in 2003, who presented an ingenious scheme for efficient and accurate evaluation of singular panel-panel integrals [45]. Taylor's method proceeds by subdividing the four-dimensional domain of integration in (D.1) into M subdomains, then introducing new integration variables in each subdomain in such a way that Duffy transformations [11] may be employed to neutralize the $r = 0$ singularities of $g(r)$. (The number of subdomains

into which the original integral is divided is $M = \{3, 6, 2\}$ for the cases in which $\mathcal{P}$ and $\mathcal{P}'$ have $\{3, 2, 1\}$ common vertices; we refer to these respectively as the *common-panel, common-edge,* and *common-vertex* cases.) As an added bonus, this reorganization turns out to allow one or more of the four-dimensional integrals in (D.1) to be evaluated *analytically,* thus leaving behind a non-singular lower-dimensional integral that may be evaluated using straightforward numerical cubature. The price paid is that the integrand of this lower-dimensional integral is so exorbitantly complicated a function—involving antiderivatives of the h and g functions and containing dozens or hundreds of terms—that even to write it down, much less to implement it numerically, is itself a nontrivial computational challenge.

Taylor's original treatment [45] was restricted to certain specific choices of the h and g functions in (D.1). In this Appendix we present a generalized version of the technique that encompasses all cases of singular panel-panel integrals encountered in the implementation of CASIMIR3D. (Incidentally, we also correct two typographical errors in Taylor's original work [45]).

D.1 Parameterization of Integral

Let the triangle vertices be

$$\mathcal{P} = \{\mathbf{V}_1, \mathbf{V}_2, \mathbf{V}_3\} \qquad \mathcal{P}' = \{\mathbf{V}_1, \mathbf{V}_2', \mathbf{V}_3'\}$$

where $\mathbf{V}_1$ is always a common vertex; in the common-edge case we have additionally $\mathbf{V}_2' = \mathbf{V}_2$, and in the common-panel case we have additionally $\mathbf{V}_3' = \mathbf{V}_3$.

Put

$$\mathbf{A} = \mathbf{V}_2 - \mathbf{V}_1, \qquad \mathbf{B} = \mathbf{V}_3 - \mathbf{V}_2, \qquad \mathbf{A}' = \mathbf{V}_2' - \mathbf{V}_1, \qquad \mathbf{B}' = \mathbf{V}_3' - \mathbf{V}_2'.$$

Following Taylor's original notation, we parameterize points in the two triangles according to

$$
\begin{aligned}
\mathbf{x}(\xi_1, \xi_2) &= \mathbf{V}_1 + \xi_1 \mathbf{A} + \xi_2 \mathbf{B}, & 0 \le \xi_1 \le 1, & \qquad 0 \le \xi_2 \le \xi_1 \\
\mathbf{x}'(\eta_1, \eta_2) &= \mathbf{V}_1 + \eta_1 \mathbf{A}' + \eta_2 \mathbf{B}', & 0 \le \eta_1 \le 1, & \qquad 0 \le \eta_2 \le \eta_1.
\end{aligned}
$$

whereupon the integral (D.1) becomes

$$\mathcal{I} = \int_0^1 d\xi_1 \int_0^{\xi_1} d\xi_2 \int_0^1 d\eta_1 \int_0^{\eta_1} d\eta_2 \, h\big(\xi_1, \xi_2, \eta_1, \eta_2\big) \, g\big(\xi_1, \xi_2, \eta_1, \eta_2\big) \qquad (\text{D.2})$$

with

$$h\big(\xi_1, \xi_2, \eta_1, \eta_2\big) = h\big(\mathbf{x}(\xi_1, \xi_2), \mathbf{x}'(\eta_1, \eta_2)\big), \qquad g\big(\xi_1, \xi_2, \eta_1, \eta_2\big) = g\Big(R(\xi_1, \xi_2, \eta_1, \eta_2)\Big)$$

140

where the squared distance between points is

$$R^2(\xi_1, \xi_2, \eta_1, \eta_2) = \left| \mathbf{x}(\xi_1, \xi_2) - \mathbf{x}'(\eta_1, \eta_2) \right|^2$$

$$= \mathbf{A}^2 \xi_1^2 + \mathbf{B}^2 \xi_2^2 + \mathbf{A}'^2 \eta_1^2 + \mathbf{B}'^2 \eta_2^2$$
$$+ 2(\mathbf{A} \cdot \mathbf{B})\xi_1\xi_2 - 2(\mathbf{A} \cdot \mathbf{A}')\xi_1\eta_1 - 2(\mathbf{A} \cdot \mathbf{B}')\xi_1\eta_2$$
$$- 2(\mathbf{B} \cdot \mathbf{A}')\xi_2\eta_1 - 2(\mathbf{B} \cdot \mathbf{B}')\xi_2\eta_2 + 2(\mathbf{A}' \cdot \mathbf{B}')\eta_1\eta_2.$$

D.2 Kernel Integrals

The kernel function $g(r)$ in (D.1) enters into the master Taylor formulae only through the quantity

$$I_n(X) \equiv \int_0^1 \omega^n g(\omega X) d\omega.$$

This quantity is only ever evaluated for indices $n > 0$ and at nonzero values of the parameter X, which means that the powers of ω in the integrand neutralize the singularities of g.

This function is tabulated for a number of relevant kernel functions in the following table.

$g(r)$	$I_n(X)$
r^p	$\dfrac{1}{p+n}X^p$
$\dfrac{e^{-r}}{r}$	$(n-1)!\dfrac{e^{-X}}{X^{n+1}}\texttt{ExpRel}(n, X)$
$(1+r)\dfrac{e^{-r}}{r^3}$	$\dfrac{e^{-X}}{X^{n+1}}\left[(n-2)! \cdot \texttt{ExpRel}(n-1, X) + (n-3)! \cdot \texttt{ExpRel}(n-2, X)\right]$

where the nth *relative exponential* function is just $\exp(X)$ with the first n terms of its Taylor series subtracted:[1]

$$\texttt{ExpRel}(n, X) \equiv e^X - \sum_{m=0}^{f-1} \frac{X^m}{m!}. \tag{D.3}$$

---

[1]Note that our relative exponential function is similar to, but distinct from, that defined by the GSL (http://www.gnu.org/software/gsl/).

D.3 Common Panel

In the common-panel case the four-dimensional integral (D.1) is reduced to a one-dimensional integral with a complicated integrand:

$$\mathcal{I} = \int_0^1 dx \left\{ \sum_{i=1}^3 \sum_\alpha S_{i\alpha}^{\mathrm{CP}}(x) I_{\alpha+1}\Big(X_i(x) \Big) \right\}. \tag{D.4}$$

Here the reduced distance functions for the three regions are

$$X_i^{\mathrm{CP}}(x) \equiv \sqrt{\mathbf{A}^2 u_{1i}^2(x) + \mathbf{B}^2 u_{2i}^2(x) + 2(\mathbf{A}\cdot\mathbf{B}) u_{1i}(x) u_{2i}(x)}$$

with the u_{ni} functions defined by

i	$u_{1i}(x)$	$u_{2i}(x)$
1	1	x
2	x	$(x-1)$
3	x	1

and the $S_{i\alpha}^{\mathrm{CP}}$ functions are defined by a two-step process:

(1) We first introduce three two-variable functions $H_i^{\mathrm{CP}}(u_1, u_2)$ defined as definite integrals involving the h polynomial:

$$H_i^{\mathrm{CP}}(u_1, u_2) \equiv \int_{L_i^{\xi_1}}^{U_i^{\xi_1}} \int_{L_i^{\xi_2}}^{U_i^{\xi_2}} h(\xi_1, \xi_2, u_1 + \xi_1, u_2 + \xi_2)\, d\xi_2\, d\xi_1 \tag{D.5}$$

with the limits of integration as tabulated below.

i	$L_i^{\xi_1}$	$U_i^{\xi_1}$	$L_i^{\xi_2}$	$U_i^{\xi_2}$
1	0	$1 - u_1$	0	ξ_1
2	$-u_2$	$1 - u_1$	$-u_2$	ξ_1
3	$u_2 - u_1$	$1 - u_1$	0	$\xi_1 - (u_2 - u_1)$

(2) Since h is a polynomial in its variables, H_i^{CP} is a polynomial in *its* variables, and thus the expressions

$$H_i^{\mathrm{CP}}\Big(\omega u_{1i}(x), \omega u_{2i}(x) \Big)$$

define polynomials in ω (whose coefficients are themselves polynomials in x). The S^{CP} functions that enter into (D.4) are just the coefficients of ω^α in these polynomials, i.e.

$$H_i^{\mathrm{CP}}\Big(\omega u_{1i}(x), \omega u_{2i}(x) \Big) \equiv \sum_\alpha S_{i\alpha}^{\mathrm{CP}}(x)\, \omega^\alpha. \tag{D.6}$$

The RHS of this equation defines not only the $S_{i\alpha}^{\mathrm{CP}}$ functions but also the limits of the α summation in (D.4).

D.4　Common Edge

In the common-edge case the four-dimensional integral (D.1) is reduced to a two-dimensional integral with a complicated integrand:

$$\mathcal{I} = \int_0^1 x_1 dx_1 \int_0^1 dx_2 \left\{ \sum_{i=1}^6 \sum_\alpha S_{i\alpha}^{\text{CE}}(x_1, x_2) I_{\alpha+2}\Big(X_i(x_1, x_2) \Big) \right\} \qquad (\text{D}.7)$$

Here the reduced distance functions for the six regions are ($\mathbf{L} \equiv \mathbf{B}' - \mathbf{B}$)

$$X_i^{\text{CE}}(x_1, x_2) \equiv \Big[\mathbf{A}^2 u_{1i}^2 + \mathbf{B}^2 u_{2i}^2 + \mathbf{L}^2 \xi_{2i}^2$$

$$+ 2(\mathbf{A} \cdot \mathbf{B}') u_{1i} u_{2i} + 2(\mathbf{A} \cdot \mathbf{L}) u_{1i} \xi_{2i} + 2(\mathbf{B}' \cdot \mathbf{L}) u_{2i} \xi_{2i} \Big]^{1/2}$$

where u_{1i}, u_{2i}, ξ_{2i} are functions of (x_1, x_2) :

i	$u_{1i}(x_1, x_2)$	$u_{2i}(x_1, x_2)$	$\xi_{2i}(x_1, x_2)$
1	$-x_1$	$-x_1 x_2$	$(1 - x_1 + x_1 x_2)$
2	x_1	$x_1 x_2$	$(1 - x_1)$
3	$-x_1 x_2$	$x_1(1 - x_2)$	$(1 - x_1)$
4	$x_1 x_2$	$-x_1(1 - x_2)$	$(1 - x_1 x_2)$
5	$-x_1 x_2$	$-x_1$	1
6	$x_1 x_2$	x_1	$1 - x_1$

and where the $S_{i\alpha}^{\text{CE}}$ functions are again defined by a two-step process:

(1) We first introduce six three-variable functions $H_i^{\text{CE}}(u_1, u_2, \xi_2)$ defined as definite integrals involving the h polynomial:

$$H_i^{\text{CE}}(u_1, u_2, \xi_2) \equiv \int_{L_i^{\xi_1}}^{U_i^{\xi_1}} h(\xi_1, \xi_2, u_1 + \xi_1, u_2 + \xi_2) \, d\xi_1 \qquad (\text{D}.8)$$

with the limits of integration as tabulated below.

i	$L_i^{\xi_1}$	$U_i^{\xi_1}$
1	$\xi_2 + (u_2 - u_1)$	1
2	ξ_2	$1 - u_1$
3	$\xi_2 + (u_2 - u_1)$	1
4	ξ_2	$1 - u_1$
5	ξ_2	1
6	$\xi_2 + (u_2 - u_1)$	$1 - u_1$

(2) Again, since h is a polynomial in its variables, H_i^{CE} is a polynomial in *its* variables, and thus the expressions

$$H_i^{\text{CE}}\Big(\omega u_{1i}(x_1, x_2), \omega u_{2i}(x_1, x_2), \omega \xi_{2i}(x_1, x_2) \Big)$$

143

define polynomials in ω (whose coefficients are themselves polynomials in x_1, x_2). The S^{CE} functions that enter into (D.7) are just the coefficients of ω^α in these polynomials, i.e.

$$H_i^{\text{CE}}\Big(\omega u_{1i}(x_1, x_2), \omega u_{2i}(x_1, x_2), \omega \xi_{2i}(x_1, x_2)\Big) \equiv \sum_\alpha S_{i\alpha}^{\text{CE}}(x_1, x_2)\, \omega^\alpha. \qquad \text{(D.9)}$$

The RHS of this equation defines not only the $S_{i\alpha}^{\text{CE}}$ functions but also the limits of the α summation in (D.7).

D.5 Common Vertex

In the common-vertex case the four-dimensional integral (D.1) is reduced to a three-dimensional integral with a complicated integrand:

$$\mathcal{I} = \int_0^1 dx_1 \int_0^1 x_2 dx_2 \int_0^1 dx_3 \left\{ \sum_{i=1}^2 \sum_\alpha S_{i\alpha}^{\text{CV}}(x_1, x_2, x_3) I_{\alpha+3}\Big(X_i(x_1, x_2, x_3)\Big) \right\} \qquad \text{(D.10)}$$

Here the reduced distance functions for the two regions are

$$
\begin{aligned}
X_i^{\text{CV}}(x_1, x_2, x_3) \equiv \Big[& \mathbf{A}^2 \xi_{1i}^2 + \mathbf{B}^2 \xi_{2i}^2 + \mathbf{A}'^2 \eta_{1i}^2 + \mathbf{B}'^2 \eta_{2i}^2 \\
& + 2(\mathbf{A} \cdot \mathbf{B})\xi_{1i}\xi_{2i} - 2(\mathbf{A} \cdot \mathbf{A}')\xi_{1i}\eta_{1i} - 2(\mathbf{A} \cdot \mathbf{B}')\xi_{1i}\eta_{2i} \\
& - 2(\mathbf{B} \cdot \mathbf{A}')\xi_{2i}\eta_{1i} - 2(\mathbf{B} \cdot \mathbf{B}')\xi_{2i}\eta_{2i} + 2(\mathbf{A}' \cdot \mathbf{B}')\eta_{1i}\eta_{2i} \Big]^{1/2}
\end{aligned}
$$

where ξ_{1i}, ξ_{2i}, η_{1i}, η_{2i} are functions of x_1, x_2, x_3:

i	$\xi_{1i}(x_1, x_2, x_3)$	$\xi_{2i}(x_1, x_2, x_3)$	$\eta_{1i}(x_1, x_2, x_3)$	$\eta_{2i}(x_1, x_2, x_3)$
1	1	x_1	x_2	$x_2 x_3$
2	x_2	$x_2 x_3$	1	x_1

and where the $S_{i\alpha}^{\text{CV}}$ functions are defined, slightly more simply than in the previous two cases, as the coefficients of powers of ω in an evaluation of the original h polynomial with arguments containing factors of ω:

$$
h\Big(\omega \xi_{1i}(x_1, x_2, x_3), \omega \xi_{2i}(x_1, x_2, x_3), \omega \eta_{1i}(x_1, x_2, x_3), \omega \eta_{2i}(x_1, x_2, x_3)\Big)
$$
$$
\equiv \sum_\alpha S_{i\alpha}^{\text{CV}}(x_1, x_2, x_3)\, \omega^\alpha. \qquad \text{(D.11)}
$$

The RHS of this equation defines not only the $S_{i\alpha}^{\text{CV}}$ functions but also the limits of the α summation in (D.10).

144

D.6 Implementation Notes

Before concluding this Appendix we pause to make some brief observations regarding numerical implementations of the master Taylor formulae.

Evaluation of the Relative Exponential Function

The relative exponential function was defined in equation (D.3). In practice we will often need to evaluate this function at small arguments $X \ll 1$, and for this purpose a naïve implementation of the defining equation (D.3) is *not* adequate—at least not in finite-precision arithmetic—as e^X will be dominated by the first few terms in its Taylor expansion, and subtracting these from the value computed by a floating-point library implementation of `exp(X)` will yield little more than numerical noise.

In practice, for positive values of the argument X, an adequate alternative strategy is simply to appeal to the equivalent alternative definition

$$\texttt{ExpRel}(n, X) \equiv \sum_{m=n}^{\infty} \frac{X^m}{m!}$$

with the infinite sum truncated as soon as the terms fall below some predefined error threshold.

Computation of the S^{CP}, S^{CE}, and S^{CV} Polynomials

The reader will not fail to have noticed the extremely unwieldy definitions (equations (D.6), (D.9), and (D.11)) of the polynomials $S_{i\alpha}^{\mathrm{CP}}(x)$, $S_{i\alpha}^{\mathrm{CE}}(x_1, x_2)$, and $S_{i\alpha}^{\mathrm{CV}}(x_1, x_2, x_3)$ that enter into the integrands of (D.4), (D.7), and (D.10).

These functions, which are defined in terms of the h polynomial in (D.1), are already complicated even for the simplest case of a *constant* h polynomial (the only case considered in Taylor's original treatment [45]), while their complexity grows rapidly as the degree of h increases. This is especially true for the particular cases of h polynomials that happen to be relevant for the purposes of this thesis (namely, the three defined by equations (6.6), which are of degrees 2, 0, and 3, and contain large numbers of terms.) To give just one example, for the particular case $h_\bullet(\mathbf{x}, \mathbf{x}') = (\mathbf{x} - \mathbf{Q}) \cdot (\mathbf{x}' - \mathbf{Q}')$ that arises when computing the $L_\bullet$ panel-panel integral discussed in Chapter 6, the function $S_{i\alpha}^{\mathrm{CE}}(x_1, x_2)$ for index values $i = 1, \alpha = 3$ reads

$$
\begin{aligned}
S_{13}^{\mathrm{CE}}(x_1, x_2) =& \left(\mathbf{B} \cdot \mathbf{B}' + \mathbf{A} \cdot \mathbf{B}\right) x_1^2 x_2 - \left(\mathbf{B} \cdot \mathbf{B}' + \frac{1}{2}\mathbf{A} \cdot \mathbf{B}\right) x_1 x_2 \\
&- \left(\mathbf{B} \cdot \mathbf{B}' + \mathbf{A} \cdot \mathbf{B}\right) x_1^2 + \left(\frac{1}{2}\mathbf{A}^2 + 2\mathbf{B} \cdot \mathbf{B}' + \frac{3}{2}\mathbf{A} \cdot \mathbf{B} + \frac{1}{2}\mathbf{A} \cdot \mathbf{B}'\right) x_1 \\
&- \frac{1}{3}\mathbf{A}^2 - \mathbf{B} \cdot \mathbf{B}' - \frac{1}{2}\mathbf{A} \cdot \mathbf{B}' - \frac{1}{2}\mathbf{A} \cdot \mathbf{B}.
\end{aligned}
\tag{D.12}
$$

For the common-edge case alone there are, in total, 24 such polynomials, in addition to 15 polynomials in the common-panel case and 12 polynomials in the common-

vertex case. And all of this only for the single choice $h = h_\bullet$; the case $h = h_\times$ is even worse!

Although each operation in the sequence of steps that defines the S polynomials is straightforward (definite integration of polynomials, collection of terms, identification of coefficients), the sheer *magnitude* of the tedious and error-prone pen-and-pencil drudgery involved in writing down the S functions for a given h polynomial strains the boundaries of human computational ability—so much so, indeed, that the Taylor method for higher-order h polynomials would be useless in practice were it not for the saving grace of *computer algebra systems*. Indeed, given an arbitrary h polynomial it is a simple matter—a few lines of code—to coax a system such as MAXIMA or MATHEMATICA to evaluate definite integrals over h, collect the terms in equations (D.6), (D.9), and (D.11), identify the coefficients of the various powers of ω, and emit expressions for all required cases of the S polynomials. These expressions will be numerous and tedious, as witness equation (D.12), but this is of little concern, as we need only copy these numerous and tedious expressions into a separate code module that will be parsed and evaluated by a different computer system (in the case of CASIMIR3D, a C++ compiler) to generate a function that calculates numerical values for the integrands in (D.4), (D.7), and (D.10). This function, in turn, we use as the integrand of a numerical quadrature scheme to evaluate the integrals, and—*voila!*—Taylor's method becomes a useful computational procedure even for complicated h polynomials.

Appendix E

Evaluation of Singular Segment-Segment Integrals

In this Appendix we discuss a series of techniques for evaluating singular segment-segment integrals of the type that enter into the computation of BEM matrix elements in Chapter 7. Although the techniques are based on standard mathematical manipulations, including change-of-integration-variables and Duffy transformations [11], we emphasize that these standard mathematical manipulations are applied here for the first time to the computation of matrix elements for two-dimensional BEM problems.

A problem that arises frequently in the numerical implementation of the FSC formulae using TDRT basis functions (Chapter 7) is the evaluation of integrals of the form

$$\int_0^1 du \int_0^1 du' \, u^p u'^q F\Big(R(u, u')\Big) \tag{E.1}$$

where u and u' parameterize distance along two line segments $(\mathbf{X}_s, \mathbf{X}_e)$ and $(\mathbf{X}'_s, \mathbf{X}'_e)$,

$$\mathbf{x}(u) = \mathbf{X}_s + u(\mathbf{X}_e - \mathbf{X}_s), \qquad \mathbf{x}'(u') = \mathbf{X}'_s + u'(\mathbf{X}'_e - \mathbf{X}'_s),$$

$$R(u, u') = \big|\mathbf{x}(u) - \mathbf{x}(u')\big|,$$

and $F(R)$ is singular at $R = 0$. If the two line segments share one or both vertices, then this singularity is encountered within the region of integration, thwarting numerical cubature and requiring more sophisticated treatment. In this Appendix we discuss general techniques for circumventing these singularities.

E.1 The Common-Segment Case

In the case $\mathbf{X}_S = \mathbf{X}'_S$, $\mathbf{X}_E = \mathbf{X}'_E$, we have $R(u, u') = l|u - u'|$ (with l the length of the line segment). In this case we put $s = (u + u')$, $t = (u - u')$ and rewrite the general

integral over the unit square in the form

$$\int_0^1 du \int_0^1 du' \, I(u, u')$$

$$= \frac{1}{2} \left[\int_0^1 ds \int_{-s}^s dt + \int_1^2 ds \int_{-(2-s)}^{2-s} dt \right] I \left(\frac{1}{2}(s+t), \frac{1}{2}(s-t) \right)$$

Change variables to $s \rightarrow 2 - s$ in the second integral:

$$= \frac{1}{2} \int_0^1 ds \int_{-s}^s dt \left[I \left(\frac{1}{2}(s+t), \frac{1}{2}(s-t) \right) + I \left(\frac{1}{2}(2-s+t), \frac{1}{2}(2-s-t) \right) \right]$$

Applying this reorganization to the particular case (E.1), we have

$$\int_0^1 du \int_0^1 du' \, u^p u'^q F \Big(R(u, u') \Big)$$

$$= \frac{1}{2^{p+q+1}} \int_0^1 ds \int_{-s}^s dt \left[(s+t)^p (s-t)^q + (2-s+t)^p (2-s-t)^q \right] F \Big(l|t| \Big)$$

$$= \frac{1}{2^{p+q}} \int_0^1 ds \int_0^s dt \left[(s+t)^p (s-t)^q + (2-s+t)^p (2-s-t)^q \right]^* F \Big(l|t| \Big). \qquad \text{(E.2)}$$

where the $*$ superscript on the square brackets indicates that we retain only even powers of t in the bracketed polynomial.

E.2   The Common-Vertex Case

The common-vertex case is that in which precisely one of $\{\mathbf{X}_s, \mathbf{X}_e\}$ coincides with one of $\{\mathbf{X}'_s, \mathbf{X}'_e\}$. There are four possibilities for how this may happen; we will consider the subcase $\mathbf{X}_s = \mathbf{X}'_s$, $\mathbf{X}_e \neq \mathbf{X}'_e$, while the other three subcases may be handled by taking $u \rightarrow 1 - u$ and/or $u' \rightarrow 1 - u'$.

The key technique that facilitates the evaluation of (E.1) in this case is the Duffy transform [11], used here for the *second* time in this thesis (the first time being in Appendix D).

In the case $\mathbf{X}_s = \mathbf{X}'_s$, $\mathbf{X}_e \neq \mathbf{X}'_e$ we have

$$R(u, u') = \sqrt{l^2 u^2 + l'^2 u'^2 - 2ll' \cos\theta \, uu'}$$

where $\theta \neq 0$ is the angle between the line segments. We note in general that integrals over the unit square may be decomposed into

$$\int_0^1 du \int_0^1 du' \{ \cdots \} = \int_0^1 du \int_0^u du' \{ \cdots \} + \int_0^1 du' \int_0^{u'} du \{ \cdots \}$$

Applying this decomposition to (E.1), in the first integral we make the Duffy trans-

formation $u' = ut, du' = udt$ and find

$$\int_0^1 du \int_0^u du'\, u^p u'^q F\big(R(u, u')\big) = \int_0^1 du\, u^{p+q+1} \int_0^1 dt\, t^q F\big(ul' X_1(t)\big),$$

$$\left(X_1(t) = \sqrt{t^2 - 2ty\cos\theta + y^2}, \qquad y = \frac{l}{l'} \right).$$

In the second integral we put $u = u't$ and find instead

$$\int_0^1 du' \int_0^{u'} du\, u^p u'^q F\big(R(u, u')\big) = \int_0^1 du'\, u'^{(p+q+1)} \int_0^1 dt\, t^p F\big(u'l X_2(t)\big),$$

$$\left(X_2(t) = \sqrt{t^2 - 2tx\cos\theta + x^2} \qquad x = \frac{l'}{l} \right).$$

Combining the two integrals and renaming $u' \to u$ in the second integral, our original integral (E.1) now reads

$$\int_0^1 du \int_0^u du'\, u^p u'^q F\Big(R(u, u')\Big)$$

$$= \int_0^1 dt \int_0^1 du\, u^{p+q+1} \left[t^q F\Big(ul' X_1(t)\Big) + t^p F\Big(ul X_2(t)\Big) \right].$$

The point of this reorganization is that, as long as $F(R)$ does not blow up more rapidly than $1/R^{p+q+1}$ at the origin, the u integral here is explicitly nonsingular.

Appendix F

Evaluation of $\mathcal{J}_r^{pq}$ Integrals

In this Appendix we evaluate the $\mathcal{J}_r^{pq}$ integrals defined in 7. (To our knowledge no explicit evaluation of these integrals has appeared in the literature before).

In Chapter 7 we introduced a quantity $\mathcal{J}_r^{pq}$ associated with a pair of line segments and defined according to

$$\mathcal{J}_r^{pq} = \int_0^1 du \int_0^1 du'\, u^p u'^q S_r\Big(R(u,u')\Big), \qquad (\text{F.1})$$

where

$$\left\{ \begin{array}{c} S_1 \\ S_2 \\ S_3 \\ S_4 \end{array} \right\}(R) = \left(\begin{array}{c} 1 \\ \log R \\ 1/R^2 \\ 1/R^4 \end{array} \right).$$

and where

$$R(u,u') = \Big|\mathbf{R}_0 + u\mathbf{l} - u'\mathbf{l}'\Big|$$

is the distance between points on two line segments. In what follows it will be convenient to recast this quadratic polynomial in the alternative form

$$R^2(u,u') = l^2\big[(u+u_0)^2 + b^2\big]$$

with the dimensionless geometrical quantities

$$u_0 \equiv r_0\cos\phi - u'x\cos\theta, \qquad b^2 \equiv r_0^2 + u'^2 x^2 - 2u'xr_0\cos\phi' - u_0^2 \qquad (\text{F.2})$$

$$r_0 \equiv |\mathbf{R}_0|/l, \qquad x = l'/l$$

$$\cos\theta \equiv \frac{\mathbf{l}\cdot\mathbf{l}'}{xl^2}, \qquad \cos\phi \equiv \frac{\mathbf{l}\cdot\mathbf{R}_0}{r_0 l^2}, \qquad \cos\phi' \equiv \frac{\mathbf{l}'\cdot\mathbf{R}_0}{xr_0 l^2}.$$

Before getting started, we note the trivial result

$$
\begin{pmatrix} \mathcal{J}_1^{00} \\ \mathcal{J}_1^{10} \\ \mathcal{J}_1^{01} \\ \mathcal{J}_1^{11} \end{pmatrix} = \begin{pmatrix} 1 \\ \frac{1}{2} \\ \frac{1}{2} \\ \frac{1}{4} \end{pmatrix} . \tag{F.3}
$$

The evaluation of (F.1) for the remaining cases now proceeds in different ways depending on the number of vertices shared by the two line segments.

F.1 Two Common Vertices

When the two line segments in question have two vertices in common (i.e. they are the same line segment, traversed either in the same or in opposite directions), only a small subset of the possible cases of (F.1) are needed, and we may evaluate these using the the common-segment technique discussed in the previous Appendix, with the results

$$
\begin{pmatrix} \mathcal{J}_2^{00} \\ \mathcal{J}_2^{10} \\ \mathcal{J}_2^{01} \\ \mathcal{J}_2^{11} \end{pmatrix} = \begin{pmatrix} \log l - \frac{3}{2} \\ \frac{1}{2} \log l - \frac{3}{4} \\ \frac{1}{2} \log l - \frac{3}{4} \\ \frac{1}{4} \log l - \frac{7}{16} \end{pmatrix} \tag{F.4}
$$

for the case in which the two line segments are traversed in the same direction (i.e. $\mathbf{l} = \mathbf{l}'$), or

$$
\begin{pmatrix} \mathcal{J}_2^{00} \\ \mathcal{J}_2^{10} \\ \mathcal{J}_2^{01} \\ \mathcal{J}_2^{11} \end{pmatrix} = \begin{pmatrix} \log l - \frac{3}{2} \\ \frac{1}{2} \log l - \frac{3}{4} \\ \frac{1}{2} \log l - \frac{3}{4} \\ \frac{1}{4} \log l - \frac{5}{16} \end{pmatrix} \tag{F.5}
$$

for the case in which the two line segments are traversed in opposite directions (i.e. $\mathbf{l} = -\mathbf{l}'$.)

Equations (F.3) and (F.4-F.5) are the only cases of (F.1) that we need for the common-segment case.

F.2 One Common Vertex

When the two line segments in question have one vertex in common, we can use the Duffy-transform technique discussed in the previous Appendix to evaluate all needed cases of (F.1) in closed form, with the following results:

1. $S(R) = \log R$:

$$\int_0^1 du \int_0^1 du' \, u^p u'^q S\Big(R(u, u')\Big)$$

$$= \int_0^1 dt \int_0^1 du \, u^{p+q+1} \left\{ t^q \big[\log u + \log l' + \log X_1(t)\big] \right.$$

$$\left. + t^p \big[\log u + \log l + \log X_2(t)\big] \right\}$$

$$= \frac{1}{p+q+2} \left[\frac{(p+1)\log l' + (q+1)\log l - 1}{(p+1)(q+1)} + \mathcal{A}_q(y, \theta) + \mathcal{A}_p(x, \theta) \right]$$

$$\tag{F.6}$$

2. $S(R) = 1/R^2$:

$$\int_0^1 du \int_0^1 du' \, u^p u'^q S\Big(R(u, u')\Big)$$

$$= \int_0^1 dt \int_0^1 du \, u^{p+q+1} \left[\frac{t^q}{u^2 l'^2 X_1^2(t)} + \frac{t^p}{u^2 l^2 X_2^2(t)} \right]$$

$$= \frac{1}{p+q} \left[\frac{1}{l'^2} \mathcal{B}_q(y, \theta) + \frac{1}{l^2} \mathcal{B}_p(x, \theta) \right]$$

$$\tag{F.7}$$

where the $\mathcal{A}$ and $\mathcal{B}$ functions are

$$\mathcal{A}_p(x, \theta) = \int_0^1 t^p \log \sqrt{t^2 - 2tx\cos\theta + x^2}$$

$$\mathcal{B}_p(x, \theta) = \int_0^1 \frac{t^p dt}{\big[t^2 - 2tx\cos\theta + x^2\big]}.$$

Both of these integrals may be evaluated in closed form for arbitrary $p \geq 0$.

Equations (F.3) and (F.6-F.7) are the only cases of (F.1) that we need for the common-vertex case.

F.3   Zero Common Vertices

Finally, we consider the evaluation of (F.1) in the case in which l, l' have no common vertices. In this case, although the full integrals may not be evaluated in closed form as in the common-segment or common-vertex cases, nonetheless it is extremely convenient that *one* of the two integrals in (F.1) (which we will here choose to be the u integral) may be performed analytically in all cases, leaving behind a one-dimensional integral over u' which we evaluate by straightforward numerical quadrature.

153

Thus we find

$$\mathcal{J}_2^{pq} = \frac{\log l}{(p+1)(q+1)} + \int_0^1 u'^q \mathcal{A}_p(u')du'$$

$$\mathcal{J}_3^{pq} = \frac{1}{l^2} \int_0^1 u'^q \mathcal{B}_p(u')du'$$

$$\mathcal{J}_4^{pq} = \frac{1}{l^4} \int_0^1 u'^q \mathcal{C}_p(u')du'$$

where we have put

$$\mathcal{A}_p(u') = \int_0^1 u^p \log\left[(u+u_0)^2 + b^2\right]du$$

$$\mathcal{B}_p(u') = \int_0^1 u^p \left[(u+u_0)^2 + b^2\right]^{-2}du$$

$$\mathcal{C}_p(u') = \int_0^1 u^p \left[(u+u_0)^2 + b^2\right]^{-4}du$$

where $u_0 = u_0(u'), b = b(u')$ as in equation (F.2). These integrals may be evaluated in closed form in all the cases we will need, with results collected below.

$$\mathcal{A}_0(u') = b\zeta_1 + \frac{1}{2}(u_0+1)\zeta_3 - \frac{1}{2}u_0\zeta_2 - 1$$

$$\mathcal{A}_1(u') = -bu_0\zeta_1 + \frac{1}{4}\zeta_3 + \frac{1}{4}(b^2 - u_0^2)\zeta_4 + \frac{1}{2}u_0 - \frac{1}{4}$$

$$\mathcal{A}_2(u') = \frac{1}{6}\zeta_3 - \left(\frac{b^2 u_0}{2} - \frac{u_0^3}{6}\right)\zeta_4 - \frac{1}{3}b(b^2 - 3u_0^2)\zeta_1 + \frac{u_0}{6} + \frac{1}{3}(b^2 - u_0^2) - \frac{1}{9}$$

$$\mathcal{B}_0(u') = \frac{1}{b}\zeta_1$$

$$\mathcal{B}_1(u') = \frac{1}{2}\zeta_4 - \frac{u_0}{b}\zeta_1$$

$$\mathcal{B}_2(u') = \frac{(u_0^2 - b^2)}{b}\zeta_1 - u_0\zeta_4 + 1$$

$$\mathcal{C}_1(u') = \frac{b(1+u_0) - u_0\left(b^2 + (1+u_0)^2\right)\zeta_1}{2b^3\left(b^2 + (1+u_0)^2\right)}$$

$$\mathcal{C}_2(u') = \frac{(b^2 + u_0^2)\left(b^2 + (1+u_0)^2\right)\zeta_1 - b(b^2 + u_0^2 + u_0)}{2b^3\left(b^2 + (1+u_0)^2\right)}$$

154

$$\zeta_1 = \arctan \frac{u_0 + 1}{b} - \arctan \frac{u_0}{b}$$

$$\zeta_2 = \log \left[b^2 + u_0^2 \right]$$

$$\zeta_3 = \log \left[b^2 + (u_0 + 1)^2 \right]$$

$$\zeta_4 = \zeta_3 - \zeta_2.$$

Appendix G

Command-Line Options for CASIMIR3D

CASIMIR3D is a standalone command-line application that applies FSC techniques to compute Casimir energies, forces, and torques among compact 3D objects of arbitrary shapes and material properties.

A command-line invocation of CASIMIR3D takes the form

where the command-line options are summarized in the following tables.

Options controlling the geometry to be simulated	
--geometry MyFile.rwggeo	Specifies the .rwggeo file that describes the Casimir geometry. This option is always mandatory.
--translist MyTransList	Specifies the file containing the list of transformations under which to compute Casimir interactions. This option is always mandatory.

Options controlling the quantities calculated	
--energy --xforce --yforce --zforce --torque x y z --alltorque	Specify which quantities to compute. You may specify any combination of these options, but at least one must be present.

157

Options controlling frequency behavior	
`--Xi 1.2`	Requests that the energy, force, and/or torque integrands be calculated at a single imaginary frequency.
`--XiList MyXiList`	Requests that the energy, force, and/or torque integrands be calculated at a series of imaginary frequencies listed in the specified file.
`--temperature T`	Requests that Matsubara sums be performed to evaluate the Casimir energy, force, and/or torque at the specified temperature.
`--fiMethod xx`	Requests that numerical quadrature method xx be used to evaluate the imaginary-frequency integral for the zero-temperature Casimir energy, force, and/or torque.

Options controlling evaluation of Casimir quantities	
`--siMethod FSC`	Requests that the Casimir energy, force, and torque at each imaginary frequency be computed using the FSC (log-det / trace) formulae. This is the default.
`--siMethod mesh` `--siMesh MySurfaceMesh.msh`	Requests that the Casimir energy, force, and torque at each imaginary frequency be computed using the numerical stress-tensor method, with the stress-tensor integrated over the specified surface mesh.

Other Options	
`--VisualizeOnly`	Requests that CASIMIR3D terminate immediately after generating visualization files, without doing any Casimir computations.
`--WriteSpatialData`	Requests that CASIMIR3D generate `.spatialdata` files containing spatially-resolved stress-tensor data. (This option may only be specified in conjunction with `--siMethod mesh`.)
`--WriteHDF5`	Requests that CASIMIR3D export the BEM matrices and their derivatives to binary `.hdf5` data files, which may subsequently be used (among other things) to import the matrices into MATLAB for inspection and analysis.

Appendix H

Command-Line Options for CASIMIR2D

CASIMIR2D is a standalone command-line application that applies FSC techniques to compute Casimir energies, forces, and torques among quasi-2D objects of arbitrary cross-sectional shapes and arbitrary material properties.

A command-line invocation of CASIMIR2D takes the form

where the command-line options are summarized in the following tables.

Options controlling the geometry to be simulated	
`--geometry MyFile.tdgeo`	Specifies the `.tdgeo` file that describes the Casimir geometry. This option is always mandatory.
`--translist MyTransList`	Specifies the file containing the list of transformations under which to compute Casimir interactions. This option is always mandatory.

Options controlling the quantities calculated	

`--energy`
`--xforce`
`--yforce`
	Specify which quantities to compute. You may specify any combination of these options, but at least one must be present.

Options controlling frequency behavior	
`--Xi 1.2 --Q 2.1`	Requests that the energy and/or force integrands be calculated at a single point in the (ξ, q) plane.
`--XQList MyXQList`	Requests that the energy and/or force integrands be calculated at a series of points in the (ξ, q) plane, as listed in the specified file.
`--Xi 1.2`	Requests that the full q integral be evaluated numerically at the specified fixed value of ξ.
`--Q 1.2`	Requests that the full ξ integral be evaluated numerically at the specified fixed value of Q.
`--temperature T`	Requests that Matsubara sums be performed to evaluate the Casimir energy and/or force at the specified temperature.
`--CubatureMethod xx`	Requests that numerical cubature method **xx** be used to evaluate the full two-dimensional integral (over the upper-right quadrant of the (ξ, q) plane) for the zero-temperature Casimir energy, force, and/or torque.

Other Options	
`--VisualizeOnly`	Requests that CASIMIR2D terminate immediately after generating visualization files, without doing any Casimir computations.
`--WriteHDF5`	Requests that CASIMIR2D export the BEM matrices and their derivatives to binary `.hdf5` data files, which may subsequently be used (among other things) to import the matrices into MATLAB for inspection and analysis.

Bibliography

[1] Temer S. Ahmadi, Zhong L. Wang, Travis C. Green, Arnim Henglein, and Mostafa A. El-Sayed. *Science*, 272:1924, 1996.

[2] J. Berntsen and T. Espelid. *ACM Trans. Math. Soft.*, 18:329, 1992.

[3] J. Berntsen, T. Espelid, and A. Genz. *ACM Trans. Math. Soft.*, 17:452, 1991.

[4] H. A. Bethe. *Phys. Rev.*, 72:339, 1947.

[5] M. Bordag, D. Robaschik, and E. Wieczorek. *Ann. Phys.*, 165:192, 1985.

[6] F. Capasso, J. N. Munday, D. Iannuzzi, and H. B. Chan. *IEEE. J. Select. Topic Quantum Electron.*, 13:400, 2007.

[7] H. B. G. Casimir. *Koninkl. Ned. Adak. Wetenschap. Proc.*, 51:793, 1948.

[8] H. B. G. Casimir and D. Polder. *Phys. Rev.*, 73:360, 1948.

[9] A. Christ and H. L. Hartnagel. *IEEE Trans. Microwave Theory*, 35:688–696, 1987.

[10] R. Cools. *J. Complexity*, 19:445, 2003.

[11] M. G. Duffy. *SIAM J. Numer. Anal.*, 19:1260, 1982.

[12] M. Bleszynski E. Bleszynski and T. Jaroszewicz. *Radio Science*, 31:1225, 1996.

[13] T. Ederth. *Phys. Rev. A*, 62:062104, 2000.

[14] T. Emig and R. Buscher. *Nucl. Phys. B.*, 696:468, 2004.

[15] T. Emig, N. Graham, R. L. Jaffe, and M. Kardar. *Phys. Rev. Lett.*, 99:170403, 2007.

[16] T. Emig, N. Graham, R. L. Jaffe, and M. Kardar. *Phys. Rev. D.*, 77:025005, 2008.

[17] Roger F. Harrington. *Field Computation by Moment Methods*. Wiley-IEEE Press, 1993.

[18] E. M. Lifshitz I. E. Dzyaloshinkii and L. P. Pitaevskii. *Sov. Phys. Usp.*, 4:153, 1961.

[19] J. D. Jackson. *Classical Electrodynamics*. John Wiley & Sons, 1999.

[20] J. Jin. *The Finite Element Method in Electromagnetics*. New York: Wiley, 2 edition, 2002.

[21] R. Jin, Y. Cao, C. A. Mirkin, K. L. Kelly, G. C. Schatz, and J. G. Zheng. *Science*, 294:1901, 2001.

[22] Steven G. Johnson. *arXiv.org e-Print archive*, July 2010. To appear in upcoming *Lecture Notes in Physics* book on *Casimir Physics*.

[23] P. Kusch and H. M. Foley. *Phys. Rev.*, 74:250, 1948.

[24] W. E. Lamb and R. C. Retherford. *Phys. Rev.*, 72:241, 1947.

[25] S. K. Lamoreaux. *Phys. Rev. Lett.*, 78:5, 1997.

[26] H. Li and M. Kardar. *Phys. Rev. Lett.*, 67:3275, 1991.

[27] H. Li and M. Kardar. *Phys. Rev. A*, 46:6490, 1991.

[28] Le-Wei Li. In *Proceedings of the 40th European Microwave Conference*, page 545, Paris, France, September 2010.

[29] M. Li, W. H. P. Pernice, and H. X. Tang. *Nature Photonics*, 3:464, 2009.

[30] E. M. Lifschitz and L. P. Pitaevskii. *Statistical Physics: Part 2*. Pergamon, Oxford, 1980.

[31] Tao Lu and David Yevick. *Journal of Lightwave Technology*, 21:1793, 2003.

[32] L. N. Medgyesi-Mitschang, J. M. Putnam, and M. B. Gedera. *J. Opt. Soc. Am. A*, 11:1383, 1994.

[33] J. N. Munday, F. Capasso, and V.A. Parsegian. *Nature (London)*, 457:170, 2009.

[34] Ardavan F. Oskooi, David Roundy, Mihai Ibanescu, Peter Bermel, J. D. Joannopoulos, and Steven G. Johnson. *Computer Physics Communications*, 181:687–702, 2010.

[35] S. Pasquali and A. C. Maggs. http://arxiv.org/abs/0801.4385 (2008).

[36] J. R. Phillips and J. K. White. *IEEE Trans. Comput.-Aided Design Integr. Circuits Syst.*, 16:1059, 1997.

[37] S. J. Rahi, Thorsten Emig, Noah Graham, Robert L. Jaffe, and Mehran Kardar. *Phys. Rev. D*, 80:085021, 2009.

[38] S. M. Rao, D. R. Wilton, and A. W. Glisson. *IEEE Trans. Antennas Propagat.*, AP-30:409, 1982.

[39] M. T. H. Reid, Alejandro W. Rodriguez, Jacob White, and Steven G. Johnson. *Phys. Rev. Lett.*, 103:040401, 2009.

[40] A. W. Rodriguez, M. Ibanescu, D. Iannuzzi, J. D. Joannopoulos, and S. G. Johnson. *Phys. Rev. A*, 76:032106, 2007.

[41] A. W. Rodriguez, A. P. McCauley, D. Woolf, F. Capasso, J. D. Joannopoulos, and S. G. Johnson. *Phys. Rev. Lett.*, 104:160402, 2010.

[42] S. Scheel and S. Y. Buhmann. *Acta Physica Slovaca*, 58:675, 2008.

[43] J. Schwinger. *Phys. Rev.*, 73:416L, 1948.

[44] J. A. Stratton and L. J. Chu. *Phys. Rev.*, 56:99, 1939.

[45] D. J. Taylor. *IEEE Trans. Antennas Propagat.*, 51:1630, 2003.

[46] J. Volakis and D. Davidson. *IEEE Antennas and Propagation Magazine*, 47:1, 2005.

[47] J. L. Volakis, A. Chatterjee, and L. C. Kempel. *Finite Element Method Electromagnetics: Antennas, Microwave Circuits, and Scattering Applications.* New York: IEEE Press, 2001.

[48] D. R. Wilton, S. M. Rao, A. W. Glisson, D. H. Schaubert, O. M. Al-Bundak, and C. M. Butler. *IEEE Trans. Antennas Propagat.*, 32:276, 1984.

[49] J. L. Xiong, M. S. Tong, P. Atkins, and W. C. Chew. *Phys. Lett. A*, 374:2517.